

RENSIT: RadioElectronics. NanoSystems. Information Technologies

Journal "Radioelectronics. Nanosystems. Information Technologies" (abbr. RENSIT) publishes original articles, reviews and brief reports, not previously published, on topical problems in **radioelectronics (including biomedical) and fundamentals of information, nano- and biotechnologies and adjacent areas of physics and mathematics.**

Designed for **researchers, graduate students, physics students of senior courses and teachers.** It turns out **2 times a year** (that includes 2 issues)

Authors of journal are academicians, corresponding members and foreign members of Russian Academy of Natural Sciences (RANS) and their colleagues, as well as other russian and foreign authors on presentation of their manuscripts by the members of RANS, which can be obtained by authors before sending articles to editors. And also after its receiving - on recommendation of a member of editorial board of journal, or another member of Academy of Natural Sciences, that gave her opinion on article at request of editor. The editors will accept articles in both **Russian and English** languages.

Articles are internally peer reviewed (**double-blind peer review**) by members of the Editorial Board. Some articles undergo external review, if necessary.

Journal RENSIT is included in the **DB SCOPUS, EBSCO Publishing**, in the international abstracts database - **Ulrich's International Periodicals Directory**, (USA, New York, <http://www.ulrichsweb.com>), in the **AJ and DB VINITI RAS** (<http://www.viniti.ru>), and DB **Russian Science Citation Index (RSCI)** (http://elibrary.ru/project_risc.asp).

Full-text content is posted in the DB of the **Russian Scientific Electronic Library** - information resource on the Internet <http://elibrary.ru> and is available for registered users. And also - in Open Access **CyberLeninka NEB** of Russian Federation <http://cyberleninka.ru>.

On journal's website <http://www.rensit.ru> posted metadata publications and **RENSIT: Radioelectronics. Nanosystems. Information Technologies - english version** (cover-to-cover translation) of journal, which is a party to **CrossRef**.

The founder - the **Russian Academy of Natural Sciences**
Publisher - Publishing Center of the Russian Academy of Natural Sciences
Publisher Address: 29/16, Sivtsev Vrazhek lane, Moscow 119002, Russian Federation

CONTENTS

MULTIDIMENSIONAL THEORIES OF PHYSICAL FIELDS

- ELECTROMAGNETIC FIELD IN THE EXTENDED SPACE
5-DIMENSIONAL MODEL, ITS LOCALIZATION AND INTERACTION
WITH WAVEGUIDE
Vladimir A. Andreev, Dmitry Yu. Tsipenyuk 93

CONDENSED MATTER PHYSICS

- FUNDAMENTAL SYSTEM OF EQUATIONS FOR MOMENTUM AND
ENERGY OF ELECTROMAGNETIC FIELD IN INHOMOGENEOUS
MEDIUM
Arthur A. Dyshekov 103
- METRIC AND STRUCTURE EQUATIONS IN RELATIVISTIC CONTINUA
Stanislav A. Podosenov, Alexander A. Potapov, Jaykov Foukzon, Ekaterina R. Men'kova 113

NUCLEAR PHYSICS

- THEORY OF COLD NUCLEAR FUSION REACTIONS
Gennady V. Myshinsky 125
- SYNTHESIS OF CHEMICAL ELEMENTS UNDER IRRADIATION BY
BRAKING GAMMA-RAYS OF PALLADIUM IN CONDENSED GASES
Alexander Yu. Didyk, Roland Wiśniewski, Teresa Wilczyńska-Kitowska, Gennady
V. Mishinsky, Vasily A. Semin 143

RADIOELECTRONICS

- GENERATION OF OPTICAL SIGNALS RESISTANT TO DISPERSION-
INDUCED POWER DEGRADATION
Vladislav V. Shcherbakov, Anatoly F. Solodkov, Anatoly A. Zadernovsky 161

NANOSYSTEMS

- LOCALIZATION OF PHOTONS IN THE OPTICAL METAMATERIAL
WITH RANDOM CLOSE TO ZERO REFLECTION INDICATOR
Oleg N. Gadomsky, Nikolay M. Ushakov, Irina V. Gadomskaya 177
- FUNCTIONAL ELASTOMERIC COMPOSITE MATERIALS BASED ON
STYRENE-BUTADIENE RUBBER AND MAGNETITE
Anton .A. Khachaturov, Alexander S. Fionov, Vladimir V. Kolesov, Evgeny E.
Potapov, Yuri V. Il'in 189
- MAGNETOCALORIC EFFECT IN CARBON-CONTAINING COMPOUNDS
Victor V. Korolev, Tatyana N. Lomova, Anna G. Ramazanova 199

INFORMATION TECHNOLOGIES

- VISUALIZATION OF GRAPHIC INFORMATION IN GENERAL-PURPOSE
OPERATING SYSTEMS
Konstantin V. Pugin, Kirill A. Mamrosenko, Alexander M. Giatsintov 217

MEDICAL PHYSICS

- INVESTIGATION OF THE 0.5-4 HZ LOW-FREQUENCY RANGE IN THE
WAVE TRAIN ELECTRICAL ACTIVITY OF MUSCLES IN PATIENTS WITH
PARKINSON'S DISEASE AND ESSENTIAL TREMOR
Olga S. Sushkova, Alexei A. Morozov, Alexandra V. Gabova, Alexei V. Karabanov,
Larisa A. Chigaleychik 225
- NEW APPROACH TO THE DETECTION OF EPILEPTIFORM ACTIVITY
IN EEG SIGNALS AND METHODS TO DIFFERENTIATE EPILEPTIC
SEIZURES FROM CHEWING ARTIFACTS
Ivan A. Kershner, Mikhail V. Sinkin, Yuri V. Obukhov 237
- ESTIMATION OF INTER-CHANNEL PHASE SYNCHRONIZATION OF
EEG SIGNALS IN THE RIDGES OF THEIR WAVELET SPECTROGRAMS
IN PATIENTS WITH TRAUMATIC BRAIN INJURY
Renata A. Tolmacheva, Yuri V. Obukhov, Lyudmila A. Zhavoronkova 243



RUSSIAN ACADEMY
OF NATURAL SCIENCES

DEPARTMENT OF
RADIOELECTRONICS,
NANOPHYSICS AND
INFORMATION TECHNOLOGIES
PROBLEMS

RENSIT:

**RADIOELECTRONICS.
NANOSYSTEMS.
INFORMATION
TECHNOLOGIES.**

2019, VOL. 11, № 2

FOUNDED IN 2009

3 ISSUES PER YEAR

MOSCOW

Editor-in-Chief

VLADIMIR I. GRACHEV
grachev@cplire.ru

Deputy Chief

ALEXANDER S. ILUSHIN

Deputy Chief

SERGEY P. GUBIN

Executive Secretary

ROSTISLAV V. BELYAEV
belyaev@cplire.ru

EDITORIAL BOARD

Anatoly V. Andreev
Vladimir A. Bushuev
Vladimir A. Cherepenin
Alexander S. Dmitriev
Yuri K. Fetisov
Yuri V. Gulyaev
Yaroslav A. Ilushin
Anatoly V. Kozar
Vladimir V. Kolesov
Albina A. Kornilova
Vladimir A. Makarov
Aleksey P. Oreshko
Andrey I. Panas
Igor B. Petrov
Alexander A. Potapov
Vyacheslav S. Rusakov
Alexander S. Sigov
Valentine M. Silonov
Eugeny S. Soldatov
Arkady B. Tsepelev
Lkhamsuren EnkhTUR (Mongolia)
Yoshiyuki Kawazoe (Japan)
Kairat K. Kadyrzhanov (Kazakhstan)
Peter Paul Mac Ken (USA)
Andre Skirtach (Belgium)
Eugeny V. Ushpuras (Republic
of Lithuania)
Enrico Verona (Italy)

ISSN 2414-1267 online

The journal is registered by the Ministry of Telecom
and Mass Communications of the Russian Federation.
Certificate El. no. FS77-60275 on 19.12.2014

All rights reserved. No part of this publication
may be reproduced in any form or by any means
without permission in writing from the publisher.

©RANS 2019

EDITORIAL BOARD ADDRESS
218-219 of., 7 b., 11, Mokhovaya str.,
125009 MOSCOW, RUSSIAN FEDERATION
TEL. +7 495 629 3368
FAX +7 495 629 3678 FOR VLADIMIR I. GRACHEV

ELECTROMAGNETIC AND GRAVITATIONAL FIELDS IN THE 5-DIMENSIONAL EXTENDED SPACE MODEL, THEIR LOCALIZATION AND INTERACTION WITH MATTER

Vladimir A. Andreev

Lebedev Physics Institute of RAS, <http://www.lebedev.ru/>
Moscow 119991, Russian Federation

Dmitry Yu. Tsipenyuk

Prokhorov General Physics Institute of RAS, <http://gpi.ras.ru/>
Moscow 119991, Russian Federation
andrvmad@yandex.ru, tsip@kapella.gpi.ru

Abstract. Electromagnetic and gravitational fields are considered within the framework of the 5-dimensional Extended space model (ESM). The action is considered as the fifth coordinate. It is shown that in this model they are combined into a single electromagnetic-gravitational field. This field has 10 components: the vector field \vec{G} and scalar field Q are added to the usual 6 fields \vec{E} and \vec{H} . These fields satisfy the system of generalized Maxwell's equations. We find an expression for the Lorentz force, which determines the interaction of these fields with charged massive bodies. In the framework of this model, the question of the origin of the photon non-zero mass and its localization is studied.

Keywords: 5-dimensional space, electromagnetic field, gravity, Maxwell's equations, photon, mass, localization

PACS 11.10 Kk, 03.50.-z, 03.65. Pm

Bibliography - 27 references

RENSIT, 2019, 11(2):93-102

Received 12.11.2018, accepted 21.1.2019

DOI: 10.17725/rensit.2019.11.093

CONTENTS

1. INTRODUCTION (93)
 2. CURRENTS AND POTENTIALS (95)
 3. STRESS FIELDS AND THE GENERALIZED SYSTEM OF MAXWELL'S EQUATIONS (96)
 4. GENERALIZED LORENTZ FORCE (98)
 5. LOCALIZATION OF FIELDS AND PARTICLES (99)
 6. CONCLUSION (100)
- REFERENCES (101)

1. INTRODUCTION

The problem of combining electromagnetic and gravitational fields into a single field has been discussed since the late 19th century. It is characteristic that all these attempts have been made on the way of constructing geometric models of physical interactions and interpretation of physics as geometry in the spaces of a larger number of dimensions. In the late 19th century, German mathematician Felix Klein [1] constructed the Hamilton-Jacobi theory as optics in the space of the highest number of dimensions. However,

at that time his ideas did not developed. A new surge of interest to the problem of geometrization of physics was stimulated by the creation of the General theory of relativity (GRT) [2]. The attempts to describe electromagnetism in geometric terms by analogy with gravity were made.

Their authors did not try to create a new model, but tried to expand the existing GRT scheme in one way or another. The most known were the models of T. Kaluza [3] and O. Klein [4]. Also noteworthy are the works of H. Mandel [5] and V. Fock [6]. It is characteristic that all they had to use a 5-dimensional space. The problem of physical interpretation of the fifth coordinate has not been solved satisfactorily. Hereinafter many scientists, including Einstein [7], de Broglie, Gamow, Rumer [8] tried to develop these approaches, but they failed to get any interesting results. In our opinion, the reason is that their works have been based on formal generalizations of existing models, without involving new physical ideas.

We should also mention the theory of gauge fields as one of the directions of geometrization of physical interactions [9]. Within this ideology, electromagnetism, gravity, and other interactions are considered from a single geometric point of view [10].

Later, in order to create the theory of elementary particles, another approach to combining gravity with other interactions was developed.

The need to take into account the gravitational field in the description of the interaction of elementary particles was indicated 50 years ago by K.P. Stanyukovich [11] and M.A. Markov [12]. They put forward the hypothesis of the existence of heavy particles – planckions and maximons.

The authors assumed that there are three fundamental constants in nature: the Planck constant \hbar , the speed of light c , and the gravitational constant G . These values can be used to construct expressions with dimensions of length, time, and mass. They are called Planck length l_{pl} , Planck time t_{pl} and Planck mass m_{pl}

$$\begin{aligned}
 l_{pl} &= \sqrt{\frac{\hbar G}{c^3}} \approx 10^{-33} \text{ sm}, \\
 t_{pl} &= \sqrt{\frac{\hbar G}{c^5}} \approx 10^{-43} \text{ sec}, \\
 m_{pl} &= \sqrt{\frac{\hbar c}{G}} \approx 10^{-5} \text{ gr}.
 \end{aligned}
 \tag{1}$$

In quantum theory a particle with a mass of m corresponds to the Compton wavelength

$$\lambda_{\bar{h}} = \frac{\hbar}{mc}.
 \tag{2}$$

This wavelength can be associated with the particle size, some of its "quantum radius". If the Planck mass m_{pl} is put in the formula (2), it turns out that the Compton wavelength coincides with the Planck length l_{pl}

$$\lambda_{\bar{h}} = l_{pl}.
 \tag{3}$$

But another linear parameter can be associated with mass m – the Schwarzschild gravitational radius

$$r_{gr} = \frac{Gm}{c^2}.
 \tag{4}$$

According to the General theory of relativity, if a spherical-symmetric distribution of matter is compressed to such dimensions, it collapses, forming a black hole. Therefore, it is now considered that the value of m_{pl} is the maximum value of the mass of an elementary particle. They are called maximons. Particles with large masses should turn into black holes. Accordingly, the corresponding gravitational radius r_{gr} can be considered as the minimum possible size of an elementary particle.

If one substitute the Planck mass m_{pl} in the formula (4), it will take the form

$$r_{gr} = 2\sqrt{\frac{\hbar G}{c^3}} = 2l_{pl}.
 \tag{5}$$

Thus, the gravitational radius of maximon coincides in order of magnitude with Planck length.

In Landau's work [13], estimates for the value of the "radius" of elementary particles were obtained, based on the limit of applicability of electrodynamics representations in quantum mechanics. Interestingly, the "radius" of the electron at the same time was equal to zero.

Such relations were discussed in an attempt to take into account the gravitational forces in the processes of interaction of elementary particles. This approach assumes the initial existence of particles with a large rest mass, and since we do not observe such objects, it is not clear how it can be used to describe the processes occurring in the laboratory.

Our approach is fundamentally different from all these and similar theories. The Extended space model (ESM) is based on the physical hypothesis that the mass (rest mass) and its conjugate action (interval) are dynamic variables, the value of which is determined by the interaction of fields and particles. In this respect, our model is a direct generalization of the special theory of relativity (SRT), in SRT the interval and rest mass of particles are invariants, in ESM they can change. In particular, a photon can acquire mass, both positive and negative. This mass can appear and change as a consequence of electromagnetic interaction and generate gravitational forces. It is

this circumstance that allows us to consider gravity and electromagnetism as a unit field.

Different aspects of the ESM are set out in articles [14-18]. In this paper, we give a systematic exposition of the formalism of the electromagnetic-gravitational field, introduce a generalized system of Maxwell's equations, which satisfy its tensions, and find an expression for the Lorentz force, which defines its interaction with matter.

2. CURRENTS AND POTENTIALS

The source of the electromagnetic field is a current. In the traditional formulation the electromagnetic current is described by (1+3) vector in Minkowski space $M(1,3)$ [18].

$$\tilde{\rho} = (\rho, \vec{j}) = \left(\frac{\rho_0 c}{\sqrt{1-\beta^2}}, \frac{\rho_0 \vec{v}}{\sqrt{1-\beta^2}} \right), \beta^2 = \frac{v^2}{c^2}, \tilde{\rho}^2 = c^2. \quad (6)$$

Here $\rho_0(t, x, y, z)$ is the density of electric charge at the point (t, x, y, z) in the space $M(1,3)$, and $v_x(t, x, y, z), v_y(t, x, y, z), v_z(t, x, y, z)$ – is local velocity of the charge density.

In transition to the extended space $G(1,4)$ the (1+3) current vector $\tilde{\rho}$ should be replaced by (1+4) vector $\bar{\rho}$. In accordance with the principles that form the basis of the developed model, the additional coordinate of the vector $\bar{\rho}$ is introduced in such a way that the resulting (1+4) vector is isotropic. In addition, we want our model to describe both the electromagnetic field and the gravitational field, so the fifth component of the current should be defined so that it serves as a source of the gravitational field.

We believe that the source of a single electromagnetic gravitational field is a particle that has both mass and charge. In this case, we assume that the mass may not have a charge, but the charge must always have a mass. In our model, we assume that the charge is a constant value, and does not change with transformations from the group of rotations $L(1,4)$ of the extended space $G(1,4)$. And the rest mass, which was a scalar with respect to the Lorentz group, is a component of the vector with respect to the group $L(1,4)$.

We want to obtain a 5-dimensional current vector $\bar{\rho}$ as a generalization of the 4-dimensional

current vector $\tilde{\rho}$. To do this, it is necessary to assign another component.

The current vector (6) is structurally similar to the energy-momentum vector of a particle, having a rest mass. The difference between them is, that in the vector (6) instead of a rest mass m_0 there is a local density of a charge ρ_0 . In the transition to the extended space $G(1,4)$ we pass from the energy-momentum vector to the energy-momentum-mass vector, and in the transition from mechanics to electrodynamics the mass changes to a charge. But, because we want to get a current that will simultaneously serve as a source of both electromagnetic and gravitational field, we multiply each component of the energy-momentum-mass vector on the density of a charge ρ_0 , while maintaining the mass density m . For brevity, we will denote the charge density by the letter e . Thus, the 5-dimensional current vector generating a single electromagnetic-gravitational field has the form

$$\bar{\rho} = (j_0, \vec{j}, j_4) = \left(\frac{emc}{\sqrt{1-\beta^2}}, \frac{em\vec{v}}{\sqrt{1-\beta^2}}, emc \right). \quad (7)$$

This is an isotropic vector $\bar{\rho}^2 = 0$.

The continuity equation, as in the usual case, is expressed as zero 5-divergence of 5-current

$$\sum_{i=0}^4 \frac{\partial j_i}{\partial x_i} = 0. \quad (8)$$

If the charge is at rest, the continuity equation takes the form

$$\frac{\partial m}{\partial t} + \frac{\partial m}{\partial x_4} = 0. \quad (9)$$

The ratio (9) can be interpreted as the law of change in the rest mass of a particle due to changes in the properties of the environment.

In ordinary electrodynamics the law of charge conservation follows from the continuity equation

$$\frac{\partial}{\partial t} \int j_0 dV = - \int \vec{j} d\vec{n}. \quad (10)$$

In the left part of this relation there is an integral on volume, and on the right – an integral on a surface limiting this volume.

In electrogravity, there is a law of conservation of the value, which is the product of the charge to the mass of the particle, which has this charge. This law has the form

$$\frac{\partial}{\partial t} \int j_0 dV = - \int \vec{j} d\vec{n} - \int \frac{\partial}{\partial x_4} j_4 dV. \quad (11)$$

In this case the change of the value of the product of em charge per mass inside a certain volume is determined both by the flow of charged particles through the surface of this volume and by change of the mass of particles inside the volume due to their dependence on the coordinate x_4 . Thus, we do not violate the law of charge conservation, since the mass changes in the product of em , and the charge remains constant.

The current (7) generates an electro-gravitational field in the extended space $G(1,4)$. This field is given by a 5-vector-potential A .

$$A = (A_t, A_x, A_y, A_z, A_s) = (A_0, A_1, A_2, A_3, A_4). \quad (12)$$

Here and below we use the notation $t = x_0, x = x_1, y = x_2, z = x_3, s = x_4$.

The components of this vector-potential are determined by the equations

$$\Pi_{(s)} A_0 = -4\pi\varphi, \quad (13)$$

$$\Pi_{(s)} \vec{A} = -\frac{4\pi}{c} \vec{j}, \quad (14)$$

$$\Pi_{(s)} A_s = -\frac{4\pi}{c} j_s. \quad (15)$$

Here

$$\Pi_{(s)} = \frac{\partial^2}{\partial s^2} + \frac{\partial^2}{\partial x^2} + \frac{\partial^2}{\partial y^2} + \frac{\partial^2}{\partial z^2} - \frac{1}{c^2} \frac{\partial^2}{\partial t^2}. \quad (16)$$

Note that in the case when the dependence on the coordinate s is absent and the mass m , which is included in the current components (7), is a constant, the system of equations (13)-(15) splits into two independent parts. The equations (13), (14) define the usual potentials of the electromagnetic field, and the equation (15) defines the potential of the scalar gravitational field. In this case these fields exist independently of each other. They are combined into one field only when the mass of m becomes a variable and there is a dependence on the coordinate s .

3. STRESS FIELDS AND THE GENERALIZED SYSTEM OF MAXWELL'S EQUATIONS

The stress tensor can be constructed from potentials $(A_0, A_x, A_y, A_z, A_s)$

$$F_{ik} = \frac{\partial A_i}{\partial x_k} - \frac{\partial A_k}{\partial x_i}; i, k = 0, 1, 2, 3, 4. \quad (17)$$

$$\|F_{ik}\| = \begin{pmatrix} 0 & -E_x & -E_y & -E_z & -Q \\ E_x & 0 & -H_z & H_y & -G_x \\ E_y & H_z & 0 & -H & -G_y \\ E_z & -H_y & H_x & 0 & -G_z \\ Q & G_x & G_y & G_z & 0 \end{pmatrix}. \quad (18)$$

Here

$$Q = F_{40} = \frac{\partial A_4}{\partial x_0} - \frac{\partial A_0}{\partial x_4} = \frac{\partial A_s}{c \partial t} - \frac{\partial \varphi}{\partial s}. \quad (19)$$

$$G_x = F_{41} = \frac{\partial A_4}{\partial x_1} - \frac{\partial A_1}{\partial x_4} = \frac{\partial A_s}{\partial x} - \frac{\partial A_x}{\partial s},$$

$$G_y = F_{42} = \frac{\partial A_4}{\partial x_2} - \frac{\partial A_2}{\partial x_4} = \frac{\partial A_s}{\partial y} - \frac{\partial A_y}{\partial s}, \quad (20)$$

$$G_z = F_{43} = \frac{\partial A_4}{\partial x_3} - \frac{\partial A_3}{\partial x_4} = \frac{\partial A_s}{\partial z} - \frac{\partial A_z}{\partial s}.$$

We give equations which satisfy the tensions F_{ik} . We call them the Maxwell extended system.

The usual system of Maxwell's equations consists of two pairs of equations that have a fundamentally different structure. They are usually called, the first and second pair of Maxwell's equations. The extended system of Maxwell equations also consists of two types of equations of fundamentally different structure, but now they are not two, but more, so we will call them not the first and second pair, but the equations of the first and second types.

The equations of the first type are formal consequence of the formula (17) expressing tensions through potentials. It directly follows from its form that for any three indices (i, j, k) the relation is executed

$$\frac{\partial F_{ij}}{\partial x_k} + \frac{\partial F_{ki}}{\partial x_j} + \frac{\partial F_{jk}}{\partial x_i} = 0. \quad (21)$$

The validity of the equation (21) is checked by direct substitution. Indeed, substituting in the equation (21) the expression (17) for stresses via potentials, we have

$$\frac{\partial^2 A_i}{\partial x_k \partial x_j} - \frac{\partial^2 A_j}{\partial x_k \partial x_i} + \frac{\partial^2 A_k}{\partial x_j \partial x_i} - \frac{\partial^2 A_i}{\partial x_j \partial x_k} + \frac{\partial^2 A_j}{\partial x_i \partial x_k} - \frac{\partial^2 A_k}{\partial x_i \partial x_j} = 0.$$

We have as many such equations as there are different sets of indices (i, j, k) , i.e. the number of combinations from 5 to 3, which is equal to 10. Let us now consider the specific forms of these equations, using the stress tensor (18).

If we limit ourselves to sets of indices that take values $(0, 1, 2, 3)$, then the corresponding 4 equations are just the first pair of Maxwell's equations

$$\text{div} \vec{H} = 0, \quad \sim \text{indexes } (1, 2, 3) \quad (22)$$

This is one equation, the other 3 corresponding to the index sets $(0, 1, 2)$, $(0, 1, 3)$, $(0, 2, 3)$, combined into a single vector equation

$$\text{rot} \vec{E} + \frac{1}{c} \frac{\partial \vec{H}}{\partial t} = 0. \quad (23)$$

Thus, the first pair of Maxwell's equations retains its form. In the extended space $G(1,4)$ six more equations are added to them. Three of them, responding sets $(1, 2, 4)$, $(1, 3, 4)$, $(2, 3, 4)$, can be combined into one vector equation

$$\text{rot} \vec{G} + \frac{\partial \vec{H}}{\partial s} = 0. \quad (24)$$

Three other threes $(0, 1, 4)$, $(0, 2, 4)$, $(0, 3, 4)$ give three remaining equations of the first class. They also can be combined into a single vector equation

$$\frac{\partial \vec{E}}{\partial s} + \frac{1}{c} \frac{\partial \vec{G}}{\partial t} + \text{grad} Q = 0. \quad (25)$$

Thus, the equations of the first type included of the extended Maxwell system equations in space $G(1,4)$ read (22)-(25). These 10 equations are combined in a vector 3 equations and one scalar. Note that the vector operators *div*, *rot*, *grad* have the usual 3-dimensional form.

Let us now proceed to construction second type Maxwell equations of the. These equations follow from the equations for potentials (13)-(15). However, it is necessary first to impose a Lorentz

gauge condition that must be satisfied by the potential (12). In the space $G(1,4)$ it reads

$$\frac{1}{c} \frac{\partial A_0}{\partial t} + \frac{\partial A_x}{\partial x} + \frac{\partial A_y}{\partial y} + \frac{\partial A_z}{\partial z} + \frac{\partial A_s}{\partial s} = 0. \quad (26)$$

The second type equations from the extended Maxwell system has the form

$$\sum_{k=0}^4 \frac{\partial F_{ik}}{\partial x_k} = -\frac{4\pi}{c} j_i; \quad i = 0, 1, 2, 3, 4. \quad (27)$$

Substituting the stress tensor elements (18) in (27) and considering the Lorentz gauge condition (26), we obtain 5 equations. In vector form they take the form

$$\text{div} \vec{E} + \frac{\partial Q}{\partial s} = 4\pi \rho, \quad (i = 0), \quad (28)$$

$$\text{rot} \vec{H} - \frac{\partial \vec{G}}{\partial s} - \frac{1}{c} \frac{\partial \vec{E}}{\partial t} = \frac{4\pi}{c} \vec{j}, \quad (i = 1, 2, 3), \quad (29)$$

$$\text{div} \vec{G} + \frac{1}{c} \frac{\partial Q}{\partial t} = 4\pi j_4, \quad (i = 4). \quad (30)$$

The stress tensor (18) contains, in addition to components that are analogous to conventional electric and magnetic fields, additional components that describe the gravitational field. More specifically, in the case where the components of the 5-current (7) depend on the coordinate x_4 , all components of the tensor (18) describe the unified electromagnetic-gravitational field, if the current does not depend on the coordinate x_4 , then the system of equations (22)-(25), (28)-(30) splits into two parts. At the system of Maxwell equations and the Laplace equation for the scalar gravitational field.

Thus, according to our model, in the empty space gravitational and electromagnetic fields exist separately, and in the area where external forces act at particles and fields, they are combined into one field.

We discuss briefly the physical meaning of the equations of extended Maxwell system (22)-(25), (28)-(30).

Equation (22) shows that there are no magnetic charges does not appear in this model and its magnetic lines of force still remain closed.

It follows from equation (23) that, as before, the circulation of the electric field in a closed loop is determined only by the change in the

magnetic field inside this contour. In this case, the fact that the fields \vec{E} and \vec{H} can now depend on the variable s , not felt by the equations (22), (23), because they include only derivatives of the usual spatial and temporal variable.

The equation (24) shows that the circulation of the new field \vec{G} by an arbitrary spatial closed loop is defined by a change of the field \vec{H} covered by this contour over the new variable s .

The physical meaning of the equation (25) is that it relates the change the old field \vec{E} by the new variable s with change of the new fields Q and \vec{G} by old variables. If the field \vec{E} is changed by the s variable, then an inhomogeneous field Q and a nonstationary field \vec{G} should exist in space.

The equation (28) shows that the electric charges of density ρ and the change of the field of Q by the variable s can be considered as the source of the electric field is \vec{E} . The electric field lines can start and end not only on electric charges, but also at those points where there is a change of the field Q on the variable s .

It follows from the equation (29) that the circulation of the magnetic field \vec{H} by a closed loop is defined not only by the current flowing inside the loop and by change of the electric field \vec{E} covered by it, but also by change of the field \vec{G} , located inside the contour on the variable s .

The equation (30) shows that the source of the field \vec{G} can be not only the charges forming the current component j_p , but also change in time of the field Q . The lines of the field \vec{G} lines can start and end not only at electric charges, but also at those points where the derivative $\partial Q/\partial t$ is different from zero.

4. GENERALIZED LORENTZ FORCE

Now we find the forces acting on the point charged particle located in the field (18), and the equations of motion of such a particle. Let us write Lagrangian of the system particle+field for a particle of mass of m and charge e and a field given by the potential (12). Choose it as

$$L = -mc^2\sqrt{1-\beta^2} + mcv_s - e\phi + \frac{e}{c}(\vec{A}\vec{v} + A_s v_s). \quad (31)$$

Here $v_s = ds/dt$.

The Lagrangian (31) differs from the usual Lagrangian describing motion of charged particle in an external field by a member $(e/c)A_s v_s$. And it is assumed in addition that all 5 components of the potentials (12) depend on the variable s . This leads to the fact that mass m of the particle depends on time $m = m(t)$. This result is quite consistent with the original postulates of the model. Indeed, according to our assumptions, only mass of free particle is constant. But if it interacts with other particles, its mass may vary.

Interaction constant e/c , with which the product $A_s v_s$ is included in the Lagrangian, is the same as at the products of spatial component of the potential and velocity of the particle $\vec{A}\vec{v}$. This is necessary for that the equations of motion of the particle include only the field strength (18), not its potentials (12). As in the usual classic electrodynamics, we believe that the observed values are intensities of the field, not its potentials.

The momentum of the particle is determined by the formula

$$P_i = \frac{\partial L}{\partial v_i}. \quad (32)$$

From the Lagrangian (31) we obtain

$$\vec{P} = \vec{p} + \frac{e}{c}\vec{A} = \frac{m\vec{v}}{\sqrt{1-\beta^2}} + \frac{e}{c}\vec{A}. \quad (33)$$

$$P_s = p_s + \frac{e}{c}A_s = mc + \frac{e}{c}A_s. \quad (34)$$

By Lagrangian one can construct Euler's equations of motion, which in general case have the form [19, 20]

$$\frac{d}{dt} \frac{\partial L}{\partial v_i} = \frac{\partial L}{\partial x_i}. \quad (35)$$

These are four equations. First three of them read

$$\frac{d\vec{p}}{dt} = e\vec{E} + \frac{e}{c}[\vec{v}, \vec{H}]. \quad (36)$$

In form they coincide with the usual equations of motion of charged particle. The only difference

is that now the particle's mass m depends on time. This dependence is determined by the equation

$$\frac{dp_s}{dt} = eQ + \frac{e}{c}[\vec{v}, \vec{G}]. \quad (37)$$

Given that $p_s = mc$ and the speed of light c is constant, we obtain the equation evolution of mass m

$$\frac{dm}{dt} = \frac{e}{c}Q + \frac{e}{c^2}(\vec{v}, \vec{G}). \quad (38)$$

Thus, four equations (37)-(38) describe the evolution of four values $v_x(t), v_y(t), v_z(t), m(t)$.

The equation (38) shows that in presence of an external field a mass of a particle changes. Below we will look at specific examples and find exact solutions equations (36)-(38) and interpret them in terms of rotations in the extended space $G(1,4)$.

5. LOCALIZATION OF FIELDS AND PARTICLES

In the framework of the ESM, it is possible to establish in natural way connection between photon mass and some linear parameter, which we will call the localization parameter. In some sense, it can be considered as the size of a photon. The starting point for us is analogy between dispersion relation of a free particle

$$E^2 = (c\vec{p})^2 + m^2c^4 \quad (39)$$

and dispersion relation of a wave mode in a hollow metal waveguide

$$\omega^2 = \omega_{kr}^2 + (c\xi)^2. \quad (40)$$

Here ω_{kr} – is the critical frequency of the waveguide mode, and ξ – is the wave propagation constant.

The similarity of the relations (39) and (40) was noticed by de Broglie [21], Feynman [22] and other scientists. The essence of the problem is that with the critical frequency ω_{kr} is associated the parameter

$$m = \frac{\hbar\omega_{kr}}{c^2}, \quad (41)$$

which has a dimension of mass, and the question arises whether this value can be interpreted as the real mass? The mass that the electromagnetic field acquires when it enters the waveguide. In the works of Rivlin, this problem has been studied in a systematic manner [23, 24].

But here we will not go into this question, and only note the fact that the mass m is related with geometry and size of a waveguide. In particular, if the waveguide has a square shape with a side size a , then this connection has the form

$$a = \frac{\sqrt{2\pi\hbar}}{mc}. \quad (42)$$

It is this value that we propose to consider as a linear parameter which is associated with a massless particle when it acquires the mass m . We believe that at the same time, when a massless particle enters the external field and acquires a nonzero mass, the corresponding infinite plane wave shrinks to finite size. And this finite size is characterized by localization parameter

$$l = \frac{2\pi\hbar}{mc}. \quad (43)$$

In form, the value (43) resembles the Compton wavelength of the electron, however, its physical meaning is quite different. In the formula for the Compton wavelength of the electron parameter m – is the rest mass of the electron, but in the formula (43) m – this is the mass, which acquires a photon, when it is exposed to external influences.

In the ESM, the external action is described by rotations in the extended space $G(1,4)$. Above we have considered such rotations from the group $O(1,4)$, and found how the photon mass changes at these rotations. Since the linear parameter l is expressed by the formula (43) through the photon mass, it can be used to find the dependence of this parameter from the values that define these rotations.

Thus, in the case of rotations in the plane (TS), the dependence of the photon mass on the rotation angle θ is determined by the formula $mc^2 = \hbar\omega \sinh \psi$ [14, 17].

Substituting this expression into a formula (43), we obtain the expression for the parameter l through the angle θ .

$$l = \frac{2\pi c}{\omega \sinh \vartheta}. \quad (44)$$

In the case of rotations in the plane (XS), the dependence of the photon mass on the rotation angle ψ is determined by the formula

$mc^2 = \hbar\omega \sinh \psi$ [14, 17]. With its help one can obtain an expression for the parameter l through the angle ψ .

$$l = \frac{2\pi c}{\omega \sin \psi}. \quad (45)$$

We now compare the formulas for the linear parameter (44) with the formula for the photon mass. If we exclude from these formulas the value $\sinh \theta$, and as the mass m substitute Planck mass m_{pl} , then we get the expression

$$l = 2\pi \sqrt{\frac{\hbar G}{c^3}}. \quad (46)$$

for the length l .

The value (46) actually coincides with the Planck length l_{pl} . Since the Planck mass m_{pl} and the Planck length l_{pl} are considered to be the limit values of length and mass, we will also consider the corresponding rotation angle \mathcal{G}_{pl} to be the limit value of such angle. Its value is

$$\sinh \mathcal{G}_{pl} = \frac{m_{pl} c^2}{\hbar \omega}. \quad (47)$$

We see that the photons of different frequencies correspond to different angles of limiting rotation \mathcal{G}_{pl} . But the corresponding values m_{pl} and l_{pl} are the same and do not depend on the frequency ω .

Within the ESM there is another mechanism of appearing a photon mass. More precisely, not for one photon, but a group of photons. Consider two free photons. Let them move in Minkowski space in the directions given by the unit vectors \vec{k}_1 and \vec{k}_2 . Then in ESM they correspond to two 5-vector energy-momentum-mass.

$$\left(\frac{\hbar\omega}{c}, \frac{\hbar\omega}{c} \vec{k}_1, 0 \right). \quad (48)$$

and

$$\left(\frac{\hbar\omega}{c}, \frac{\hbar\omega}{c} \vec{k}_2, 0 \right). \quad (49)$$

We emphasize that in this case we are not talking about the interaction of these photons with each other, their scattering on each other, etc. Here we are talking only about the fact that in 3-dimensional spaces there are two photons. We consider a system consisting of these photons

and try to find a 5-vector that corresponds to it in the ESM. Since these photons do not interact, the energy of the system is equal to the sum of their energies.

Similarly, the momentum of the system is equal to the vector sum of their pulses. Since this is an isolated system, which is not affected by any external forces, it, according to the ideology of ESM, corresponds to the isotropic 5-energy-momentum-mass vector. This vector can be obtained by adding vectors (48) and (49) and adding a mass such that it becomes isotropic.

$$\begin{aligned} & \left(2 \frac{\hbar\omega}{c}, \frac{\hbar\omega}{c} (\vec{k}_1 + \vec{k}_2), m_{1+2} c \right) = \\ & = \left(2 \frac{\hbar\omega}{c}, \frac{\hbar\omega}{c} (\vec{k}_{1+2} \cos \frac{\alpha}{2}), m_{1+2} c \right). \end{aligned} \quad (50)$$

The mass value m_{1+2} must be such that the vector (50) is isotropic. Because

$$\begin{aligned} |\vec{k}_1 + \vec{k}_2|^2 &= 2 + 2(\vec{k}_1, \vec{k}_2) = \\ &= 2 + 2 \cos \alpha = 4 \cos^2 \frac{\alpha}{2}, \end{aligned} \quad (51)$$

for the mass of a system of two photons we obtain the expression

$$m_{1+2} = 2 \frac{\hbar\omega}{c^2} \sin \frac{\alpha}{2}. \quad (52)$$

Here α is the angle between vectors \vec{k}_1, \vec{k}_2 .

The isotropic 5-vector (50) now takes the form

$$\left(2 \frac{\hbar\omega}{c}, 2 \frac{\hbar\omega}{c} \cos \frac{\alpha}{2}, 2 \frac{\hbar\omega}{c} \sin \frac{\alpha}{2} \right). \quad (53)$$

The expression (52) for the mass of a system of two photons can be obtained using the formula for the mass of a system of n particles [25, 26]

$$m^2 c^4 = \left(\sum_{i=1}^n E_i \right)^2 + c^2 \left(\sum_{i=1}^n \vec{p}_i \right)^2. \quad (54)$$

It is with the help of the formula (54) that the expression (53) for the mass of a system of two photons was obtained in [27].

Note that the question of the moment of a system of two photons was studied in [28].

CONCLUSION

According to the ideology of ESM the union of electromagnetic and gravitational fields occurs due to the fact that the interaction of particles

and fields changes their mass. Including the photon, getting into the medium, or in an external field, acquires mass. At the same time, it is being localized. In the empty Minkowski space, an infinite plane wave is compared to the photon, which contains the components \vec{E} and \vec{H} of the electric and magnetic fields. After the photon is exposed to external action, it is localized, acquires mass and, in addition to the fields \vec{E} and \vec{H} , it acquires additional field components: the vector field \vec{G} and the scalar field Q .

These 10 fields form a single object, they satisfy the extended system of Maxwell equations and can transform into each other. Each of them interacts with the environment in its own way and, thanks to the presence of additional components, they can penetrate through such barriers that are inaccessible to the usual electromagnetic field. An important role is played by the fact that photons have mass, and in addition to electromagnetic interaction, there is a gravitational interaction between photons and the external environment.

The appearance of a non-zero mass in a photon and the simultaneous change mass of other particles leads to a change in the nature of their interaction. The developed formalism of ESM allows us to take into account these changes.

The ideology of ESM and the formalism developed with its help can be useful in discussing a number of other problems in physics. One of them may be the construction of gauge theories for massive fields.

Also within the framework of the ESM there is an opportunity to take a new look at the nature of wave-particle dualism. The particle located far from the detectors is distributed over a large area of space and exhibits wave properties. Flying up to the detector, it is localized, and behaves like a corpuscle. This mechanism allows us to understand the nature of nonlocality.

REFERENCES

1. Klein Felix. Über neuere englische Arbeiten zur Gesammelte matematische Abhandlungen. *Zeit. f. Math. u. Phys.*, 1901, s. 375.
2. Einstein A. Die Grundlage der allgemeinen Relativitätstheorie. *Annalen der Physik*, 1916, 49:769-822.
3. Kaluza Th. Zum Unitätsproblem der Physik. *Sitzungsberichte der Preussischen Akademie der Wissenschaften*, 1921, 966-972.
4. Klein Oskar. Quantentheorie und fünfdimensionale Relativitätstheorie. *Zeitschrift für Physik*, 1926, 37(12):895-906; doi: 10.1007/BF01397481.
5. Mandel H. Über den Zusammenbang zwischen der Einsteinschen Theorie des Fern. Parallelismus und der Fünfdimensionalen Fieldtheorie. *Zeitschrift für Physik*, 1926, 39:136-145.
6. Fock VA. Über die invariante Form der Wellen- und der Bewegungsgleichungen für einen geladenen Massenpunkt. *Zeitschrift für Physik*, 1926, 39:226-232.
7. Einstein A, Bergmann P. Generalization of Kaluza's Theory of Electricity. *Ann. Math., Ser. 2*, 1938, 39:683-701.
8. Rumer YuB. *Issledovaniya po pyatimernoy optike* [Studies on five-dimensional optics]. Moscow, URSS Publ., 2010, 152 p.
9. Konopleva NP, Popov VN. *Kalibrovochnye polya* [Gauge fields]. Moscow, Atomizdat Publ., 1972, 240 p.
10. Rubakov VA. *Klassicheskie kalibrovochnye polya* [Classical gauge fields]. Moscow, Editorial URSS Publ., 336 p.
11. Stanyukovich KP. *Gravitatsionnoe pole i elementarnye chastitsy* [Gravitational field and elementary particles]. Moscow, Nauka Publ., 1965, 312 p.
12. Markov MA. Elementary Particles of Maximally Large Masses (Quarks and Maximons). *Soviet Physics JETP*, 1967, 24:584-592.
13. Landau LD. On the radius of elementary particles. *Soviet Physics JETP*, 1940, 10:718-722.
14. Tsipenyuk DYU, Andreev VA. Structure of Extended Space. *Bulletin of the Lebedev Physics Institute*, 2000, 6:23-34; arXiv:gr-qc/0106093, 2001.
15. Andreev VA, Tsipenyuk DYU. The 5-dimensional model for electromagnetism and gravity. *Natural Science*, 2014, 6:248-253.

16. Andreev VA, Tsipenyuk DYu. Tunneling of the potential barrier and particle's size in the Extended Space Model, Physical Interpretation of Relativity Theory: *Proc. of Intern. Meeting, Bauman Moscow State Technical University, Moscow, 29 June-02 July, 2015*: 20-32.
17. Andreev VA, Tsipenyuk DYu. The Mass and Size of Photons in the 5-Dimensional Extended Space Model. *Journal of Modern Physics*, 2016, 7:1308-1315; DOI: 10.4236/jmp.2016.711116.
18. Andreev VA, Tsipenyuk DYu. Problema vvedeniya konechnogo razmera i peremennoy massy fotona [The problem of introducing finite size and variable mass of the photon]. *Inzhenernaya fizika*, 2017, 5:17-28 (in Russ.).
19. Landau LD, Lifshitz EM. *The Classical Theory of Fields* (Vol. 2 of A Course of Theoretical Physics). Pergamon Press, 1971, 372 p.
20. Arnold VI. *Mathematical Methods of Classical Mechanics*. Springer-Verlag, 1989, 432 p.
21. De Broglie Louis. *Problemes de Propagations Guidees des Ondes Electromagnetiques*. Paris, 1941, 104 p.
22. Feynman RP., Leighton RB., Sands M. The Feynman lectures on physics, v 2, 1964, ADDISON-WESLEY PUBLISHING COMPANY INC.
23. Rivlin LA. Photons in a waveguide (some thought experiments). *Phys. Usp.*, 1997, 40:291-303.
24. Rivlin LA. Ostanovlenny svet (k elektrodinamike bez ploskikh voln [Stopped light (on the electrodynamics of without plane waves)]. *Kvantovaya elektronika*, 2003, 33(9):777-797 (in Russ.).
25. Okun' LB. The concept of mass. *Physics-Uspеkhi*, 1989, 32:629-638.
26. Okun' LB, Selivanov KG, Telegdi VL. Gravitation, photons, clocks. *Physics-Uspеkhi*, 1999, 42:1141-1147.
27. Fedorov MV, Vintskevich SV. Invariant mass and propagation speed of light pulses in vacuum, *arXiv:1604.00227v3 [quant-ph] 19 May 2016*.
28. Landau LD. O momente sistemy iz dvukh fotonov [On the moment of a system of two photons]. *DAN USSR*, 1948, 60:207-210 (in Russ).

FUNDAMENTAL SYSTEM OF EQUATIONS FOR MOMENTUM AND ENERGY OF ELECTROMAGNETIC FIELD IN INHOMOGENEOUS MEDIUM

Arthur A. Dyshekov

Berbekov Kabardino-Balkarian State University, <http://www.kbsu.ru>

Nalchik 360004, Russian Federation

dyshekov@yandex.ru

Abstract. An alternative approach to the description of the interaction of the electromagnetic field with the crystal is proposed, in which the main characteristics are the energy and pulse densities. The reaction of the medium to the external perturbation is considered as a local change in geometry – the rotation of the orthogonal basis built on the induction vectors and the pulse of the field, determined by the structural characteristics of the medium. The equations that allow calculating the momentum and energy of the field in its interaction with the crystal are obtained.

Keywords: Energy-momentum tensor, electromagnetic field, Maxwell tensor, Gâteaux derivative, canonical form of the field tensor

PACS: 61.05.C

Bibliography – 16 references

Received 13.06.18, accepted 13.01.19

RENSIT, 2019, 11(2):103-112

DOI: 10.17725/rensit.2019.11.103

CONTENTS

1. INTRODUCTION (103)
 2. LAWS TO CHANGE THE MOMENTUM AND ENERGY OF THE FIELD (104)
 3. THE CANONICAL FORM OF THE MAXWELL TENSOR AND CONDITIONS FOR THE FIELDS (105)
 4. RELATIVISTIC SUBSTANTIATION (106)
 5. FUNDAMENTAL EQUATIONS IN THE LOCAL BASIS (107)
 6. CONCLUSION OF DIFFERENTIAL OPERATIONS $\nabla' \cdot \mathbf{P}$, $\nabla' \cdot \mathbf{T}$, $\nabla' \cdot \boldsymbol{\varepsilon}$ (108)
 - 6.1. CALCULATION $\nabla' \cdot \mathbf{P}$ (108)
 - 6.2. CALCULATION $\nabla' \cdot \boldsymbol{\varepsilon}$ (109)
 - 6.3. CALCULATION $\nabla' \cdot \mathbf{T}$ (109)
 7. THE CALCULATION OF THE ROTATION VECTOR $\boldsymbol{\varphi}$ (109)
 8. CONCLUSION OF THE BASIC EQUATION SYSTEM IN THE CARTESIAN BASIS (110)
 9. CONCLUSION (110)
- REFERENCES (111)

1. INTRODUCTION

A new approach to describing the interaction of the electromagnetic field with a substance based on the density of energy and momentum is proposed. Known approaches for describing wave fields in matter are based on the analysis of Maxwell's equations with respect to inductions [1-4]. However in the experiment field strengths are not measured

for obvious reasons. In the experiment, the wave intensity is measured, and the direction of wave propagation, the Umov-Poynting vector, is associated with the wave momentum. Compliance with experiment is achieved by calculating these characteristics through field strengths. For example, to find the reflection coefficient of a wave from a medium, it is necessary to calculate the Poynting vector component, normal with respect to the surface.

Momentum and energy (or rather, their densities) are quadratic in fields. As a result they cannot be directly represented as a superposition of the resulting field solutions. The answer is only in the final stage, when the solutions for the fields have already been received. On the one hand, this is a definite plus (it is much easier to solve linear equations than nonlinear ones). On the other hand, such a procedure makes it difficult to directly analyze the intensity distribution in a given direction of space, depending on the characteristics of the scattering object.

In this regard we can formulate the following problem statement. Describe the interaction of the field and matter by means of the energy and momentum densities in accordance with the equations of motion of the electromagnetic field.

As is known, the equations of motion of a dynamical system (the Euler-Lagrange equations) are obtained from the variational principle as a condition for the extremality of a certain action functional. This principle is valid both for mechanical systems and for fields – systems with an infinite number of degrees of freedom. In this case, the invariance of an action with respect to a certain group of coordinate transformations (external symmetries) or gauge transformations (internal symmetries) leads to covariant equations of motion and to fundamental conservation laws.

The conservation laws follow from the first theorem of Noether [5–7] which is formulated for global and local symmetry transformations of the action functional. The meaning of this theorem is as follows. If the action is invariant with respect to transformations of global symmetries that form a certain Lie group [7] then for each symmetry transformation and any solution of the Euler-Lagrange equations, the quantities called currents are saved. Keeping current means that its 4-divergence is zero. Global invariance means that the transformation parameter is independent of space-time points. In turn the integration of currents over specially selected areas of space-time gives the remaining charges corresponding to each current.

Let the action be invariant with respect to translations in space-time. Then the general expression for the current passes into the expression for the energy-momentum tensor for fields whose 4-divergence turns to zero by virtue of the first Noether theorem. It is the 4-divergence of the energy-momentum tensor that describes the electromagnetic field as a dynamic system.

Note that the first Noether theorem is formulated for infinitesimal space-time translations. The Lie group in the formulation of the first Noether theorem [6] is directly related to the continuity of space-time symmetries. This circumstance is of decisive importance in the future case of the X-ray wavelength range.

Since for an X-ray wave, the dielectric constant is a function of coordinates, the continuity of translations on atomic scales is incompatible with the condition of medium homogeneity. Only in the particular case of the crystalline medium is the invariance of the

action functional ensured and only with respect to the discrete and not continuous, group of spatial translations on the Bravais lattice vectors. Thus the direct application of the first theorem of Noether to construct the energy-momentum tensor as the dynamic basis of the theory taking into account the microscopic structure of the medium, is impossible.

2. LAWS TO CHANGE THE MOMENTUM AND ENERGY OF THE FIELD

In connection with the above, a different approach is proposed, which allows us to obtain the relations of interest directly from the equations of classical macroscopic electrodynamics.

We proceed from the Maxwell equations for the field in the absence of charges and currents in the medium:

$$\begin{aligned}\nabla \times \mathbf{E} &= -\frac{1}{c} \frac{\partial \mathbf{H}}{\partial t} \\ \nabla \times \mathbf{H} &= \frac{1}{c} \frac{\partial \mathbf{D}}{\partial t}.\end{aligned}\quad (1)$$

For the X-ray wavelength range the permittivity ε and hence the polarizability χ is a function of the coordinates:

$$\mathbf{D} = \varepsilon(\mathbf{r})\mathbf{E} = (1 + \chi(\mathbf{r}))\mathbf{E}.\quad (2)$$

In addition the interaction of electromagnetic waves with the medium and in other ranges can be described by the formula (2). For example artificial periodic structures – photonic crystals [8], objects of X-ray optics for soft X-rays [9] also formally correspond to (2) since the elements scattering radiation form a certain spatial structure.

In formulas (1), (2) and further standard notation is used, ∇ – Hamilton operator in some Cartesian basis \mathbf{i}_k , summation is performed on the mute index k .

Let us give a generalization to the case of $\varepsilon = \varepsilon(\mathbf{r})$ of the well-known in electrodynamics of the derivation of the law of momentum variation [10]. Consider the value $(\nabla \times \mathbf{E}) \times \mathbf{D}$ in some orthonormal cartesian basis \mathbf{i}_m :

$$\begin{aligned}(\nabla \times \mathbf{E}) \times \mathbf{D} &= \nabla \cdot (\mathbf{D}\mathbf{E}) - \\ &= -\frac{1}{2} \nabla \cdot (\mathbf{I} \cdot (\mathbf{D} \cdot \mathbf{E})) + \frac{E^2}{2} \nabla \varepsilon.\end{aligned}\quad (3)$$

Similarly we find the value $(\nabla \times \mathbf{H}) \times \mathbf{H}$:

$$(\nabla \times \mathbf{H}) \times \mathbf{H} = \nabla \cdot (\mathbf{H}\mathbf{H}) - \frac{1}{2} \nabla \cdot (\mathbf{I} \cdot H^2). \quad (4)$$

In (3) and (4) the values $\mathbf{D}\mathbf{E} = D_i E_j$; $\mathbf{H}\mathbf{H} = H_i H_j$, representing dyads (external products) [11] as well as the unit tensor $\mathbf{I} = \mathbf{i}_m \mathbf{i}_m$. In the sequel an expression of the form $\mathbf{a}\mathbf{b}$ will mean the outer product of vectors \mathbf{a} and \mathbf{b} . In deriving (3) and (4), it was taken into account that according to Maxwell's equations in the absence of charges $(\nabla \cdot \mathbf{D}) = 0$ and $(\nabla \cdot \mathbf{H}) = 0$. Note that due to the invariance of the operator ∇ , formulas (3) and (4) are valid in any basis.

Find the sum of (3) and (4) and, taking into account (1), after a series of transformations we get

$$\nabla \cdot \left(\mathbf{D}\mathbf{E} + \mathbf{H}\mathbf{H} - \frac{1}{2} \mathbf{I} \cdot (\mathbf{D} \cdot \mathbf{E} + H^2) \right) + \frac{E^2}{2} \nabla \varepsilon = \frac{1}{c} \frac{\partial}{\partial t} (\mathbf{D} \times \mathbf{H}).$$

Imagine this equation as

$$\nabla \cdot \mathbf{T} + \frac{E^2}{2} \nabla \varepsilon = \frac{\partial \mathbf{P}}{\partial t}. \quad (5)$$

The following values are entered here: Maxwell stress tensor in medium \mathbf{T}

$$\mathbf{T} = \mathbf{D}\mathbf{E} + \mathbf{H}\mathbf{H} - \frac{1}{2} \mathbf{I} (\mathbf{D} \cdot \mathbf{E} + H^2) = \mathbf{D}\mathbf{E} + \mathbf{H}\mathbf{H} - w\mathbf{I}. \quad (6)$$

energy density

$$w = \frac{1}{2} (\mathbf{D} \cdot \mathbf{E} + H^2). \quad (7)$$

and also the bulk density of the total momentum of the field $\mathbf{P} = \frac{1}{c} (\mathbf{D} \times \mathbf{H})$ (we will briefly call it the momentum).

As can be seen from (5) the change in the field momentum in the general case is associated not only with the Maxwell tensor \mathbf{T} but also depends on the permittivity gradient $\nabla \varepsilon$. According to (6) taking into account (2) the tensor \mathbf{T} turns out to be symmetric.

Now form the expression $\mathbf{H} \cdot (\nabla \times \mathbf{E}) - \mathbf{E} \cdot (\nabla \times \mathbf{H})$ and using (1) we get:

$$\begin{aligned} \nabla \cdot (\mathbf{E} \times \mathbf{H}) &= \mathbf{H} \cdot (\nabla \times \mathbf{E}) - \mathbf{E} \cdot (\nabla \times \mathbf{H}) = \\ &= -\frac{1}{c} \frac{\partial}{\partial t} (\mathbf{H} \cdot \mathbf{H} + \mathbf{D} \cdot \mathbf{E}) = -\frac{1}{c} \frac{\partial w}{\partial t}. \end{aligned} \quad (8)$$

Calculate the divergence $c\mathbf{P}$:

$$c(\nabla \cdot \mathbf{P}) = \varepsilon \nabla \cdot (\mathbf{E} \times \mathbf{H}) + \frac{\nabla \varepsilon}{\varepsilon} \cdot (\mathbf{D} \times \mathbf{H}).$$

From here

$$\nabla \cdot (\mathbf{E} \times \mathbf{H}) = \frac{1}{\varepsilon} \cdot (\nabla \cdot (\mathbf{D} \times \mathbf{H}) - \frac{\nabla \varepsilon}{\varepsilon^2} \cdot (\mathbf{D} \times \mathbf{H})). \quad (9)$$

Substituting (9) into (8), we have

$$\nabla \cdot \mathbf{P} - \frac{\nabla \varepsilon}{\varepsilon} \cdot \mathbf{P} = -\frac{\varepsilon}{c^2} \frac{\partial w}{\partial t}. \quad (10)$$

3. THE CANONICAL FORM OF THE MAXWELL TENSOR AND CONDITIONS FOR THE FIELDS

Equations (5) and (10) form the basic system for momentum and field energy. They generalize the laws of change of momentum and energy of the electromagnetic field in the case $\varepsilon = \varepsilon(\mathbf{r})$. However, the system (5), (10) is generally unclosed with respect to w and \mathbf{P} since the tensor \mathbf{t} includes the dyads $\mathbf{D}\mathbf{E}$ and $\mathbf{H}\mathbf{H}$. In addition the change in the momentum according to (5) depends on the amplitude of the electric field through $E^2/2$. Find out what it's connected to and try to shut down the system.

In deriving equations (5) and (10), we used an arbitrary Cartesian basis not related to the electromagnetic field in any way. However it is obvious that the form of the Maxwell tensor \mathbf{T} depends on the choice of the basis in accordance with the transformational properties of the second rank tensor. This circumstance suggests that the dynamic nature of the tensor \mathbf{T} is associated with some selected directions in space, and these directions are determined by the vectors \mathbf{D} , \mathbf{H} , and \mathbf{P} . We show that this is indeed the case.

The simplest (canonical) form of the tensor \mathbf{T} is in a basis built on eigenvectors. Since the tensor \mathbf{T} is symmetric, its canonical form is a diagonal tensor.

We define the canonical form of the Maxwell tensor (6). To do this we find the eigenvalues λ_j and the eigenvectors \mathbf{e}_j of the tensor \mathbf{T} in the normalized basis, satisfying the well-known equation:

$$\mathbf{T} \cdot \mathbf{e}_j = \lambda \mathbf{e}_j. \quad (11)$$

The characteristic equation is

$$\det(\mathbf{T} - \lambda \mathbf{I}) = -\lambda^3 + I_1 \lambda^2 - I_2 \lambda + I_3 = 0,$$

where I_j are the main invariants of the tensor \mathbf{T} :

$$I_1 = \text{Tr}(\mathbf{T}), I_2 = \frac{1}{2} (\text{Tr}(\mathbf{T})^2 - \text{Tr}(\mathbf{T}^2)), I_3 = \det(\mathbf{T}).$$

Here $Tr(\mathbf{T})$ is the trace of the tensor \mathbf{T} . From the form (6) we obtain one eigenvalue $\lambda_3 = -w$. In fact direct verification ensures that

$$\mathbf{T} - \lambda \mathbf{I} = \mathbf{DE} + \mathbf{HH} - w\mathbf{I} + w\mathbf{I} = \mathbf{DE} + \mathbf{HH},$$

$$\det(\mathbf{DE} + \mathbf{HH}) = 0.$$

Find the eigenvector \mathbf{u}_3 corresponding $\lambda_3 = -w$. Solving (11) for $\lambda_3 = -w$, we obtain the components of the corresponding vector \mathbf{u}_3 :

$$u_{31} = E_2 H_3 - E_3 H_2, u_{32} = E_3 H_1 - E_1 H_3, u_{33} = E_1 H_2 - E_2 H_1,$$

which form a vector

$$\mathbf{u}_3 = u_{3j} \mathbf{e}_j = \mathbf{E} \times \mathbf{H}.$$

From here

$$\mathbf{e}_3 = \frac{\mathbf{E} \times \mathbf{H}}{|\mathbf{E} \times \mathbf{H}|}.$$

We write \mathbf{T} in the orthonormal basis \mathbf{e}_j :

$$T'_{ij} = \mathbf{e}_i \cdot \mathbf{T} \cdot \mathbf{e}_j$$

$$T'_{ij} = \begin{pmatrix} T_{11} & T_{12} & 0 \\ T_{21} & T_{22} & 0 \\ 0 & 0 & -w \end{pmatrix}.$$

Now we require that $T_{12} = T_{21} = 0$, then, obviously, $T_{11} = \lambda_1$, $T_{22} = \lambda_2$, and $\mathbf{e}_{1,2}$ are eigenvectors. We get the conditions:

$$\mathbf{T}_{12} = \mathbf{e}_1 \cdot \mathbf{T} \cdot \mathbf{e}_2 = (\mathbf{e}_1 \cdot \mathbf{D})(\mathbf{E} \cdot \mathbf{e}_2) + (\mathbf{e}_1 \cdot \mathbf{H})(\mathbf{H} \cdot \mathbf{e}_2) = 0,$$

$$\mathbf{T}_{21} = \mathbf{e}_2 \cdot \mathbf{T} \cdot \mathbf{e}_1 = (\mathbf{e}_2 \cdot \mathbf{D})(\mathbf{E} \cdot \mathbf{e}_1) + (\mathbf{e}_2 \cdot \mathbf{H})(\mathbf{H} \cdot \mathbf{e}_1) = 0.$$

It follows

$$\mathbf{e}_1 \cdot \mathbf{D} = D; \mathbf{e}_1 \cdot \mathbf{E} = E; \mathbf{e}_1 \cdot \mathbf{H} = 0,$$

$$\mathbf{e}_2 \cdot \mathbf{D} = \mathbf{e}_2 \cdot \mathbf{E} = 0; \mathbf{e}_2 \cdot \mathbf{H} = H.$$

Then

$$T_{11} = \mathbf{e}_1 \cdot \mathbf{T} \cdot \mathbf{e}_1 = DE - w = \lambda_1 = \frac{1}{2}(DE - H^2);$$

$$T_{22} = \mathbf{e}_2 \cdot \mathbf{T} \cdot \mathbf{e}_2 = H^2 - w = \lambda_2 =$$

$$= -\lambda_1 = \frac{1}{2}(H^2 - DE).$$

And the eigenvectors are equal

$$\mathbf{e}_1 = \frac{\mathbf{D}}{D} = \frac{\mathbf{E}}{E}; \mathbf{e}_2 = \frac{\mathbf{H}}{H}; \mathbf{e}_3 = \frac{\mathbf{P}}{P}. \tag{12}$$

Now we require the fulfillment of the additional condition $\lambda_1 = \lambda_2 = 0$, the justification of which is given below. In this case, an additional bond $DE = H^2$ should be imposed on the fields.

Therefore, the following conditions are necessary for the tensor \mathbf{T} to describe the field:

1) Orthogonality of fields

$$\mathbf{D} \cdot \mathbf{H} = \mathbf{D} \cdot \mathbf{H} = 0, \tag{13}$$

2) Connection amplitude fields

$$DE = \varepsilon E^2 = H^2. \tag{14}$$

The existence of the connection of field amplitudes (14) as will be seen further is crucial for the construction of a closed theory. In this case, if $\varepsilon = \varepsilon(\mathbf{r})$ conditions (13) and (14) are realized locally. Also these conditions are for the full field. Thus we obtain a canonical form of the Maxwell tensor \mathbf{T} in the \mathbf{e}_j basis:

$$\mathbf{T} = -w(\mathbf{e}_3 \mathbf{e}_3).$$

As can be seen the Maxwell tensor \mathbf{T} is locally determined by the energy density w and the direction of momentum transfer \mathbf{e}_3 . Moreover, in accordance with the theorems on eigenvalues and eigenvectors of the symmetric tensor, the eigenvalues turn out to be real and the eigenvectors corresponding to these values are orthogonal.

4. RELATIVISTIC SUBSTANTIATION

To substantiate these conditions, we turn to the results of relativistic electrodynamics. We introduce the four-dimensional tensor of the field F_{ik} [12] in a vacuum in the Minkowski space $R_{1,3}^4$. By definition, invariants of the tensor F_{ik} are called the coefficients of the characteristic polynomial

$$P(\lambda) = \det(F_{ik} - \lambda g_{ik}),$$

where g_{ik} is the Minkowski metric (+, -, -, -).

Direct calculation leads to the following form of the characteristic polynomial:

$$P(\lambda) = -\lambda^4 + (E^2 - H^2)\lambda + (\mathbf{E} \cdot \mathbf{H})^2,$$

whence we get the well-known invariants of the field $E^2 - H^2$ and $\mathbf{E} \cdot \mathbf{H}$.

The question of reducing the skew-symmetric tensor of a field F_{ik} to Lorentz transformations to the canonical form is solved by the following theorem [12].

Theorem 1.

1. Suppose that the invariants of the field $E^2 - H^2$ and $\mathbf{E} \cdot \mathbf{H}$ are not equal to zero.

a) If $\mathbf{E} \cdot \mathbf{H} \neq 0$, then the Lorentz transformation can reduce the tensor F_{ik} to such a form that the vectors \mathbf{E} and \mathbf{H} are parallel and both are nonzero.

b) If $\mathbf{E} \cdot \mathbf{H} = 0$, $E^2 - H^2 \neq 0$, then we can reduce the tensor F_{ik} to the form that $\mathbf{E} \neq 0$ $\mathbf{H} = 0$ for $E^2 - H^2 > 0$ or $\mathbf{E} = 0$ $\mathbf{H} \neq 0$ for $E^2 - H^2 < 0$.

2. Let $E^2 - H^2 = 0$ and $\mathbf{E} \cdot \mathbf{H} = 0$. Then, after any Lorentz transformation, the vectors \mathbf{E} and \mathbf{H} will

be mutually perpendicular and equal in length. The tensor F_{ik} can be reduced in this case to the form:

$$F_{ik} = \begin{pmatrix} 0 & E & 0 & 0 \\ -E & 0 & 0 & E \\ 0 & 0 & 0 & 0 \\ 0 & -E & 0 & 0 \end{pmatrix}.$$

We are interested in the second point of this theorem, since it corresponds to a special state of the field, the electromagnetic wave. It is in this case that the condition of coupling the field amplitudes and the transverse condition of the fields arise. As can be seen, condition (14) can be considered as a generalization of the classical invariant of the field $E^2 - H^2$ to the case of electrodynamics of a continuous medium.

Now we justify the condition $\lambda_1 = \lambda_2 = 0$. As is known, for the tensor of the field F_{ik} with respect to the scalar Lagrangian

$$L = -\frac{1}{4} F^{ik} F_{ik}$$

a symmetric four-dimensional energy-momentum tensor \mathbf{T} is constructed. The explicit form of this tensor is determined from the first theorem of Noether [7]. According to the theorem of Noether, since the action for a free electromagnetic field in Minkowski space is invariant with respect to the global action of the Poincaré group (space-time translations plus reflections) there exists a second-rank tensor, whose 4-divergence is zero:

$$\partial_k T_i^k = 0.$$

This quantity, called the current, is the energy-momentum tensor:

$$T_i^k = \frac{1}{2} (-F_{ik} F_m^k + \frac{1}{4} g_{ik} F^2) g_{km}.$$

Find the eigenvalues of the tensor T_i^k :

$$\det(T_i^k - \lambda \delta_i^k) = 0.$$

Due to the symmetry of the tensor we obtain four pairwise coinciding eigenvalues:

$$2\lambda_1 = 2\lambda_3 = H^2 + \frac{1}{2} (E^4 + H^4 - 4(\mathbf{E} \cdot \mathbf{H})^2 + 2E^2 H^2)^{1/2},$$

$$2\lambda_2 = 2\lambda_4 = H^2 - \frac{1}{2} (E^4 + H^4 - 4(\mathbf{E} \cdot \mathbf{H})^2 + 2E^2 H^2)^{1/2}.$$

This shows that if the conditions $E = H$, $\mathbf{E} \cdot \mathbf{H} = 0$ are fulfilled the eigenvalues take the following form:

$$\lambda_1 = \lambda_3 = E^2 = w,$$

$$\lambda_2 = \lambda_4 = 0.$$

Thus, we arrive at the condition that the two eigenvalues of the energy-momentum tensor are zero. Since the Maxwell tensor is the spatial part of the energy-momentum tensor it is clear that this condition must also be satisfied for the Maxwell tensor \mathbf{T} defined by formula (6).

It should be noted that the given justifications used field and energy-momentum tensors in vacuum. The above conclusion for the Maxwell tensor is more General, since we consider the field in the substance.

5. FUNDAMENTAL EQUATIONS IN THE LOCAL BASIS

Now, taking into account (14), we can associate the field energy density with the amplitude of the electric vector:

$$w = \frac{1}{2} \left(\frac{1}{\epsilon} D^2 + H^2 \right) = \frac{E^2}{2} \epsilon (1 + \epsilon).$$

From here

$$\frac{E^2}{2} = \frac{w}{\epsilon (1 + \epsilon)}.$$

As a result, equation (5) takes on a compact form:

$$\nabla \cdot \mathbf{T} + \frac{w}{\epsilon (1 + \epsilon)} \nabla \epsilon = \frac{\partial \mathbf{P}}{\partial t}. \tag{15}$$

Thus we have ensured that system (10), (15) is closed with respect to \mathbf{P} and w .

However such a “simplification” entails consequences. Here, as always, the general principle operates: any generalization of a theory with a reduction in the axiomatic base (“entities”) entails the inevitable complication of descriptive means in this case the mathematical apparatus. The generalization here refers to the reference to the general physical categories – energy and momentum obeying global conservation laws.

Indeed the above derivation of the basic equations shows that they are valid in the most compact (canonical) form only in a special local basis. Thus, we must consider all differential operations in an orthogonal curvilinear coordinate system defined by basis (10).

To emphasize this circumstance, we write the system (10), (15) in the following form:

$$\begin{aligned} \nabla' \cdot \mathbf{T} + \frac{w}{\varepsilon(1+\varepsilon)} \nabla' \varepsilon &= \frac{\partial \mathbf{P}}{\partial t} \\ \nabla' \cdot \mathbf{P} - \frac{\nabla' \varepsilon}{\varepsilon} \mathbf{P} &= -\frac{\varepsilon}{c^2} \frac{\partial w}{\partial t}. \end{aligned} \quad (16)$$

Here the stroke means differentiation in the basis (12).

System (16) with external formal simplicity cannot be directly used to calculate the momentum and field energy. In fact to solve such a problem it is necessary to have explicit expressions for the transition from the local coordinate system defined by basis (12) to the laboratory coordinate system in which the experiment is fixed. In other words, geometry remains unknown.

Now we use the condition of local orthogonality of the field and the condition of amplitude coupling. This makes it possible to establish a connection between the geometry of the field and the geometry of the experiment, which is our further goal.

The problem is divided into two stages. First, we will find expressions for the divergence and gradient in the field basis through the Cartesian basis and the additional characteristic is the local rotation of the basis. Then we calculate the explicit form of the rotation angle vector.

6. CONCLUSION OF DIFFERENTIAL OPERATIONS $\nabla' \cdot \mathbf{P}$, $\nabla' \cdot \mathbf{T}$, $\nabla' \varepsilon$

First of all it is necessary to introduce a Cartesian basis, which will correspond to the geometry of the propagation of a plane wave in a crystal as a continuum, when the response of the medium to an external action reduces to the material equation $D = \varepsilon E = (1+\chi_0)E$. It is natural to take this state as the initial state, in relation to which, in the process of interaction of the X-ray wave with the crystal, a local variation of the basis \mathbf{e}_m occurs. Thus, we will consider the scattering problem in a special orthonormal basis \mathbf{i}_k defined by the vectors \mathbf{D}_0 , \mathbf{H}_0 , \mathbf{P}_0 in the continuous approximation:

$$\mathbf{i}_1 = \frac{\mathbf{D}_0}{D_0}; \mathbf{i}_2 = \frac{\mathbf{H}_0}{H_0}; \mathbf{i}_3 = \frac{\mathbf{P}_0}{P_0}.$$

This means that all differential operators must be expressed precisely in this basis.

6.1. CALCULATION $\nabla' \cdot \mathbf{P}$

We find $\nabla \cdot \mathbf{P}$ in the basis \mathbf{i}_k . The basic idea of the calculation is as follows. From the vector $\mathbf{P}(\mathbf{r})$ a second rank tensor can be constructed $\partial \mathbf{P} / \partial \mathbf{r}$ – a derivative with respect to the direction. By definition $\nabla \cdot \mathbf{P}$ is a trace of a tensor $\partial \mathbf{P} / \partial \mathbf{r}$ as one of its invariants. We obtain $\partial \mathbf{P} / \partial \mathbf{r}$ in coordinateless form, using the so-called a Gâteaux derivative, or a weak derivative. This concept is a tool for nonlinear functional analysis, which, in particular, includes the classical calculus of variations [13, 14]. The weak derivative is defined in terms of a Gâteaux differential (a weak differential), which is introduced as the limit as $t \rightarrow 0$ of the mapping of one normalized space X to another Y at an increment $x + th$ of an element of the space X .

Using the representation $\mathbf{P} = P^m \mathbf{e}_m$, we obtain:

$$\frac{\partial \mathbf{P}}{\partial \mathbf{r}} = P^m \frac{\partial \mathbf{e}_m}{\partial \mathbf{r}} + \left(\frac{\partial P^m}{\partial \mathbf{r}} \cdot \mathbf{i}_s \right) \cdot (\mathbf{e}_m \mathbf{i}_s).$$

The base \mathbf{e}_m is orthogonal at each point of \mathbf{r} , so it should be obtained by rotating the base \mathbf{i}_m around a certain axis at a small angle φ . It is clear that if the polarizability $\chi(\mathbf{r})$ is constant, then the angle φ does not change. The smallness of the angle φ is due to the small difference between the bases \mathbf{e}_m and \mathbf{i}_m by the variable component $\chi(\mathbf{r})$.

Thus a key concept is introduced into the theory – the local angle of rotation of the basis \mathbf{e}_m . In the case of an ideal crystal, the angle φ is determined by the three-dimensionally periodic polarizability $\chi(\mathbf{r})$ as a characteristic of the medium.

Introducing the vector $\varphi = \varphi \mathbf{k}$, where \mathbf{k} is a unit vector along the axis of rotation, for small φ from the Euler theorem [14] we obtain the law of the basis transformation \mathbf{e}_m :

$$\mathbf{e}_m = \mathbf{i}_m + \varphi \times \mathbf{i}_m.$$

Obviously, due to the locality of the basis \mathbf{e}_m , the vector φ is a local characteristic of the medium (field variable): $\varphi = \varphi(\mathbf{r})$.

Carrying out the corresponding calculations, we obtain the final expression for the momentum divergence:

$$\nabla' \cdot \mathbf{P} = \nabla \cdot \mathbf{P} - \nabla \cdot (\varphi \times \mathbf{P}). \quad (17)$$

6.2. CALCULATION $\nabla' \cdot \varepsilon$

We find the expression for the gradient ε . We will consider the transition from the basis \mathbf{e}_m to the basis \mathbf{i}_m as a substitute for the variable of the scalar function of the vector argument. With regard to connection

$$\mathbf{r}' = \mathbf{r} + \boldsymbol{\varphi} \times \mathbf{r},$$

using the Gâteaux derivative, we find:

$$\frac{\partial \mathbf{r}'}{\partial \mathbf{r}} = \mathbf{I} + \boldsymbol{\varphi} \times \mathbf{I} + \frac{\partial \boldsymbol{\varphi}}{\partial \mathbf{r}} \times \mathbf{r},$$

$$\left(\frac{\partial \mathbf{r}'}{\partial \mathbf{r}}\right)^T = \nabla \mathbf{r}' = \mathbf{I} - \mathbf{I} \times \boldsymbol{\varphi} - \mathbf{r} \times \left(\frac{\partial \boldsymbol{\varphi}}{\partial \mathbf{r}}\right)^T = \mathbf{I} - \mathbf{I} \times \boldsymbol{\varphi} - \mathbf{r} \times \nabla \boldsymbol{\varphi}.$$

Here the sign T means transposition.

Then the gradient of ε is equal to:

$$\nabla \varepsilon = (\mathbf{I} - \mathbf{I} \times \boldsymbol{\varphi} - \mathbf{r} \times \nabla \boldsymbol{\varphi}) \cdot \nabla' \varepsilon.$$

As a result, taking into account the smallness of $\boldsymbol{\varphi}$, inverting the operator $\mathbf{I} - \mathbf{I} \times \boldsymbol{\varphi} - \mathbf{r} \times \nabla \boldsymbol{\varphi}$, we get

$$\nabla' \varepsilon = (\mathbf{I} + \mathbf{I} \times \boldsymbol{\varphi} + \mathbf{r} \times \nabla \boldsymbol{\varphi}) \cdot \nabla \varepsilon. \tag{18}$$

6.3. CALCULATION $\nabla' \cdot \mathbf{T}$

To calculate this we use the formula for the divergence of the dyad:

$$\nabla \cdot (\mathbf{u}\mathbf{v}) = (\nabla \cdot \mathbf{u})\mathbf{v} + \mathbf{u} \cdot (\nabla \mathbf{v}),$$

as well as well-known vector analysis formulas. We get:

$$\begin{aligned} \nabla' \cdot \mathbf{T} = & -(\nabla w \cdot \mathbf{e}_3)\mathbf{e}_3 - (w\nabla \cdot \mathbf{e}_3)\mathbf{e}_3 - \\ & -((\nabla \times \boldsymbol{\varphi}) \cdot w\mathbf{e}_3)\mathbf{e}_3 + ((\nabla \times w\mathbf{e}_3) \cdot \boldsymbol{\varphi})\mathbf{e}_3 - w\mathbf{e}_3 \cdot (\nabla' \mathbf{e}_3). \end{aligned}$$

Using the Gâteaux derivative, in the first approximation in $\boldsymbol{\varphi}$, we get:

$$\begin{aligned} \nabla' \cdot \mathbf{T} = & -(\nabla w \cdot \mathbf{i}_3)(\mathbf{i}_3 + \boldsymbol{\varphi} \times \mathbf{i}_3) - \\ & -2w(\nabla \cdot (\boldsymbol{\varphi} \times \mathbf{i}_3))\mathbf{i}_3. \end{aligned} \tag{19}$$

7. THE CALCULATION OF THE ROTATION VECTOR $\boldsymbol{\Phi}$

In order to explicitly take into account the locality of the basis, and therefore the dependence on $\chi(\mathbf{r})$ we turn to the orthogonal basis \mathbf{m}_j , that is not normalized to one. We select the new normalization from the requirement that when passing to the continual approximation ($\chi(\mathbf{r}) = \chi_0 = \text{const}$, respectively, $\varepsilon(\mathbf{r}) = \varepsilon_0 = \text{const}$) the vectors \mathbf{m}_j pass into \mathbf{e}_j . This takes into account the refraction of a wave in a crystal:

$$\begin{aligned} \mathbf{m}_1 &= \frac{\mathbf{D}}{D_0} = \frac{\varepsilon \mathbf{E}}{\varepsilon_0 E} = \frac{\varepsilon}{\varepsilon_0} \mathbf{e}_1, \\ \mathbf{m}_2 &= \frac{\mathbf{H}}{H_0} = \frac{\sqrt{\varepsilon} \mathbf{E}}{\sqrt{\varepsilon_0} E} = \sqrt{\frac{\varepsilon}{\varepsilon_0}} \mathbf{e}_2, \\ \mathbf{m}_3 &= \frac{\mathbf{P}}{P_0} = \frac{\sqrt{\varepsilon} |\mathbf{E}|^2}{\sqrt{\varepsilon_0} |E|^2} \mathbf{e}_3 = \sqrt{\frac{\varepsilon}{\varepsilon_0}} \mathbf{e}_3. \end{aligned}$$

In this basis, the tensor \mathbf{T} has the form

$$\mathbf{T} = -w(\mathbf{e}_3 \mathbf{e}_3) = -w \frac{\varepsilon}{\varepsilon_0} (\mathbf{m}_3 \mathbf{m}_3).$$

Lamé coefficients [15] for the basis \mathbf{m}_j are equal

$$h_1 = |\mathbf{m}_1| = \frac{\varepsilon}{\varepsilon_0}; h_2 = |\mathbf{m}_2| = \sqrt{\frac{\varepsilon}{\varepsilon_0}}; h_3 = |\mathbf{m}_3| = \sqrt{\frac{\varepsilon}{\varepsilon_0}}.$$

Let us determine the microscopic displacement vector $\mathbf{u} = \mathbf{m}_j - \mathbf{e}_j$ during the transition from one basis to another along the corresponding directions of the axes of coordinates. Note that the vector \mathbf{u} introduced by us, unlike the displacement vector of atomic planes in the formalism of the dynamic theory of X-ray diffraction for imperfect crystals [2–4] is not a macroscopically averaged value used in the continuum theory of elasticity [15]. Our microscopic displacement vector \mathbf{u} , due to locality $\chi(\mathbf{r})$ changes in the unit cell scale.

In this case we assume that $\varepsilon(\mathbf{r}) = \varepsilon(\mathbf{h}\mathbf{r})$ where \mathbf{h} is the reciprocal lattice vector. Thus we actually use the model of an ideal crystal. Note that this restriction is by no means fundamental. If necessary you can enter all sorts of deviations from the ideal periodicity, i.e. to carry out a generalization of the theory on the deformed state of the crystal. For definiteness we choose the standard form of polarizability used in the dynamic theory of diffraction:

$$\begin{aligned} \varepsilon &= 1 + \chi_0 + \chi_h \left(\exp(i\mathbf{h}\mathbf{r}) + \frac{\chi_{\bar{h}}}{\chi_h} \exp(-i\mathbf{h}\mathbf{r}) \right) = \tag{20} \\ &= \varepsilon_0 + \chi_h f(\mathbf{h}\mathbf{r}). \end{aligned}$$

Then for the microscopic displacement vector \mathbf{u} , we have:

$$\mathbf{u} = (h_j - 1)\mathbf{e}_j = (h_j - 1) (\mathbf{i}_j + \boldsymbol{\varphi} \times \mathbf{i}_j). \tag{21}$$

Introduction of the vector \mathbf{u} actually means using an alternative concept of describing the interaction of a field with a substance. In the usual description, we use the representation of interaction unfolding in Euclidean space with invariable metric

characteristics. The space in this concept plays the passive role of the “container” of events.

An alternative concept gives the theory a geometric interpretation, which goes back to Einstein's idea that the geometry of space is not given *ad hoc* but is determined by the interaction in this case, the field and matter. Thus, the geometry acquires a dynamic nature [6].

In this case the response of the medium to external disturbance is considered as a local change in the geometry – a rotation of the base determined by the structural characteristics of the medium. Or otherwise the interaction changes the geometry.

Next we use the results of the linear theory of elasticity [16], in which small displacements of the medium are considered as field variables determining the symmetric deformation tensor $\mathbf{\epsilon}(\mathbf{r})$ and the antisymmetric rotation tensor $\mathbf{\omega}(\mathbf{r})$. As is known any antisymmetric tensor is associated with its dual vector. In the case of $\mathbf{\omega}(\mathbf{r})$ this vector is the axial vector of small rotations $\boldsymbol{\varphi}$. The geometric meaning of the vector $\boldsymbol{\varphi}$ is to rotate a neighborhood of a given point of the medium as a whole around the axis of rotation and the angle and direction of rotation coincide respectively with the length and direction of the vector $\boldsymbol{\varphi}$.

Based on this interpretation, the following fundamental relation is derived in the theory of elasticity which determines the rotation vector $\boldsymbol{\varphi}$ through the rotor of the displacement vector [16]:

$$\boldsymbol{\varphi} = \frac{1}{2} \nabla \times \mathbf{u}. \quad (22)$$

According to (22) using (21) we get:

$$\begin{aligned} 2\boldsymbol{\varphi} &= \nabla \times \mathbf{u} = \nabla \times (h_j - 1)(\mathbf{i}_j + \boldsymbol{\varphi} \times \mathbf{i}_j) = \\ &= \nabla (h_j - 1) \times \mathbf{i}_j + \nabla \times ((h_j - 1)(\boldsymbol{\varphi} \times \mathbf{i}_j)). \end{aligned}$$

Or, taking into account (20) and the smallness of χ :

$$\begin{aligned} 2\boldsymbol{\varphi} &= \frac{\chi_h}{2} \nabla f \times (2\mathbf{i}_1 + \mathbf{i}_2 + \mathbf{i}_3) + \\ &+ \frac{\chi_h}{2} \nabla \times (f(2\boldsymbol{\varphi} \times \mathbf{i}_1 + \boldsymbol{\varphi} \times \mathbf{i}_2 + \boldsymbol{\varphi} \times \mathbf{i}_3)). \end{aligned} \quad (23)$$

We look for the solution of equation (23) in the form of a series expansion in a small parameter χ_h :

$$\boldsymbol{\varphi} = \boldsymbol{\varphi}_0 + \chi_h \boldsymbol{\varphi}_1 + \dots$$

Acting by the standard perturbation theory method, we obtain the solution in the

zero approximation $\boldsymbol{\varphi}_0 = 0$ and the first order approximation:

$$\boldsymbol{\varphi}_1 = \frac{1}{4} (\nabla f \times (2\mathbf{i}_1 + \mathbf{i}_2 + \mathbf{i}_3)).$$

Then the solution of equation (23) in the first order approximation takes the form:

$$\boldsymbol{\varphi} = \frac{\nabla \chi}{4} \times (2\mathbf{i}_1 + \mathbf{i}_2 + \mathbf{i}_3). \quad (24)$$

According to (24), the value of $\boldsymbol{\varphi}$ is a local measure of the deviation of the geometric characteristics of the medium with respect to the propagation of electromagnetic waves from the continual approximation.

The vector $\boldsymbol{\varphi}$ under the condition $\chi = \chi(\mathbf{hr})$ i.e. if the crystal is perfect, it retains its orientation in space and does not coincide with the basis vectors \mathbf{i}_m . If it coincided with \mathbf{i}_1 , then σ -polarization would be realized, and if with \mathbf{i}_2 – π -polarization. Consequently, with the transmission of a wave a superposition of σ - and π -polarizations is realized and this is apparently a general result. Hence the conclusion: the separation of waves by polarization when considering problems of X-ray wave scattering on a crystal is not quite correct even in the case of an ideal crystal.

Of course, the conservation of the orientation of the vector $\boldsymbol{\varphi}$ in space is a specific property of only an ideal crystal. In other cases say when taking into account the deformation of the crystal the vector $\boldsymbol{\varphi}$ will locally change its orientation in space, for example, precess around the original direction corresponding to the ideal crystal.

8. CONCLUSION OF THE BASIC EQUATION SYSTEM IN THE CARTESIAN BASIS

Linearize the fundamental system (16) by a small quantity χ :

$$\begin{aligned} \nabla' \cdot \mathbf{T} + w \nabla \varepsilon &= \frac{\partial \mathbf{P}}{\partial t}, \\ \nabla' \cdot \mathbf{P} - \nabla \varepsilon \mathbf{P} &= -\frac{\varepsilon}{c^2} \frac{\partial w}{\partial t}. \end{aligned}$$

Then using explicit expressions for divergences and gradient (17-19), we obtain:

$$\begin{aligned}
 & -(\nabla w \cdot \mathbf{i}_3)(\mathbf{i}_3 + \boldsymbol{\varphi} + \mathbf{i}_3) - 2w(\nabla \cdot (\boldsymbol{\varphi} \times \mathbf{i}_3))\mathbf{i}_3 + \\
 & + w \nabla \chi = \frac{\partial \mathbf{P}}{\partial t},
 \end{aligned} \tag{25}$$

$$\nabla \cdot \mathbf{P} - \nabla \cdot (\boldsymbol{\varphi} \times \mathbf{P}) - \nabla \chi \cdot \mathbf{P} = -\frac{1 + \chi(\mathbf{r})}{c^2} \frac{\partial w}{\partial t}.$$

These relations represent the fundamental equations of the above theory, which allow one to calculate the momentum and energy of a field when it interacts with a crystal. As in the usual dynamic theory of diffraction (say, the Takagi equations), such an interaction is parametric in nature, which means that a parametric resonance should be observed under certain geometric conditions. Of course one should expect that these conditions correspond to the Laue equation, and the resonance physically corresponds to the appearance of a diffraction wave (in terms of this theory the appearance of the corresponding component of the total momentum).

Equations (25) in contrast to the diffraction equations for fields depend parametrically not only on χ , but on $\nabla \chi \sim \mathbf{h}$. Note that the equations are linear which makes it possible to use the principle of superposition when constructing the solution.

9. CONCLUSION

Let us outline the further development of the theory as applied to the description of diffraction scattering in a crystal. The basic equations (25) obviously cannot be solved exactly therefore it is necessary to use the methods of perturbation theory. In this case, as a small parameter, as in the theory [3, 4], the Fourier component of polarizability χ_n is used which is associated with diffraction scattering. Unperturbed equations (zero approximation)

$$\begin{aligned}
 & -(\nabla w_0 \cdot \mathbf{i}_3)\mathbf{i}_3 = \frac{\partial \mathbf{P}}{\partial t}, \\
 & \nabla \cdot \mathbf{P} = -\frac{1 + \chi_0}{c^2} \frac{\partial w_0}{\partial t}
 \end{aligned} \tag{26}$$

describe the momentum-energy propagation in a medium as in a continuum.

At the same time unlike the usual wave equations the physical solution for the zero approximation is formed not from harmonic waves but from their products. In fact, for harmonic waves, there is a dependence:

$$\begin{aligned}
 \mathbf{P} & \sim \mathbf{E}e^{i\psi} \times \mathbf{H}e^{i\psi} \sim E\mathbf{H}e^{i2\psi} \\
 w & \sim (Ee^{i\psi})^2 + (He^{i\psi})^2 \sim E\mathbf{H}e^{i2\psi}.
 \end{aligned}$$

Then for \mathbf{P}_0 and w_0 , functionally invariant solutions in the form of squares of harmonic waves containing constant (non-oscillating) components should be chosen. Obviously it is these components that are fixed in the experiment. Such solutions are not harmonic therefore it is impossible to get rid of time derivatives and go to a purely spatial problem by simple substitution. Consequently, it is necessary to develop a perturbation theory for a system of partial differential equations of the type (26).

This problem is the subject of further research.

ACKNOWLEDGMENT

The author expresses deep gratitude to Professor Yu.P. Khapachev for a number of valuable comments on the merits and useful discussion.

REFERENCES

1. James RW. *The Optical Principles Of The Diffraction Of X Rays. Vol II.* London, G. Bell and sons Ltd. 1962, 664 p.
2. Pinsker ZG. *X-ray crystal optics.* Moscow, Nauka Publ., 1982, 392 p.
3. Dyshekov AA, Khapachev YuP. *New analytical approaches to the problems of X-ray diffraction crystal optics.* Nalchik, Kabardino-Balkarian State. university Publ., 2010, 45 p.
4. Dyshekov AA. Generalization of the nonstandard approach in the dynamic theory of diffraction for deformed crystals. *Crystallography Reports*, 2013, 58(7):984-989.
5. Polak LS (ed.). *Variational principles of mechanics. Collection of articles of the classics of science.* Moscow, Fizmatlit Publ., 1959, 932 p.
6. Konopleva NP, Popov VN. *Gauge fields.* Moscow, Atomizdat Publ., 1972, 240 p.
7. Katanaev MO. *Geometric methods in mathematical physics.* Moscow-Kazan, Steklov Math.Inst- Kaz. Fed. Univ. Publ., 2016, 1570 p. <https://arxiv.org/pdf/1311.0733> (in Russian).
8. Lourtioz J.-M., Benisty H., Berger V., Gerard J.-M, Maystre D., Tchelnokov A. *Photonic crystals. Towards Nanoscale Photonic Devices.* Springer-Verlag Berlin Heidelberg, 2008, 514 p.; DOI: 10.1007/978-3-540-78347-3.

9. Aristov VV, Shabelnikov LG. Modern advances in X-ray refractive optics. *UFN*, 178(1):61-83 (in Russ.).
10. Novozhilov YuV, Yappa YuA. *Electrodynamics*. Moscow, Nauka Publ., 1978, 352 p.
11. Fedorov FI. *Theory of gyrotropy*. Minsk, Science and technology Publ., 1976, 456 p.
12. Dubrovin BA, Novikov SP, Fomenko AT. *Modern geometry. Methods and applications*. Moscow, Nauka Publ., 1986, 760 p.
13. Kolmogorov AN, Fomin SV. *Elements of the theory of functions and functional analysis*. Moscow, Nauka Publ., 1981, 544 p.
14. Vilchevskaya EN. Tensor algebra and tensor analysis. Tutorial. St. Petersburg, SPb State Technical University Publ., 2012, 45 p.
15. Lurie AI. *Theory of elasticity*. Moscow, Nauka Publ., 1970, 940 p.
16. Sirotin YuI, Shaskolskaya MP. *Fundamentals of crystal physics*. Moscow, Nauka Publ., 1975. 680 p.

METRIC AND STRUCTURE EQUATIONS IN RELATIVISTIC CONTINUA

Stanislav A. Podosenov, Elena R. Men'kova

All-Russian Research Institute for Optical and Physical Measurements, <http://www.vniiofi.ru/>
Moscow 119361, Russian Federation

Alexander A. Potapov

Kotelnikov Institute of Radioengineering and Electronics, Russian Academy of Sciences, <http://cplire.ru/>
Moscow 125009, Russian Federation

Jaykov Foukzon

Center for Mathematical Sciences, Israel Institute of Technology, <http://www.technion.ac.il/>
Haifa 3200003, Israel

podosenov@mail.ru, potapov@cplire.ru, jaykovfoukzon@list.ru, e_menkova@mail.ru

Abstract. The proper expression describing physical lengths and times in arbitrary relativistic moving continua is presented. To investigate the structure equations determining the space-time geometry at specified medium characteristics are applied. In the elementary case, the geometry is the Riemannian one that does not connect with the Einstein's general relativity theory. The relativistic Born rigid uniformly accelerated reference frame realized in the Riemannian space-time is considered as an example. The relativistic Born rigid uniformly rotating reference frame without a horizon but requiring the Riemannian space-time has been constructed. The Bell inequality solution is obtained and the comparison with the Mössbauer rotor experiment is made.

Keywords: relativistic continuum, structure equations, space-time, general relativity theory, reference frame, Born rigidity, Riemannian, Einstein, Bell inequality, Mössbauer rotor

UDC 530.12, 531.134, 537.9

Bibliography – 37 references

Received 10.8.2018, accepted 12.03.2019

RENSIT, 2019, 11(2):113-124

DOI: 10.17725/rensit.2019.11.113

CONTENTS

1. INTRODUCTION (113)
 2. DISTANCE DETERMINATION METHODS IN THE LAGRANGIAN CO-MOVING NONINERTIAL REFERENCE FRAMES IN THE SPECIAL RELATIVITY THEORY (114)
 3. THE CONNECTION OF THE SPACE-TIME GEOMETRY WITH CONTINUUM PROPERTIES AND FORCE FIELDS (116)
 4. RELATIVISTIC RIGID ROTATING NONINERTIAL REFERENCE FRAMES (118)
 5. DISCUSSION OF THE MÖSSBAUER ROTOR EXPERIMENT (119)
 6. CONCLUSION (121)
- REFERENCES (122)

1. INTRODUCTION

It was shown, that in the general case flat space-time proved to be “cramped” to describe the continuum motion in the inertial reference frame (IRF) and the transition to the noninertial

reference frame (NRF) [1]. That is connected both with the force field acting on the medium particles and with the conditions imposed on the kinematic characteristics of the continuum by means of the structure equations [2-6]. These equations connect the Riemannian-Christoffel tensor and the strain velocity tensor, rotational velocity tensor and the first curvature vectors of the world lines of the medium particles. As a result, the system provided to be overdetermined and it can not be realized in the Minkowski space. This system can be solved in considering the medium motion in the Riemannian space or in the general case in the space of metric connectivity.

However if one does not constrain on the continuum characteristics and only integrates the motion equations, for example, in a flat space-time, then no transformation of coordinates permit go beyond the scope of the flat space-time. In applying nonholonomic transform the curvature tensor obtained from the Minkowski

space in nonholonomic coordinates is identically zero. Provided that this zero tensor can be divided into two nonzero parts. One of them is expressed by the Christoffel symbols and other one depends on the moving medium characteristics [2-5].

2. DISTANCE DETERMINATION METHODS IN THE LAGRANGIAN CO-MOVING NONINERTIAL REFERENCE FRAMES IN THE SPECIAL RELATIVITY THEORY

In the Bell's problem [7], it was shown that the string connecting identical uniformly accelerated point rockets moving with uniform acceleration in the cosmonaut system is broken. However, its length in the inertial reference frame (IRF) does not change. Solution [7] was used to calculate the motion of an electron bunch in linear colliders in constant electric field [8]. In noninertial reference frame (NRF) frozen into a bunch or a string in the Bell's problem, the correct formula of instantaneous length does not exist. Let signature of the Minkowski space-time is (+ - -), the Greek and Latin indices run values from 0 to 3 and from 1 to 3, respectively. Standard formula [9] for the calculation of the square element of a physical distance dL^2 by means of the spatial metric tensor

$$\gamma_{ik} = -g_{ik} + \frac{g_{0i}g_{0k}}{g_{00}} \tag{1}$$

is used incorrectly. The correct (in accordance with special relativity theory (SRT)) application of this formula on the hypersurface orthogonal to the world lines of the bunch particles that is the instantaneous physical space of co-moving medium observers results in the relation [10-12]

$$L(t) = \frac{c^2}{a_0} \ln \left(\cosh \left(\frac{a_0 L_0}{c^2} \right) + \sinh \left(\frac{a_0 L_0}{c^2} \right) \sqrt{1 + \beta^2} \right), \tag{2}$$

where $L(t)$ is the bunch length (or the string in the Bell's problem) in the reference frame co-moving to the bunch as IRF time function t , L_0 is the initial bunch (string) length, a_0 is the uniform acceleration, $\beta = a_0 t / c$. The latter formula is original and unknown in scientific literature from before [10-12].

Standard calculation accordingly to formula (1) from [9] in [8], [13]

$$L(t) = L_0 \sqrt{1 + a_0^2 t^2 / c^2} = \frac{L_0}{\sqrt{1 - v^2(t) / c^2}}, \tag{3}$$

where the curvature of a space-like curve orthogonal to the world lines of the medium particles is neglected, at the end of speed-up in the Lagrangian co-moving NRF, results in increase of the bunch length in modern linear collider [8] in tens of thousands times. In (2) under the same conditions the bunch length increases in 1.003 times, but it does not solve the Bell's problem in principle. The approach [14] based on the calculation of the distance along the unit vector of some instantly co-moving inertial reference frame (ICIRF) from the bunch beginning to its end, results in practical nulling of the bunch length at the end of speed-up. In the Bell's problem provided $\alpha_0 L_0 / c^2 \ll 1$ all formulae from the works above mentioned coincide.

Since many questions connected with the Bell's problem arise, we would like to give some elementary explanations. Instead of the rockets connected with a string, let us firstly consider two non-commuted identical charged particles, which interact only with the external field (the model of charged dust widely used in physics). We place these particles in the uniform electric field, let the axis coincides with the field direction. Let the second particle is located at origin, and the first particle is located at the distance L from the second one. The particle interaction can be neglected as compared with the interaction with the external field. In the IFR we release these particles simultaneously at $t = 0$.

The first question is. How the distance between the particles in the initial IRF at any instant of time t will change? To answer the question it is necessary to consider the problem solution [9] for relativistic uniformly accelerated rectilinear motion with uniform acceleration in a proper (at the each instant of time) reference frame. Then we calculate the displacement of both particles relatively the origin of coordinates. For the first particle at the right side of the equation, we add the L value (original Lagrangian coordinate). The second particle is placed at the origin of coordinates. Then we have the obvious equality $x_1(t) - x_2(t) =$

$x(t, L) - x(t, 0) = L = \text{const}$. Thus, the distance between the particles remains constant. So in the initial IRF there are no any Lorentz contractions. If the distance between two particles is filled with the similar ones that turns into the dust-like bar which we call the Logunov's system [15].

It follows from the considered example that the Logunov's system is a classical rigid one. The drawback of this system is: from the viewpoint of other IRF moving relatively the initial one $t = \text{const}$ is not a simultaneity surface. Therefore, the Logunov's system is not the Lorentz-covariant one.

Let us continue the consideration of two particles (we will connect the Fermi-Walker tetrad with each particle [16]). We place the massless observer on each particle, each observer will move with constant acceleration (that is that will have a fixed first curvature vector of the world line or constant acceleration α_0 in the proper NRF). Physical observer space in NRF in Fermi-Walker transport will be stretched on the Fermi triads. For our particular case, when all Fermi triads in the initial time coincide with the affine triads of Minkowski space with zero initial velocity, one of the triad reference mark always will be directed perpendicularly to one of the neighboring world lines 1 or 2. The own world line corresponds to each particle in initial IRF. In this plane at $t = \text{const}$ the distances between the neighboring world lines remain steady and equal to L . However the length of perpendicular from the cross point of the line $t = \text{const}$ with the world line of the second particle on the world line of the first one will not be kept in moving the particles as opposed to L . On the basis of the property of projection operators it follows that the distance in Fermi triads in particle motion will increase. Thus, the first particle will run from the second one. The observers on the particles will see the Lorentz elongation instead of the Lorentz contraction.

It is easy to see that if one connects two particles with a thin massless glass string then the fiber will be broken due to the Lorentz elongation but not from the Lorentz contraction. Such a viewpoint is the most famous in literature [7, 8, 13], but it contradicts to the relativistic elasticity theory. The

basis of the theory was developed by Pauli and Herglotz [17] in terms of the Born conception. Neither Lorentz contraction nor Lorentz elongation can cause the stress in a rigid body and break the string. Up to date this crude error exists in scientific literature for the explanation of the Bell's problem.

In order to generalize the classical conception of the rigid motion Born introduced the definition consistent with SRT and GRT. According to the definition the continuum motion is called rigid (in the Born's sense) if for any pair of neighboring body particles the orthogonal interval between corresponding pairs of world lines of medium particles remains constant during the motion. The difference between the classical and relativistic rigidity conditions is in the selection of spatial hypersurfaces along which distances between world lines of body particles are measured. Obviously in rigid moving hypersurfaces orthogonal to world lines in one IRF are hyperplanes orthogonal to world lines in all other IRF, that makes the Born-rigid NRF the Lorentz-covariant one as opposed to the classical rigid NRF.

According to Pauli, it is the deviation from the Born's rigidity but not the Lorentz contraction (Lorentz elongation) that results in deformations and tensions in the body.

It turns out that the standard formula for the Lorentz elongation is wrong. In non-rigid (in the Born's sense) motion, the spatial hypersurface orthogonal to the world lines is curved and this curvature is not taken in to account in the Lorentz elongation.

This solution is used to calculate the motion of electron bunch in linear colliders in constant electric field [10]. Thus, we got a paradoxical result. Particles being in completely identical conditions run from each other! Thus, the relativistic Logunov's NRF results in paradox. The main drawback of the Logunov's NRF is the absence of relativistic rigidity.

The Möller-Rindler NRF is an alternative of the Logunov NRF. The Rindler NRF is obtained from the Möller NRF [18] by simple re-designation of the Lagrangian coordinates and the transition to the dimensionless variables. The Möller NRF

advantage is: the system is a relativistic rigid (in the Born's sense) one. Its drawback is: this NRF is not a global uniformly accelerated system and it has horizon. Each particle of the Möller medium moves with the uniform acceleration, but these accelerations are not equal each other. Therefore, the designation of the Möller transform as the transform to the uniformly accelerated NRF (as it is, for example, in Fok's book [19]) is not quite correct.

Thus, both Logunov's NRF and Möller's NRF do not eliminate all SRT paradoxes. We proved the statement that the Born rigid relativistic uniformly accelerated NRF can be realized in the Riemannian space-time which in the general case is not connected with GRT [1].

3. THE CONNECTION OF THE SPACE-TIME GEOMETRY WITH CONTINUUM PROPERTIES AND FORCE FIELDS

In the Newton's mechanics and SRT a mass point has zero absolute acceleration relatively IRF when the forces applied to it are absent or their vector sum is equal to zero. In GRT this rule is not fulfilled. The mass point being at rest on the surface of the gravitating sphere in accordance with GRT has the first curvature vector (4-acceleration) different from zero. Absolute acceleration is directed along external normal to the sphere and it is equal to the Newton's free fall acceleration near the surface. The support reaction force from the sphere surface moves the body from its geodesic line having zero first curvature vector only when the support reaction is absent. According to Newton, absolute acceleration of a mass point on the sphere surface is equal to zero. For weak fields Einstein's equations coincide with the Newton's theory, however the correspondence principle is not applied to absolute accelerations.

One can judge about the force field by the motion or the rest of test particles. By definition, test particles do not interact with each other, and they interact only with external field. Let test particles are identical and represent some continuum. The 4-acceleration, the strain rate tensor and the tensor of the angular velocity

are the characteristics of the continuum in four-dimensional space-time. 4-acceleration is entered into the law of motion and, at the known plane metric, the field of the 4-velocity and the main medium tensors are determined by the integration of the equation of motion. Continuum in the force field specifies some reference frame (RF). For RF with the specified properties one must know the additional conditions of the main medium tensors depending on 4-velocities and 4-accelerations. For example, the demand of the rotation absence and the Born rigidity. The number of the equations for determination of the 4-velocity becomes overdetermined and the integrability conditions must be fulfilled. They are fulfilled when both 4-velocities of the medium and the metric coefficients are sought. The integrability conditions were obtained

$$R_{\varepsilon\sigma,\nu}^{\mu}V_{\mu} = 2\nabla_{[\varepsilon}\Sigma_{\sigma]\nu} + 2\nabla_{[\varepsilon}\Omega_{\sigma]\nu} + 2\nabla_{[\varepsilon}(V_{\sigma]}F_{\nu}), \quad (4)$$

for which in moving continuum in four-dimensional space-time the equations are valid

$$\nabla_{\mu}V_{\mu} = \Sigma_{\mu\nu} + \Omega_{\mu\nu} + V_{\mu}F_{\nu}, \quad (5)$$

where V_{μ}^{μ} is the field of four-velocity, which satisfies the normalizing condition

$$g_{\mu\nu}V^{\mu}V^{\nu} = 1, \quad (6)$$

$g_{\mu\nu}$ is the metric tensor in the Euler frame of reference,

$$\Sigma_{\mu\nu} = \nabla_{(\mu}V_{\nu)} - V_{(\mu}F_{\nu)}, \quad (7)$$

$$\Omega_{\mu\nu} = \nabla_{[\mu}V_{\nu]} - V_{[\mu}F_{\nu]}, \quad (8)$$

$$F_{\mu} = V^{\nu}\nabla_{\nu}V_{\mu}, \quad (9)$$

where $\Sigma_{\mu\nu}$ is the strain-rate tensor, $\Omega_{\mu\nu}$ is the tensor of angular velocity of rotation, and F_{μ} are the first curvature vectors of the world lines of the medium particles.

One can obtain the Raychaudhuri equation [20] from the structure equation (4).

Can we repeat on their basis our NRF results? It is the technical question and does not have practical significance.

Integration of system (4-9), where $R_{\varepsilon\sigma,\nu}^{\mu}$ is the curvature tensor (conventionally expressed in terms of the metric tensor), yields a solution to the problem on the space-time geometry, in which NRF with a specified structure is implemented.

Equations (4) will be referred to as structural equations for the NRF. The theorem, that the Born rigid uniformly accelerated motion is shown to be realizable in the Riemannian space, is proved [4], [21]. The structure equations are not connected with GRT but they impose additional conditions to the Einstein's equations. A theorem, according to which all static spherical symmetrical GRT solutions are compatible with the structure equations, was proven. One-dimensional solution beyond the plane infinite massive source does not exist in GRT, but the structure equation has it and it induces the metric for constant uniform static field [21].

The calculation in the Lagrangian co-moving NRF results in the metric

$$dS^2 = \exp\left(\frac{2a_0 y^1}{c^2}\right) (dy^0)^2 - (dy^1)^2 - (dy^2)^2 - (dy^3)^2, \quad (10)$$

where the acceleration α_0 is directed along the y_1 axis. First metric [10] was obtained in [1] and repeated in [22, 23]. One independent component of the curvature tensor calculated by metric (10) is of the form

$$R_{10,10} = -\frac{a_0^2}{c^4} \exp(2a_0 y^1 / c^2). \quad (11)$$

The components of the Ricci tensor $R_{\beta\gamma} = g^{\alpha\gamma} R_{\alpha\beta,\gamma\delta}$ and the scalar curvature R can be written as

$$R_{00} = -R_{10,10}, R_{11} = -\frac{a_0^2}{c^4}, R_{10} = 0, R = 2\frac{a_0^2}{c^4}. \quad (12)$$

One can directly be convinced of the uniformly accelerated NRF (12)

$$\begin{aligned} F^1 &= \frac{DV^1}{dS} = \frac{dV^1}{dS} + \Gamma_{00}^1 (V^0)^2 = \\ &= \frac{1}{g_{00}} \Gamma_{00}^1 = -\frac{g^{11}}{2g_{00}} \frac{\partial g_{00}}{\partial y^1} = \frac{a_0}{c^2}. \end{aligned} \quad (13)$$

The rest of the components of 4-accelerations are equal to zero. The metric (10) can be interpreted as the equilibrium of the probe particles in any constant uniform force field. Let the identical probe charges with the identical masses are hanged up on the weightless threads at the uniform constant electric fields. It is clear from the physical consideration that the charges are at rest relatively

each other (the model of charged dust) and the tensions of all threads are identical.

Two points of view are permissible.

1. The space-time is a plane one and the sum of the forces on each charge is equal to zero.

2. The space-time is a Riemannian with the plane section and the vector of 4-acceleration is constant and it is calculated in accordance with formula (13).

Investigation of electrostatics in the Riemannian space is considered in detail in [21] and the system of the solutions of the Einstein-Maxwell equations consistent with the structure equations was obtained in [24, 25].

We shall develop the second point of view in accordance with GRT.

In the Riemannian geometry, the particle fixed in the field has nonzero first curvature vector (4-acceleration), and in the Minkowski space the same particle has a straight world line with zero 4-acceleration.

From the global equivalence principle, the locking of the particles in the uniform constant force field is equivalent to their occurrence in Born's rigid relativistic global uniformly accelerated NRF. In releasing the particles from the bonds, they begin to move at the starting IRF in the Minkowski space in the constant uniform electric field and the distance between the particles in IRF is not changed [2] as well as in NRF (10). In Bell's problem when starting of two point-like rockets with identical constant accelerations in the astronauts' reference frame, after the oscillation damping in the thread the world lines of the thread particles will be "parallel" to the world lines of the point-like rockets in IRF. Perfect weightless accelerometers, fixed at the weightless thread and the rockets, will show identical values. Consequently, the metric for the thread in the astronauts' reference frame coincides with (10). In NRF, the thread length is kept as well as in IRF since the initial Eulerian coordinates coincide with the Lagrange coordinates. The thread will not be broken. The paradox arises because of the standard accepted at the moment transition from IRF to NRF.

Deduced formula (2) in SRT is correct only in the case of the standard transition from IRF to NRF.

We shall point out that the space-time is curved in the accelerated point-like rockets and the thread only in the limit of the world band. The world lines of the starting IRF particles of the Minkowski space are the straight lines parallel to the time axis and having zero first curvature vectors. From the viewpoint of any NRF, these vectors will remain zero as it is impossible to create or to zero out 4-vectors by means of the transition from NRF to IRF and conversely with the transformation of coordinates containing the time in non-linear form. Namely such transformations of coordinates are considered by the orthodox persons as the transition from IRF to NRF and conversely. From the astronauts' viewpoint the worlds lines of the IRF particles seem not to be parallel and the medium particles of the IRF basis move on the geodetic lines relatively NRF (10). The interval element has the form [2, 3]

$$dS^2 = c^2 dt^2 - (1 - v^2/c^2)(dx^1)^2 - (dx^2)^2 - (dx^3)^2, \quad (14)$$

containing in an explicit form the Lorentz contractions and describing a synchronous RF in the Riemannian space-time. The velocity v of IRF basis particles relatively NRF has the form $v = c \sin(\alpha_0 t/c)$.

4. RELATIVISTIC RIGID ROTATING NRF

Usually when considering the rotating disk one selects the rest-frame in which the cylindrical coordinates $r_\rho, \varphi_\rho, z_\rho, t_\rho$ are introduced and passes to the rotating reference frame r, φ, z, t in accordance with formulae:

$$r_\rho = r, \psi = \varphi_0 + \Omega t, z_\rho = z, t_\rho = t,$$

where the rotational speed Ω relatively z axis is considered as constant. The interval element has the form

$$dS^2 = \left(1 - \frac{\Omega^2 r^2}{c^2}\right) c^2 dt^2 - 2\Omega r^2 d\varphi dt - dz^2 - r^2 d\varphi^2 - dr^2. \quad (15)$$

The formula holds when $r\Omega/c < 1$. In [26-28] other velocity distributions, which restrict the linear velocity of the disk at $r \rightarrow \infty$ with the value of velocity of light c and at $\Omega r/c \ll 1$ form $v = \Omega r$, are discussed. However only usual distribution law $v = \Omega r, \Omega = \text{const}$, satisfies to the stiffness

criterion both the classic and the relativistic one (in Born's sense).

Let us determine the metric of the rigid relativistic uniformly rotating NRF by means of our method supposing in the formulae the strain velocity tensor $\Sigma_{\mu\nu} = 0$ and demanding the constancy of the invariant characterizing the relativistic generalization of the square of the disk angular velocity ω

$$\Omega_{\mu\nu} \Omega^{\mu\nu} = \frac{2\omega^2}{c^2} = \text{const}. \quad (16)$$

In the Lagrangian co-moving frame of reference connected with the rotating disk we have

$$dS^2 = D(r)c^2 dt^2 - 2P(r)cd\varphi dt - dz^2 - r^2 d\varphi^2 - dr^2. \quad (17)$$

$$F^1 = \frac{1}{2D} \frac{dD}{dr}, F^2 = F^3 = F^0 = 0. \quad (18)$$

Afterwards the cumbersome calculations we have two independent equations

$$\frac{P}{D} \frac{dD}{dr} - \frac{dP}{dr} = -2 \frac{\omega}{c} (Dr^2 + P^2)^{1/2}, \quad (19)$$

$$\frac{dD}{dr} = -2 \frac{\omega}{c} DP (Dr^2 + P^2)^{1/2}, \quad (20)$$

Condition (16) is equivalent to the constancy of the value of chronometrically invariant angular velocity vector [29] and the constancy of the value of the angular velocity in the co-moving tetrads [28].

The relativistic ω and the classic angular velocity Ω are connected by the relation

$$\omega = \Omega \left(1 - \frac{\Omega^2 r^2}{c^2}\right)^{-1}. \quad (21)$$

For metric (17) there is a steady-state solution applied in the whole sphere $0 < r < \infty$ but realized in the Riemannian space-time.

The solution of the system (19), (20) in quadratures is absent. Numerical analysis showed that at $\omega r/c \ll 1$ metric (17) coincides with metric (15). Centripetal acceleration in the rotating NRF is determined with the formula

$$a = c^2 F^1 = -\frac{\omega c P}{\sqrt{Dr^2 + P^2}}, \quad (22)$$

which at small r passes to the classical one and at $r \rightarrow \infty$ gives $a = -\omega c$. The calculation of the independent nonzero components of the

curvature tensor are cumbersome, and we omit them (see [2], [3]).

After simplifications the system [24, 25] is represented in the form

$$\frac{dv}{dx} + \frac{v}{x}(1-v^2) = (2-v^2)(1-v^2), \quad (23)$$

$$D = \exp(-2 \int v dx), \quad v = \frac{U}{\sqrt{1+U^2}}, \quad U = \frac{P}{r\sqrt{D}}, \quad x = \frac{\omega r}{c}. \quad (24)$$

Physical interpretation of function $v(x)$ means the dimensionless linear velocity of the disk. For small velocities

$$D = \exp(-2 \int v dx) = \exp(-x^2) = 1 - x^2, \quad P = \frac{\omega r^2}{c}. \quad (25)$$

that is equivalent to the classic expression. It follows from the analysis of (23) that for $x \rightarrow \infty$ the equation has the solution $v = 1$. This solution is markedly differed from the classic rigid disk where the velocity field at infinity is indefinitely great. Apparently the diagram of the numerical solution (23) is resemble the diagram of the hyperbolic tangent or the deformed step function for $x > 0$.

5. DISCUSSION OF THE MÖSSBAUER ROTOR EXPERIMENT

It is known [9] that on a revolving disk at all points, the clocks can not be identically synchronized.

From our point of view, this opinion is erroneous and it is investigated in detail in [6], [30], [31].

We refer to as "physical" space orthogonal to the world lines of medium particles. In rotating at the medium, the hypersurfaces orthogonal to particle world lines are absent [16, 29].

However, for subspaces it is not universally true. Let us divide the rotating thin disk into concentric thin hoops and consider particles located in one of them. World lines of this hoop particles in the Minkowski space (that is true for small velocities Ω) form the congruence of the helical lines on the cylinder with radius r and axis ct , and the congruence of space-like helical lines orthogonal to the congruence of world lines of hoop's particles will be a "physical space". This congruence is found from Pfaff's equation

$$V_0 dx^0 + V_\varphi d\varphi = 0, \quad \Omega \approx \omega, \quad \psi = \varphi + \omega t. \quad (26)$$

Integrating (26), we have

$$\begin{aligned} t(r, \psi) &= \frac{\omega r^2 \psi}{c^2}, \quad (a), \\ t(r, \varphi) &= \frac{\omega r^2 \varphi}{c^2(1-x^2)}, \quad (b), \\ x &= \frac{\omega r}{c}. \end{aligned} \quad (27)$$

In accordance with [9] "on a revolving body at all points the clocks can not be identically synchronized. So synchronizing along a closed circuit and returning to the reference point, we obtain that the time differs from the original one by the value"

$$\Delta t = -\frac{1}{c} \oint \frac{g_{02}}{g_{00}} d\varphi = \frac{1}{c^2} \oint \frac{\omega r^2}{(1-x^2)} d\varphi. \quad (28)$$

We believe that the clock synchronization on the closed circuit for the rotating hoop makes sense only in a hypersurface $t = const$. If one selects $t = 0$ as zero readings then in all other hypersurfaces $t = const$ the clocks in different Lagrangian points of the hoop will synchronize as any hypersurface $t = const$ cuts off the world lines of identical length. Formula (27 b) coincides with (28) if $\varphi = 2\pi$, but these formulae make different sense.

We point out that formula (28) can be obtained from the solution of the Pfaff's equation in the Lagrangian co-moving RF in which the solution (27b) was obtained by integration of the Pfaff's equation

$$\begin{aligned} V_0 dx^0 + V_\varphi d\varphi &= 0, \quad V_0 = g_{00} V^0, \quad V_\varphi = g_{0\varphi} V^0, \\ V^0 &= \frac{1}{\sqrt{g_{00}}}, \quad V^2 = 0, \quad dt = -\frac{1}{c} \frac{g_{02}}{g_{00}} d\varphi. \end{aligned} \quad (28a)$$

Whence from metric (15) taking into account (26) we have (27b). However, unlike (28) the contour integral is absent and it is changed by the integral in finite limits.

The time gap in (27b) corresponds to the time distance along the cylinder generatrix from the plane $t = 0$ to the "physical" spatial similar line with φ number. In 2π angle the Lagrangian point φ in "physical" space coincides with the world line of the hoop particle with φ number.

Let us solve the following model problem. We cut a thin hollow tube from the disk center to the external radius R_j . We place a light source in

the disk center. The tube axis has the Lagrangian coordinate $\varphi = 0$, which is unchanged for all tube length. Let us define the signal frequency ν_R at the tube output if the frequency of the source signal is equal to ν_0 .

The world line of the end of the tube with radius R forms a helical line on the surface of the cylinder with radius R . The cylinder axis coincides with the time line \mathcal{A} .

From the point $z = 0, y = 0, x = R$ coinciding with the beginning of the world line of the tube on the edge of the disk at time $t = 0$ there is a "physical" spatially similar line orthogonal (in the sense of pseudo-Euclidean geometry with signature (+ - -)) to the world line of the tube end. Let at time $t = 0$ the source emits a very short light pulse. In some point of time t_1 the light signal comes out of the tube end and crosses its world line. The cylinder generatrix passing through the indicated intersection point crosses the "physical" line at time $t_2 < t_1$. It follows from (26), (27) that per time t_1 the end of the tube turned a corner

$$\psi = \omega t^1, t_2(R, \psi) = X^2 t_1, X^2 = \frac{\omega^2 R^2}{c^2}. \quad (29)$$

The time distance from the "physical" line to the world line of the hoop particle at the point of its intersection with the isotropic geodesic is

$$t_1 - t_2 = \Delta t = (1 - X^2)t_1. \quad (30)$$

For the light signal propagating inside the tube for a fixed Lagrangian coordinate $\varphi = 0, z = 0$, at $\Omega \approx \omega$ we obtain from (15)

$$dS^2 = 0, \frac{dr}{c\sqrt{1-x^2}} = dt, \frac{dr}{dt} = c\sqrt{1-x^2}. \quad (31)$$

One can see from (31) that the coordinate speed of light tends to zero with increasing the distance from the center. However the "physical" speed of light is $dr/dt = c$. As we consider the nonrelativistic disk rotation then accurate within $\omega^2 r^2 / c^2 = x^2 \ll 1$ we obtain

$$\int_0^R \frac{dr}{c\sqrt{1-x^2}} = \int_0^{t_1} dt, t_1 - t_2 = (1 - X^2)t_1 = \frac{R}{c}(1 + X^2/6). \quad (32)$$

The proper time is $\tau_1 = \sqrt{1 - X^2}t_1$, then

$$\tau_1 = \frac{R(1 + X^2/6)}{c\sqrt{1 - X^2}} = \tau \left(1 + \frac{2X^2}{3}\right). \quad (33)$$

The value $R/c \approx \tau$ is the time of a signal propagation from the disk center to the edge in NRF on a rotating disk. One can see from (33) that $\tau_1 > \tau$. That means that the length of the world line of the tube end is greater than the radius R .

Formula (33) in the equivalent form using IRF time can be represented as

$$t_1 = t \left(1 + \frac{2X^2}{3}\right). \quad (34)$$

Let us carry out the following gedanken experiment to obtain the frequency change at the input ν_0 and at the output ν of the tube. Let the radiator in the disk center generates two flashes with the δt interval. The first flash is generated at $t = 0$ and the other one δt later. The second flash will reach the tube end at $t + \delta t$ in accordance with the IRF clock and at $t_1 + \delta t_1$ accordingly to the time of the rotating disk IRF where from (34) $t_1 = 0$. Whence we have

$$t_1 + \delta t_1 = (t + \delta t) \left(1 + \frac{2X^2}{3}\right). \quad (35)$$

Subtracting (34) from (35) and turning to frequencies, $1/\delta t = \nu_R, 1/\delta t_1 = \nu_0$, we obtain

$$\nu_R = \nu_0 \left(1 + \frac{2X^2}{3}\right). \quad (36)$$

It is clear that instead of red shift we have violet one. It is caused by increasing the centrifugal inertial force for the observer inside the rotating tube. With increase of a distance from the radiator to the disk edge the centrifugal acceleration increases as $\omega^2 r$.

Let us analyze the results obtained. The experimental setup of the Mössbauer rotor is described in detail in [32-34]. Our aim is the comparison with theoretical results [32, 33].

In deriving of formula (8) in [33] the author [32, 33] made a mistake. The reference to formula (10) from [35] is incorrect. We present formula (8) from [33] in our designations

$$d\tau = dt \left(1 - \frac{\omega^2 r^2}{c^2}\right). \quad ([33], 8)$$

In accordance with [33], ([33], 8) represents increment of proper time on moving clock having the radial coordinate r for $\omega r \ll c$. According to

standard viewpoint [9], true time τ is connected with the coordinate time t , for the same space point, by the relation

$$d\tau = \sqrt{g_{00}} dt. \tag{37}$$

For the Langevin's rotating disk metric (15) we have

$$d\tau = dt \sqrt{1 - \frac{\omega^2 r^2}{c^2}}. \tag{38}$$

Relations ([33], 8) and (38) are differed by the root in (38). In deriving this formula, the author [33] refers to [35] and formula (10) in it. In our designations, the formula has the form

$$d\tau = dt - \frac{\omega r^2 d\varphi}{c^2}. \tag{[35], 10}$$

Formula ([33], 8) was obtained by the author from the "equality" formula

$$d\varphi = \omega dt. \tag{*}$$

The equality (*) is not mentioned in [33] but it is implied. We point out that ([33], 8) is unrelated to [35] where the author considers the Global Positioning System (GPS) and in calculations he keeps only the first order of smallness of $\omega r/c$ parameter, the second order is neglected but in [32, 33] it is taken into account.

Further the author [32, 33] considers the questions of radial propagation of light in NRF of a hard disk for which the increment of Lagrangian coordinates is $d\varphi = d\zeta = 0$. Thus, the reference of [33] to [35] is pointless. Instead of ([33], 8) the "equality" $d\tau = dt$ is obtained.

Though in [33] the formula coinciding with the Mössbauer rotor experiment was obtained [34], we consider that the theoretical results are not satisfying.

Our results also coincide with the experiment. To obtain them we used the concept of the "physical space" orthogonal to the world lines of the tube elements along which light is propagated.

6. CONCLUSION

There are some difficulties in describing extensive bodies in SRT [36]. The reason is misunderstanding of the concepts of a coordinate system and a reference frame. Beginning with the Einstein's works one connects the transition from IFR to NRF with the transformation of coordinates containing the

time in non-linear form [19]. Therefore, at present in SRT the conventional definition of elementary rigid uniformly accelerated RF is absent. Fok considers that the Möller's NRF is such a system [18]. However, it is not a globally uniformly accelerated one. Each medium particle moves with a constant acceleration but these accelerations of different particles are not equal each other. In the alternative uniformly accelerated Logunov's NRF [15], all particles have identical acceleration but the relativistic Born's stiffness criterion is not fulfilled. From the starting IRF viewpoint, the Lorentz contraction between adjacent consecutive particles is absent. The Logunov's system is a classical rigid one. The enigma and difficulty of SRT is. How electrostatics describing the motion of charged dust without the initial velocity results in the violation of relativistic rigidity?

In [5, 30, 31] the theorem is proved, that in the Minkowski space the Born-rigid and relativistic uniformly accelerated translational continuum motion is absent.

If one imposes supplementary conditions for rigidity or continuum rotations, besides the continuum motion equations, these conditions "take away" the moving medium from the flat space-time.

The obtained metric of the Born rigid globally uniformly accelerated continuum is realized in the Riemannian space-time. This metric combines the Möller's metric properties (the Born rigidity) and the Logunov's metric properties (the global uniformly acceleration). It should be noted that the proper time obtained by Einstein [37], which was called the exact time, can be obtained from the metric (10)

$$\tau_s = \exp\left(\frac{a_0 y^1}{c^2}\right) \tau,$$

where τ_s is the proper time for the given space point, τ is the universal time for the fixed Lagrangian particle. But Einstein dismissed the exact expression for the approximate (Möller) one.

Derived structure equations impose constraints connected with integrability of motion equations in SRT and GRT.

The relativistic Born rigid uniformly revolving NRF without the restriction of the radius value and having at infinity the linear velocity, which is equal to the light velocity, and finite acceleration, and realized in the Riemannian space-time, is obtained. The problem concerning clock synchronization on a rotating disk was solved contrary to the statement [9] that "on a revolving body at all points the clocks can not be identically synchronized". From our viewpoint, the derivation [9] is erroneous. In formula (28), the contour in the "physical" space is unclosed. This is obvious in dividing the rotating thin disk into concentric thin hoops and considering particles located on one of them.

World lines of this hoop's particles in the Minkowski space form the congruence of the helical lines on the cylinder with radius r and axis ct , and the congruence of space-like helical lines orthogonal to the congruence of world lines of hoop's particles will be a "physical space".

This congruence is found from Pfaff's equation. Each spacelike line is unclosed and formula (28) is inapplicable.

Time interval $t(r,\varphi)$ from (27b) corresponds to the time distance along the element of cylinder from the plane $t = 0$ up to the "physical" spatially similar line $t(r,\varphi)$.

If one places identical clocks along the hoop and initially time at all clocks $t = t_0$, then on any hypersurface $t = const$ lengths of world lines of all clocks will be identical, that means all clocks on the hoop are synchronized. It must be from physical considerations as clocks placed at identical distances from the hoop center are in equal terms.

The solution of Bell inequality is proposed. In SRT, the Bell's paradox is not solved as according to the proved theorem [5, 31] in the Minkowski space conditions of relativistic rigidity and global relativistic uniform acceleration are not simultaneously satisfied.

To solve the paradox one must admit that it is impossible to realize the transition to NRF with the transformation of coordinates containing the time in non-linear form. Such transformations can not result in nonzero space-time curvature tensor.

The theory explaining the Mössbauer rotor experiment was developed.

REFERENCES

1. Podosenov SA. Geometric properties of noninertial bases in relativistic mechanics. In: *Debatable Problems of Theory of Relativity and Gravitation*. Ed. V. I Rodichev, N. V. Mitskevich. Moscow, Nauka Publ., 1982, 95-103.
2. Podosenov SA. *Space, time and classical fields of bound structures*. Moscow, Sputnik+ Publ., 2000, 445 p.
3. Podosenov SA, Potapov AA, Sokolov AA. *Pulse electrodynamics of wideband radio systems and fields of bound structures*. Moscow, Radiotekhnika Publ., 2003, 720 p.
4. Podosenov SA. *New method of field calculation in space-time of bound structures*. Saarbrücken: LAP LAMBERT Academic Publishing, 2011, 352 p.
5. Podosenov SA, Potapov AA, Foukzon J, Men'kova ER. Negolonomnye, fraktalnye i svyazannye struktury v ralyativistskilh sploshnykh sredakh, elektrodinamike, kvantovoy mekhanike i kosmologii. *V 3 tomalsh. Tom 2. Silovye polya v svyazannykh i negolonomnykh strukturakh [Nonholonomic, fractal and bound structures in relativistic continua, electrodynamics, quantum mechanics and cosmology. In three books. Book 2. Force Fields in Bound and Nonholonomic Structures]*. Moscow, LENAND Publ., 2016, 440 p.
6. Podosenov S, Foukzon J, Men'kova E. *Difficulties in the Interpretation of the Einstein's Relativity Theory. Basics, Concepts, Methods*. Saarbrücken, Germany: LAP LAMBERT Academic Publishing, 2017, 105 p. ISBN: 978-3-330-06799-8.
7. Bell JS. *Speakable and Unsayable in Quantum Mechanics*. Cambridge University Press, 1993, 67 p.
8. Gerstein SS, Logunov AA. Zadacha JS Bella [JS Bell's problem]. *Elementary Particle and Nuclear Theory Physics*, 1998, 29(5):1119-1132 (in Russ.).
9. Landau LD, Lifshits EM. *Teoriya polya [Field theory]*. Moscow, Nauka Publ., 1988, 512 p.
10. Podosenov SA, Foukzon J, Potapov AA. Zadacha Bella i issledovanie elektronnykh puchkov v lineynykh kollayderakh [Bell's problem and investigation of electron bunches

- in linear colliders]. *Nelineinyy Mir*, 2009, 7(8):612-622 (in Russ.).
11. Podosenov SA, Foukzon J, Potapov AA. A Study of the Motion of a Relativistic Continuous Medium. *Gravitation and Cosmology*, 2010, 16(4):307-312.
 12. Foukzon J, Podosenov SA, Potapov AA. Relativistic Length Expansion in General Accelerated System Revisited. URL: <http://arxiv.org/pdf/0910.2298v1>.
 13. Ginzburg VL, Eroshenko YuN. Eshche raz o printsipe ekvivalentnosti [Once more about the equivalence principle]. *UFN*, 1995, 165(2):205-211 (in Russ.).
 14. Redzic DV. Note on Devan-Beran-Bell's Spaceship Problem. *Eur. J. Phys.*, 2008, 29(11):11-19.
 15. Logunov AA. *Lectures on theory of relativity and gravitation. Modern Problem Analysis*. Moscow, Nauka Publ., 1987.
 16. Singe JL. *Relativity: the general theory*. Amsterdam, Nerth-Holland Publ., 1960, 417 p.
 17. Pauli W. *Theory of Relativity*. Pergamon Press, 1958, 320 p.
 18. Möller K. *The theory of relativity*. Clarendon Press Oxford, 1972, 390 p.
 19. Fok VA. *Teoriya prostranstva-vremeni i tyagoteniya* [Theory of space-time and gravitation]. Moscow, Fizmatgiz Publ., 1961, 564 p.
 20. Kramer D, Stephani H, Maccallum M, Herlt E. *Exact Solutions of the field equations*. Ed. E. Schmutzer. Berlin: Deutscher Verlag der Wissenschaften, 1980.
 21. Podosenov SA, Potapov AA, Foukzon J. Electrodynamics of a Continuous Medium in a System with Specified Structure. *Physics of Wave Phenomena*, 2012, 20(2):143-157.
 22. Desloge EA. Nonequivalence of a Uniformly Accelerating Reference Frame and a Frame at Rest in a Uniform Gravitational Field. *Am. J. Phys.*, 1989, 57(12):1121-1125.
 23. Desloge E. A. Relativistic Motion of Free Particles in a Uniform Gravitational Field. *Int. J. Theor. Phys.*, 1990, 29(2):193-208.
 24. Podosenov SA. Struktura prostranstva-vremeni i polya svyazannykh zaryadov [Space-time Structure and Fields of Bound Charges]. *Izvestia Vuzov, Ser. Phys.*, 1997, 40(10):63-74 (in Russ.).
 25. Podosenov SA. Space-time structure and bound-charge fields. *Russian Physics Journal*, 1997, 40(10):985-994. New York: Springer. ISSN 1064-8887 (Print), 1573-9228 (Online).
 26. Hill EL. A Note on the Relativistic Problem of Uniform Rotation. *Phys. Rev.*, 1946, 69(9):488-491.
 27. Rosen N. Notes on Rotation and Rigid Bodies in Relativity Theory. *Phys. Rev.*, 1947, 71(1):54-58.
 28. Podosenov SA. Tetradnoe rassmotrenie vrashchatelnogo i kolebatelnogo dvizheniya v spetsialnoy teorii otnositelnosti [Tetrad consideration of rotary and oscillatory motion in Special Relativity Theory]. *Izvestia Vuzov, Ser. Phys.*, 1970, 11:74-80 (in Russ.).
 29. Zel'manov L. K relyativistskoy teorii anizotropnoy neodnorodnoy vselennoy [To the relativistic theory of anisotropic nonhomogeneous universe]. Proc. VI Conf. on Cosmology Problems. Moscow, AN SSSR Publ., 1959, 144-174 (in Russ.).
 30. Podosenov SA, Foukzon J, Men'kova ER. Structure equations of continuum in the Newton's, Maxwell's and Einstein's theories. *Sciences of Europe*, 2017, 2(20 (20)):43-57.
 31. Podosenov SA, Foukzon J, Men'kova ER. Structure Equations, Permitted Movement of Relativistic Continuum and Sagnac's, Erenfest's and Bell's Paradoxes. *Physical Science International Journal (PSIJ)*, 2017, 13(2): 1-18. <http://www.sciencedomain.org/issue/2320>; DOI: 10.9734/PSIJ/2017/30616.
 32. Corda C. Interpretation of Mössbauer experiment in a rotating system: A new proof for general relativity. *Annals of Physics*, 2015, 355:360-366.
 33. Corda C. The Mossbauer rotor experiment and the general theory of relativity. *Annals of Physics*, 2016, 368:258-266.
 34. Kholmetskii A. L., Yarman T., Missevitch O. V., Rogozev B. I. A Mossbauer experiment in a rotating system on the second-order Doppler shift: confirmation of the corrected result by Kundig. *Physica Scripta*, 2009, 79(6): 065007.

35. Ashby N. Relativity in the Global Positioning System. *Living Reviews in Relativity*, 2003, 6(1). Published on 28 January 2003, by the Max Planck Institute for Gravitational Physics Albert Einstein Institute, Germany. <http://www.livingreviews.org/Articles/Volume6/2003-1ashby/>.
36. Rodichev VI. *Evolution of reference frame conception and Einstein's Programme. In book: Einstein's Collection.* Ed. V. L. Ginzburg and G. I. Naan. Moscow, Nauka Publ., 1974,286-334.
37. Einstein A. Über das Relativitätsprinzip und die aus demselben gezogenen Folgerungen. *Jahrb. d. Radioaktivität u. Elektronik*, 1907, 4:411-462.

*Dedicated to Scientists
involved in LENR research*

THEORY OF COLD FUSION REACTIONS

Gennady V. Mishinsky

International Intergovernmental Organization Joint Institute for Nuclear Research, <http://www.jinr.ru/>
6, Joliot-Curie St., Dubna 141980, Moscow Region, Russian Federation
mysh@jinr.ru

Abstract. The reaction of radiative capture of neutron by the nucleus and the nonradiative reaction of cold fusion are based on the same resonant interference exchange interaction. The exchange interaction is manifested not only between identical particles, but also between a particle and its image - an object that has a resonant state with that particle (R-state). The wave function of a particle excites the R-state along its length. The appeared wave function of R-state overlaps and interferes with wave functions of a particle. Thereby, an exchange interaction is generated, which attracts a particle and an object with an R-state to each other. The energy of exchange interaction is an additional contribution to the total energy of overall system simultaneously for all fundamental interactions, including the strong interaction. The exchange energy caused by strong interaction increases the radiative capture cross-section of the neutron by the nucleus, forming a potential pit for it far from the nucleus, and creates a potential well on the slope of the Coulomb repulsion potential for protons or deuterons in case of their resonant interaction with the nucleus. Two protons or two deuterons trapped in such a potential well trigger nonradiative cold fusion.

Keywords: quantum physics, atomic physics, nuclear physics, neutron physics, radiative neutron capture, solid state physics, exchange interaction, resonant interaction, cold nuclear fusion, low-energy nuclear reactions

PACS: 03.65.-w; 25.60.Pj; 25.40.Ny; 28.20.-v

Bibliography - 49 references

Received 15.05.2019, *accepted* 20.05.2019

RENSIT, 2019, 11(2):125-142

DOI: 10.17725/rensit.2019.11.125

CONTENTS

- 1. INTRODUCTION (125)**
- 2. FIRST CF EXPERIMENTS (126)**
- 3. PARTICIPANTS OF CF REACTIONS (127)**
- 4. ON POTENTIAL WELL AND COULOMB BARRIER (128)**
- 5. INTERACTION OF THERMAL NEUTRONS WITH NUCLEI (130)**
- 6. RESONANT INTERFERENCE EXCHANGE INTERACTION OF NEUTRONS WITH NUCLEI (131)**
- 7. RIEX-INTERACTION OF PROTONS AND DEUTERONS WITH NUCLEI (135)**
- 8. CONCLUSION (139)**
- REFERENCES (140)**

1. INTRODUCTION

Low-energy nuclear reactions [1-6] occurring in a weakly excited condensed matter are divided into two types: cold fusion (CF) reactions and

low-energy transmutation reactions of chemical elements (LET or transmutation).

The reactions of CF include reactions involving hydrogen or deuterium, namely: protons or deuterons, and the nuclei of the main element, for example: palladium, zirconium, nickel, titanium, boron, lithium... These reactions can proceed spontaneously, without external influence. In solids, they occur preferably in samples that have a size of an order of several nanometers. Such a size of samples allows to create a concentration of 2-3 atoms of hydrogen or deuterium per one atom of the main element. The CF reactions can also proceed in solutions and in melts.

Transmutation reactions are realized for all chemical elements, starting with hydrogen, and occur, as a rule, with the participation of a large number of atomic nuclei. The LET reactions include both multinuclear fusion and

multinuclear fission. They occur only as a result of external influence. Transmutation reactions predominantly occur in melts, in solutions and in dense gases, i.e. on free atoms.

Some experimental similarity in the results of these types of reactions, in the case of CF reactions, is explained by the initial excitation of the condensed matter due to cold fusion reactions with a subsequent triggering of low-energy transmutation reactions. The theory of low-energy transmutation reactions proposed by the author of this article is presented in [7–11].

Below we will discuss the mechanism of cold fusion reactions.

2. FIRST CF EXPERIMENTS

On March 23, 2019, it turned 30 years since Martin Fleischman and Stanley Pons announced at a press conference that they had executed nuclear fusion at room temperature. The nuclear fusion reaction was implemented by them during the electrolysis of a solution of deuterated lithium hydroxyl in heavy water with a palladium cathode (0.1M LiOD in a solution of 99.5% D₂O + 0.5% H₂O) [12]. They reported that a significant amount of excess heat is released during electrolysis, which cannot be explained by chemical reactions. In addition, a weak neutron flux and tritium generation was detected in those experiments. Those results allowed the authors to draw a conclusion about the nuclear origin of excess heat and to assume that the following nuclear reactions take place in palladium cathode:



These reactions are carried out at a low deuteron energy, therefore, thanks to journalists, this phenomenon is called Cold Fusion.

In Russia, the reaction of nuclear synthesis of helium from deuterium was carried out by Filimonenko I.S. [13] thirty years before the press conference of Fleischman M. and Pons S., as early as 1957. The synthesis took place by

the electrolysis of heavy water with a palladium cathode at a temperature of $\sim 1150^\circ\text{C}$. Unfortunately, for domestic political reasons, all research on this topic was stopped in 1968. Work was resumed in 1989-1990 after the press conference of Fleischman M. and Pons S. Three therm-emission devices with an electrical power of 12.5 kW each were recreated. However, the termination of funding for the project led to the loss of both devices and the technology itself. Filimonenko I.S. no longer returned to this work and did not share the technology on this topic.

It should be noted that, perhaps, thanks to the press conference, and not to the “boring” article, the message of Fleischman M. and Pons S. provoked a strong reaction from scientists who began to check their results all over the world. It is noteworthy that from the very beginning of their CF research, physicists and chemists did not limit themselves to electrolysis with a palladium-deuterium pair, and, due to their facilities and theoretical assumptions about the synthesis mechanism, developed new techniques.

Subsequent experiments on CF performed by other researchers showed that the ratio of the reaction leading to the production of tritium T (2) to the reaction leading to the production of helium ${}^3\text{He}$ (1) reaches values up to 10^9 [14]. At conventional thermonuclear fusion, both reactions proceed with almost the same probability. McKubre M. wrote: “The production of tritium was not only the first solid evidence for cold fusion – it was the first modern evidence of condensed matter nuclear” [15].

Soon, helium-4 was found in experiments on cold fusion involving deuterium and palladium or other metals, such as titanium, nickel and zirconium [16]. Further studies have shown that the reaction with the release of ${}^4\text{He}$ is the main channel in the process of CF, and the amount of ${}^4\text{He}$ strictly correlates with the amount of excess heat in the reaction:



“Mil’s results [16], reported at ICCF-2 in 1991 in Como, Italy, were stunning. When excess heat was present in the electrochemical experiment, helium-4 appeared approximately commensurately in the evolved electrolysis gas. When excess heat was not present, neither was helium-4. Finally, we had a product that made sense thermodynamically and explained the absence of radiation” – stated McKubre M. [15].

In thermonuclear fusion involving two deuterons, the reaction with the release of ⁴He is known, but a high-energy gamma quantum is always emitted:



The reaction (4) proceeds at a level of $\sim 10^{-7}$ from the main channels: (1) and (2). No high-energy gamma quanta were detected in the CF reaction (3).

Note that the replacement of deuterium with hydrogen did not lead, in many experiments, to the appearance of neither excess heat nor the appearance of synthesis products. I.e., no assumed reaction: $p + p \rightarrow d + e^+ + \nu_e + 0.42 \text{ MeV}$, other things being equal, was observed.

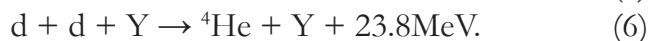
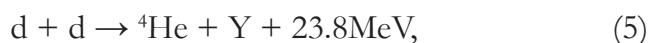
In [17], “extraneous” chemical elements were produced with a glow discharge in deuterium or hydrogen plasma with a palladium cathode, with predominant synthesis in the case with deuterium. The presence of “extraneous” elements can be explained, as mentioned above, by the initial activation of the cathode surface, due to the reactions of cold fusion followed by the launch of low-energy transmutation reactions.

It should also be recalled that in 1992 F. Piantelli discovered an anomalously high heat release when nickel Ni was saturated with hydrogen H₂ [18, 19]. Subsequently, those experiments formed the basis of technologies for the production of excess heat produced installations of A. Rossi [20].

3. PARTICIPANTS OF CF REACTIONS

Obviously, the reaction (3) cannot take place for kinematic reasons. For this reaction to become possible at least one more participant of reaction

“Y” must be available, with which ⁴He can share energy of 23.8 MeV. I.e., reactions (5) or (6) should occur:



Let us formulate the requirements for this “Y” participant. First, to get its share of energy, it must be “strongly” coupled to the ⁴He nucleus. The “Y” participant must create a potential well with a depth of several MeV for deuterons or with deuterons. Secondly, it must be a heavy, highly ionizing particle, so that when passing through a condensed medium at a short distance from the place where the reaction proceeds, it was able to lose all energy derived from the processes (5, 6). The “Y” participant should not fly out of reaction chamber; otherwise it would have been registered by external detectors.

Let us list all possible candidates for the role of “Y” participant: *a*) atomic electrons; *b*) crystal lattice – as a whole; *c*) an unknown particle born during the reaction; *d*) a neutral, heavy particle with a mass comparable to proton mass constantly present in a medium and which is manifested in CF reactions only; *e*) a nuclear molecule, which consists of several deuterons (≥ 3); *f*) atomic nucleus.

a) It was shown in [21] that in nuclear fusion reactions occurring in a crystalline solid, the solid-state processes of internal conversion involving both individual electrons and the entire crystal lattice should be taken into account. However, it is impossible to fully explain the course of reaction (3) by the processes of internal conversion due to the inhibition in the redistribution of the released energy due to electromagnetic interaction between ⁴He and electrons of the crystal lattice only.

b) The energy released as a result of CF reaction (3) is so great that the effect of receiving at least part of the energy by the entire crystal lattice, similar to the Mössbauer effect, is impossible.

c) The birth of an unknown, heavy, hadronic particle in a weakly excited condensed medium is not possible for energy reason.

d) The participation of hypothetical neutral or charged heavy hadrons, free or weakly bound to atomic nuclei, at low concentrations in the substance (10^{-14} per nucleon) as mediators in CF reactions [22] cannot explain the high intensity of CF reactions. In case of their high concentration in the substance, they would have been found long ago in conventional nuclear reactions.

e) To create a nuclear molecule, which consists of several deuterons, a potential well of several MeV in a solid should be formed. The deuterons themselves are unable to form such a potential well, despite the fact that deuterons are bosons.

Thus, the only candidate remaining from the list of possible CF reactions to the role of “Y” is the atomic nucleus.

It was noted that the intensity of CF reactions and, accordingly, the ^4He yield increases with increasing number of deuterium atoms per atom of the main element. This increase is achieved by using metal clusters of a size of several nanometers [23]. The nanoscale metallic cluster has additional electronic energy levels common to all atoms of the cluster. In a solid metal, this is an extended, linear conduction zone. In a cluster, these are separate electronic levels. At absorption of D_2 (deuterium)- or H_2 (hydrogen)-molecules by a cluster, the latter dissociate. And the formed D-, H-atoms lose their electrons, which fill the cluster electronic levels. Thus, in the cluster volume, d deuterons and p protons are present in the form of a “gas”. They “freely” move in the whole cluster space: they penetrate into the electron shell of main element atom, come close to its nucleus and interact with it and with similar deuterons or protons. The more electrons can be located at cluster levels, the higher is the concentration of protons or deuterons per one atom of main element in the cluster. The concentration of deuterons or protons can reach 300% (three d or p nuclei

per cluster atom) in a wide pressure range with cluster sizes of ~ 5 nm (50\AA) (**Fig. 1**) [24]. It is important to prevent clusters from sticking together, which leads to the elimination of additional electronic levels. This can be achieved by adding an insulating composite to the cluster powder of main element, for example, ZrO_2 cluster powder.

It is curious that nanoclusters of a 6-7 nm size are formed near metal surfaces, simply as a result of heating the sample to a temperature of 300-400°C [25]! Such nanoclusters levitate over a metal surface! If CF reactions occur in the volume of nanoclusters formed by any method, then as a result of the bombardment of metal surface by reaction products, it is locally heated, and both additional local defects and new nanoclusters are produced on it. Emerged “hot” defects and nanoclusters can become centers for the formation of solid structures and the synthesis of “extraneous” chemical elements in low-energy nuclear transmutation reactions [17, 20, 26].

4. ON POTENTIAL WELL AND COULOMB BARRIER

Since all the above d + d reactions proceed at low energy of deuterons, one of the main problems

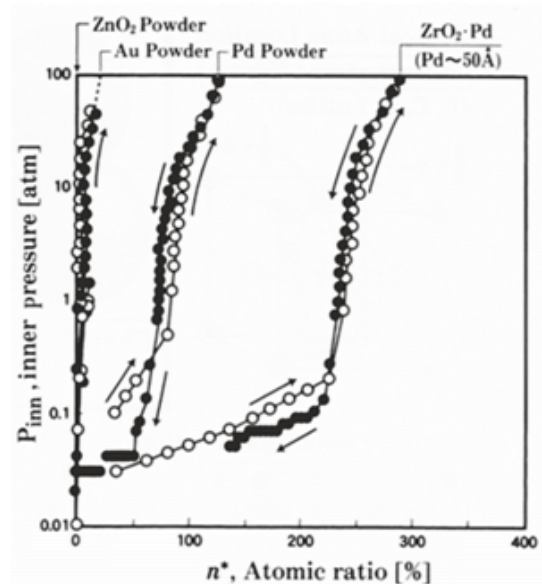


Fig. 1. The concentration of deuterons/protons per atom of the main element (n^*) in a wide range of their pressure for different materials with different grain sizes [24].

of cold fusion is the problem of overcoming the Coulomb barrier by deuterons during their fusion.

The reaction (3) is more probable than reaction (2), and reaction (2) is more probable than reaction (1): $W(3) > W(2) > W(1)$. The energies released as a result of these reactions are in the same relation: $23.8\text{MeV} > 4.03\text{MeV} > 3.26\text{MeV}$. A natural solution to the problem of overcoming the Coulomb barrier and the ratio observed in reaction probabilities would be the fact that a potential well of sufficient depth exists in a condensed matter so that two deuterons or two protons can get into it and stay in it before fusion. Inside such a potential well, protons or deuterons will occupy the same energy state, with minimal potential energy.

Since reactions (1) and (2) proceed through the compound nucleus ${}^4\text{He}$, ($d + d \rightarrow {}^4\text{He} \rightarrow {}^3\text{He} + n + 3.26\text{MeV}$ and $d + d \rightarrow {}^4\text{He} \rightarrow t + p + 4.03\text{MeV}$), the CF process can be considered, in the first approximation, as the process of a certain alpha decay. First of all, deuterons must get into a potential well. The probability of this process is proportional to the probability of one deuteron to get in a potential well and is proportional to the number of deuterons per one atom of main element. Inside the potential well, two deuterons merge to create an α -particle (${}^4\text{He}$). Further, the formed ${}^4\text{He}$ nucleus tunnels through the potential barrier with decay over channels: (1) $\rightarrow {}^3\text{He} + n$, (2) $\rightarrow t + p$ or (6) $\rightarrow {}^4\text{He}$ (Fig. 2). The probability

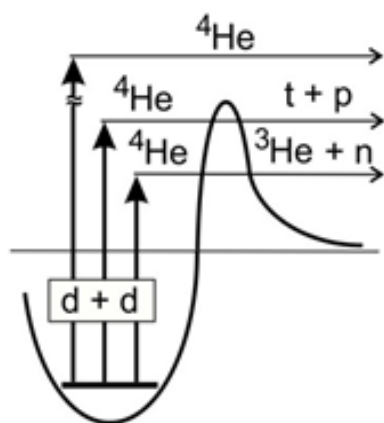


Fig. 2. ${}^4\text{He}$ tunneling through a potential barrier with subsequent decay through channels: ${}^4\text{He} \rightarrow {}^3\text{He} + n$, ${}^4\text{He} \rightarrow t + p$.

of α -particle tunneling through the barrier is known to be proportional to the transparency coefficient D :

$$D = \exp\left[-(2/\hbar)\int_{r_1}^{r_2}\sqrt{2m(U_b - E)}\right], \tag{7}$$

where m is the mass of α -particle, U_b is barrier height, E is the kinetic energy of α -particle, which approximately can be considered equal to the decay energy of ${}^4\text{He}$. Since the reaction energy $d + d \rightarrow t + p + 4.03\text{ MeV}$ is greater by 0.77 MeV than reaction energy $d + d \rightarrow {}^3\text{He} + n + 3.26\text{ MeV}$, the probability of its realization is also greater. The probabilities ratio of these reactions may be several orders of magnitude. For example, the tellurium isotope Te-106 decays by emitting an α -particle with an energy of $E_\alpha = 4.16\text{ MeV}$ and a half life of $T_{1/2} = 0.07\text{ms}$, and the isotope Te-108 emits an α -particle with $E_\alpha = 3.32\text{ MeV}$ and with $T_{1/2} = 3.15\text{s}$ (decay time over α -channel). Thus, the probability ratio of α -decays for two tellurium isotopes with energy difference $\Delta E = 0.84\text{ MeV}$ is four and a half orders of $3.15\text{s}/0.07\text{ms} = 4.5 \cdot 10^4$.

Therefore, if the barrier height U_b is greater than 3.26 MeV , then the reaction $d + d \rightarrow t + p + 4.03\text{ MeV}$ prevails over the reaction $d + d \rightarrow {}^3\text{He} + n + 3.26$. And the reaction $d + d \rightarrow {}^4\text{He} + \text{“Y”} + 23.8\text{ MeV}$ becomes dominant, firstly, due to the huge energy release and, secondly, due to the absence of further decay of ${}^4\text{He}$ compound nucleus (Fig. 2).

However, the crystalline lattice of a solid does not create potential well of such depth. Such a well is formed as a result of resonant interference exchange interaction of the atomic nucleus with deuteron or proton.

5. INTERACTION OF THERMAL NEUTRONS WITH NUCLEI

Rukhadze A.A. and Grachev V.I. wrote in the article: “LENR in Russia” [27]: “From the first steps of nuclear physics, its development has been largely, in General, in two directions – of high- and low-energetic. E. Rutherford (1871-1937), the

“father” of nuclear physics who discovered (1919) artificial “transmutation of elements” – nuclei (${}^4_2\text{He} + {}^{14}_7\text{N} \rightarrow {}^{17}_8\text{O} + {}^1_1\text{H}$), by fast alpha particles, have interpreted this “modern alchemy” as the area of high-energy processes, which opening the era of nuclear power. Available by the time the works on nuclear transmutations of stable isotopes in natural conditions, and primarily the receipt by the American chemists K. Irion and J. Wendt (1922) [28, 29], of helium in alpha-decay of tungsten, induced of electric explosion, Rutherford declared as error. After such a statement by E. Rutherford, the low-energy trend faded away and “cold” nuclear transmutation became “pseudoscience” for many years.”

However, the low-energy processes, of course, could not disappear nowhere, they simply “disguised” themselves as high-energy processes. One such world-famous process that laid the foundation for creating an entire industry is the process of resonant absorption of a thermal neutron by atomic nucleus.

Such phenomena as resonant radiation capture of neutron by nucleus and nuclear fission by a thermal neutron are widely known. As a result of the radiation neutron capture, an energy of ~ 8 MeV is released in the reaction. In this case, several gamma quanta are emitted with an average energy of ~ 2 MeV. In these reactions, radioactive isotopes are often formed, experiencing β^- – или β^+ –decay. In the process of fission of heavy nuclei by thermal neutrons, prompt gamma quanta, neutrons are emitted, and two radioactive fragments are formed. The energy released in the process of nuclear fission, for example: ${}^{235}\text{U} + n$, is ~ 200 MeV, and its fission cross-section by a thermal neutron is 586 barn.

Both of these processes with thermal neutrons are high-energy processes on the output channel. Perhaps that is why there is no comparison of reactions of cold nuclear fusion with reactions of radiative capture of a thermal neutron and, especially, with nuclear fission in the scientific LENR-literature. However, the ideology associated with the screening of a

proton by an electron: the “transformation” of a proton into a neutron is present in theoretical models of the CF [30, 31].

In the input channel, both reactions with thermal neutrons are low-energy reactions. And the fission of a nucleus by a thermal neutron can be called, just right, a “cold” nuclear fission. Indeed, all three processes: radiation neutron capture, and “cold” nuclear fission, and cold fusion are low-energy processes in the input channel, but high-energy processes in the output channel. The only difference is that in the first two cases a thermal neutron participates in the input channel, and either a thermal proton or thermal deuteron participates in the third case.

The process of radiative capture of a slow neutron with the formation of a compound nucleus has a pronounced resonant character when the neutron energy is close to one of the values, corresponding to quasistationary state of the compound system: the neutron plus the target nucleus [32]. The energy level of neutron resonance R-state is characterized by the energy width Γ , which is inversely proportional to its lifetime $\tau = \hbar/\Gamma$. The level widths of compound nuclei at excitation energies close to the neutron binding energy are usually small compared with the distances between them. The full width of the level Γ consists of two parts: the radiation width Γ_γ and the neutron width Γ_n . The radiation width corresponding to slow neutron capture is $\Gamma_\gamma \sim 0.1$ eV. The neutron width Γ_n at low neutron energies is proportional to its speed and can be much smaller than the radiation width. Thus, the full width of nuclear levels $\Gamma = \Gamma_\gamma + \Gamma_n$ at excitation energies close to neutron binding energy has the order $\Gamma \sim 0.1$ eV. The distances between levels, as shown by numerous experimental data, have values of ~ 10 eV.

To characterize radiation capture, the dependence of neutron absorption cross-section on its energy $\sigma(E)$ is usually used. The effective capture cross-section of a slow neutron in the presence of a single resonance level, which corresponds to the resonant energy value E_0 and of the width Γ_γ, Γ_n , is described by the Breit-Wigner formula:

$$\sigma = g\pi\lambda_0\lambda \frac{\Gamma_n\Gamma_\gamma}{(E - E_0)^2 + \Gamma^2},$$

where $g = \frac{2j+1}{2(2i+1)}$, i – nuclear spin, $j = i \pm 1/2$ – compound nuclear moment, λ_0 – neutron wavelength in accordance with energy E_0 , λ – neutron wavelength $\lambda = h/m_n v$, m_n, v – neutron mass and speed. The peak value of capture cross-section at neutron energy $E = E_0$ is equal to

$$\sigma_0(E_0) = \lambda_0^2 \left[g\pi \frac{\Gamma_n\Gamma_\gamma}{\Gamma^2} \right].$$

Experiments on resonant capture of thermal neutrons show that at energies slightly higher than the neutron binding energy, the number of R-levels is significant, and the distances between them become much less than 1 eV. As is known, the majority of isotopes in the region of thermal energy of neutrons show noticeable cross-sections of their capture. There are isotopes, which cross-sections are equal to tens to hundreds of thousands of barn. If these cross-sections σ_τ are reduced to potential interaction radii R_τ ($\sigma_\tau = 4\pi R_\tau^2$), then it turns out that the radii R_τ are also thousands or hundreds of thousands times greater than the isotope nuclei radii R_{nucl} (see **Table**). Such increased values of cross-sections are connected with a large number of closely spaced, resonant R-levels and are explained by resonant interference exchange interaction (RIEX-interaction).

6. RIEX-INTERACTION OF NEUTRONS WITH NUCLEI

This article argues that exchange interaction takes place both between identical particles and between a particle and a resonant R-state.

Table

Thermal neutron capture parameters, $\lambda \approx 2 \cdot 10^5$ fm.

Isotope	σ_τ , barn	R_{nucl} , fm	R_τ , fm
⁶ Li	940	2.4	$1.2 \cdot 10^4$
¹⁰ B	3840	2.8	$2.5 \cdot 10^4$
⁶⁴ Ni	1.49	5.2	340
¹¹³ Cd	$2.06 \cdot 10^4$	6.3	$4.1 \cdot 10^4$
¹³⁵ Xe	$2.65 \cdot 10^6$	6.7	$4.6 \cdot 10^5$
¹⁵⁷ Gd	$2.54 \cdot 10^5$	7.0	$1.4 \cdot 10^5$
²³⁵ U	586	9.3	$6.8 \cdot 10^3$

Neutrons trapped in any medium and interacting with its nuclei are finally thermalized, acquire the temperature of that medium. At room temperature $T = 300K$, the average neutron energy is $E = 0.025$ eV, and the neutron de Broglie wavelength is $\lambda_n = h/mv \approx 2 \cdot 10^5$ fm. Since neutrons have no charge, they move freely in the medium, representing a neutron “gas”. If a compound nucleus has a resonance state with a neutron, then it begins to interact resonantly with that R-state.

The resonant R-state present in the nucleus is a certain analog of the neutron, its “image”. This “image” is “identical” to neutron. The “image” becomes real when the neutron excites the R-state at its wavelength (**Fig. 3**). Thus, the neutron is simultaneously in two states: in its own state $\psi_n(n)$ and partially in the R-state $\psi_R(n)$. Accordingly, the R-state is also in two states: in its own state $\psi_R(R)$ and partially in the neutron state $\psi_n(R)$. The appeared R-state wave function overlaps and interferes with the neutron wave function. Thus, a resonant interference exchange interaction is generated.

As is well known, there is an exchange interaction in quantum physics between identical particles, which is characterized by exchange energy [33]. The more wave functions of identical particles overlap, the greater is the exchange energy value. The exchange interaction between

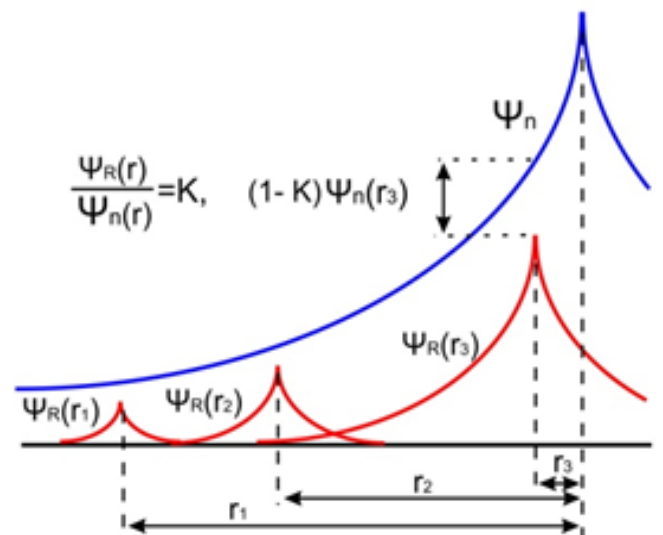


Fig. 3. The wave function of the R-state depending on the distance to the neutron.

identical particles can have a different character: to have either attraction potential or repulsion potential. Since the exchange interaction energy is an additional contribution to the total energy of overall system, this contribution can be both negative and positive. So, this contribution is positive in a parahelium atom, in which electron spins are antiparallel, - electrons repel each other, and this contribution is negative in an orthohelium atom with parallel spins of electrons - electrons attract each other. When two hydrogen atoms interact, on the contrary, hydrogen atoms with parallel electron spins repel each other, and they attract each other with antiparallel electron spins. Such a difference is explained by the fact that, in the helium atom, the exchange integral of two electrons has a positive value, and for two hydrogen atoms the exchange integral of their electrons has a negative value. The latter is associated with the Coulomb interaction of electrons not only among themselves, but also with the protons of neighboring hydrogen atoms [34].

The exchange energy of electrons is caused by their electromagnetic interaction. But the neutron is a neutral particle. However, the exchange energy is an additional contribution to the total energy of the system at the same time for all fundamental interactions, and not only for the electromagnetic interaction. The first correction to the system energy $\Delta E^{(1)}$ is calculated in the perturbation theory by means of equation (8). All fundamental interactions always and simultaneously stand in the perturbing potential of interacting particles, including identical particles or other “identical objects”: strong interaction F , electromagnetic interaction EM, weak interaction W and gravitational interaction G .

$$\Delta E^{(1)} = \frac{\int \psi^*(A, B)[F, EM, W, G]\psi(A, B)dV_A dV_B}{\int \psi^*(A, B)\psi(A, B)dV_A dV_B} \quad (8)$$

where $\psi(A, B) = [\psi_A^V \psi_B^V] \{S_A S_B\}$ is full wave function of two resonant interacting, “identical objects” A and B , which consists of spacial $[\psi_A^V \psi_B^V]$ and

spin $\{S_A S_B\}$ parts. $dV_A = dx_A dy_A dz_A$, $dV_B = dx_B dy_B dz_B$ is elementary spatial volume for objects A and B . The denominator has normalizing integral.

The spatial region of exchange interaction for all fundamental potentials is determined by the lengths of wave functions of any resonantly interacting “identical objects” A and B , since then they are simultaneously in two states: proper state $\psi_a(A)$, $\psi_b(B)$ and identical state $\psi_b(A)$, $\psi_a(B)$. The proper part $\psi_a(A)$ interacts in its place a with the identical part $\psi_a(B)$, and the proper part $\psi_b(B)$ interacts in its place b with $\psi_b(A)$. Thus, due to the resonant interference exchange interaction, the short-range strong and local weak interactions become “long-range” interactions.

For interacting neutron and R-state, their full wave function $\psi(n, R) = [\psi_n^V \psi_R^V] \{S_n S_R\}$ and the potential making the main contribution to the exchange energy is the strong interaction F :

$$\Delta E_{nR}^{(1)} = \frac{\int \psi^*(n, R)[F]\psi(n, R)dV_n dV_R}{\int \psi^*(n, R)\psi(n, R)dV_n dV_R}. \quad (9)$$

Since the total wave function of two fermions should be an antisymmetric function, either the spatial wave function $[\psi_n^V \psi_R^V]$ should be antisymmetric and the spin wave function $\{S_n S_R\}$ symmetric (10a, b, c), or vice versa (10d). Thus, for neutron and R-state, the following combinations are acceptable:

$$[\psi_n(n)\psi_R(R) - \psi_n(R)\psi_R(n)][\{S^+(n)S^+(R)\}], \quad (10a)$$

$$[\psi_n(n)\psi_R(R) - \psi_n(R)\psi_R(n)][\{S^-(n)S^-(R)\}], \quad (10b)$$

$$[\psi_n(n)\psi_R(R) - \psi_n(R)\psi_R(n)] \times \{S^+(n)S^-(R) + S^-(n)S^+(R)\}, \quad (10c)$$

$$[\psi_n(n)\psi_R(R) + \psi_n(R)\psi_R(n)] \times \{S^+(n)S^-(R) - S^-(n)S^+(R)\}. \quad (10d)$$

The energy of a strong perturbation F depends on spin variables. However, suppose that the perturbation F does not change the orientation of neutron spin and R-state. Therefore, when averaging the spin wave functions in the numerator and the denominator (9), the same factors appear, which are reduced.

As a result, $\psi(n, R)$ corresponds to the parts of wave functions (10), depending on coordinates $\psi(n, R) = [\psi_n^V \psi_R^V]$ only. Then:

$$\begin{aligned} & [\psi_n^V \psi_R^V]^* [\psi_n^V \psi_R^V] = \psi_n^*(n) \psi_R^*(R) \psi_n(n) \psi_R(R) + \\ & + \psi_n^*(R) \psi_R^*(n) \psi_n(R) \psi_R(n) \pm \\ & \pm [\psi_n^*(n) \psi_R^*(R) \psi_n(R) \psi_R(n) + \\ & + \psi_n^*(R) \psi_R^*(n) \psi_n(n) \psi_R(R)]. \end{aligned} \quad (11)$$

The function integral in square brackets is the exchange integral. The plus sign in front of the square bracket in equation (11) corresponds to the symmetric coordinate wave function (10d), the minus sign corresponds to antisymmetric wave function in (10a,b,c).

The integrals of the first two terms (11) characterize the strong interaction F at a distance exceeding its action between neutron and R-state, as well as between the part of neutron in R-state and part of R-state in the neutron. Therefore, these integrals are equal to zero.

$$\begin{aligned} & \int |\psi_n(n)|^2 F |\psi_R(R)|^2 dV_n dV_R = 0, \\ & \int |\psi_n(R)|^2 F |\psi_R(n)|^2 dV_n dV_R = 0. \end{aligned}$$

Thus, we can consider that in the numerator (9) for strong interaction:

$$\begin{aligned} & [\psi_n^V \psi_R^V]^* [\psi_n^V \psi_R^V] = \\ & = \pm [\psi_n^*(n) \psi_R^*(R) \psi_n(R) \psi_R(n) + \\ & + \psi_n^*(R) \psi_R^*(n) \psi_n(n) \psi_R(R)]. \end{aligned} \quad (12)$$

Potential F is negative. The exchange integral in this case also has a negative value. Therefore, a neutron (spin $s = 1/2$) and a nucleus with R-state are attracted to each other when their spatial wave function is symmetric (plus in front of square bracket in (12)) and their spins are antiparallel.

The intensity of neutron excited R-state, and, consequently, the amplitude of its wave function $\psi_R(r)$ is determined by the amplitude of the neutron wave function $\psi_n(r)$ in the region of nucleus at a distance r from it (Fig. 3) and is proportional to some coefficient K : $\psi_R(r) = K \psi_n(r)$ or $\psi_R(R) = K \psi_n(n)$. As the neutron approaches the nucleus, the intensity

of the R-state will increase. The overlap of the neutron wave functions and the R-state $\psi_n(r) \psi_R(r) = K |\psi_n(r)|^2$ will increase. It can be seen that the overlap increases in proportion to the neutron density $|\psi_n(r)|^2$ at a distance r from nucleus.

The value of coefficient K depends on the affinity of R-state with neutron. This affinity is determined, in addition to the coincidence of their energy, by coincidence of their spins, parities. The value of coefficient K also depends on the oscillator strength of R-state. Thus, the coefficient K depends on the properties of a particular isotope with which the neutron interacts. For two neutrons and two protons in identical states, the coefficient K equals to one $K = 1$. Due to the charge independence of the strong interaction, $K = 1$ for neutron-proton pair and for deuteron. For interacting neutron and R-state, the coefficient K for most isotopes will generally be less than one $K < 1$. It can be greater than one $K > 1$, in case when the R-state has a collective nature.

The wave function of R-state $\psi_R(r) \equiv \psi_R(R)$ will be present in the neutron state $\psi_n(R)$ with the same coefficient K : $\psi_n(R) = K \psi_R(R) = K^2 \psi_n(n)$, $\psi_R(R) \equiv \psi_R(n)$. The overlap of their wave functions, $\psi_n(R) \psi_R(R) \equiv \psi_n(R) \psi_R(n) = K^3 |\psi_n(n)|^2 \equiv K^3 |\psi_n(r)|^2$, and it also increases in proportion to the neutron density $|\psi_n(r)|^2$ at a distance r from the nucleus. Consequently, the integral of (12) and the energy of the exchange interaction $\Delta E^{(1)}(r)$ (9) are written:

$$\Delta E_{nR}^{(1)} \sim 2 \int K |\psi_n(r)|^2 F |\psi_n(r)|^2 K^3 d^2V_n \quad (13)$$

As strong interaction is a short-range interaction, the integral (13) is important only in a volume of nucleus V_A , whose diameter is equal to $\varnothing A$. Therefore, the action magnitude of F in the exchange interaction of neutron with R-state on the entire interval L - from the start of this interaction to the nucleus, will be considered constant: $F_R = \text{const}$. I.e., F_R does not depend on the distance r between the neutron and the nucleus. The gap L is related to neutron wavelength as $L \sim K^4 \cdot \lambda_n$.

Since $\psi_n(r) \gg \emptyset A$, than $\psi_n(r) = \text{const}$ in a volume equal V_A . It follows from (13) that exchange interaction energy $\Delta E^{(1)}(r)$ is proportional to squared neutron density in the region of nucleus $|\psi_n(r)|^2_{V_A}$ when the neutron is located at a distance r to it.

$$\Delta E_{nR}^{(A)}(r) \sim 2K^4 \int_{V_A} |\psi_n(r)|^2 F_R |\psi_n(r)|^2 d^2V_n,$$

$$\Delta E_{nR}^{(A)}(r) \sim 2F_R K^4 |\psi_n(r)|^4 \int d^2V_n. \quad (14)$$

The integral in (14) is squared nuclear volume. It is proportional to squared mass number of the nucleus $\sim \rho M^2$. Let's introduce the notation U , which includes $2F_R$, ρ and the normalization integral (9).

$$\Delta E_{nR}^{(A)}(r) = UK^4 M^2 |\psi_n(r)|^4.$$

Let's estimate the value of U , which characterizes the potential of strong interaction. In the theory of a deuteron, at nuclear potential well radius of 1.45-1.7 fm, the well depth is 50-35 MeV. This value characterizes the potential of a neutron-proton strong interaction. In the deuteron, the neutron density is $|\psi_n(r)|^2 = 1$, the coefficient $K = 1$, and $M^2 = 4$. Then $U = 9-12$ MeV.

When a neutron interacts with R-state, its wave function is transformed from a plane wave into a bound state wave function. The orbital moment of a thermal neutron interacting with nucleus is $\ell = 0$. Therefore, we represent the neutron wave function $\psi_n(r)$ in the form of radial part of the S-wave function of electron located on orbital with radius a_ρ which rotates around a nucleus with quantum numbers $n = 1$ and $\ell = 0$. The density distribution of such an electron in the radial direction is characterized by function $P(r) = C[r^2 \exp(-2r/a_0)]$, where C is normalization constant, a_0 is electron orbital radius [34]. The red line in Fig. 4 represents, in relative units, the values of the function from nucleus to a_0 (500 fm); the green line gives the neutron density in the region of nucleus when neutron is at a distance r from nucleus: $|\psi_n(r)|^2 = P(a_0 - r)$ and the blue line gives the exchange interaction potential

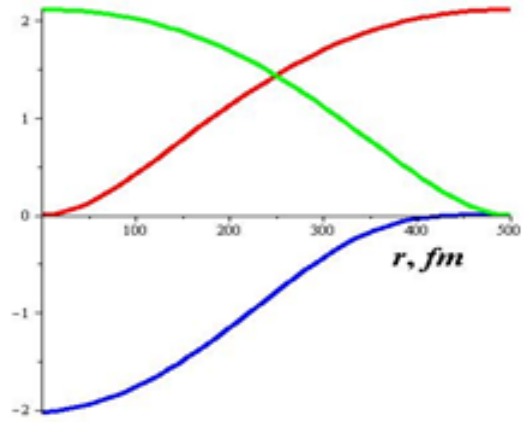


Fig. 4. The red line is the radial density of the orbital electron; green – the density of a neutron located at a distance r from the nucleus; blue – RIEKX potential.

$\Delta E_{nR}^{(1)}(r) = -[P(a_0 - r)]^2$ (the values $a_0 = 500$ fm and $UK^4 M^2 = -2$ MeV are chosen arbitrarily).

Thus, when a neutron interacts with R-state at a distance of $L \sim K^4 \cdot \lambda_n$ to the nucleus, a potential pit is formed, which depth is equal to $UK^4 M^2$ (Fig. 5). Distance L can also be correlated with potential interaction radius R_T (see Table). The red line in Fig. 5 represents the nuclear potential of nickel, for example, ^{64}Ni c $R_T = 340$ fm (see Table), the blue line represents the potential of RIEKX interaction, and the green line represents the summarized potential (the value $UK^4 M^2 = -2$ MeV is chosen arbitrarily).

Once in the potential pit, the neutron is in a region below neutron binding energy, where the density of neutron energy levels is significant, and, therefore, the resonant interaction of neutron with them is also large. Thus, the neutron “rolls”, like downhill, along a potential pit into a potential well of the nucleus. Consequently,

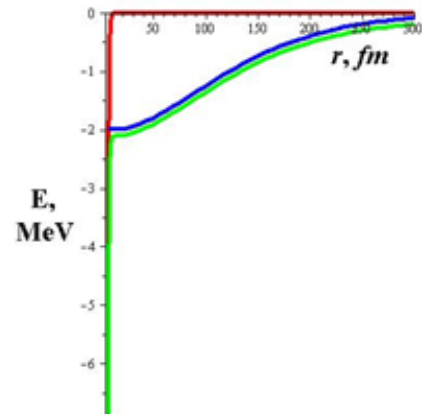


Fig. 5. Red line - nuclear potential Ni; blue – RIEKX potential Ni-n; green - total potential Ni+n.

the neutron is captured by nucleus, due to the resonant interference exchange interaction, at a distance $L \approx R_T$.

7. RIEX INTERACTION OF PROTONS AND DEUTERONS WITH NUCLEI

Unlike neutron, proton and deuteron have electric charge that prevents them from approaching the nucleus. On the way to the nucleus, proton and deuteron meet a Coulomb barrier. If for resonant neutron capture it is necessary for the corresponding compound nucleus to have resonant R-states, then for the proton and, apparently, for the deuteron behind the Coulomb barrier of the compound nucleus there is a large number of resonance levels, up to the height of Coulomb barrier (Fig. 6). A proton, once in resonance with one of these R-levels, begins to RIEX-interact with it. It is noteworthy that the proton energy can be from thermal energy to energy equal to the height of Coulomb barrier. Therefore, losing energy when approaching the nucleus, the proton, thereby, scans the energy levels of nucleus beyond the Coulomb barrier, until it gets into resonance with a suitable R-level (Fig. 6). The resultant, due to the exchange interaction, attraction force of the proton to the nucleus, increases the proton energy, bringing it out of resonance. The appeared Coulomb braking returns the proton back into resonance with R-level. Thus, the

energy of a proton that got into resonance with a suitable R-level remains constant.

For interacting proton and R-state, their total wave function is $\psi(p, R) = [\psi_p^V \psi_R^V] \{ \psi_p^S \psi_R^S \}$. Just like a neutron, a proton (spin $s = 1/2$) and a nucleus with R-state are attracted to each other when their spins are antiparallel and their spatial wave function is symmetric

And since proton and deuteron have an electric charge equal to one +1, then both strong F and electromagnetic, namely Coulomb $EM = k \cdot q^2 / r_{pN}$, interactions will make up the disturbing potential:

$$\Delta E_{pR}^{(1)} = \frac{\int \psi^*(p, R) [F, EM] \psi(p, R) dV_p dV_R}{\int \psi^*(p, R) \psi(p, R) dV_p dV_R}$$

Since strong interaction does not depend on the charge, than

$$\Delta E_{pR}^{(1)} = \Delta E_F^{(1)} + \Delta E_{EM}^{(1)} = \frac{\int \psi^*(p, R) [F] \psi(p, R) dV_p dV_R}{\int \psi^*(p, R) \psi(p, R) dV_p dV_R} + \frac{\int \psi^*(p, R) [kq^2 / r_{pN}] \psi(p, R) dV_p dV_R}{\int \psi^*(p, R) \psi(p, R) dV_p dV_R} \approx \Delta E_F^{(1)}$$

where $k = 1/4\pi\epsilon_0 = 8.99 \cdot 10^9 \text{ N} \cdot \text{m}^2 / \text{C}^2$ ($\epsilon_0 = 8.85 \cdot 10^{-12} \text{ F/m}$ – electric constant), r_{pN} is a distance between proton and nucleus, $q = 1.6022 \cdot 10^{-19} \text{ C}$ is proton charge. Note that the potentials of strong and electromagnetic interaction have opposite signs.

Let us estimate the energy contribution of Coulomb interaction to the exchange energy. The ground state of parahelium atom $2E_a + C + A$, 1^1S_0 has energy of 79.0 eV. “A” is exchange energy. “C” is the energy of usual Coulomb repulsion of electrons. $2E_a$ is the electron energy without taking into account their interaction, $2E_a = 2 \cdot 54.4 = 108.8 \text{ eV}$ is the doubled ionization energy of helium ion He^+ . Electrons in 1^1S_0 are in the same state and for them “A” = “C” = 15 eV [34]. The parahelium diameter is $D_{\text{He}} = 62000 \text{ fm}$. As will be seen below, thanks to the RIEX interaction, a proton (deuteron) creates a bound, nuclear molecule with the target nucleus (Fig. 6). Estimates showed that the radius of the

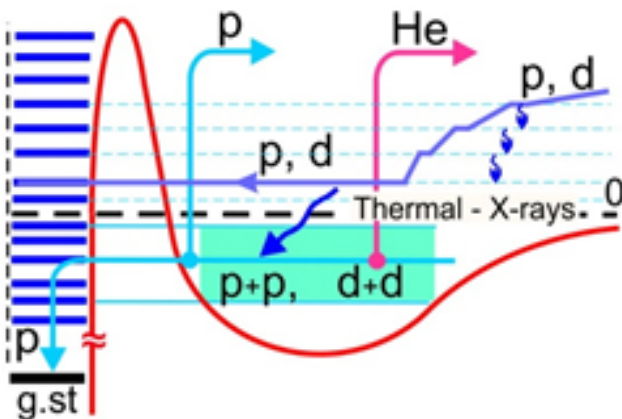


Fig. 6. The levels of the compound nucleus $N + p$ (d) beyond the Coulomb barrier and the interaction with them of a proton or deuteron.

proton orbitals in a nuclear molecule (**Fig. 7**) is, for different nuclear charges, in the range $R_p = 50\text{-}150$ fm for $UK^4M^2 \sim -2$ MeV. It is clear that bottom position and potential well depth depend on the value UK^4M^2 . The ratio D_{He}/R_p is three orders of magnitude; accordingly, the ratio in energies will have the same value. Thus, the energy contribution of the exchange Coulomb interaction $\Delta E_{EM}^{(1)} \sim 15$ keV to the total exchange energy, as compared with the strong interaction $UK^4M^2 \sim -2$ MeV, can be neglected. Energy contributions from weak W and gravitational G interactions can also be neglected. But it should be remembered that they are always present in the perturbing potential of exchange interaction.

Let us produce for the proton or deuteron with wave function $\psi_p(r)$ the same procedures as for the neutron, relative to the energy of its exchange interaction with the R -state. Then $\Delta E_{PR}^{(A)} = UK^4M^2 |\psi_p(r)|^4$. As a result, a “exchange” potential well forms at the Coulomb barrier (**Fig. 7**). It should be emphasized that the emerging nuclear molecule is formed as a result of a strong interaction between proton and nucleus, and not due to the electromagnetic, collective response of internal atomic electrons, which shield the slow proton charge [35]. The red line in **Fig. 7** represents the nuclear plus Coulomb potential of nickel Ni plus Coulomb potential Ni + p, the blue line represents the RIEEX potential (values

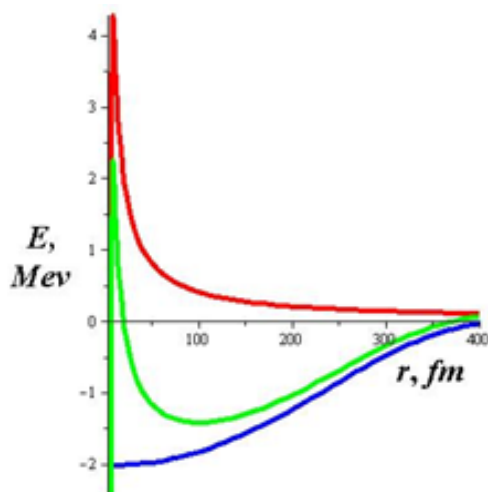


Fig. 7. Red line - nuclear plus Coulomb potentials Ni+p; blue - RIEEX potential Ni-p; green - total potential Ni+p.

400 fm and $UK^4M^2 = -2$ MeV are chosen arbitrarily) and the green line shows summarized potential.

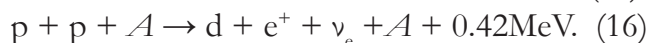
Such a picture resembles the double-humped barrier present in spontaneous fission isomers (SFI) in the region of nuclei of transuranium chemical elements with a nuclear charge of 92 to 97 [36]. The states of spontaneous fission isomers are characterized by a high degree of deformation. Therefore, sometimes SFI are called shape isomers. The nature of SFI is associated with nuclear shell corrections, which give their energy contribution, in calculating the potential fission barrier for heavy nuclei, which are performed in the framework of the droplet model. The excitation energy of shape isomers is from 2 to 4 MeV, and the half-lives vary from nanoseconds to milliseconds.

Unlike SFI, which potential well is above the potential energy zero line, the exchange potential well is located below the zero line. Therefore, a proton or deuteron that hits it, remains in it and creates a nuclear molecule with a target nucleus. Another important condition is needed for the formation of nuclear molecule: it is necessary that the nucleus on the inside of its Coulomb barrier has resonant R -states with a proton (deuteron) located in the well on barrier outside (**Fig. 6**). This condition is satisfied when the width of the proton or deuteron level in the exchange potential well is greater than the distance between the resonant R -levels on the inner side of the barrier. This is realized when the exchange potential well is wide and not deep. A thermal proton or deuteron, as well as a thermal neutron, is captured by the nucleus into this potential well at a distance L . When a neutron or proton, deuteron is captured, they transfer between levels in a potential pit or in a potential well of a nuclear molecule with electromagnetic radiation in the range from thermal waves to X-ray quanta. Protons, deuterons will radiate in the same range when braking in the Coulomb field of the nucleus (**Fig. 6**) [37-40, 43].

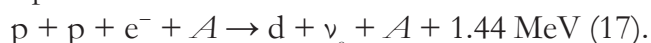
Thus, the resonant interference exchange interaction between a proton or deuteron and the R-state creates an exchange potential well on the Coulomb barrier of nucleus A . As a result, a nuclear molecule is formed: $A + p$ or $A + d$. The lifetime of such a molecule is determined by the transparency of Coulomb barrier (7). It is obvious that electronic levels in the nuclear molecule ${}_Z A + p$ shift relative to electronic levels in the atom ${}_{Z+1} B$, where Z is the nuclear charge.

At a high concentration of protons (deuterons) per one nucleus of the main element a second proton or a second deuteron can get into in exchange well: $A + p + p$ or $A + d + d$. Protons-fermions in the ground state will have antiparallel spins in the well, deuterons-bosons can have differently directed spins, since deuteron levels are closely spaced triplet states ($S_d = 1, m_s = +1, 0, -1$).

As a result, a possibility for cold fusion reactions opens up (Fig. 6):



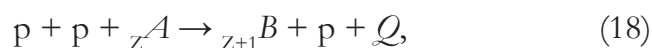
The reaction (16) with positron emission can be strongly decelerated because of the need to fulfill the angular momentum conservation law. Strong deceleration of reaction (16) opens up the possibility of a reaction with orbital K-electron capture:



It is clear that, other things being equal, the registration of released energy and the detection of deuterons during that reaction are difficult compared with reactions (15 and 16) ($e^+ + e^- \rightarrow 2\gamma + 1.022 \text{ MeV}$). Perhaps, it is for that reason that the reaction (17) cannot be registered in experiments.

Fig. 7 shows that for a proton or deuteron located in the exchange well, the transparency of the Coulomb barrier increased (7) as the height and width of the barrier decreased. In addition, the permeability of the barrier should additionally increase due to the existing resonant levels on the inner side of the Coulomb barrier [41]. Recall that the probability of absorption

of a neutron by a nucleus, among other things, depends on the probability of gamma transitions ($\sim 8 \text{ MeV}$), when the neutron “descends” to the ground state from upper level at which it was captured. The probabilities of gamma transitions are strongly suppressed, since they are carried out by electromagnetic, rather than strong, interactions. In the case when there are two protons (deuterons) in the exchange well, the probability of tunneling one of the protons through the Coulomb barrier directly into the ground state of the compound nucleus without gamma transitions appears (Fig. 6). This reaction becomes possible due to the strong interaction of protons with the nucleus and the reaction pulse transfer to the second proton:



where Q is energy released in the reaction. With such a transition to ground state, the ${}_{Z+1} B$ nucleus may turn out to be beta β^+ -radioactive nucleus. Since the disturbing potential of the exchange interaction includes a weak interaction W , the reaction can proceed with the capture of the orbital K-electron. Then the reaction produces a stable isotope.



It is such reactions (18, 19) that can explain the appearance of stable copper isotopes in the $\text{Ni} + p$ reaction with a changed isotope ratio in nickel [19, 20].

Obviously, with the preservation of coefficients UK^4M^2 , the barrier transparency also increases at nuclear charge decrease. **Fig. 8** shows the formation of an exchange potential well for titanium Ti, and **Fig. 9** - for lithium Li with coefficients $UK^4M^2 = -2 \text{ MeV}$ and $UK^4M^2 = -0.7 \text{ MeV}$, respectively. The red line in Fig. 8, 9 is nuclear potential plus Coulomb potential of $\text{Ti}+p$ and $\text{Li}+p$, the blue line is the RIEK interaction potential (values of 400 fm and 300 fm and UK^4M^2 are chosen arbitrarily) and the green line is summarized potential.

For lithium, the resonant proton is surprisingly absorbed by the nucleus without

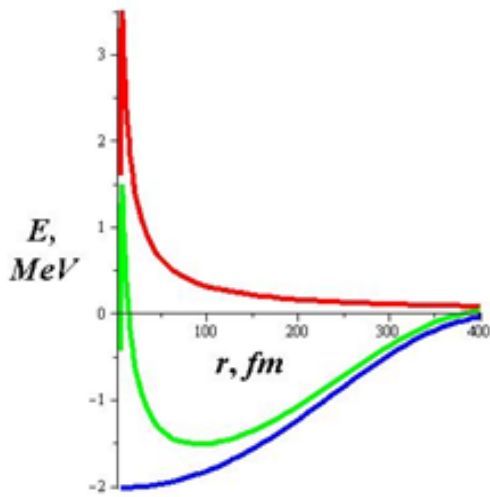


Fig. 8. Red line - nuclear plus Coulomb potentials $Ti+p$; blue - RIEX potential $Ti-p$; green - total potential $Ti+p$.

Coulomb barrier, like a resonant neutron, if the coefficient $|UK^4M^2|$ exceeds the height of Coulomb barrier $|UK^4M^2| > 0.5$ MeV (Fig. 9). For lithium and boron (${}_5B$), exchange barrier or barrier-free transitions are all the more likely because they can occur with one proton or one deuteron, since the compound nucleus decays into fragments [20, 42]. No energy mediator “Y” is needed in these reactions. The height of boron Coulomb barrier is 0.9 MeV. Thermal neutron capture cross-section is $\sigma_T({}^6Li) = 940$ barn, $\sigma_T({}^{10}B) = 3840$ barn (see Table).

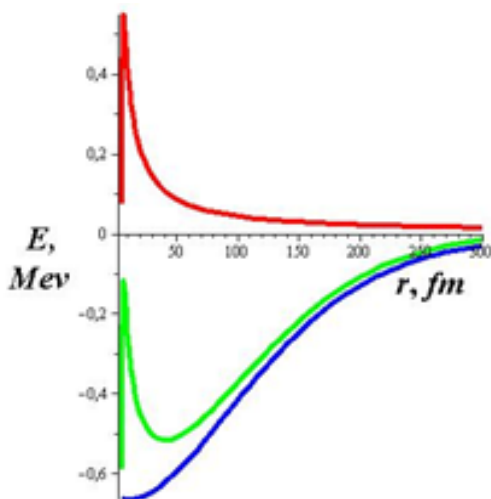
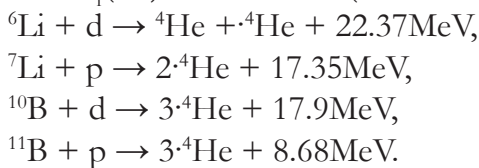


Fig. 9. Red line - nuclear plus Coulomb potentials $Li+p$; blue - RIEX potential $Li-p$; green - total potential $Li+p$.

However, both for neutrons and for protons and deuterons, there seems to be a limited number of isotopes that have significant potential for RIEEX interaction with a large UK^4M^2 coefficient and which are capable of forming a deep exchange nuclear well with protons and deuterons. Most isotopes have probably small coefficient K : $K < 1$ and $K \ll 1$. Therefore, not a deep potential well, but a shallow potential “pool” is formed in some of them as a result of the RIEEX interaction (Fig. 10). The bottom of such a “pool” and corresponding levels of protons (deuterons) in it can exceed the zero line of potential energy. The lifetime of such a nuclear molecule, the residence time of protons and deuterons in such a “pool” are supposed to be limited. And if external conditions change and do not allow to reproduce again unstable nuclear molecules, they disappear in some time [43].

Since the proton and neutron in the deuteron have a noticeable probability of $\sim 65\%$ to be outside the nuclear potential well, i.e. to stay in a quasi-free state for some time, the proton and neutron can be assumed to interact independently with their R-states. It follows from this that cold fusion reactions on deuterons should have noticeable cross-sections on isotopes, for which the neutron resonance absorption cross-sections are also significant (see Table).

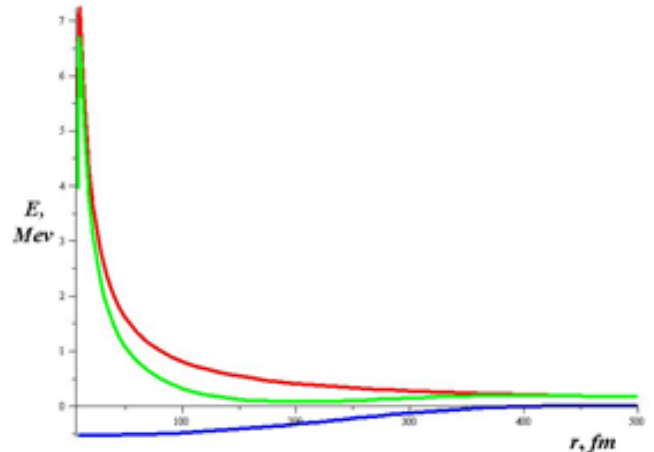


Fig. 10. Formation of a potential “pool”. Red line - nuclear plus Coulomb potentials ${}_{56}Ba$; blue - RIEX potential; green - total potential.

The possibility of a proton and a neutron to be outside the nuclear potential well of the deuteron can be interpreted as the existence of RIEX interaction between them. Neutron and proton spins in the deuteron are parallel, and their spatial wave function is symmetric. At that, their total wave function is antisymmetric because of the antisymmetric isotopic spin part of their wave function - n, p .

Based on the isotopic invariance of strong interaction, it can be assumed that proton can resonantly interact with neutron R -levels, both located behind the Coulomb barrier (Fig. 6) and those of isotopes with significant resonant absorption of neutrons (see Table) [43].

8. CONCLUSION

Several conditions should be met for the implementation of cold fusion reactions. First of all, it is necessary that the molecules of hydrogen or deuterium dissociate into atoms in a condensed solid or liquid matter.

It also requires that hydrogen or deuterium atoms in a condensed matter transform into protons or deuterons. It is important that protons or deuterons have maximum possible concentration (> 2) per nucleus of main element. The latter is achieved either by electrolysis or electrical discharge by means of saturating the cathode material with protons or deuterons, or by high hydrogen (deuterium) pressure or by nanoclustering the substance, or by its melt, or by aqueous solution of a substance in which hydrogen atoms are present in the form of proton, including biological systems [12, 13, 17, 19, 20, 23-26, 37-40, 42-47].

For CF reactions, it is absolutely necessary that the protons or deuterons incident on the nucleus have R -levels resonant with a compound nucleus. Due to the existence of R -levels between the nucleus and the proton (deuteron), a resonant interference exchange interaction arises, the disturbing potential of which are all types of interactions simultaneously. The disturbing potential that makes the main

contribution to the exchange energy is strong interaction. The spatial domain of the resonant interference exchange interaction is related to the wavelength of the proton (deuteron) as $L = K^4 \lambda_p$. The value of coefficient K depends on the affinity of R -state with a proton (deuteron).

The exchange energy between the proton (deuteron) and the compound nucleus with the R -state makes an additional contribution to the energy of their Coulomb and nuclear interaction. Due to this exchange energy, an exchange potential well appears on the Coulomb repulsion barrier. A proton (deuteron), trapped in exchange well, forms a nuclear molecule with a nucleus, and it can tunnel through a reduced Coulomb barrier in the case when a compound nucleus decays into two or three fragments.

The probability of passing through the Coulomb barrier for the proton also increases when a second proton enters the exchange well, which can perform the function of an energy mediator in the reaction.

In the case when there are two protons or two deuterons in the exchange well, they can merge. Thus, cold fusion reactions begin in condensed matter.

The exchange interaction represents a purely quantum effect, which disappears with the limiting transition to classical mechanics. Up to now, the exchange interaction has been considered as an interaction between identical particles. This article argues that the resonant interference exchange interaction does exist. The RIEX interaction is an exchange interaction between any object and resonant R -state belonging to any system. RIEX interaction is a development of resonant synchronization principle and its mechanism [48, 49]. All fundamental interactions form simultaneously the disturbing potential of the RIEX interaction: strong, electromagnetic, weak, and gravitational (8). The spatial domain of the resonant interference exchange interaction for all fundamental potentials is determined by the lengths of the wave functions for any resonantly interacting “identical” objects. Due to the RIEX

interaction, the short-range strong and local weak interactions become “long-range” interactions.

The formulated RIEEX interaction goes beyond pure quantum effects. Resonance is nothing else but RIEEX interaction.

The world around us consists of identical particles: protons, neutrons and electrons, which in turn form identical objects and identical systems. All types of fundamental interactions occur between identical particles, objects, systems including the RIEEX interaction. The RIEEX-interaction on a par with other interactions creates the Universe. It is a Universal interaction because it includes all other Four interactions.

Resonant Interference Exchange interaction is the Fifth type of interaction.

REFERENCES

1. *Proceedings of the 1-25th Russian Conferences on Cold Transmutation of Nuclei of Chemical Elements*. Dagomys, Sochi, 1993-2018.
2. *Proceedings of the 1-21th International Conferences on Condensed Matter Nuclear Science (Cold Fusion) - ICCF*. USA, Canada, France, Italy, Japan, China, Korea, India etc. 1990-2018.
3. Balakirev VF, Krymsky VV, Bolotov BV, Vasilieva NV, Vachaev AV, Ivanov NI, Kazbanov VI, Pavlova GA, Solin MI, Trofimov VI, Urutskoev LI. *Vzaimoprevrashcheniya khimicheskikh elementov* [Mutual transformation of chemical elements]. Ekaterinburg, Urals Branch of RAS Publ., 2003, 64 p.
4. *Radioelectronics. Nanosystems. Information Technologies (RENSIT)*, 2017, 9(1); DOI: 10.17725/rensit.2017.9.
5. *Zhurnal formiruyushchikhsya napravleniy nauki* [International Journal of Unconventional Science (IJUS)], 2017, No.17-18 (in Russ.); <http://www.unconv-science.org/>.
6. Prosvirnov AA, editor of the LENR-site; <http://www.lenr.seplm.ru/>.
7. Mishinsky GV, Kuznetsov VD, Penkov FM. Nizkoenergeticheskaya transmutatsiya atomnykh yader khimicheskikh elementov. Raspredelenie po elementam v produktakh transmutatsii. nukleosintez [Low energy transmutation of atomic nuclei of chemical elements. Element distribution in the products of low energy transmutation. Nucleosynthesis]. *IJUS*, 2017, No.17-18 (5):61-81 (in Russ.).
8. Mishinsky GV. Spin electron condensate. Spin nuclide electron condensate. *RENSIT*, 2018, 10(3):411-424. DOI: 10.17725/rensit.2018.10.411.
9. Mishinsky GV. Non-Coulomb nuclear reactions of transatoms. Stellar energy and nucleosynthesis. *RENSIT*, 2018, 10(1):35-52. DOI: 10.17725/rensit.2018.10.035.
10. Mishinsky GV. Atom in a strong magnetic field. Transformation of atoms to transatoms. *RENSIT*, 2017, 9(2):147-160. DOI: 10.17725/rensit.2017.09.147.
11. Mishinsky GV. Multinuclear reactions in condensed helium. *RENSIT*, 2017, 9(1):94-105. DOI: 10.17725/rensit.2017.09.094.
12. Fleishmann M, Pons S, Hawkins M. Electrochemically induced nuclear fusion of deuterium. *J. Electroanal. Chem.* 1989, 261:301-308.
13. Filimonenko IS. Demonstratsionnaya termoemissionnaya ustanovka dlya yadernogo sinteza [Demonstrational therm-emission device for nuclear fusion]. *Materials 3 Sci. Symp. "Perestroyka estestvoznaniya* [Restructuring of Natural history]"-92, Volgodonsk, Russia, 17-19 apr. 1992 (in Russ.).
14. Iyengar PK. Cold Fusion Results in BARC Experiments. *Proc. 5 Intern. Conference On Emerging Nuclear Energy Systems (ICENES)*, Karlsruhe, FRG, Singapore, 1989; Iyengar PK. and Srinivasan M. Overview of BARC Studies in Cold Fusion. *Proc. 5 Intern. Conference on Cold Fusion (ICCF-5)*, 1990, Utah, Salt Lake City.
15. McKubre MCH. CMNS Research – Past, Present and Future. *J. Condensed Matter Nuclear Science*, 2017, 24:15-24.
16. Miles MH. Heat and helium production in cold fusion experiments. *2nd Int. Conf. on Cold Fusion "The Science of Cold Fusion"*, Como, Italy: Societa Italiana di Fisica, Bologna, Italy, 1990. Miles MH, Hollins RA, Bush BF, Lagowski JJ, Miles RE. *J. Electroanal. Chem.*, 1993, 346:99. Miles MH, *Proc. ICCF-10*, 2003, Cambridge.

17. Karabut AB, Kucherov YaR, Savvatimova IB. Nuclear product ratio for glow discharge in deuterium. *Phys.Letters A*, 1992, 170: 265-272. Savvatimova IB, Karabut AB. The products of nuclear reactions recorded at the cathode after experiments in a glow discharge in deuterium. *Povernocit'* [Surface Investigation: X-Ray, Synchrotron and Neutron Techniques], 1996, 1:63-75-81.
18. Focardi S, Habel R and Piantelli F. Anomalous Heat Production in Ni-H Systems. *Nuovo Cimento*, 1994, 107(1):163-166.
19. Parkhomov AG, Alabin KA, Andreev SN, Zabavin SN, Sobolev AG, Timerbulatov TR. Nickel-hydrogen reactor: heat generation, isotopic and elemental composition of fuel. *RENSIT*, 2017, 9(1):74-93. DOI: 10.17725/rensit.2017.09.074.
20. Levi G, Foschi E, Höistad B. Observation of abundant heat production from a reactor device and of isotopic changes in the fuel. [Http://www.sifferkoll.se/sifferkoll/wp-content/uploads/2014/10/LuganoReportSubmit.pdf](http://www.sifferkoll.se/sifferkoll/wp-content/uploads/2014/10/LuganoReportSubmit.pdf).
21. Kalman P, Keszthelyi T. Lattice effect in solid state internal conversion. *Phys. Rev. C*, 2009, 79(0316026):1-4.
22. Bazhutov YuN. Possible generation of neutrons bursts in framework of erzion model and their possible registration; Essence of erzion model. *Proc.13th Intern. Conference on Condensed Matter Nuclear Science*. Moscow, MITI, 2008:581-589.
23. Arata Y, Zhang Y-C. Characteristics of Compact and Practical "Solid Deuterium Nuclear Fusion Reactor". *Proc. 10th Intern. Conference on Cold Fusion*, 2003, Cambridge, Massachusetts, USA.
24. Arata Y and Zhang YC. Formation of Condensed Metallic Deuterium Lattice and Nuclear Fusion. *Proc. Jpn. Acad., Ser. B*, 2002, 78:57.
25. Nesvizhevsky VV, Voronin AYu, Lambrecht A, Reynaud S, Lychagin EV, Muzychka AYu, Strelkov AV. Observation of quantum levitation of nanoparticles by the method of ultracold neutrons. *Crystallography*, 2013, 58(5):730-736 (in Russ.).
26. Didyk AYu, Wisniewski R. Nuclear reactions, induced by gamma quanta, in palladium saturated with deuterium surrounded by dense deuterium gas. *Euro. Phys. Lett.*, 2012, 99, 22001:1-6.
27. Rukhadze AA, Grachev VI. LENR in Russia. *RENSIT*, 2017, 9(1):5-7. DOI: 10.17725/rensit.2017.09.005.
28. Wendt GL, Irion CE. Experimental attempts to decompose tungsten at high temperatures. *J. of the American Chemical Society*, 1922, 44(9):1887-1894.
29. Smits A, Karssen A. Vorläufige Mitteilung über einen Zerfall des Bleiatoms. *Naturwissenschaft*, 1925, 13:699. Ein Zerfall des Bleiatoms, *Z. Elektrochemie*, 1926, 32:577-586.
30. Mills R, Ray P. Extreme ultraviolet spectroscopy of helium-hydrogen plasma. *J. Phys. D:Appl. Phys.*, 2003, 36:1535-1542.
31. Tsyganov EN. Kholodny yaderny sintez [Cold fusion]. *Yadernaya fizika*, 2012, 75(2):174-180 (in Russ.).
32. Vlasov NA. *Neytrony* [Neutrons]. Moscow, Nauka Publ., 1971, 552 p.
33. Heisenberg W. Über die Spektra von Atomsystemen mit zwei Elektronen. *Z. Phys.*, 1926, 39(7):499-518.
34. Matveev AN. *Atomnaya fizika* [Atomic physics]. Moscow, Vysshaya shkola Publ., 1989, 439 p.
35. Gurevich VL, Pogorelsky MJ, Chaly VP. Dvukhyadernoe atom-svyazannoe sostoyanie protona i tyazhelogo atoma [Binuclear atom-bound state of proton and heavy atom]. *Zhurnal tekhnicheskoy fiziki*, 2009, 79(2):1-5 (in Russ.).
36. Polikanov SM. *Izomeriya formy atomnykh yader* [Isomerism of atomic nuclei form]. Moscow, Atomizdat Publ., 1977, 200 p.
37. Vysotskii VI, Kornilova AA, Vasilenko AO, Krit TB, Vysotskyy MV. The prediction, observation and study of long-distant undamped thermal waves generated in pulse radiative processe. *Nuclear Instruments and Methods in Physics Research B*, 2017, 402:251-255.
38. Vysotskii VI, Kornilova AA, Sysoev NN. X-ray radiation by cavitation of rapid liquid jet. *RENSIT*, 2010, 2(1-2):57-69.

39. Klimov A, Grigorenko A, Efimov A, Evstigneev N, Ryabkov O, Sidorenko M, Soloviev A, Tolkunov B. High-energetic nano-cluster plasmoid and its soft X-radiation. *Proc.19th Intern. Conference on Condensed Matter Nuclear Science*, 2015. *J. Condensed Matter Nucl. Sci.*, 2016, 19:145-154.
40. Klimov A. Energy Release and Transmutation of Chemical Elements in Cold Heterogeneous Plasma. *Proc.19th Intern. Conference on Condensed Matter Nuclear Science*. Padua, Italy, 2015. *J. Condensed Matter Nucl. Sci.*, 2016, 19:155-163.
41. Demikhovskiy VYa, Vugalter GA. *Fizika kvantovykh nizkorazmernykh struktur* [Physics of quantum low-dimensional structures]. Moscow, Logos Publ, 2000, 248 p.
42. Vysotskii VI, Kornilova AA, Chernysh VS, Gavrilova ND, Lotonov AM. Stimulated (B11p) LENR and Emission of Nuclear Particles in Hydroborates in the Region of Phase Transfer Point. *J. Condensed Matter Nucl. Sci.*, 2014, 13:608-614.
43. Klimov AI. Will Russia be among the leaders of new energy technologies? *LA REGNUM*, 2019, (in Russ.); <https://regnum.ru/news/2625783.html>.
44. Didyk AYu, Wiśniewski R, Wilczyńska-Kitowska T, Mishinsky GV, Semin VA. Synthesis of chemical elements under irradiation by bremsstrahlung gamma-rays of palladium in condensed gases. *RENSIT*, 2019, 11(2):143-160.
45. Andreev SN, Shafeev GA. Nelineynoe tushenie radioaktivnosti vodnykh rastvorov soley nuklidov pri lazernoy ablyatsii nanochastits metallov [Onlinear quenching of the radioactivity of aqueous solutions of salts of nuclides by laser ablation of nanoparticles of metals]. *RENSIT*, 2017, 9(1):65-73. DOI: 10.17725/rensit.2017.09.065.
46. Astakhov BA. Nekotoryye predlozheniya o puskovom mekhanizme CF. [Some suggestions about the trigger mechanism CF]; <http://lenr2019.ru/>.
47. Kornilova AA, Vysotskii VI. Synthesis and transmutation of stable and radioactive isotopes in biological systems. *RENSIT*, 2017, 9(1):52-64. DOI: 10.17725/rensit.2017.09.052.
48. Gareev FA, Gareeva GF, Zhidkova IE. Mekhanizm protsessa kholodnoy transmutatsii yader khimicheskikh elementov [The mechanism of the process of cold nuclear transmutation of chemical elements]. *Geoinformatics*, 2003, 1:51-53. (in Russ.).
49. Gareev FA, Gareeva GF, Zhidkova IE. Printsip rezonansnoy sinkhronizatsii dlya proryvnykh tekhnologiy [The principle of resonant synchronization for breakthrough technologies]. *Collected Works of the Sustainable Innovative Development Department of the International University of Nature, Society and Man "Dubna"*. K. 89-1, Moscow, RAEN Publ., 2007:138-154.

SYNTHESIS OF CHEMICAL ELEMENTS UNDER IRRADIATION BY BRAKING GAMMA-RAYS OF PALLADIUM IN CONDENSED GASES

Alexander Yu. Didyk, Gennady V. Mishinsky, Vasily A. Semin

Joint Institute for Nuclear Research, <http://www.jinr.ru/>
6, str. Joliot Curie, Dubna 141980, Moscow Region, Russian Federation

Roland Wiśniewski, Teresa Wilczyńska-Kitowska

National Centre for Nuclear Research, <https://www.ncbj.gov.pl/>
ul. Andrzeja Sołtana 7, 05-400 Otwock, Świerk, Poland

roland.wisniewski@gmail.com, teresa.wilczynska@gmail.com, mysh@jinr.ru, seminva@jinr.ru

Abstract. The article is a review of the experimental results obtained by the authors over the past 8 years on the synthesis of chemical elements in gases compressed up to 3 kbar with its long (up to tens of hours) gamma irradiation in the presence of cylindrical samples of metallic palladium. The chambers were irradiated by braking gamma rays with a maximum energy of 10 MeV at the electron accelerator of the Joint Institute for Nuclear Research in Dubna (Moscow region). In addition to palladium, the reaction chamber contained other structural details made of brass or copper, beryllium bronze and manganin foil. Experiments were carried out with palladium in deuterium, with palladium and tin in hydrogen, with palladium in helium. In all experiments, after irradiation, numerous solid-state microstructures of various sizes (up to 1 mm) and shapes were found on the surfaces of the chamber's parts, as well as on the surface of the palladium. X-ray micro-probe analysis of these structures showed the presence of a wide range of chemical elements (from carbon to lead), which were absent in the reaction chamber prior to irradiating. The article presents numerous quantitative histograms of concentrations of the elements found. Preliminary hypotheses are proposed for the synthesis of chemical elements under the experimental conditions.

Keywords: condensed gas, high-pressure chambers, gamma radiation, surface microstructures, X-ray analysis, photonuclear reactions, low-energy nuclear reactions, cold nuclear fusion

PACS: 25.20.-x; 25.70.-z; 25.70.Jj

Bibliography - 45 references

Received 24.05.2019, accepted 30.05.2019

RENSIT, 2019, 11(2):143-160

DOI: 10.17725/rensit.2019.11.143

CONTENTS

1. INTRODUCTION (143)
 2. RECEIVING BRAKING GAMMA RADIATION (145)
 3. THE METHODS OF THE EXPERIMENTS (146)
 4. THE EXPERIMENTS WITH PALLADIUM IN DEUTERIUM (147)
 5. THE EXPERIMENTS WITH PALLADIUM AND TIN IN HYDROGEN (150)
 6. THE EXPERIMENT WITH PALLADIUM IN HELIUM (153)
 7. DISCUSSION OF THE EXPERIMENTAL RESULTS (154)
 8. CONCLUSION (157)
- REFERENCES (157)

1. INTRODUCTION

The phenomenon of synthesis of chemical elements and solid-state structures in a medium of condensed gases under the action of gamma quanta was discovered by A.Yu.Didyk and R.Wiśniewski. The first experiment was carried out in 2011 with a palladium sample (Pd) in the form of a cylinder placed in a chamber with a deuterium pressure of 3 kbar [1-3]. At pressures of 0.5–3 kbar, the density of gas atoms is comparable with the density of atoms in the solid and liquids. Therefore, the term condensed gas is used. Irradiation by braking gamma-quanta was carried out during 6 hours at the MT-25 microtron [4]

with an electron energy of 9.3 MeV and an average electron current of $7 \mu\text{A}$ ($\sim 4.4 \cdot 10^{13} \text{ s}^{-1}$).

The motivation for setting up such an experiment was two competing ideas in how to produce energy: the thermonuclear fusion reaction and the cold nuclear fusion reaction (CF).

To carry out thermonuclear fusion reactions in the planned experiment, an approach was proposed basing on the photodisintegration of deuterons in condensed deuterium under the action of gamma quanta with energies up to 10 MeV. In each deuteron photodecay event, a neutron and a proton are formed with energies determined by the reaction kinematics. The binding energy of the deuteron is 2.224 MeV. With the elastic interaction of photo-neutrons and photo-protons with gas deuterons, the latter acquire the energy $> 40 \text{ keV}$, sufficient to launch thermonuclear reactions through the channels: $d + d \rightarrow {}^3\text{He} + n + 3.26 \text{ MeV}$ and $d + d \rightarrow t + p + 4.03 \text{ MeV}$. The resulting products of thermonuclear reactions, in their turn, give a part of their energy to the deuterons, and they again enter into thermonuclear fusion reaction. It was expected that under the action of gamma rays in deuterium, thermonuclear energy would be produced, sufficient to heat the reaction chamber to a high temperature.

The effect of heating the reaction chamber was also expected in the case of the implementation of cold fusion reactions [5]. Therefore, palladium was placed in the reaction chamber. It is known from literature [6] that the intensity of the reactions of CF enhances with the growing number of deuterium atoms per palladium atom. It was proposed to increase the concentration of deuterium in palladium with the help of the high gas pressure and its irradiation with braking gamma quanta. Moreover, the author of this article R. Wiśniewski registered an unexpected strong explosion of the high-pressure chamber while saturating the palladium powder with gaseous deuterium at a pressure of about 22 kbar (private communication).

The use of intense gamma-ray fluxes turns out to be the most suitable method for photodecay and ionization of deuterium due to their high penetrating power through the thick walls of the high-pressure

reaction chamber. Other radiation emissions do not possess such penetrating ability.

During the first and subsequent irradiations, there was no critical increase of the temperature or pressure in the reaction chamber. However, after irradiation unusual solid-state structures and “extraneous” chemical elements were found in the chamber, which were absent before the start of the experiment. The following elements were thus registered: Na, Mg, Al, Si, P, S, Cl, K, Ca, Ti, V, Cr, Fe, Nb, Ru, Ag, La, W, Pt, Pb. Later, an experiment was carried out at a deuterium pressure of 1.2 kbar [7–10].

Similar studies were performed with samples of other metals and alloys: Al, V, Cu, Sn, Re, YMn₂, in the form of cylinders and wires. The samples were in the atmosphere of gaseous deuterium at a pressure of hundreds, thousands of bars, and were irradiated with braking radiation with the $E_{\text{max}} = 10 \text{ MeV}$ and $E_{\text{max}} = 23 \text{ MeV}$ [11–15]. Positive results on the synthesis of new structures and “extraneous” elements in the deuterium atmosphere led to similar studies with palladium [16–18] and tin [19–21] cylinders in condensed hydrogen and with a palladium cylinder [22, 23] in condensed helium. The same studies were carried out in chambers with condensed pure gases: hydrogen [24–26], deuterium [27], helium [28–31] and xenon [32–36] when irradiated by γ -rays with energies up to the $E_{\text{max}} = 10 \text{ MeV}$. Experimental reviews in the H₂, D₂, He and Xe gases are presented in [37–39].

In this article, we present the processed and presented in an illustrative graphical form main results of the experiments on the synthesis of “extraneous” elements when irradiating palladium samples with the $E_{\text{max}} = 10 \text{ MeV}$ by braking gamma-rays in condensed deuterium with a pressure of 1.2 and 3 kbar, in hydrogen with a pressure of 0.5 and 2.5 kbar, and in helium with a pressure of 2.4 kbar. Here, for comparison, the results of experiments on the irradiation of pure gases without metal samples inside the reaction chambers are presented.

In this paper, the experiments were carried out and results discussed were obtained with the ideological organizational guidance and most active participation of A.Yu.Didyk to whom this article is dedicated.

2. RECEIVING BRAKING GAMMA RADIATION

As a source of braking gamma radiation the electron accelerator microtron MT-25 of the Flerov Laboratory of Nuclear Reactions at JINR. The acceleration of electrons occurs in a pulsed mode with a pulse duration of 2.5 μs and a repetition frequency of 400 Hz. The design of the microtron allows one to receive electron beams with energies from 5 to 24 MeV. The maximum current of the electron beam at the target is 25 μA (1.56·10¹⁴ s⁻¹). After acceleration, an electron beam of Ø 6–7 mm is released into the atmosphere through a 70 μm titanium foil (1, Fig. 1), upon which irradiation takes place. In experiments, both the electron beam and radiations produced by convectors can be used: braking gamma radiation intensity of 10¹⁴/s, fast neutrons with an intensity of 10¹²/s, thermal neutrons with a flux density of 10⁹/s·cm², resonant neutrons with a flux density of 8·10⁷/s·cm².

To obtain the braking gamma-rays, electrons bombard a tungsten converter – a disk with a thickness of 1 to 3.8 mm and Ø40 mm (3, Fig. 1). The electron beam enters the converter, passing through the diaphragm with a hole of Ø12 mm (2, Fig. 1) and a thickness of 18 mm. The converter is fixed in a holder with the help of an aluminum cylinder with a thickness of 8-25 mm, which also serves to absorb low-energy electrons (4, Fig. 1). The diaphragm and the holder of the converter with an aluminum absorber are cooled with running distilled water. In the process of irradiation, the electron current on the Al-absorber and on the diaphragm is controlled. In all experiments, a tungsten converter with a thickness of 2.8 mm and an electron absorber – 25 mm were used.

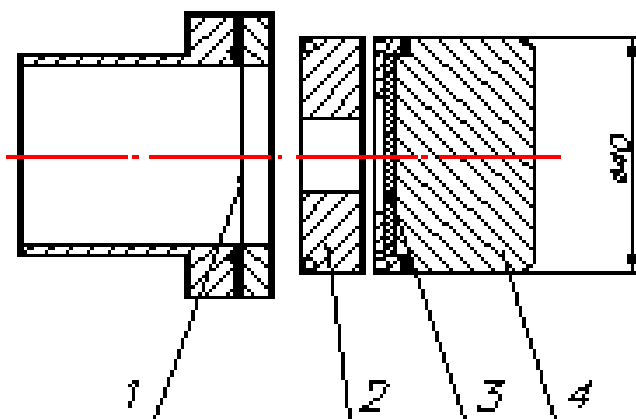


Fig. 1. Extraction of the electron beam from the electron guide and its conversion into a beam of gamma quanta.

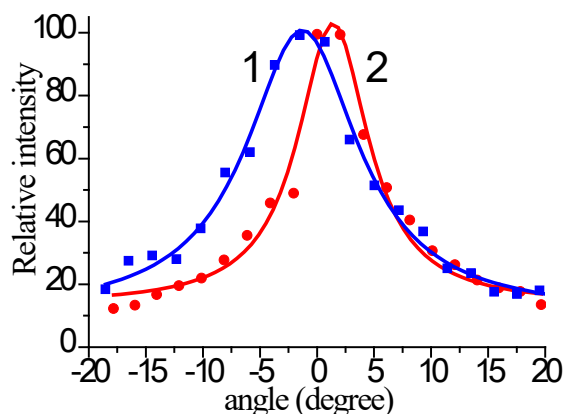


Fig. 2. The gamma-quanta beam divergence.

The gamma quanta beam divergence at half-height of intensity is horizontally 10°±1° (Fig. 2, curve 1) and 8°±1° along the vertical (Fig. 2, curve 2). The difference in half widths in the horizontal and vertical planes is explained by the different angular divergence of the electron beam in these planes. Experimentally, the divergence was determined by the method of activating targets: uranium with a threshold of 6 MeV and nickel with a threshold of 12.2 MeV, completely covering the braking radiation beam. In both cases, the angular distribution is approximated with good accuracy by the Lorentz distribution. The values obtained in the experiment are in good agreement with the calculation of the angular distribution of braking using the Giant package, which predicts an angular divergence of the beam of 9.9 degrees, and the authors of [40].

Fig. 3 shows the calculated energy spectrum of braking radiation emitted in a 10° cone for electrons with energies of 10, 14, 18, and 22 MeV on a 3 mm thick tungsten converter [41]. The intensities of gamma quanta from 1 MeV to the E_{max} for these

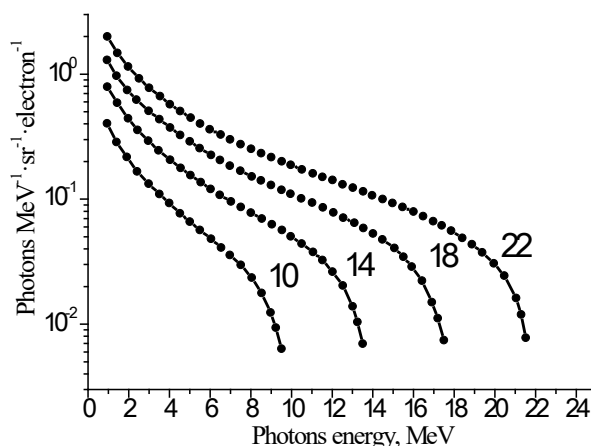


Fig. 3. A gamma-quanta spectrum for electron energies of 10, 14, 18 and 22 MeV.

electron energies, normalized to the intensity at $E = 10$ MeV, correspond 1: 4.52: 13.24: 32.13. For the range of gamma quanta from 1 to 10 MeV, the intensities correspond to 1: 4.50: 13.04: 31.03.

3. THE METHODS OF THE EXPERIMENTS

The irradiation of palladium samples in a medium of condensed gases was carried out using a braking gamma-quantum with the $E_{\max} = 10$ MeV. The energy range of gamma quanta (<10 MeV) lies below the characteristic excitation energies in the atomic nuclei of a giant dipole resonance. This avoids the activation of the structural materials of the reaction chambers. The decay of a giant dipole resonance occurs mainly with the emission of a proton or a neutron, often followed by the formation of radioactive isotopes. In the experiments, the chamber shown in **Fig. 4** was used. Each experiment used its own chamber. The inner diameter of the chambers was 4 mm, the length was 21 mm, the volume was 0.264 cm^3 . The palladium samples (9, Fig. 4) with a diameter of 3.8–3.9 mm and a length of 4–5.5 mm (of volume $0.045\text{--}0.065 \text{ cm}^3$) had a purity of $\sim 99.995\%$. The atomic mass of Pd is 106.42; the density of palladium is 12.02 g/cm^3 . The maximum concentrations of impurities (10^{-6} mass in ppm) in palladium are as follows: Ca, Zn, Ag < 3 ; Mg, Mn, Ni, Pb, Bi < 5 ; Si, As, Sn, Sb, Ru, Rh, Ir, Pt < 10 ; Cu(12), Al(15), Fe(19), Au(48). In the experiments, brass (Zn+Cu) or copper (Cu) with a purity of 99.99% was used as sleeves (8, Fig. 4) and collectors (12, Fig. 4). The composition of the brass sleeves and the collectors measured by x-ray micro-probe analysis included: Cu – 59.61 and Zn – 40.39 (at.%). The pressure in the chambers varied from 0.5 to 3 kbar. **Table 1** presents the parameters of exposure.

After irradiation, the gas was released into the atmosphere and the chamber was opened. In all experiments, after the end of irradiation new objects

Table 1

Parameters of the experiments.

Chamber	D1	D2	H1	H2	He
Electron energy, MeV	9.3	10	10.3	9.7	10
Exposure time, hours	6	18	7	14	96
Average current, mA	7	12	2.5	20.5	20.5
Electron flux, 10^{13} c^{-1}	4.4	7.5	1.6	12.8	12.8
Integral charge, C	0.15	0.78	0.14	1.03	7.1
Pressure, kbar	3	1.2	2.5	0.5	2.4
Atomic density, 10^{22} at/cm^3	5.2	2.95	9.12	1.82	2.23
Weight density, g/cm^3	0.155	0.088	0.154	0.0307	0.15
\varnothing Pd-cylinder, mm	3.8×5	3.8×5.5	3.8×5	3.8×5	3.9×5
Material of sleeve and collector	Zn+Cu	Zn+Cu	Zn+Cu	Zn+Cu	Cu
References	1-3	7-10	16	17-18	22-23

were found in the reaction chambers: microparticles with the size from $0.5 \mu\text{m}$ to 1 mm, and anomalous solid-state structures were observed on the walls of the reaction chambers and on the surface of the palladium cylinder. Solid-state structures were: crystalline, amorphous and spherical structures; ring-shaped, filamentary and tubular formations; loose and hard inclusions and influx on the surfaces of the reaction chamber parts. Using the methods of scanning electron microscopy (SEM) and x-ray micro-probe analysis (XRMPA), the elemental compositions of the chamber parts were investigated: on the inner surfaces of the entrance window made of beryllium bronze ($\text{Cu}_{0.92}\text{Be}_{0.08}$) (4, Fig. 4), at the sleeves and collectors, at the $\text{Cu}_{84}\text{Mn}_{14}\text{Ni}_2$ manganine foils (10, Fig. 4), as well as at the anomalous structures and microparticles formed as a result of irradiation of the palladium cylinder surface and the chamber inner surfaces.

In most of the objects, when they were studied using the SEM and XRMPA methods, “extraneous” chemical elements, which were absent in the reaction chambers before the onset of irradiation, were detected. For each object selected for the study: microparticles or a solid-state structure, several measurements of XRMPA were carried out in different regions of their surface. Each such measurement corresponded to its own set of chemical elements with its own concentration. The total number of XRMPA measurements for a particular experiment was several dozens. When processing the data, we first obtained averaged concentrations of chemical elements separately for each part of the reaction chamber in contact with the condensed gas. Taking into account the entire set of data obtained by the XRMPA method, it

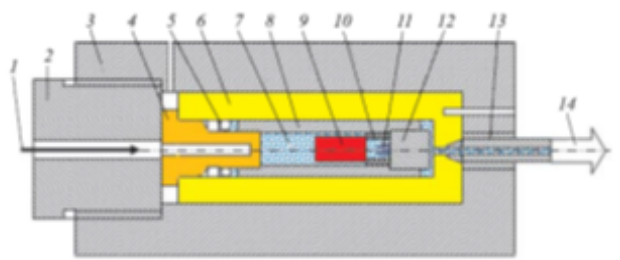


Fig. 4. The high pressure gas chamber with a palladium sample.

can be argued that there is no significant difference in the distribution of chemical elements for the input window, sleeve, collector, manganin foil, and the particles. In this article, we also present in the form of histograms the concentrations of chemical elements averaged over all measurements performed for this experiment.

SEM and XRMPA studies were conducted at three independent certified laboratories: at the analytical center of the D.V. Skobeltsyn INP, Lomonosov MSU; at the Research Institute of Advanced Materials and Technologies, and at the Fiber Optics Research Center of the Russian Academy of Sciences. The energy of the electron beam exciting the x-rays ranged from 10 to 20 keV. The penetration depth of the electron beam was 1-2 μm . The measurements were carried out using two modes: “at a point” and “over the area”. For the mode “at the point”, the measurement area was $\sim 1\text{--}4 \mu\text{m}^2$. For the “area” mode, the measurement area was more than $20 \times 20 \mu\text{m}^2$.

We note several important points in our SEM and XRMPA studies:

- the program for processing spectra obtained using XRMPA selects the lines only of those elements which exceed no less than thrice the measurement error;

- the program calculates the estimated element concentrations in weight and atomic percent if the spectrum contains the main characteristic x-ray lines of this element;

- the concentrations of “extraneous” elements in the objects given in the article are not quantitative but qualitative. The choice of objects for measurement was purely subjective. As a rule, the most appealing, bright and light objects with the presence of elements of large atomic numbers were measured;

- microparticles and structures located on the surfaces of collectors, inserts and sleeves were selected as objects for measurements. Analysis of the element compositions at the surfaces of the palladium cylinder was made as well;

- for reliable spectra processing, a set of considerable amount of statistical data are required, which was not always done in our measurements;

- the dimensions of the studied structures were far greater than the regions of excitation and emission of characteristic x-radiation. Therefore the measurements done cannot correspond to the

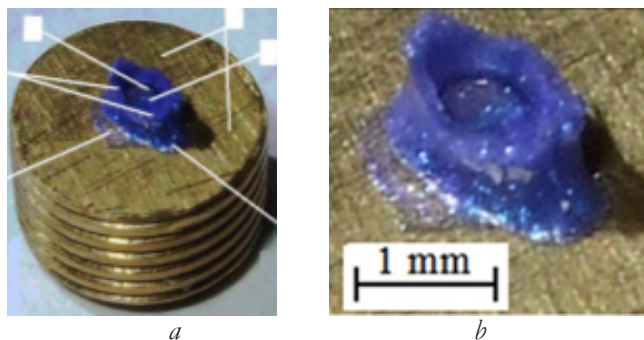


Fig. 5. Photos of the synthesized sample: a) at the brass collector; b) enlarged image.

element concentration in the entire volume of the measured objects;

- during the measurements of the objects at the points with local concentrations of “extraneous” chemical elements could amount to several tens percent. Besides, such measurements have certain restrictions relating to spatial resolutions of the equipment used.

4. THE EXPERIMENTS WITH PALLADIUM IN DEUTERIUM

In the very first experiment, after irradiating a sample of palladium at a deuterium pressure of 3 kbar, when the chamber D1 was opened (Table 1), a synthesized blue object was detected on the brass collector 5 mm in diameter, (Fig. 5a) and (Fig. 5b). The object was shaped like a “volcano with a crater” with smooth walls. At the top of the “crater”, frozen drops were observed, and at its bottom, various structures in the form of plates (Fig. 6a) and crystalline formations (Fig. 6b). Here and hereinafter, the widths of photographs are given in brackets. The synthesized object had dielectric properties. For SEM and XRMPA, this required deposition of a gold layer of Au $\sim 0.1 \mu\text{m}$. The x-ray micro-probe analysis revealed “extraneous” chemical elements in the object which had been absent in the reaction

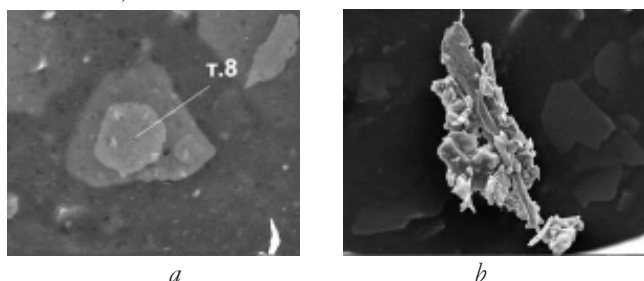


Fig. 6. The SEM images of the structures found at the bottom of the “crater”: a) in the form of plates a (the photo width is $60 \mu\text{m}$) and b) the crystalline formations (the photo width is $150 \mu\text{m}$).

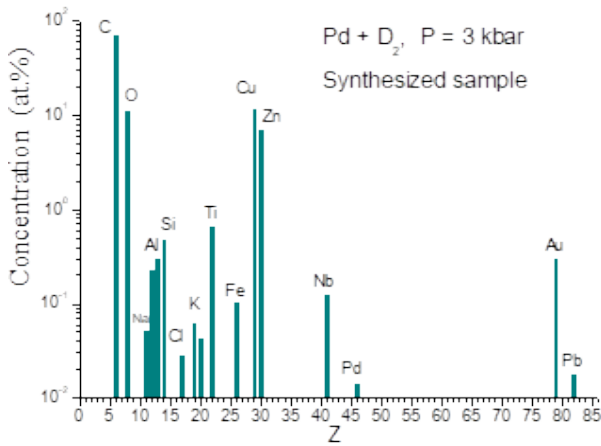


Fig. 7. The concentrations of chemical elements in the synthesized sample (12 measurements).

chamber before the start of the experiment. **Fig. 7** shows the concentrations of chemical elements in the synthesized sample, averaged over 12 measurements, which were carried out both on its surface and in the various structures found inside the crater. It is noteworthy that the synthesized object mainly consists of carbon, oxygen and titanium. Subsequent x-ray diffraction analysis showed that titanium is present in the synthesized object in the form of dioxide (TiO_2).

The irradiated Pd-cylinder has undergone significant changes. The SEM images of the original and irradiated surfaces of the Pd-cylinder are shown in **Fig. 8a,b**. The surface of the Pd-cylinder, especially close to the synthesized object, turned from smooth into non-uniform, consisting of individual clusters, with a lot of cracks in the surface and, moreover, with a modified composition of the chemical elements. **Fig. 9** presents atomic percent concentrations of chemical elements averaged over 12 XRMPA measurements of the palladium cylinder surface.

The changes affected the surface structure and the content of chemical elements, both at the entrance window (4, Fig. 4), made of beryllium bronze, and

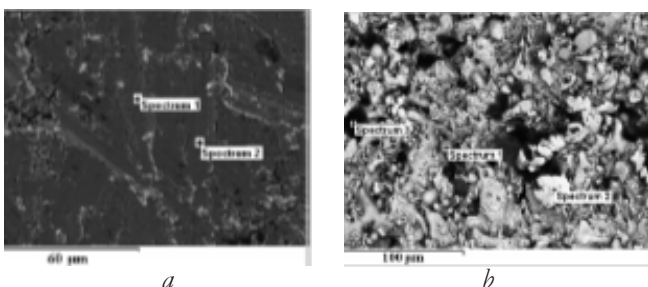


Fig. 8. SEM images of the Pd-cylinder surfaces: a) before the irradiation and b) after the irradiation.

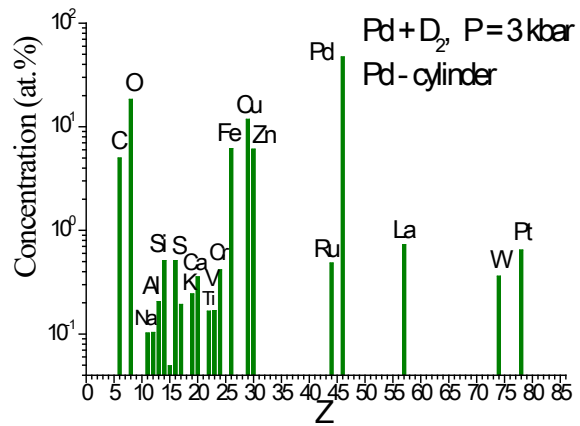


Fig. 9. The concentrations of chemical elements at the Pd-cylinder (12 measurements).

at the brass sleeve (8, Fig. 4). **Fig. 10** shows the concentrations of chemical elements at the entrance window, averaged over 5 measurements, and for the brass sleeve, averaged over 10 measurements.

Fig. 11 gives the concentrations of chemical elements averaged over all 39 measurements. Thus, the following chemical elements were registered in the reaction chamber: C, O, Na, Mg, Al, Si, P, S, Cl, K, Ca, Ti, V, Cr, Fe, Nb, Ru, Ag, La, W, Pt, Pb.

For comparison, **Fig. 12** shows the averaged concentrations of chemical elements obtained in an experiment on irradiating a chamber with deuterium at a pressure of 2.2 kbar without a Pd-cylinder inside it [27]. Averaging was carried out over 42 measurements performed for the structures of the entrance window, the sleeve, the collector, and the synthesized microparticles. The internal dimensions of the chamber filled with deuterium were: length - 15 mm, diameter - 8 mm, volume - 0.75 cm³. The sleeve and the collector were made of pure copper, 99.99%. The irradiation was carried out during 49

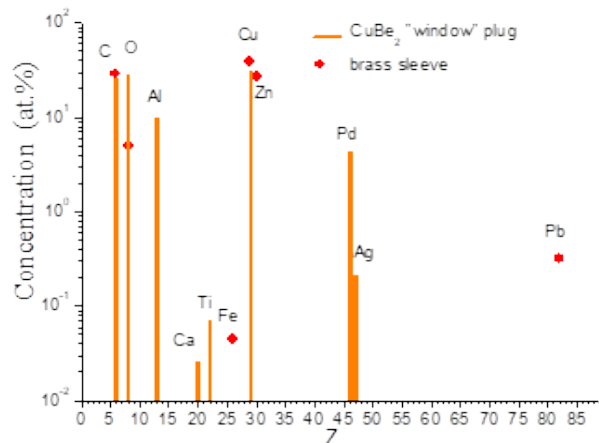


Fig. 10. The concentrations of chemical elements at the surface of the "entrance window" and the sleeve.

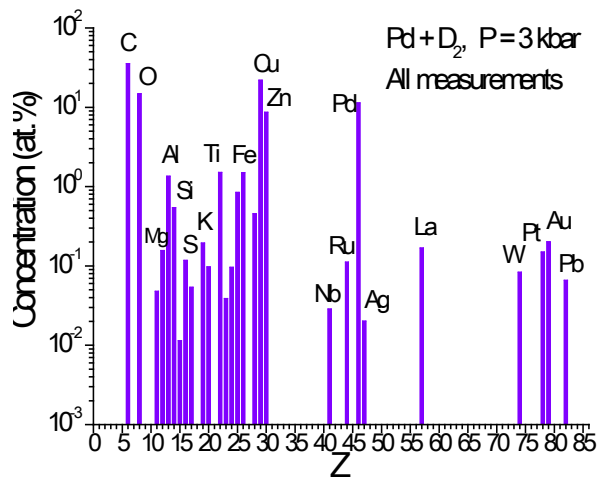


Fig. 11. The concentrations of chemical elements (39 measurements).

hours. The electron beam energy was 10 MeV. The current of the electrons was $(1.2-1.3) \cdot 10^{14} \text{ s}^{-1}$.

The experiment described above was repeated (D2, Tab. 1), but with a deuterium pressure of 1.2 kbar and an irradiation duration of 18 hours. The most impressive result of this experiment was the detection of a $^{82}_{\text{Pb}}$ layer covering all the inner surfaces of the reaction chamber and microparticles up to 50 microns in size, consisting mainly of lead. Fig. 13 presents averaged concentrations of chemical elements in atomic percentage from the 44th XRPMA measurements of the palladium cylinder surface. Without palladium, the weight concentration of lead is $\sim 36\%$, oxygen $\sim 29\%$.

Fig. 14 shows SEM images of one of the characteristic elliptically-shaped formations with a size of $17 \times 22 \mu\text{m}$ (Fig. 14a) and individual lead microparticles (Fig. 14b) found on the surface of the brass collector. The lead concentration over the area of $5.3 \times 6.3 \mu\text{m}$, noted as “spectrum 1” (Fig. 14a),

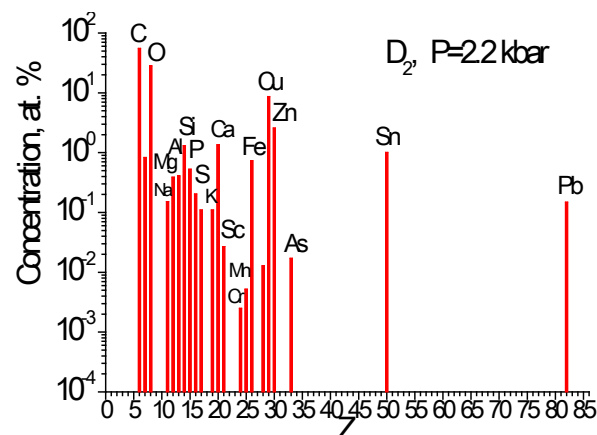


Fig. 12. The average concentrations of chemical elements over 42 measurements.

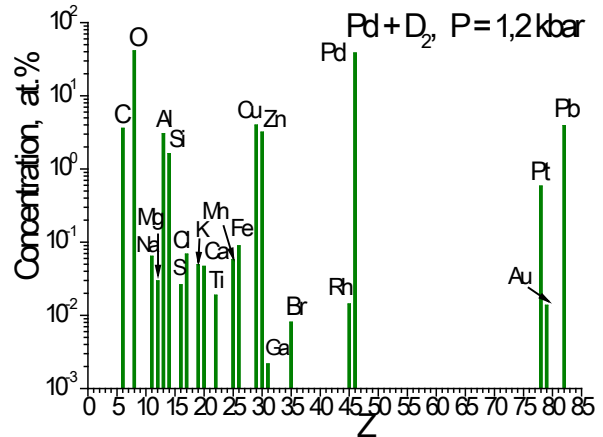


Fig. 13. The concentrations of chemical elements at the Pd-cylinder (44 measurements).

is 21.3 wt.%. Lead concentrations, measured at points 1 and 2 (Fig. 14b), are 65.1 and 10.9 wt.%, respectively. Lead was not detected at point 3. It contains: copper-62.9 and zinc-37.1 wt.%. Table 2 shows the concentrations of chemical elements averaged over 15 measurements made for different microparticles, and 8 measurements made at points or from the area next to the microparticles. The lead concentration in the microparticles varied from 31.5 to 71.9 wt.%, and in the areas near the microparticles, from 0 to 10.9 wt.%. In five measurements out of 23 (15 + 8), $^{14}_{\text{Si}}$, $^{20}_{\text{Ca}}$, $^{26}_{\text{Fe}}$ were registered. Subsequent studies carried out by the method of secondary mass-ion spectroscopy showed that the isotopic composition of the synthesized lead does not differ from the natural composition within the limits of measurement errors [40]. In the same studies, lines corresponding to the masses of protactinium ($^{231}_{\text{Pa}}$) and curium ($^{246}_{\text{Cm}}$) were recorded in the mass spectrum.

The initial weight of the Pd-cylinder was 0.7509 g. After irradiation, its weight decreased by 0.03245 g, which is 4.3%. The authors of [9] believe that the decrease in the weight of the Pd sample is mainly due to the formation of lead: $32450 \mu\text{g} \cdot 36\% = 11682 \mu\text{g}$ or $3.4 \cdot 10^{19}$ Pb atoms. The impurity of

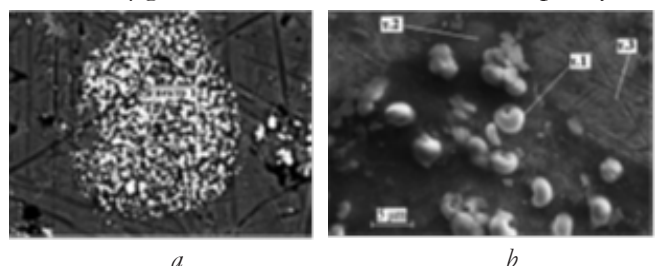


Fig. 14. SEM images: a) an elliptical formation consisting of lead microparticles; b) lead microparticles.

Table 2

Averaged concentrations of chemical elements for the microparticles and at the surface of the brass collector.

Element	C	O	Cu	Zn	Pb	%
Microparticles, 15 meas.	9.88	15.78	9.91	7.88	56.27	weight.
	34.92	41.81	6.63	5.12	11.52	atom
Brass surface, 8 meas.	14.6	6.76	43.12	27.0	8.53	weight.
	43.92	15.24	24.48	14.9	1.47	atom

Pb in the palladium sample before irradiation was < 5 ppm or < 3.7 μg. The number of γ-quanta with energy from 1 to 10 MeV at the entrance to the internal volume of the reaction chamber during the entire irradiation period is estimated as ~1.2·10¹⁷, which << 3.4·10¹⁹ Pb atoms. From this we can conclude that gamma quanta stimulate the launch of “extraneous” chemical elements.

Studies of the chemical composition of the synthesized structures on the surfaces of the brass collector (25 measurements), the entrance window (6 measurements), sleeve (17 measurements) and manganin foil (10 measurements) showed the presence of “extraneous” chemical elements in them. A feature of these measurements was the detection of a large amount of silver (Ag) in the structures and microparticles, up to 98.4% of their weight. Fig. 15 shows the concentrations of chemical elements averaged over these 58 measurements.

Fig. 16 shows the concentrations of chemical elements averaged over all 102 measurements. The following elements which were previously absent in the reaction chamber were recorded at the surfaces of the chamber, Pd cylinder, and microparticles: ₆C,

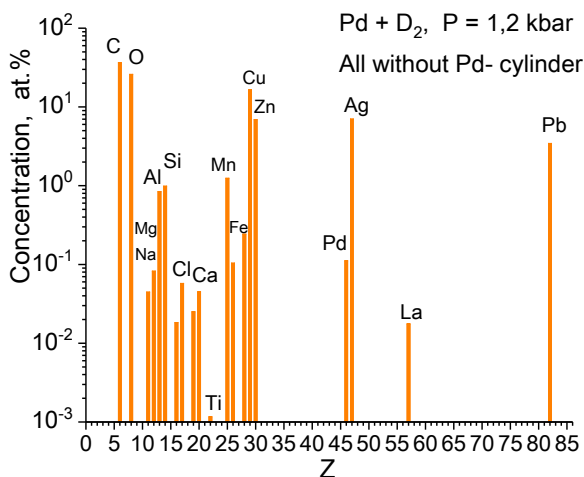


Fig. 15. The concentrations of chemical elements (58 measurements).

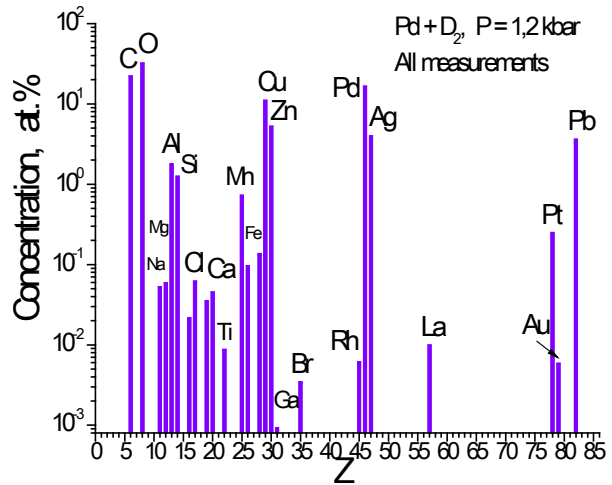


Fig. 16. The concentrations of chemical elements (102 measurements).

₈O, ₁₁Na, ₁₂Mg, ₁₃Al, ₁₄Si, ₁₆S, ₁₇Cl, ₁₉K, ₂₀Ca, ₂₂Ti, ₂₄Cr, ₂₆Fe, ₂₇Co, ₃₁Ga, ₃₅Br, ₄₅Rh, ₄₇Ag, ₇₈Pt, ₇₉Au, and ₈₂Pb.

5. THE EXPERIMENTS WITH PALLADIUM AND TIN IN HYDROGEN

In the experiment with a pressure of 2.5 kbar (H1, Tab. 1), chamber H1 was located at a distance of 5 mm from the electron absorber – 25 mm. After irradiation with gamma quanta, the chamber was irradiated for 12 minutes with electrons at a current of (1.55-2.1)·10¹³ s⁻¹. After that, the pressure in the chamber decreased by 80 bar.

In both experiments with a hydrogen pressure of 0.5 kbar (H2, Tab. 1) and 2.5 kbar after the end of the irradiation, newly formed structures were found in the reaction chambers. The side and end surfaces of the Pd-cylinders had significantly changed: they had cracks, craters and microparticles. Fig. 17 shows SEM images of the two cracks. Inside and along the edges of these formations and also, on the surfaces of the Pd-cylinders, “extraneous” chemical elements were discovered which were formed as a result of irradiation. Fig. 18 presents the averaged over 15 measurements concentrations of the synthesized chemical elements found on the Pd cylinder at

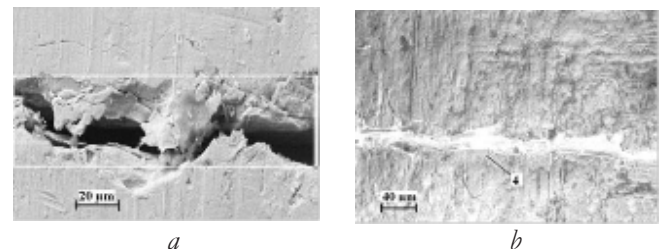


Fig. 17. a) a crack on the side surface of the Pd-rod; b) a narrow crack filled with synthesized elements.

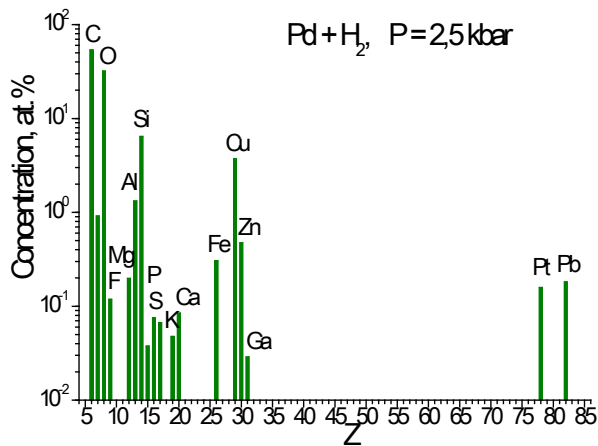


Fig. 18. The concentrations of chemical elements at the Pd-cylinder (15 measurements).

the pressure $P = 2.5$ kbar, excluding palladium. Measurements are made on the areas from 16 to $5600 \mu\text{m}^2$. Fig. 19 shows a comparison of the average element concentrations for the Pd-cylinders measured in the experiments with the hydrogen pressure 0.5 and 2.5 kbar. For the experiment performed at the pressure $P = 0.5$ kbar, the element concentrations averaged over 6 measurements of different objects made “at points” are given [17].

Fig. 20 shows a comparison of the average element concentrations measured in the microstructures found at the entrance windows, brass collectors and microparticles in the experiments with the hydrogen pressure 0.5 and 2.5 kbar. For the experiment at the pressure $P = 2.5$ kbar, the averaging was performed over 4 measurements. For the experiment performed at the pressure $P = 0.5$ kbar, the element concentrations are averaged over 15 measurements of different objects. Along with light chemical elements from carbon ${}_6\text{C}$ to zinc ${}_{30}\text{Zn}$,

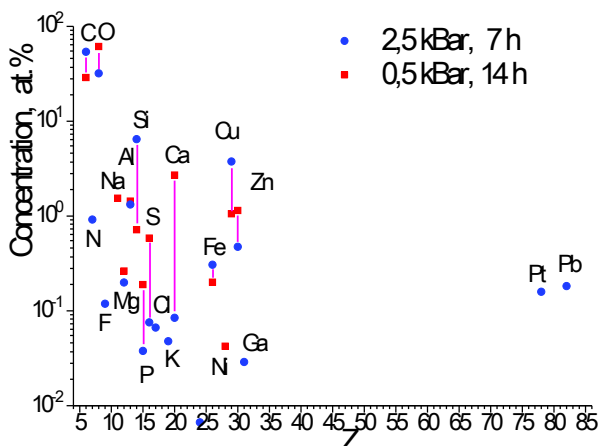


Fig. 19. A comparison of the concentrations of chemical elements at the Pd-cylinder.

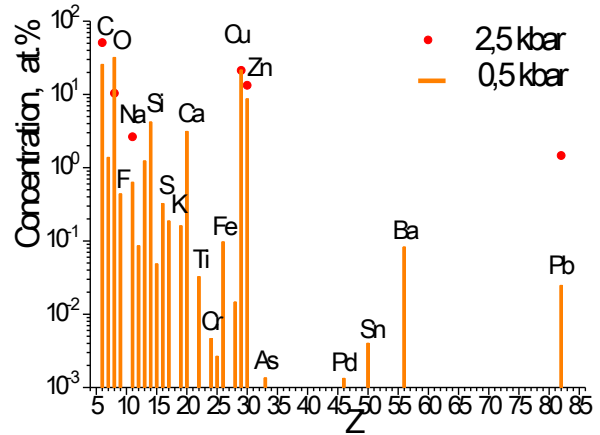


Fig. 20. A comparison of concentrations of chemical elements for microscopy.

in the experiment with $P = 0.5$ kbar, arsenic (${}_{33}\text{As}$), tin (${}_{50}\text{Sn}$), barium (${}_{56}\text{Ba}$), and lead (${}_{82}\text{Pb}$), were found.

Measurement of one of the synthesized structures over the area $35 \times 28 \mu\text{m}^2$ was done by an electron beam along an $\sim 2 \mu\text{m}$ strip through its center from one edge to another. Based on the many x-ray spectra obtained, the concentration distribution of chemical elements along the strip was determined in [18]. In this study, along with such elements as barium and lead, the x-ray spectra processing program found lines corresponding to protactinium (${}_{91}\text{Pa}$). The two Pa peaks are clearly visible in Fig. 21 on the right. Protactinium (${}^{231}\text{Pa}$) is a radioactive element, usually resulting from the alpha decay of the (${}^{235}\text{U}$) uranium isotope. ${}^{235}\text{U}$ has a half-life of $7 \cdot 10^8$ years and an isotopic content of 0.72%. If protactinium were a daughter product of alpha decay of ${}^{235}\text{U}$, then we would have to observe in the set of x-ray spectra of the uranium line and, most likely, thorium (${}^{230}\text{Th}$), as a result of alpha decay of ${}^{234}\text{U}$. Since such lines were not recorded in the spectra, it is very likely that protactinium was synthesized independently.

Fig. 22 shows the total averaged over 40 measurements element concentrations found at the palladium cylinder (19 measurements) and at the microstructures (21 measurements).

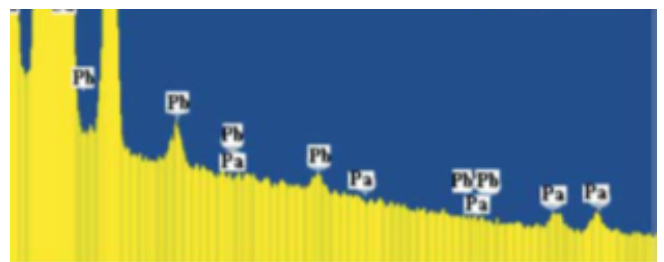


Fig. 21. The total x-ray spectrum after scanning.

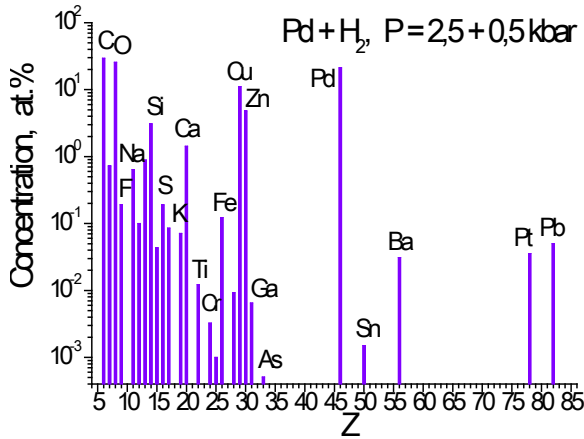


Fig. 22. The concentrations of chemical elements (40 measurements).

For comparison, Fig. 23 presents concentrations of chemical elements averaged over 35 measurements and obtained in two experiments with pure hydrogen (H₂) at the pressure 1 and 3.4 kbar [39]. Irradiation was carried out for 14 and 62 hours, respectively, at the electron current (1.2-1.5)·10¹⁴ s⁻¹. The electron beam energy was 10 MeV.

For completeness, we present here the results of an experiment on the irradiation of tin (⁵⁰Sn) with gamma quanta in condensed hydrogen [19–21]. A sample of natural Sn with a purity of 99.9% was a cylinder with a diameter of 9.5 mm, a length of 17 mm, and a weight of 8.5731 g. On both sides, the cylinder was fixed with two collectors made of beryllium bronze. The inner chamber, the sleeve for the reaction products and the entrance window were also made of beryllium bronze. The initial hydrogen pressure inside the reaction chamber was 3.5 kbar. At this pressure, the mass density of hydrogen was 0.0868 g·cm⁻³, and the atomic density of hydrogen was 5.186·10²² at·H·cm⁻³. The irradiation energy of

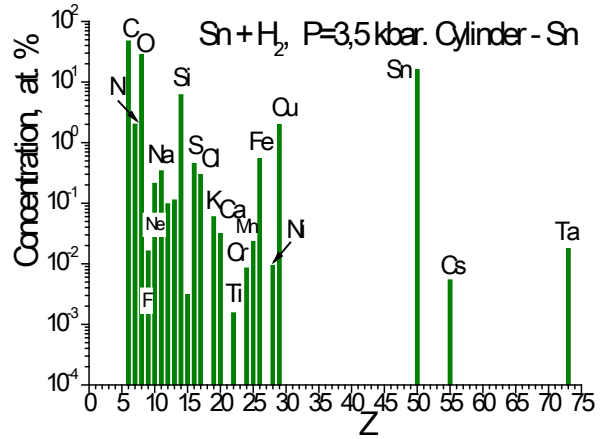


Fig. 24. The concentrations of chemical elements at the Sn-cylinder (13 measurements).

electrons was E = 10 MeV, and the current was varied within (1.3–1.5)·10¹⁴ s⁻¹. Irradiation was carried out for 2.51·10⁵ s (~70 h). The hydrogen pressure in the chamber after irradiation was 3.0 kbar. After opening the chamber, 30 black particles fell out of it. All surfaces of the parts of the reaction chamber, which had contact with hydrogen, and a significant part of the synthesized particles were investigated by SEM and XRMPA.

Fig. 24 shows the element concentrations averaged over 13 measurements of the synthesized structures found at the surface of the tin cylinder. For comparison, Fig. 25 presents the concentrations of chemical elements found at the sleeve, input window, collector, and the particles. For the sleeve, averaging was carried out over 13 measurements, for the input window – over 7 measurements, for the collector – over 9 measurements, and for the particles – over 21 measurements. Fig. 26 shows the concentrations of chemical elements averaged

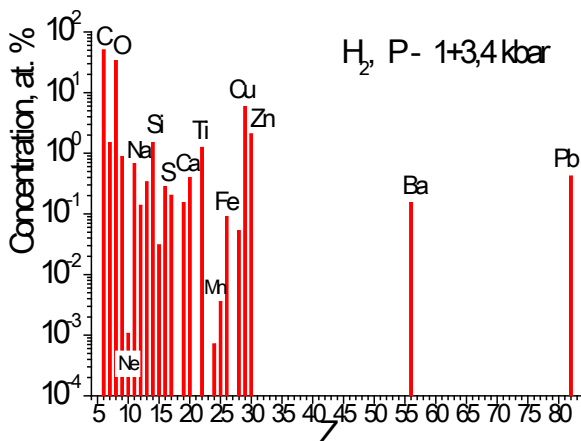


Fig. 23. The element concentrations for two experiments with H₂ (35 measurements).

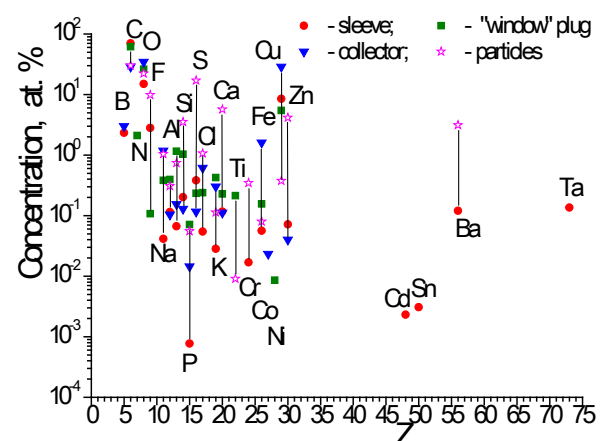


Fig. 25. A comparison of the element concentrations found at the sleeve, “window” plug, collector and the particles.

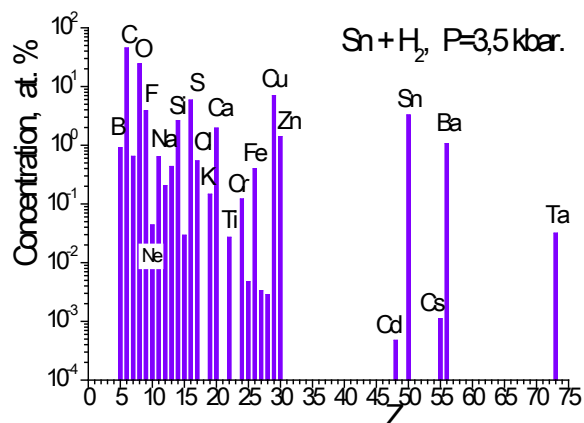


Fig. 26. The concentrations of chemical elements (63 measurements).

over all 63 measurements of synthesized solid-state structures.

6. THE EXPERIMENT WITH PALLADIUM IN HELIUM

The latest experiment in the series was the experiment with a palladium cylinder placed in condensed helium (He, Tab. 1) [22–23]. The chamber was filled with helium to a pressure of 2.4 kbar. The irradiation was carried out using a tungsten convector with the thickness 1 mm and an Al-absorber with the thickness 25 mm. The exposure time was 96 hours. In the process of irradiation, the pressure in the chamber did not fall, and even grew somewhat. When the chamber was opened after irradiation, 13 dark-colored particles up to 1 mm fell out of it. The entrance window, made of beryllium bronze, was covered with a thick visible layer of green-and-yellow color. The thread of the entrance window was filled with small particles - balls of about 2 microns in size (Fig. 27). Fig. 28 shows the element concentrations in these balls, averaged over 4 measurements. Dark spots were found at the entire lateral surface of the palladium cylinder. Fig. 29 shows SEM images of these spots. Fig. 30 indicates the element concentrations at

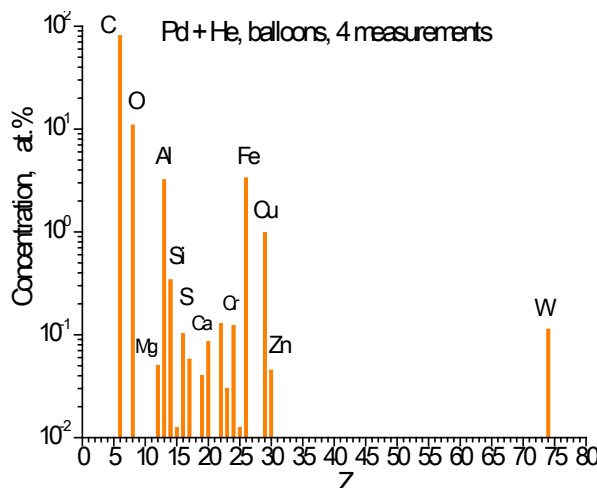


Fig. 28. The concentrations of chemical elements for the balloons.

these spots, averaged over 5 measurements. At these spots, besides carbon and oxygen, a high content of nitrogen, iron, and zinc was found. The total, averaged over 15 measurements concentrations of chemical elements at the surfaces of the palladium cylinder are presented in Fig. 31.

Studies of the chemical compositions of the synthesized structures on the surfaces of the entrance window (21 measurements), copper collector (3 measurements) and copper sleeve (16 measurements), as well as microparticles (13 measurements), showed the presence of “extraneous” chemical elements in them. Fig. 32 shows the total, averaged over 53 measurements concentrations of chemical elements for these chamber parts. A feature of this experiment with helium is the registration at the sleeve and at the particles of inert gases: neon and argon.

Fig. 33 shows the averaged over 68 measurements, including the surface of the Pd cylinder, concentrations of chemical elements measured in the experiment with helium. For comparison, Fig. 34 shows the concentrations of chemical elements averaged over 28 measurements and obtained in two experiments with pure helium at the pressure 1.1

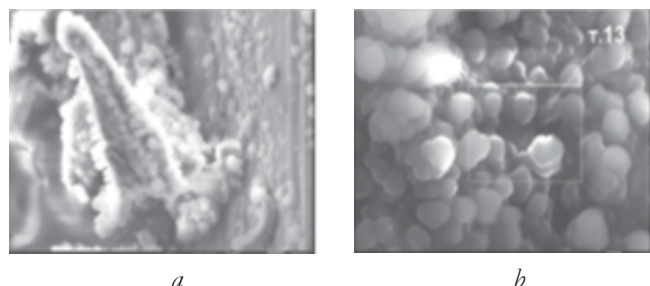


Fig. 27. The images showing structures in the threaded grooves: a) (65 μm); b) (14 μm).

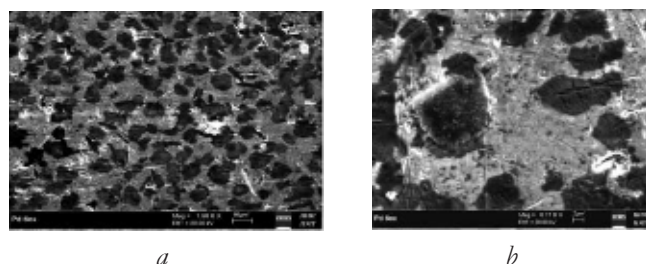


Fig. 29. A SEM image of the side surface of the Pd cylinder littered with black spots: a) (150 μm); b) (50 μm).

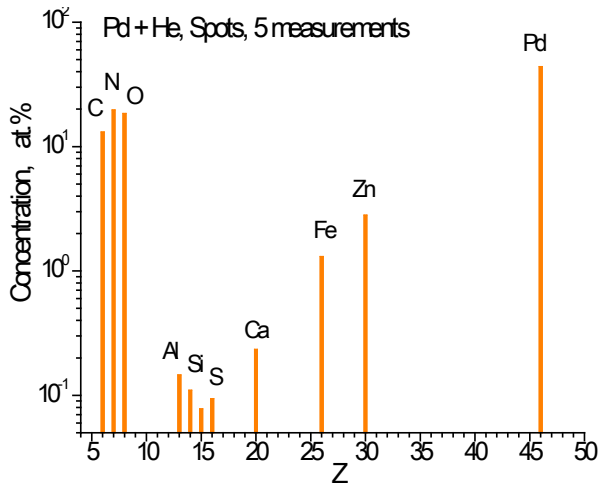


Fig. 30. The concentrations of chemical elements for the black spots.

and 3.05 kbar [39]. Irradiation was carried out for 28 hours each experiment, and the electron current was $(1.0-1.5) \cdot 10^{14} \text{s}^{-1}$. The electron beam energy was 10 MeV.

To complete the picture in Fig. 35, we present the general result on the irradiation by braking gamma quanta during 43 to 72 hours at the maximum energy 10 MeV in condensed xenon ($_{54}\text{Xe}$) in three experiments [32–37, 39]. The figure shows the concentrations of the synthesized chemical elements averaged in these experiments at xenon pressures of 250, 270 and 550 bar. Averaging was performed for 289 measurements. It should be especially noted that due to the xenon irradiation, such radioactive elements as technetium ($_{43}\text{Tc}$) and actinium ($_{89}\text{Ac}$) (francium ($_{87}\text{Fr}$) is the daughter product of actinium) were synthesized. Their appearance can be explained neither by pollution nor by secondary processes. It should also be noted that as a result of long-term

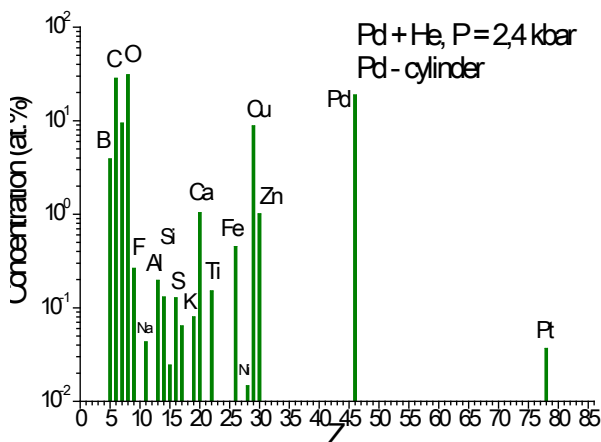


Fig. 31. The concentrations of chemical elements (15 measurements).

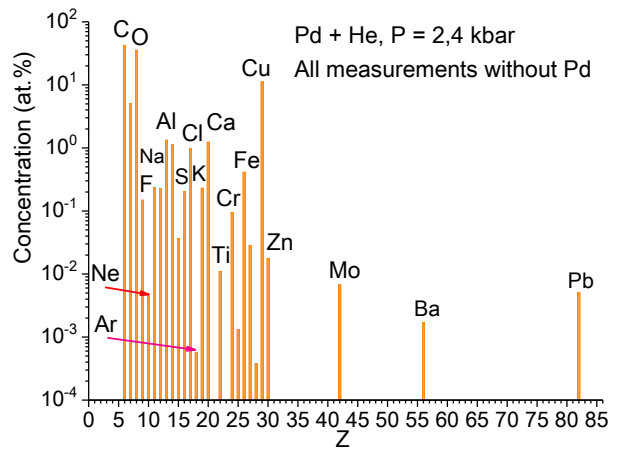


Fig. 32. The concentrations of chemical elements (53 measurements).

exposure to the braking gamma quanta of condensed xenon, “almost all elements” of the Periodic Table were synthesized here.

7. DISCUSSION OF THE EXPERIMENTAL RESULTS

First of all, it should be emphasized that, despite the striking results obtained in our numerous experiments and the interest of the scientific community, they were not reproduced at other scientific centers. Therefore, we are forced to compare the results of different experiments on the basis of our experimental data solely.

1. In all experiments with condensed gases, without exception, after the end of the irradiation, newly formed objects were found in the reaction chambers: microparticles ranging in size from 0.5 μm to 1 mm and anomalous solid-state structures at the parts of the reaction chambers and at the surface of the palladium. Since the

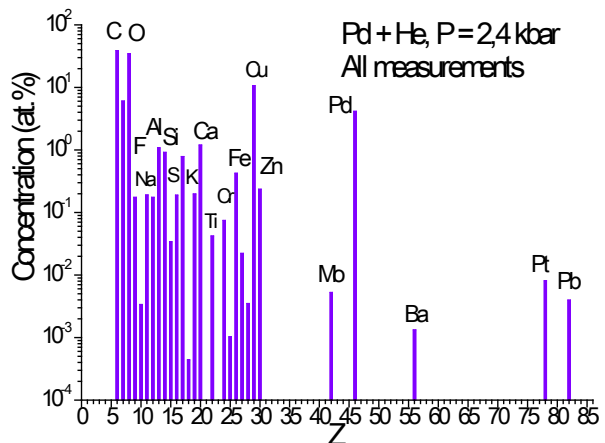


Fig. 33. The concentrations of chemical elements (68 measurements).

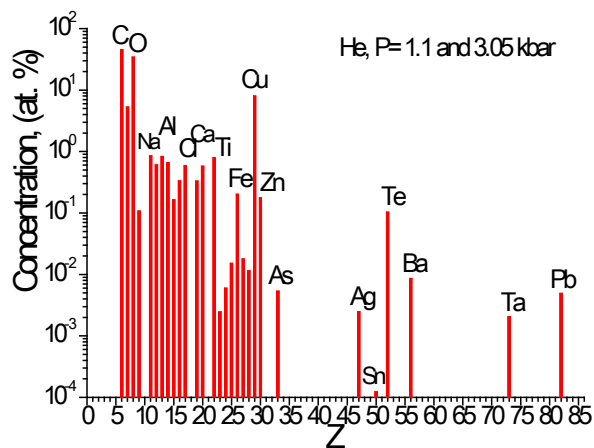


Fig. 34. The concentrations of elements for two experiments with He (28 measurements).

structures formed contain a large number of “extraneous” chemical elements, it should be assumed that the structures and chemical elements were synthesized at the surfaces of the palladium cylinders and at the surfaces of the parts of the reaction chamber.

2. Studies performed by scanning electron microscopy, found significant changes in the surfaces of the irradiated Pd-cylinders. Smooth surfaces of the Pd-cylinders were transformed into inhomogeneous surfaces consisting of separate clusters with lots of cracks and spots. We interpret irregularities, cracks and ruptures which appear at the surface of the Pd-cylinders as radiation damage and microexplosions of the near-surface layer produced by nuclear reactions.
3. Measurements carried out using x-ray microprobe analysis showed that the surfaces of the Pd-cylinders, solid structures and microparticles contain chemical elements which were absent

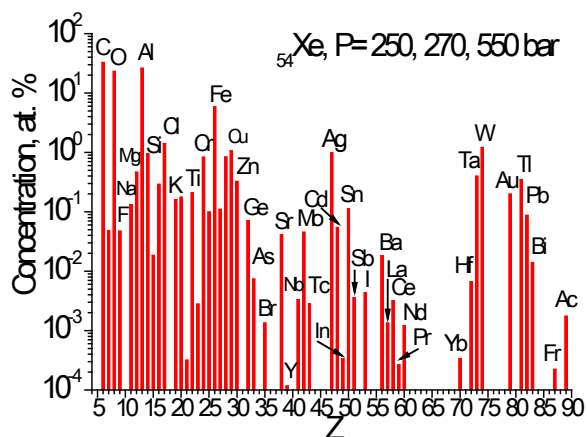


Fig. 35. The concentrations of chemical elements for three experiments with Xe (289 measurements).

in appreciable quantities in the volumes of the reaction chambers before they were irradiated.

4. The range of the synthesized elements extends from carbon to lead. A characteristic feature for all of the obtained concentrations of chemical elements is the constant presence of the group with practically all light elements having the nuclear charge $6 \leq Z \leq 30$, from carbon to zinc. The maximum yield in the reactions is as follows: carbon and oxygen. Light elements up to carbon (in some cases, boron) are not recorded by x-ray microprobe analysis.
5. In addition to the group of light elements in the reaction products, there are always representatives from the group of elements with nuclear charge Z from 30 to 70 and there are representatives from the group of heavy elements with Z greater than 70. Almost always lead is present in the set of synthesized elements.
6. Taking into account the entire set of data obtained by the XRMPA method, it can be argued that in each individual experiment on the irradiation of gamma-quanta of palladium in condensed gases there is no significant difference in the distribution of chemical elements for the parts of the reaction chamber: the input window, sleeve, collector, manganin foil, and particles.
7. The most impressive experiments are the experiments with irradiation of palladium in a condensed deuterium atmosphere. In these experiments such elements as titanium ($_{22}\text{Ti}$), silver ($_{47}\text{Ag}$) and lead ($_{82}\text{Pb}$), were synthesized in macroquantity. The isotopic composition of lead in the range of measurement errors corresponds to the natural ratio of isotopes.
8. In the experiment with condensed helium such inert gases as neon and argon were recorded at the sleeve and at the particles. These elements do not form chemical compounds, so they could be synthesized and stored only inside and in the surface layers of the sleeves and particles.
9. In the experiments with condensed hydrogen and deuterium, radioactive elements were registered: protactinium ($_{91}\text{Pa}$) and, possibly, curium ($_{96}\text{Cm}$) [42]. With a high degree of probability, these chemical elements were synthesized directly as a result of nuclear reactions.
10. The distributions of the synthesized chemical elements in the experiments with palladium

and tin in condensed hydrogen differ little in character from each other (Fig. 22 and Fig. 26).

11. The distributions of synthesized chemical elements in the experiments on the irradiation of high-pressure chambers filled by condensed gases, with and without palladium, have a similar character [39].

A trivial explanation for the appearance of all “extraneous” chemical elements registered in experiments is their uncontrolled introduction into the internal volume of the reaction chambers during the process of filling the chambers with condensed gases. However, in addition to the fact that special measures were taken to eliminate the importation of “extraneous” chemical elements, special, “background” experiments were carried out to test this assumption: a) after several procedures for filling the reaction chamber with deuterium and evacuating it, the chamber was opened without irradiation; b) in the following experiment, the Pd-sample was held in the chamber for 10^5 s without irradiation at a deuterium pressure of 20 kbar; c) separately, irradiation was carried out at an electron energy of 10 MeV for an empty chamber with all internal sleeves and collectors. The chamber between the exposures was constantly pumped out to the pressure 10^{-4} Pa. The exposure time was $2 \cdot 10^5$ s, for the average electron beam current $1.2 \cdot 10^{14}$ s $^{-1}$; d) in another experiment, a chamber filled with deuterium at the pressure 60 bar with a palladium cylinder of $\varnothing 4.9 \times 8$ mm 3 in size was irradiated for $1.3 \cdot 10^5$ s, with an average electron beam current of $1.1 \cdot 10^{14}$ s $^{-1}$. Palladium was 99.997% pure. This experiment was aimed at the synthesis of chemical elements under reduced pressure of deuterium, which is compared to other experiments where the pressure of deuterium was 1.2 and 3 kbar [1-3, 7-10]. In all cases, the studies of the internal sleeves, collectors and the surface of the palladium cylinder made by SEM and XRMPS showed the absence of new synthesized structures and different elemental compositions in them.

Consequently, the appearance of “extraneous” elements in the internal volume of the reaction chambers, with a high degree of probability, is determined by non-nuclear interaction of gamma radiation in the atmosphere of condensed gases and with metal atoms surrounding the gas [43]. The interaction of gamma quanta with a substance is characterized

by: the photoelectric effect, the Compton effect, and the production of electron-positron pairs. All three effects lead to the formation of electrons and positrons with the energies < 10 MeV which ionize the gas atoms and atoms of the materials surrounding the gas. Thus, a dense plasma with a high electron temperature is created in the irradiated volume. Consequently, the production of “extraneous” elements in the chamber is associated with the creation in its volume of a non-equilibrium dense plasma.

There are two nontrivial possibilities for the appearance of chemical elements. One of them is connected with the hypothesis of “plasma diffusion” of already existing impurity elements from the depth of materials surrounding the gas to the interface between two media: solid state and gas. In this case, the density of atoms in the gas must be comparable with the density of the solid. The second possibility is associated with the hypothesis of the emergence in dense plasma of conditions for the multinuclear fusion of several atomic nuclei into a common compound with its subsequent multinuclear fission into other fragment nuclei [43], i.e. implementation of low-energy nuclear reactions.

Indeed, strictly speaking, trace amounts of practically all elements, including radioactive elements, can be found in all metal alloys. Therefore, if there were a mechanism of “plasma diffusion” of impurity chemical elements from the depth of materials onto their surface with the obligatory presence of condensed gases, then this could somehow explain the appearance of “extraneous” elements, though in nano- and micro-quantities. But such a mechanism is unknown.

The introduction stated that one of the motivations in the formulation of the experiments discussed here was the implementation of cold fusion reactions for a palladium-deuterium pair. It is noteworthy that the most impressive experiments are experiments, just with the irradiation of palladium in a condensed deuterium atmosphere. In these experiments, such chemical elements as titanium, silver and lead were synthesized in macroquantities. From scientific literature it is known that cold nuclear fusion reactions are accompanied by transmutation reactions – the transformation of some chemical elements into others. Consequently, in our experiments with a palladium-deuterium

pair, gamma-stimulated reactions of the cold fusion produce the energy necessary for transmutation reactions. In the experiments using other gases: hydrogen and helium, and in the experiments with pure gases, transmutation reactions occur directly. As was already mentioned, the intensity of cold fusion reactions increases with increasing number of deuterium atoms per palladium atom. "It is curious that nanoclusters of 6-7 nm size are formed near the metal surfaces, simply as a result of heating the sample to a temperature of 300-400°C! Such nanoclusters levitate over a metal surface [44]! If cold fusion reactions occur in the volume of nanoclusters formed by any method, then due to the bombardment of metal surface by the reaction products, the metal surface is locally heated, and both additional local defects and new nanoclusters are produced on this surface. The "hot" defects and nanoclusters which emerge can become centers for the formation of solid structures and for the synthesis of "extraneous" chemical elements in low-energy nuclear transmutation reactions." [45, c. 128]. It seems that we register such processes in our experiments.

8. CONCLUSION

This article provides an overview of eight years of experimental work on the synthesis of chemical elements from the gas phase of deuterium, hydrogen and helium in the presence of metallic palladium during long-term γ -irradiation of gases under high pressure. Numerous data have been obtained on the synthesis of for a wide range of chemical elements from carbon to lead. Preliminary hypotheses are proposed for the synthesis of chemical elements under the experimental conditions.

Based on the assumptions made, it is necessary to conduct new experiments that can confirm or disprove both the results obtained and the indicated hypotheses.

REFERENCES

1. Didyk AYu, Wiśniewski R. Nuclear reactions, induced by gamma quanta, in palladium saturated with deuterium surrounded by dense deuterium gas. *Eur. Phys. Lett.*, 2012, 99:P.22001-P1-22001-P6.
2. Didyk AYu, Wiśniewski R. Chemical Composition and Structural Phase Changes of Novel Synthesized Structure and of Pd Sample under γ -Quanta Irradiation in Dense Deuterium Gas. *Phys. Part. Nucl. Lett.*, 2012, 9(8):615-631.

3. Didyk AYu, Wiśniewski R. Sintezy nowych struktur w gęstym gazowym deuterium i nasyczonego deuterium palladiu przy jądrowych reakcjach, inicjowanych γ -kwantami [Synthesis of new structures in dense gaseous deuterium and in deuterium-saturated palladium during nuclear reactions initiated by γ -quanta]. *Physics and chemistry of materials processing*, 2012, 5:5-13 (in Russ.).
4. Belov AG. Microtron MT-25. *Workshop on the use of microtrons in nuclear physics*. Plovdiv. September 22-24.1992. Δ 15-93-80, pp.12-19. Dubna, 1993.
5. Fleishmann M, Pons S, Hawkins M. Electrochemically induced nuclear fusion of deuterium. *J. Electroanal. Chem.* 1989, 261:301-308.
6. Arata Y, Zhang Y-C. Characteristics of Compact and Practical "Solid Deuterium Nuclear Fusion Reactor". *Proc. 10th Intern. Conference on Cold Fusion*, 2003, Cambridge, Massachusetts, USA.
7. Didyk AYu, Wiśniewski R, Wilczynska-Kitowska T, Shilov VM. Changes in the Chemical Composition of Nuclear Reaction Products Irradiated with 10 MeV γ -Quanta in Deuterium Saturated Palladium. (1.2kbar). *J. Surface Investigation. X-ray, Synchrotron and Neutron Techniques*, 2014, 8(6):1100-1112.
8. Didyk AYu, Wiśniewski R. Nuclear reactions in deuterium-saturated palladium under irradiation by 10 MeV γ -quanta in dense molecular deuterium at 1.2 kbar pressure. *Eur. Phys. Lett.*, 2013, 103:42002-P1-42002-P6.
9. Didyk AYu, Wiśniewski R, Wilczynska-Kitowska T. Changes of surface structure and elemental composition of Pd rod and collector of nuclear reaction products irradiated with 10-MeV γ -quanta in dense deuterium gas. *Phys. Part. Nucl. Lett.*, 2013, 10(7):804-819.
10. Didyk AYu, Wiśniewski R, Wilczynska-Kitowska T. Changes of surface structure and elemental composition of components of deuterium high-pressure chamber with Pd rod inside irradiated with 10-MeV γ -quanta in dense deuterium gas. *Phys. Part. Nucl. Lett.*, 2013, 10(7):820-832.
11. Didyk AYu, Wiśniewski R. Nuclear reactions in deuterated palladium and rhenium irradiated by γ quanta with a continuous spectrum at a threshold energy of 23 MeV in dense deuterium gas. *Phys. Part. Nucl. Lett.*, 2013, 10(4):381-392.

12. Didyk AYu, Wiśniewski R. The Study of Changes in the Element Compositions of Pd and Re Specimens Irradiated in Dense Gaseous Deuterium by γ -Quanta with Boundary Energy up to 23 MeV. *Journal of Physical Science and Application*, 2013, 3(4):209-217.
13. Didyk AYu, Wiśniewski R. Izmeneniya poverkhnosti, ob'emnykh svoystv obraztsov vanadiya i nerzhavayushchey stali, obluchennykh v plotnom gazoobraznom deyterii γ -kvantamy s porogovoy energiy 23 MeV [Changes observed in the surfaces, bulk properties and chemical composition of vanadium and stainless steel specimens irradiated in dense gaseous deuterium by γ -quanta of threshold energy 23 MeV]. *Preprint JINR P15-2012-75*, Dubna, 2012, 15 p (in Russ.).
14. Didyk AYu, Wiśniewski R. Results of irradiation of aluminum and a homogeneous alloy $Y\text{Mn}_2$ γ -quanta with energy of 23 MeV in the atmosphere of molecular deuterium at a pressure of 2 kbar. *Phys. Part. Nucl. Lett.*, 2014, 11, 2:169-179.
15. Didyk AYu, Wiśniewski R. Results from the irradiation of stainless steel and copper by 23 MeV γ -quanta in the atmosphere of molecular deuterium at a pressure of 2 kbar. *Particles and Nuclei Letters*, 2014, 11(3):309-328.
16. Didyk AYu, Wiśniewski R. Structure and chemical composition changes of Pd rod and reaction product collector irradiated by 10 MeV braking gamma quanta inside high pressure chamber filled with 2.5 kbar molecular hydrogen. *Phys. Part. Nucl. Lett.*, 2014, 11(4):513-527.
17. Didyk AYu, Wiśniewski R. Synthesis of new structures on the surface of Pd rod and HHPC elements and their chemical composition in nuclear reactions induced by bremsstrahlung γ quanta with threshold energy of 10 MeV in molecular hydrogen at a pressure of 0.5 kbar. *Phys. Part. Nucl. Lett.*, 2015, 12(4):603-617.
18. Didyk AYu, Wiśniewski R. Chemical composition and structure of particles synthesized on the surface of HHPC in nuclear reactions induced by bremsstrahlung γ quanta with threshold energy of 10 MeV in molecular hydrogen at a pressure of 0.5 kbar. *Phys. Part. Nucl. Lett.*, 2015, 12(7):836-849.
19. Didyk AYu, Wiśniewski R. Yadernye reaktsii s sintezom mikrochastits v vodorode pri davlenii 3.5 kbar v prisutstvii olova pri obluchenii tormoznymi γ -kvantami s porogovoy energiy 10 MeV [Nuclear reactions with synthesis of microparticles in hydrogen at a pressure of 3.5 kbar in the presence of Tin under irradiation by braking γ -quanta with a threshold energy of 10 MeV]. *Preprint JINR P15-2014-89*, Dubna, 2014, 26 p (in Russ.).
20. Didyk AYu, Wiśniewski R. Yadernye reaktsii s sintezom mikrochastits v HHPC pri davlenii 3.5 kbar vodoroda s tsilindrom iz olova pod deystviem oblucheniya tormoznymi γ -kvantami s porogovoy energiy 10 MeV [Nuclear reactions with synthesis of structures in HHPC with hydrogen at a pressure of 3.5 kbar and a Tin rod under irradiation of braking γ -rays with a threshold energy of 10 MeV]. *Preprint JINR P15-2014-88*, Dubna, 2014, 43 p (in Russ.).
21. Didyk AYu, Wiśniewski R, Wilczynska-Kitowska T, Ishakova LD. Sintez mikrochastits v plotnom vodorode pri davlenii 3.5 kbar s olovyannym sterzhnem pod deystviem tormoznykh γ -kvantov s porogovoy energiy 10 MeV [Synthesis of microparticles in dense hydrogen at a pressure of 3.5 kbar with a Tin rod under irradiation with braking γ -rays of a threshold energy of 10 MeV]. *Preprint JINR P15-2014-104*, Dubna, 2014, 23 p (in Russ.).
22. Didyk AYu, Wiśniewski R, Semin VA. Sintez mikrochastits v gelii pri davlenii 2.4 kbar s palladiem pri obluchenii tormoznymi γ -kvantami s maksimalnoy energiy 10 MeV (chast' 1) [The synthesis of microparticles in helium at a pressure of 2.4 kbar with a palladium rod inside HeHPC under Irradiation by braking γ -rays with a maximum energy of 10 MeV. (part 1)]. *Preprint JINR P15-2015-33*, Dubna, 2015, 37 p (in Russ.).
23. Didyk AYu, Wiśniewski R, Semin VA. Issledovanie protsessov obrazovaniya novykh struktur i elementov v gelii pri davlenii 2.4 kbar s palladiem pri vozdeystvii tormoznykh γ -kvantov s maksimalnoy energiy 10 MeV (chast' 2) [A study of the formation of new structures and elements in HeHPC with palladium inside at a pressure of 2.4 kbar under the influence of braking γ -rays with a maximum energy of 10 MeV (part 2)].

- Preprint JINR P15-2015-34*, Dubna, 2015, 34 p (in Russ.).
24. Didyk AYu, Wiśniewski R. Synthesis of microobjects in 1 kbar hydrogen induced by 10 MeV bremsstrahlung γ quanta on inner surfaces of components of a high pressure chamber (Part 1). *Phys. Part. Nucl. Lett.*, 2015, 12(1):125-144.
 25. Didyk AYu, Wiśniewski R. Synthesis of microparticles in 1kbar hydrogen induced by 10MeV bremsstrahlung γ quanta in a reaction chamber (Part 2). *Phys. Part. Nucl. Lett.*, 2015, 12(1):145-165.
 26. Didyk AYu, Wiśniewski R. Sintez novykh struktur, obrazovannykh v rezul'tate yadernykh reaktsiy v HHPC s davleniem vodoroda 3.4 kbar pri obluchenii tormoznymi γ -kvantami s porogovoy energiy 10 MeV [New structures synthesized by nuclear reactions in HHPC with a hydrogen pressure of 3.4 kbar under irradiation by braking γ -rays with a threshold energy of 10 MeV]. *Preprint JINR P15-2015-79*, Dubna, 2015, 27 p (in Russ.).
 27. Didyk AYu, Wiśniewski R, Mishinsky GV, Semin VA, Wilczynska-Kitowska T. Sintez tverdotelnukh struktur i khimicheskikh elementov pri obluchenii tormoznymi γ -kvantami s $E_{\max} = 10$ MeV kondensirovannogo deyteriya davleniem 2.2 kbar [Synthesis of solid-state structures and chemical elements under irradiation by bremsstrahlung γ rays with a maximum energy of 10 MeV in condensed deuterium at a pressure of 2.2 kbar]. *Preprint JINR P15-2018-3*, Dubna, 2018, 27 p (in Russ.).
 28. Didyk AYu, Wiśniewski R., Wilczynska-Kitowska T. The carbon-based structures synthesized through nuclear reactions in helium at 1.1 kbar pressure under irradiation with braking γ -rays of 10 MeV threshold energy. *Eur. Phys. Lett.*, 2015, 109:22001-P.1-22001-P.6.
 29. Didyk AYu, Wiśniewski R. Properties of carbon-based structures synthesized in nuclear reactions induced by bremsstrahlung γ quanta with threshold energy of 10 MeV at helium pressure of 1.1 kbar. *Phys. Part. Nucl. Lett.*, 2016, 13(4):492-503.
 30. Didyk AYu, Wiśniewski R. Yadernye reaktsii, sintez khimicheskikh elementov i novykh struktur v plotnom gelii pri davlenii 1.1 kbar pod deystviem oblucheniya tormoznymi γ -kvantami s porogovoy energiy 10 MeV [Nuclear reactions, synthesis of chemical elements and new structures in dense helium at 1.1 kbar pressure under irradiation with braking γ -quanta with a threshold energy of 10 MeV]. *Preprint JINR P15-2014-50*, Dubna, 2014, 40 p (in Russ.).
 31. Didyk AYu, Wiśniewski R. Sintez novykh struktur i obrazovanie khimicheskikh elementov v plotnom gelii pri davlenii 3.05 kbar pri obluchenii tormoznymi γ -kvantami s porogovoy energiy 10 MeV [Synthesis of new structures and formation of chemical elements in dense helium at a pressure of 3.05 kbar under irradiation of braking γ -rays with a threshold energy of 10 MeV]. *Preprint JINR P15-2014-87*, Dubna, 2014, 23 p (in Russ.).
 32. Didyk AYu, Gulbekian GG, Mishinsky GV. SEM i RMPA-issledovaniya sintezirovannykh chastits i ob'ektov pri obluchenii plotnogo ksenona (270 atm) tormoznymi γ -kvantami s maksimalnoy energiy 10 MeV [SEM and RMPA research of synthesized particles and objects in dense xenon (270 bar) irradiated by braking γ -rays with a maximum energy of 10 MeV]. *Preprint JINR P15-2015-71*, Dubna, 2015, 38 p (in Russ.).
 33. Didyk AYu, Gulbekian GG, Mishinsky GV. Issledovanie izmeneniy elementnogo sostava i struktury poverkhnostey pri obluchenii plotnogo ksenona (270 atm) tormoznymi γ -kvantami s maksimalnoy energiy 10 MeV [A study of the element composition and surface structure changes during irradiation of dense xenon (270 atm) by braking γ -rays with a maximum energy of 10 MeV]. *Preprint JINR P15-2015-72*, Dubna, 2015, 32 p (in Russ.).
 34. Didyk AYu, Gulbekian GG, Mishinsky GV. Anomalii na vnutrennikh poverkhnostyakh kamery vysokogo davleniya ksenona XeHPC (250 bar) s obrazovaniem mikrochastits slozhnogo sostava pri obluchenii tormoznym izlucheniem s porogovoy energiy 10 MeV [Anomalies on the inner surfaces of the xenon high-pressure chamber XeHPC (250 Bar) with the synthesis of microparticles of complex composition under irradiation with bremsstrahlung threshold energy of 10 MeV]. *Preprint JINR P15-2016-1*, Dubna, 2016, 47 p (in Russ.).
 35. Didyk AYu, Gulbekian HS, Mishinsky GV, Sabelnikov AV. Sintez mikrochastits slozhnogo

- coctava v kamere vysokogo davleniya ksenona (550 bar) pti obluchenii tormoznym izlucheniem s maksimal'noy energiyey 10 MeV [The synthesis of micro particles of complex composition in the chamber high-pressure xenon (550 bar) when irradiated by bremsstrahlung with maximum energy of 10 MeV]. *Preprint JINR P15-2016-19*, Dubna, 2016, 49 p (in Russ.).
36. Didyk AYu, Gulbekian GG, Mishinsky GV, Wiśniewski R. A study of changes of the element composition and structure of surfaces under irradiation of dense xenon gas (270 bar) by γ -rays with maximum energy of 10 MeV. *JPSA*, 2016, 6(2):18-28.
37. Didyk AYu. Yadernye reaktsii sinteza i deleniya khimicheskikh elementov i obrazovaniye novykh struktur v plotnykh gazakh H_2 , D_2 i He pri obluchenii 10 MeV γ -kvantami [Nuclear reactions of fusion and fission chemical elements and the formation of new structures in dense gases H_2 , D_2 and He at irradiation 10 MeV-tion of γ -quanta]. *Physics and chemistry of materials processing*, 2015, 2:5-19.
38. Wiśniewski R, Didyk AYu. Synthesis of New Structures and Substances in Dense Gases H_2 , D_2 and He under Irradiation by Braking 10MeV γ -rays in CuBe2 Pressure Chamber. *JPSA*, 2016, 6(4):13-21.
39. Wiśniewski R, Mishinsky GV, Gulbekian GG, Wilczyńska-Kitowska T, Semin VA. Sintez khimicheskikh elementov i tverdotelnukh struktur pri obluchenii γ -kvantami kondensirovannykh gazov [Synthesis of chemical elements and solid-state structures under irradiation by γ -quanta in condensed gases]. *Zhurnal Formiruyushchekhsya Napravleniy Nauki (ZhFNN)*, 2017, 17-18(5):6-15 (in Russ.). <http://www.unconv-science.org/>.
40. Berger MJ, Seltzer SM. Bremsstrahlung and Photoneutrons from Thick Tungsten and Tantalum Targets. *Phys. Rev. C*, 1970, 2(2):621-631.
41. Kondev Ph, Tonchev A, Khristov Kh, Zhuchko V. The calculated bremsstrahlung spectrum. *Nucl. Instr. Meth. B71*, 1992, 126.
42. Didyk AYu, Konarsky P, Sabelnikov AV, Wiśniewski R. Obrazovanie Pa i Cm pri oblychenii palladiyevogo sterzhnya v DHPC, zapolnennoy molekulyarnym deyteriem pri davlenii 1.2 kbar, tormoznym izlucheniem s maksimalnoy energiyey 10 MeV [Pa and Cm production under irradiation of palladium rod in the molecular deuterium at a pressure of 1.2 kbar by braking radiation with a 10 MeV maximum energy]. *Preprint JINR P15-2015-78*, Dubna, 2018, 39 p (in Russ.).
43. Mishinsky GV, Kuznetsov VD, Penkov FM. K voprosu o mekhanizme sinteza khimicheskikh elementov pri obluchenii kondensirovannykh gazov tormoznymi gamma-kvantami [To the question of mechanism of synthesis of chemical elements at irradiation of condensed gases by bremsstrahlung gamma quanta]. *ZhFNN*, 2017, 17-18(5):45-57 (in Russ.).
44. Nesvizhevsky VV, Voronin AYu, Lambrecht A, Reynaud S, Lychagin EV, Muzychka AYu, Strelkov AV. Observation of quantum levitation of nanoparticles by the method of ultracold neutrons. *Crystallography*, 2013, 58(5):730-736.
45. Mishinsky GV. Theory of cold fusion reactions. *Radioelectronics. Nanosystems. Information Technologies (RENSIT)*, 2019, 11(2):125-142. DOI: 10.17725/rensit.2019.11.125.

GENERATION OF OPTICAL SIGNALS RESISTANT TO DISPERSION-INDUCED POWER DEGRADATION

Vladislav V. Shcherbakov, Anatoly F. Solodkov

Center for Fiber-Optic Information Transmission Systems, <http://www.centervospi.ru/>
3 Vvedenskogo St., Moscow 117342, Russian Federation

Anatoly A. Zadernovsky

MIREA-Russian Technological University (RTU MIREA), <http://mirea.ru/>
78 Vernadskogo Av., Moscow 119454, Russian Federation

info@centervospi.ru, zadernovsky@mirea.ru

Abstract. A theoretical analysis is performed of transmission of optical signals in a fiber-optic link with external light intensity modulation by an electro-optic dual-drive Mach-Zehnder modulator and direct detection of the signals. The most general analytical expressions are obtained for the optical signals at the output from the modulator and at the receiving end of the fiber-optic link. Special attention is paid to the single-sideband-with-carrier (SSB+C) and the double-sidebands-with-suppressed-carrier (DSB+SC) modulation formats. A family of new SSB+C modulation formats of dual-drive Mach-Zehnder modulator is determined. Within the framework of linear approximation, the explicit expressions for SSB+C and DSB+SC optical signals are obtained. Transmission of such signals without dispersion-induced power degradation is clearly demonstrated.

Keywords: fiber-optic links, dual-electrode Mach-Zehnder modulator, fiber chromatic dispersion, single-sideband intensity modulation, suppressed-carrier intensity modulation

PACS: 85.60.Bt

Bibliography – 48 references

Received 07.04.2019, *accepted* 22.04.2019

RENSIT, 2019, 11(2):161-176

DOI: 10.17725/rensit.2019.11.161

CONTENTS

1. INTRODUCTION (161)
2. ELECTRO-OPTIC MACH-ZEHNDER MODULATOR (163)
 - 2.1. ELECTRO-OPTIC EFFECT (163)
 - 2.2. OPERATION PRINCIPLE OF THE ELECTRO-OPTIC MACH-ZEHNDER MODULATOR (165)
 - 2.3. BALANCED MACH-ZEHNDER MODULATOR (165)
 - 2.4. DUAL-DRIVE MACH-ZEHNDER MODULATOR (167)
3. MODULATION FORMATS OF DUAL-DRIVE MACH-ZEHNDER MODULATOR (168)
 - 3.1. DOUBLE-SIDEBAND-WITH-CARRIER (DSB+C) MODULATION FORMAT (169)
 - 3.2. SINGLE-SIDEBAND-WITH-CARRIER (SSB+C) MODULATION FORMAT (169)
 - 3.3. DOUBLE-SIDEBAND-WITH-SUPPRESSED-CARRIER (DSB+SC) MODULATION FORMAT (171)
4. TRANSPORTATION OF OPTICAL SIGNALS OVER A FIBER (171)

- 4.1. TRANSPORTATION OF THE DOUBLE-SIDEBAND-WITH-CARRIER (DSB+C) MODULATION SIGNAL (172)
- 4.2. TRANSPORTATION OF THE SINGLE-SIDEBAND-WITH-CARRIER (SSB+C) MODULATION SIGNAL (172)
- 4.3. TRANSPORTATION OF THE DOUBLE-SIDEBAND-WITH-SUPPRESSED-CARRIER (DSB+SC) MODULATION SIGNAL (173)
5. CONCLUSION (173)
- REFERENCES (174)

1. INTRODUCTION

Analog fiber-optic transmission systems remain in demand for various applications. Among them: on-board fiber-optic networks, antenna systems remote from the control and signal processing points, signal distribution systems for either on-board radars or ground-based radars with phased antenna arrays, radio-over-fiber systems, CATV networks, remote

cellular antenna service systems and many others. Standard fiber-optic link includes a transmitter, which converts an input electrical signal into a signal of intensity modulation of light produced by a semiconductor laser, transportation of the optical signal over a fiber and, finally, direct detection of the signal by a photodiode at the receiving end of the fiber. There are two basic schemes for the light intensity modulation, which compete with regard to simplicity and performance. The first scheme uses direct intensity modulation, which can be produced by varying the drive current of the semiconductor laser. Unfortunately, this current variation not only modulates the laser light intensity, but induces a parasitic optical frequency modulation, the effect which is referred to as frequency chirp.

The second scheme was proposed as a solution to the problem of chirp. This scheme employs external intensity modulation of the laser light by a balanced electro-optic Mach-Zehnder modulator (MZM), which produces the chirp-free optical signals. Unfortunately, the fiber-optic link with balanced MZM suffers from severe degradation of light intensity modulation response. At certain modulation frequencies, transmission of the optical signals is completely suppressed. Such behavior is typical, for the fiber-optic link with externally modulated 1550 nm laser light source and standard single-mode optical fiber. It is caused by chromatic dispersion of the group velocity of electromagnetic waves in the fiber.

As an optical signal is transported over a fiber, the different spectral components of modulated electromagnetic wave are traveling, due to dispersion, with different velocities. As a consequence, they form at the fiber output a superposition of waves with the phase relationships which differ from that of in the input signal. This leads to a distortion of the transmitted signal. At first approximation, the detected signal of light intensity at the modulation frequency

can be regarded as a result of interference of two waves of beats between the first order and the minus first order sidebands and the carrier electromagnetic wave. At the receiving end of the fiber these beating waves acquire, because of dispersion, different phase shifts, the magnitude of which depends on the modulation frequency. In particular, at certain modulation frequencies, these waves turn out to be in opposite phases, so that destructive interference occurs and the output signal is completely suppressed. Such a modulation format is referred to as the double-sideband-with-carrier (DSB+C) modulation.

To overcome the dispersion-induced power degradation, a special modulation format is used to generate optical single-sideband signals containing only one of the two spectral sidebands near to the carrier. It is referred to as the single-sideband-with-carrier (SSB+C) modulation format. In the absence of second sideband, the single wave of beats simply does not have a pair for the interference.

Another possibility is to use the double-sidebands-with-suppressed-carrier (DSB+SC) modulation format. In this case, there are no two waves of beats between the sidebands and the carrier, due to absence of the latter. Accordingly, the signal of light intensity results from the beats between the upper and the lower sidebands. The beat frequency is twice the modulation frequency. Since only single wave of beats occurs, DSB+SC optical signal is not affected by the dispersion-induced power degradation.

Various techniques for generating such optical signals have been repeatedly discussed in the literature. For instance, to eliminate one of the two spectral sidebands and, thus, to obtain SSB+C modulation signal, the frequency filtering was employed in [1-3]. In some schemes, special operation modes of a dual-drive electro-optic Mach-Zehnder modulator [4, 5] or an electro-absorption modulator [6-8] were employed. In others, direct modulation of a injection-locked semiconductor laser was used [9-12].

The carrier wave suppression techniques for generation of DSB+SC signals of double modulation frequency were considered in [13-17], and further development of these techniques with the aim of obtaining the 4-tupled frequency signals was proposed in [18-21], the 6-tupled frequency signals in [22], the 8-tupled signals in [23], the 12-tupled signals in [24-26] and the 16-tupled signals in [27].

Evolution of the methods for generating SSB+C optical signals has led to development of the single-sideband-with-suppressed-carrier (SSB+SC) modulation format [28-31]. The main advantages of this format are in improved spectral and energy efficiency of signal transmission and in tolerance to dispersive signal distortions. The disadvantages include significant complication of the processes of signal generation and detection. In order to demodulate SSB+SC signal, an additional copy of the carrier wave is necessary to have at the receiving end of the fiber-optic link, since the original carrier, according to the format name, is not transmitted over the fiber. The photodetector registers the signal of beats between the local carrier and the sideband received over the fiber.

The most effective and simplest way of generating the optical signals free of dispersion-induced power degradation is the use of dual-drive electro-optic Mach-Zehnder modulator [4, 5]. Study of the operation modes of such a modulator in a fiber-optic link was carried out by many authors. In some works [32], the calculations are limited to small-signal approximation, which involves into consideration only two harmonics at the fundamental frequency. A more general analysis, which takes into account an entire spectral composition, was performed in [33]. However, the results of this analysis are presented in the form of infinite series. This drawback was overcome in [34], where summation of the series was performed and more compact expressions were obtained (a

generalization to a modulator with asymmetric arms is presented in [35]). Nevertheless, the obtained formulas are still cumbersome and hard to engineering perception. Matching of these formulas with more simple expressions, obtained in the small signal approximation, is difficult, since the calculations were performed separately for even and odd spectral components.

In this paper, we will obtain the most general analytical expressions for optical signals at the output from the modulator and at the receiving end of a fiber-optic link. Despite the entire spectral composition of the signals is taken into account, the final formulas are quite compact and make it possible straightforward matching with the approximate expressions for a small modulation depth. Based on the performed calculations, a family of new SSB+C modulation formats will be determined. Within the framework of linear approximation, the explicit expressions for SSB+C and DSB+SC optical signals will be obtained and the transmission of such signals without dispersion-induced power degradation will be clearly demonstrated.

2. ELECTRO-OPTIC MACH-ZEHNDER MODULATOR

2.1. ELECTRO-OPTIC EFFECT

Electro-optic modulators are widely used in modern optical communication systems. The physics behind the operation of such modulators is the electro-optic Pockels effect. In a broad sense, the electro-optic effect [36] consists in changing the optical properties of some materials in response to applying a constant or slowly varying (compared to the frequency of the light) electric field. In particular, certain materials change their refractive index when subjected to an electric field. For classification of the electro-optic effect, we expand the dependence of refractive index n on electric field strength \hat{E} in a power series

$$n = n_0 + a_1 \hat{E} + (a_2 / 2) \hat{E}^2 + \dots, \quad (1)$$

where $a_n = (d^n n / d\hat{E}^n)_{\hat{E}=0}$. If the third term can be neglected, then n is a linear function of the electric field strength \hat{E} (Pockels effect). The linear electro-optic effect can occur only in the crystals with non-centrosymmetric lattice. Among them: potassium dihydrogen phosphate KH_2PO_4 (KDP), barium titanate BaTiO_3 , lithium niobate LiNbO_3 , lithium tantalate LiTaO_3 and $A^{\text{III}}B^{\text{V}}$ semiconductors, such as gallium arsenide – GaAs, indium phosphide – InP and others. Lithium niobate, gallium arsenide and indium phosphide are the most often materials used for manufacturing of Mach-Zehnder modulators. If the coefficient $a_1 = 0$, the quadratic dependence of the refractive index n on the electric field strength \hat{E}^2 is advanced to the forefront (Kerr effect).

In crystal optics, it is assumed to consider, instead of (1), a series

$$\frac{1}{n^2} = \frac{1}{n_0^2} + r\hat{E} + \xi\hat{E}^2 + \dots, \quad (2)$$

where electro-optic coefficients $r = -2a_1/n_0^3$ and $\xi = -a_2/n_0^3$ are known as Pockels and Kerr coefficients, respectively. Typical values of Pockels coefficients r are in the range of $10^{-12} \div 10^{-10} \text{ m/V}$, and typical values of the Kerr coefficients ξ are $10^{-18} \div 10^{-14} \text{ m}^2/\text{V}^2$ in solid-state materials and $10^{-22} \div 10^{-19} \text{ m}^2/\text{V}^2$ in liquids.

Lithium niobate is the most popular and widely used material exhibiting linear electro-optic effect [37]. It is optically transparent in the wavelength range of 400–5000 nm. Lithium niobate is an uniaxial crystal, this crystallographic axis is usually denoted by the letter Z . Lithium niobate is anisotropic crystal – its Pockels coefficient depends on the direction of the external electric field strength and on the direction of propagation and polarization of the light wave. The Pockels effect in lithium niobate is most pronounced when the external electric field is directed along the Z -axis of the crystal (the Pockels coefficient is 30 pm/V) and the electromagnetic wave propagates along the

crystallographic Y -axis with polarization in the ZY plane. For the manufacture of Mach-Zehnder modulators, monocrystalline lithium niobate plates, cut perpendicularly to one of the crystallographic axes are used. The most widespread are two types of modulators: with Z -cut plates and X -cut plates.

Organic polymers occupy a special position among electro-optic materials [38]; they have a number of advantages over inorganic crystals. Polymers differ in chemical diversity, relative simplicity of synthesis, ease of processing, and high values of electro-optic coefficients. If in inorganic crystals, the Pockels coefficient varies in the range of $1 \div 100 \text{ pm/V}$, then for organic polymers it reaches the values of $100 \div 500 \text{ pm/V}$.

The electro-optical properties of polymers are due to chromophores, which are special organic molecules that have an electric dipole moment. Chromophores can be introduced into polymer matrix either as impurities or as a part of the side or main chain of the polymer material. In order for the polymer becomes non-centrosymmetric and, thus, is capable to exhibit the electro-optic Pockels effect, it is subjected to so-called poling. During this process, the polymer is heated to a high temperature, at which local mobility of the chromophores and segments of the polymer chains appears. Then the polymer is placed in a strong electric field. In this field, the electric dipole moments of the chromophores become oriented in the direction of the vector of electric field strength. Further, the polymer is cooled without turning off the electric field, and, thereby, a material with “frozen” macroscopic polarization is obtained. For electro-optic devices, polymeric materials are used with a long-term orientation conservation of the chromophore dipoles in the polymer matrix.

The electro-optic effect is practically non-inertial. In inorganic crystals, the response time for Pockels effect consists $10^{-10} \div 10^{-11} \text{ s}$, and in polymer materials $10^{-12} \div 10^{-13} \text{ s}$. Thus,

the upper limit for the modulation frequency of the refractive index can reach hundreds of gigahertz for inorganic crystals, and for electro-optic polymers it falls into a terahertz frequency range.

Electro-optic modulators according to the scheme of the Mach-Zehnder interferometer [39-41] are the most widely used in fiber-optic transmission systems. The operation of such modulators is based on the transverse Pockels effect (the external electric field is perpendicular to the direction of light propagation), and lithium niobate is usually used as a material.

2.2. OPERATION PRINCIPLE OF THE ELECTRO-OPTIC MACH-ZEHNDER MODULATOR

A schematic diagram of Mach-Zehnder modulator is shown in Fig. 1. The modulator includes a system of optical waveguide channels with single input and single output, which are formed on a monocrystalline lithium niobate substrate by thermal diffusion of titanium. The input optical channel splits into two independent waveguides, providing a spatial separation of the input laser radiation into two light beams, which, then, are combined together in the output channel. The drive electrodes are mounted on the substrate. A voltage, applied to the electrodes, creates an electric field, which penetrates into the waveguides cross sections. This field changes the optical path length of the waveguides. The drive voltages U_1 and U_2 govern the phase shifts φ_1 and φ_2 , acquired each of the light waves on passing through their own waveguides.

The input electromagnetic wave with the frequency ω_0 and the amplitude E_0 is split in the modulator with symmetric waveguide geometry

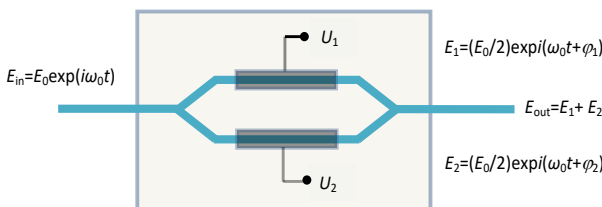


Fig. 1. Schematic diagram of electro-optic Mach-Zehnder modulator.

into two waves of equal amplitude $E_0/2$. At the modulator output we obtain

$$E_{out} = (E_0/2) \exp i(\omega_0 t + \varphi_1) + (E_0/2) \exp i(\omega_0 t + \varphi_2) = E_0 \exp(i\omega_0 t) \cos[(\varphi_1 - \varphi_2)/2] \exp[i(\varphi_1 + \varphi_2)/2]. \tag{3}$$

Since the output light intensity P_{out} is proportional to $|E_{out}|^2$ then

$$P_{out} = P_0 \cos^2[(\varphi_1 - \varphi_2)/2]. \tag{4}$$

Varying the drive voltages U_1 and U_2 leads to a modulation of the light intensity at the output of the modulator, and the corresponding electromagnetic wave (3) proves to be modulated, in general, not only in amplitude, but also in phase. Thus, the optical signal at the output of the modulator suffers from a frequency chirp. In a particular case, when $\varphi_1 = -\varphi_2$, the phase modulation of the light electromagnetic wave disappears and the modulator operates in a mode of amplitude modulation without chirp. If $\varphi_1 = \varphi_2$, then there is no amplitude modulation, and the modulator operates in a mode of phase modulation.

The mode of chirp-free amplitude modulation can be achieved with antiphase variation of the controlling electric fields strength in the channel waveguides. This can be ensured by a special arrangement of the electrodes with an employment of single drive electrode common to both waveguides. Such a modulator is called as a single-drive or balanced Mach-Zehnder modulator.

2.3. BALANCED MACH-ZEHNDER MODULATOR

A schematic diagram of the balanced MZM is shown in Fig. 2, and its cross-section – in Fig. 3. Such a modulator automatically provides antiphase changes in the strength vectors of controlling electric fields in channel waveguides. Due to linearity of Pockels effect, the signs of the refractive index changes in the channel waveguides will be opposite to each other. In order for the controlling electric field strength to be directed along the Z-axis (direction of the strongest Pockels effect),

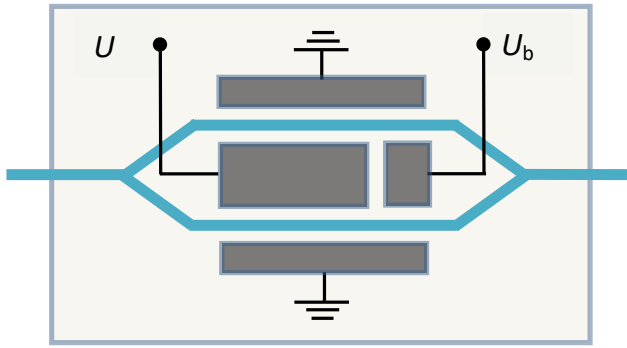


Fig. 2. Schematic diagram of the balanced Mach-Zehnder modulator.

the X-cut lithium niobate crystals are used as a substrate.

With the help of (1) the relation between the drive voltage U and the phases φ_1 and φ_2 can be written as

$$\varphi_1 = \frac{2\pi l}{\lambda_0} n_0 + \frac{2\pi l}{\lambda_0} a_1 \alpha U, \quad (5)$$

$$\varphi_2 = \frac{2\pi l}{\lambda_0} n_0 - \frac{2\pi l}{\lambda_0} a_1 \alpha U, \quad (6)$$

where λ_0 is the wavelength of light, l is the length of channel waveguides of the modulator. It is assumed that the strengths of the controlling electric fields in the cross sections of the waveguides are proportional to the applied voltage U , and the coefficient of proportionality α is the same for each channel and depends only on the geometry of the electrodes location. Such an assumption is justified only when the modulator electrodes are arranged symmetrically relative to the channel waveguides. The minus sign in the relation (6) is due to the fact that the electric fields strength vectors in the waveguides are directed oppositely (see Fig. 3). Due to linearity of the Pockels effect, the reversal in

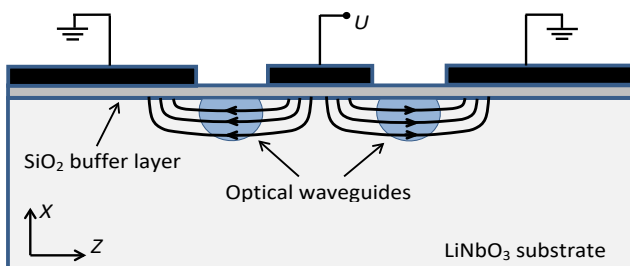


Fig. 3. Cross-section of the balanced Mach-Zehnder modulator.

direction of the applied electric field, results in the reversal in sign of the refractive index change.

For the quantitative characteristics of the Pockels effect, the voltage $U = U_\pi$ is used, at which the phase difference between (5) and (6) will be equal to π . With such a voltage, the electromagnetic waves at the interferometer output cancel each other and the light intensity becomes equal to zero. The voltage U_π is specific to each device and it is called the half-wave voltage of the modulator or the switch-off voltage. With this parameter, the electromagnetic wave (3) takes the form

$$E = E_0 \exp i(\omega_0 t + \varphi_0) \cos \frac{\pi U}{2 U_\pi}, \quad (7)$$

and the intensity of light (4) at the output of the modulator can be written as (we neglect the insertion loss)

$$P_{\text{out}} = P_0 \cos^2 \frac{\pi U}{2 U_\pi}. \quad (8)$$

The plot of the relative intensity P_{out}/P_0 versus the normalized voltage U/U_π is shown in Fig. 4. It is called the transfer function of modulator. It can be seen from the figure that small voltage modulations near the operating points with $U = \pm U_\pi/2$ should lead to a linear modulation of the light intensity. The choice of the operating point of modulator is achieved with the help of a constant bias voltage, which introduces an additional controlled phase shift between the

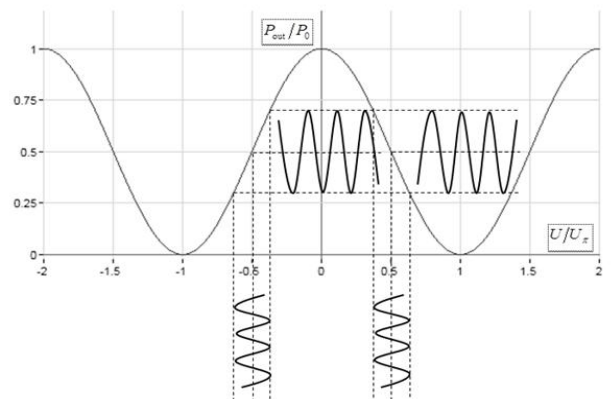


Fig. 4. Plot of the relative light intensity P_{out}/P_0 at the output of modulator versus the normalized drive voltage U/U_π . Transfer function of modulator.

light waves in the arms of the interferometer. To ensure biasing, a separate set of electrodes is usually used (see Fig. 2).

One of the main requirements to operation of the Mach-Zehnder modulator is the minimum of introduced nonlinear distortions. It is necessary for use in transmission systems with high sensitivity and large dynamic range. In general, the conversion of an electrical signal into an optical one with the help of Mach-Zehnder modulator is non-linear. Indeed, let the total drive voltage U (taking into account the bias voltage) be harmonically modulated

$$U / U_{\pi} = u_b + u_0 \cos(\omega_m t + \varphi_m) \quad (9)$$

with normalized bias voltage u_b , normalized modulation amplitude u_0 , modulation frequency ω_m and initial phase φ_m . Then, the electromagnetic wave (7) at the output of the modulator can be represented as a spectral sum

$$E = E_0 e^{i(\omega_0 t + \varphi_0)} \sum_{n=-\infty}^{+\infty} C_n e^{in(\omega_m t + \varphi_m)} \quad (10)$$

with the coefficients

$$C_n = \cos\left(\frac{\pi u_b}{2} + n \frac{\pi}{2}\right) J_n(\pi u_0 / 2). \quad (11)$$

The spectral representation of the light intensity modulation signal (8) at the output of the modulator,

$$P_{\text{out}} = (P_0 / 2) \left[1 + \sum_{n=-\infty}^{+\infty} \cos\left(\pi u_b + n \frac{\pi}{2}\right) J_n(\pi u_0) e^{in(\omega_m t + \varphi_m)} \right] \quad (12)$$

reveals the presence not only the first order harmonics at the fundamental frequency ω_m but also all the higher order harmonics. Here J_n is the Bessel function of the first kind of order n .

The degree of non-linearity can be reduced by selecting the operating point of modulator. Indeed, at the normalized bias voltages $u_b = m + 1/2$, where $m = 0, \pm 1, \pm 2, \pm 3, \dots$, (so called quadrature operating points) all the even harmonics in (12) disappear and only the fundamental harmonics at the modulation frequency ω_m and all the higher odd harmonics of this frequency are present in the output

optical signal. The power of these harmonics at the normalized voltage amplitude, for example, $u_0 = 1/2$ (this corresponds to 100% depth of modulation at the normalized bias voltage $u_0 = \pm 1/2$) are proportional to $J_1(\pi/2) = 0.567, J_3(\pi/2) = 6.894 \times 10^{-2}$ and $J_5(\pi/2) = 2.240 \times 10^{-3}$, so that the power of the third harmonic amounts to -9.15 dB of the fundamental harmonic power, whereas the power of the fifth harmonic is -24.03 dB. At a smaller signal modulation with $u_0 = 1/4$ we obtain $J_1(\pi/4) = 0.363, J_3(\pi/4) = 9.696 \times 10^{-3}, J_5(\pi/4) = 7.566 \times 10^{-5}$, so that the third and the fifth harmonic powers are only -15.73 dB and -36.8 dB, accordingly. One can see, therefore, that at $\pi u_0 < 1$ we can restrict ourselves only by the fundamental harmonics. In this approximation, the power of the output optical signal is reduced to

$$P_{\text{out}} = P_0 \left[1/2 + (-1)^{m+1} J_1(\pi u_0) \cos(\omega_m t + \varphi_m) \right], \quad (13)$$

and it is worth noting that at even m the signal of light intensity modulation is in opposite phases with the drive voltage signal (9), whereas at odd m these signals are in-phase. Taking for definiteness that $u_b = \pm 1/2$, which gives the minimum magnitude of the bias voltage, we obtain

$$P_{\text{out}} = (P_0 / 2) \left[1 \mp \pi u_0 \cos(\omega_m t + \varphi_m) \right], \quad (14)$$

where it is taken into account that in the region $\pi u_0 < 1$, one can accept $J_1(\pi u_0) \approx \pi u_0 / 2$. Thus, the quadrature biased balanced Mach-Zehnder modulator provides a chirp-free amplitude modulation of the carrier wave with the minimal non-linear distortions of the light intensity modulation signal.

2.4. DUAL-DRIVE MACH-ZEHNDER MODULATOR

The Mach-Zehnder modulator can be designed to have two separate signal electrodes and to control the electric fields in the arms of the interferometer independently of each other. A schematic diagram of such a modulator is shown in **Fig. 5**, and its cross-section – in **Fig. 6**. It is called a dual-drive MZM. Here, to achieve

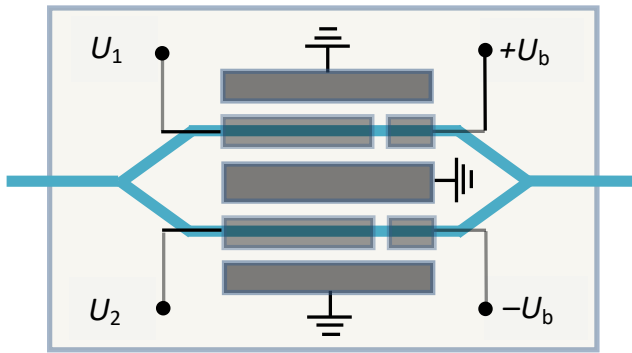


Fig. 5. Schematic diagram of the dual-drive Mach-Zehnder modulator.

maximum electro-optic effect, the Z-cut lithium niobate crystals are used as a substrate.

It is worth noting that a buffer dielectric layer is coated between the electrodes and the substrate surface, as shown in Fig. 3, 6. In the case of Z-cut modulator, the presence of this layer is obligatory, since the electromagnetic field of an optical wave, goes, as a rule, beyond the channel waveguide and in the absence of the dielectric layer between the crystal surface and the metal, a strong attenuation of the optical radiation appears due to large losses in metal electrodes. In the case of X-cut modulator, the buffer layer is used to better matching between the speed of the traveling microwaves of driving voltage and the speed of light in the channel waveguides. Such speed matching plays a key role in increasing the frequency modulation bandwidth.

Despite the high modulation rate of the refractive index (about of 100 GHz) inherent in lithium niobate, the operating frequency range of the Mach-Zehnder modulators is much smaller because of a number of physical limitations. To understand these limitations, we

note that the typical magnitudes of changes in the refractive index caused by the driving electric field are much smaller than the refractive index itself. Therefore, to achieve effective modulation, one has to either increase the driving voltage or increase the interaction length of the electrical and optical fields in the channel waveguides. Large electric voltages are undesirable because they lead to an increase in non-linear distortion of the optical signal. An increase in the interaction length is achieved by using the traveling-wave electrodes, in which the electric signal propagates in the same direction as the optical wave. In this case, it is necessary that the speeds of light and the traveling electric wave coincide. It is the mismatch between the phase velocities of microwaves and optical waves that determines the practical limit of the modulation bandwidth. Reducing the mismatch is achieved by decreasing the effective dielectric constant with the help of the buffer dielectric layer between the electrodes and the substrate, which leads to an increase in the phase velocity of the microwaves. In addition, the design optimization of the modulator electrodes, aimed at reducing the attenuation of microwaves, also contributes to an increase in the effective interaction length. As a result, in modern modulators based on lithium niobate crystals, the -3 dB modulation bandwidth amounts to 30-50 GHz. In the polymer-based modulators with inherent faster Pockels effect the bandwidth reaches 100 GHz and more.

Dual-drive Mach-Zehnder modulator provides a wide variety of modulation formats. In particular, it can operate in a mode of the balanced modulator, if the signal electrodes are supplied with the same, but antiphase voltage.

3. MODULATION FORMATS OF DUAL-DRIVE MACH-ZEHNDER MODULATOR

We consider in more detail the operation of a dual-drive Mach-Zehnder modulator. Let us apply to signal electrodes the driving

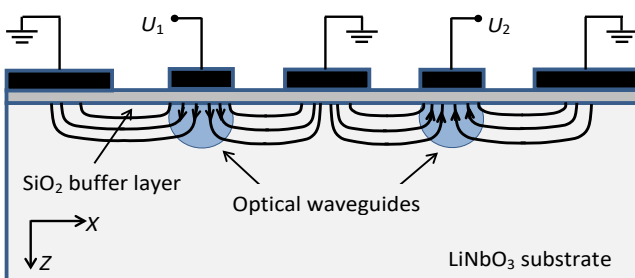


Fig. 6. Cross-section of the dual-drive Mach-Zehnder modulator.

voltages $U_1 = U_0 \cos(\omega_m t + \varphi_{m1})$ and $U_2 = U_0 \cos(\omega_m t + \varphi_{m2})$ with the equal frequencies ω_m , the equal amplitudes U_0 , but with different initial phases φ_{m1} and φ_{m2} . The operating point can be selected by applying to the bias electrodes an equal constant voltage U_b with opposite polarity (see Fig. 5). Such a voltage produces the equal in magnitude, but opposite in sign, phase shifts of light waves in the arms of the interferometer. When $U_b = U_\pi$ the modulator does not pass the light, since the corresponding electromagnetic waves are in antiphase and cancel each other at the output from the modulator. As a result, the phases of electromagnetic waves in the arms of the interferometer can be written as

$$\varphi_1 = \varphi_0 + \pi U_b / 2U_\pi + \pi U_1 / 2U_\pi, \quad (15)$$

$$\varphi_2 = \varphi_0 - \pi U_b / 2U_\pi + \pi U_2 / 2U_\pi, \quad (16)$$

and the electromagnetic light wave at the exit of the modulator is

$$E = E_0 \exp i(\omega_0 t + \varphi_0) \cos \frac{\pi}{2} \left(\frac{U_b}{U_\pi} + \frac{U_1 - U_2}{2U_\pi} \right) \exp \frac{i\pi}{4} \frac{U_1 + U_2}{U_\pi}. \quad (17)$$

The spectral representation of the wave (17) can be written as a sum

$$E = E_0 e^{i(\omega_0 t + \varphi_0)} \sum_{n=-\infty}^{+\infty} C_n e^{in \left(\omega_m t + \frac{\varphi_{m1} + \varphi_{m2}}{2} \right)} \quad (18)$$

with the coefficients

$$C_n = i^n J_n(\pi u_0 / 2) \cos \left(\frac{\pi u_b}{2} + n \frac{\varphi_{m1} - \varphi_{m2}}{2} \right), \quad (19)$$

where normalized variables $u_b = U_b / U_\pi$ and $u_0 = U_0 / U_\pi$ are introduced again. Accordingly, the spectral representation of the signal of light intensity modulation at the output of the modulator is

$$P_{out} = \frac{P_0}{2} \left[1 + \sum_{n=-\infty}^{+\infty} i^n J_n \left(\pi u_0 \sin \frac{\varphi_{m1} - \varphi_{m2}}{2} \right) \times \cos \left(\pi u_b + n \frac{\pi}{2} \right) e^{in \left(\omega_m t + \frac{\varphi_{m1} + \varphi_{m2}}{2} \right)} \right]. \quad (20)$$

With an antiphase variation of the signal voltages, when $\varphi_{m1} - \varphi_{m2} = \pm\pi$, the dual-drive modulator switches to an operation mode of the balanced modulator, and formulas (18) ÷ (20), as it should be, turn into (10) ÷ (12).

We consider the modulation formats that are most commonly used in analog transmission systems.

3.1. DOUBLE-SIDEBAND-WITH-CARRIER (DSB+C) MODULATION FORMAT

The format parameters: $\varphi_{m1} = \varphi_m$, $|\varphi_{m1} - \varphi_{m2}| = \pi$, $u_b = \pm 1/2$, $\pi u_0 < 1$. Dual-drive modulator operates in a mode of the quadrature biased balanced modulator. The signal of intensity modulation (20) contains only odd harmonics. At small modulation depths, the optical signal is described by the function

$$P = (P_0 / 2) [1 \mp \pi u_0 \cos(\omega_m t + \varphi_m)], \quad (21)$$

and the corresponding electromagnetic wave (17) does not suffer from the frequency chirp, it has a spectral composition (19) and contains three main spectral components: the carrier wave with the amplitude $C_0 = 1/\sqrt{2}$ and two sidebands with the amplitudes $C_1 = C_{-1} = i(\pi u_0 / 4) C_0$ at $\varphi_{m1} - \varphi_{m2} = +\pi$, $u_b = -1/2$, or at $\varphi_{m1} - \varphi_{m2} = -\pi$, $u_b = +1/2$; and with the amplitudes $C_1 = C_{-1} = -i(\pi u_0 / 4) C_0$ at $\varphi_{m1} - \varphi_{m2} = +\pi$, $u_b = +1/2$, or at $\varphi_{m1} - \varphi_{m2} = -\pi$, $u_b = -1/2$. As it should be, the expression (21) is obviously matched to (14).

3.2. SINGLE-SIDEBAND-WITH-CARRIER (SSB+C) MODULATION FORMAT

From (19) it is easy to see that the condition that the harmonic with, for example, $n = -1$ disappears from the light wave spectrum looks like

$$u_b - \frac{\varphi_{m1} - \varphi_{m2}}{\pi} = (2p + 1), \quad p = 0, \pm 1, \pm 2, \dots \quad (22)$$

Taking into account that the range of the bias voltage $-1 \leq u_b \leq 1$ exhausts all kinds of operating points of modulator, and the interval $-1 \leq (\varphi_{m1} - \varphi_{m2})/\pi \leq 1$ gives all possible phase differences of driving voltages, we obtain, instead of (22), the condition

$$\left| u_b - \frac{\varphi_{m1} - \varphi_{m2}}{\pi} \right| = 1. \tag{23}$$

Similarly, the condition that the harmonic with $n = +1$ disappears is determined by the equality

$$\left| u_b + \frac{\varphi_{m1} - \varphi_{m2}}{\pi} \right| = 1. \tag{24}$$

It should be noted that at $u_b = 0$ and fulfillment of the above conditions (23) or (24), all the odd harmonics are completely disappeared together with the harmonics -1 or $+1$. At $u_b = \pm 1$ and fulfillment of the condition (23) or (24), modulation of light intensity does not occur. These extreme cases should be excluded from the consideration.

Table 1 presents examples of the single-sideband modulation formats obtained with the help of the requirements (23), (24). Some of them are well known. For instance, the format $u_b = \pm 1/2, (\varphi_{m1} - \varphi_{m2})/\pi = \pm 1/2$ was historically the first proposed single-sideband optical modulation format [4, 5]. Another format with $u_b = \pm 1/3, (\varphi_{m1} - \varphi_{m2})/\pi = \pm 2/3$ was proposed relatively recently [42].

Not all formats included in the family (23), (24) are equivalent. From (20), for example, one can see that the choice of the quadrature operating points $u_b = \pm 1/2$, located on linear segment of the modulator transfer function,

Table
Examples of the single-sideband modulation formats

Harmonic number with zero amplitude n	Normalized bias voltage $u_b = U_b/U_\pi$	Normalized phase difference of drive voltages $(\varphi_{m1} - \varphi_{m2})/\pi$
-1	-1/2	+1/2
	+1/2	-1/2
	-1/3	+2/3
	+1/3	-2/3
	-2/3	+1/3
	+2/3	-1/3
+1	-1/2	-1/2
	+1/2	+1/2
	-1/3	-2/3
	+1/3	+2/3
	-2/3	-1/3
	+2/3	+1/3

lead to suppression of all even harmonics of the intensity modulation signal. Thus, in this case the nonlinear distortions of the signals at the output of the modulator are minimal. Another interesting example [42] is the format $u_b = -1/3, (\varphi_{m1} - \varphi_{m2})/\pi = +2/3$, or $u_b = +1/3, (\varphi_{m1} - \varphi_{m2})/\pi = -2/3$ for which not only the harmonic $n = -1$ disappears but also the harmonic $n = +2$. And if one selects the following modulation parameters $u_b = -1/3, (\varphi_{m1} - \varphi_{m2})/\pi = -2/3$, or $u_b = +1/3, (\varphi_{m1} - \varphi_{m2})/\pi = +2/3$ the harmonics $n = +1$ and $n = -2$ disappear simultaneously. It is seen, that in this case the modulation becomes “single-sideband” with regard to not only the fundamental, but also to the second harmonic. As a result, we should expect a decrease in nonlinear distortions of the signal transmission over dispersive fiber.

As an illustration, we consider a few examples in more detail. Let the modulation format $\varphi_{m1} = \varphi_m, \varphi_{m2} = \varphi_m \pm \pi/2, u_b = \pm 1/2, \pi u_0 < 1$ is employed. Two cases can be calculated separately.

1) If $\varphi_{m1} = \varphi_m, \varphi_{m2} = \varphi_m + \pi/2, u_b = \pm 1/2$, then the optical intensity modulation signal is described in linear approximation by the function

$$P_{out} = \frac{P_0}{2} \left[1 \mp \frac{\pi u_0}{\sqrt{2}} \cos \left(\omega_m t + \varphi_m - \frac{\pi}{4} \right) \right], \tag{25}$$

and the corresponding electromagnetic wave has a spectral composition (19), which contains the following main spectral components: the carrier wave with the amplitude $C_0 = 1/\sqrt{2}$ and the sidebands with the amplitudes $C_1 = 0, C_{-1} = -i(\pi u_0/4)C_0$ at $u_b = -1/2$ or $C_1 = i(\pi u_0/4)C_0, C_{-1} = 0$ at $u_b = +1/2$.

2) If $\varphi_{m1} = \varphi_m, \varphi_{m2} = \varphi_m - \pi/2, u_b = \pm 1/2$, then the optical intensity modulation signal is given by

$$P_{out} = \frac{P_0}{2} \left[1 \mp \frac{\pi u_0}{\sqrt{2}} \cos \left(\omega_m t + \varphi_m + \frac{\pi}{4} \right) \right], \tag{26}$$

and the electromagnetic wave has a spectral composition (19) with the following main spectral components: the carrier wave with the amplitude $C_0 = 1/\sqrt{2}$ and the sidebands with

the amplitudes $C_1 = i(\pi u_0/4)C_0$, $C_{-1} = 0$ at $u_b = -1/2$; or $C_1 = 0$, $C_{-1} = -i(\pi u_0/4)C_0$, at $u_b = +1/2$.

Now, we choose the modulation format $\varphi_{m1} = \varphi_m$, $\varphi_{m2} = \varphi_m \pm 2\pi/3$, $u_b = \pm 1/3$, $\pi u_0 < 1$. Two cases can be considered.

1) If $\varphi_{m1} = \varphi_m$, $\varphi_{m2} = \varphi_m + 2\pi/3$, $u_b = \pm 1/3$, then the optical intensity modulation signal takes the form

$$P_{out} = \frac{3P_0}{4} \left[1 \mp \frac{\pi u_0}{\sqrt{2}} \cos \left(\omega_m t + \varphi_m - \frac{\pi}{6} \right) \right], \quad (27)$$

2) If $\varphi_{m1} = \varphi_m$, $\varphi_{m2} = \varphi_m - 2\pi/3$, $u_b = \pm 1/3$, then the optical intensity modulation signal looks like

$$P_{out} = \frac{3P_0}{4} \left[1 \mp \frac{\pi u_0}{\sqrt{2}} \cos \left(\omega_m t + \varphi_m + \frac{\pi}{6} \right) \right], \quad (28)$$

3.3. DOUBLE-SIDEBAND-WITH-SUPPRESSED-CARRIER (DSB+SC) MODULATION FORMAT

If the minima of the modulator transfer function are used as operating points, for example the points with $u_b = \pm 1$, then, according to (19), the carrier amplitude C_0 is equal to zero. At a variety of phases of the driving voltages, we obtain a family of modulation formats with suppressed carrier. The optical intensity modulation signal (20) takes the form

$$P_{out} = \frac{P_0}{2} \left[1 - \sum_{n=-\infty}^{+\infty} i^n J_n \left(\pi u_0 \sin \frac{\varphi_{m1} - \varphi_{m2}}{2} \right) \times \cos \left(n \frac{\pi}{2} \right) e^{in \left(\omega_m t + \frac{\varphi_{m1} + \varphi_{m2}}{2} \right)} \right] \quad (29)$$

which contains only even harmonics. In particular, at a small modulation depth, $\pi u_0 < 1$, we obtain

$$P_{out} = \frac{P_0}{2} \left(\frac{\pi u_0}{2} \right)^2 \sin^2 \frac{\varphi_{m1} - \varphi_{m2}}{2} \times \left[1 - \cos 2 \left(\omega_m t + \frac{\varphi_{m1} + \varphi_{m2}}{2} \right) \right], \quad (30)$$

where the following approximate relations $J_0(z) \approx 1 - (z/2)^2$, $J_2(z) \approx (1/2)(z/2)^2$ were used. It is seen that at the modulator output an optical

signal with double modulation frequency is generated.

As an illustration, we consider the modulation format $\varphi_{m1} = \varphi_m$, $\varphi_{m2} = \varphi_m \pm \pi$, $u_b = \pm 1$. In this case, the dual-drive modulator operates in a mode of the balanced modulator and the spectrum of the corresponding electromagnetic wave (18) contains only odd harmonics. The main components of this spectrum are: $C_0 = 0$, $C_1 = C_{-1} = \pm i(\pi u_0/4)$ at $\varphi_{m1} = \varphi_m$, $\varphi_{m2} = \varphi_m + \pi$, $u_b = \pm 1$; or $C_0 = 0$, $C_1 = C_{-1} = \mp i(\pi u_0/4)$ at $\varphi_{m1} = \varphi_m$, $\varphi_{m2} = \varphi_m - \pi$, $u_b = \pm 1$. Provided that $\pi u_0 < 1$, we obtain the following light intensity modulation signal

$$P_{out} = \frac{P_0}{2} \left(\frac{\pi u_0}{2} \right)^2 \left[1 + \cos 2(\omega_m t + \varphi_m) \right]. \quad (31)$$

4. TRANSPORTATION OF OPTICAL SIGNALS OVER A FIBER

Due to chromatic dispersion, each spectral wave from the composition (18) travels in a fiber at its own velocity. This leads to a distortion of the optical signal at the output of the fiber. Indeed, after passing the distance L , a spectral wave with a frequency ω takes the form $E = E_0 e^{i(\omega t - \beta L)}$, where β is the propagation constant at the specified frequency (we neglect the attenuation). Dispersion is expressed in dependence of the propagation constant on frequency. In the vicinity of the carrier frequency ω_0 the function $\beta(\omega)$ can be represented as a power series $\beta(\omega) = \beta_0 + \beta_1(\omega - \omega_0) + (\beta_2/2)(\omega - \omega_0)^2 + \dots$, where β_0 is the propagation constant at the carrier frequency, $\beta_1 = 1/u$ is equal to the inverse group velocity, $u = d\omega/d\beta$, at the carrier frequency and the coefficient β_2 is associated with the group velocity dispersion. It can be determined through the so-called chromatic dispersion coefficient D of a fiber by means of the well-known relation [43] $\beta_2 = -\lambda_0^2 D / 2\pi c$, where c – the speed of light in vacuum, λ_0 – laser emission wavelength. Typical values for D at the wavelength 1550 nm are in the range (16 – 18) ps/(nm km).

As a result, at the output of a fiber of length L , each spectral component in (18) acquires its own phase shift equal to $-\beta L$. In particular, for the harmonic with the frequency $\omega_0 + n\omega_m$ it consists $-\beta L = -\beta_0 L - \beta_1 n\omega_m L - (1/2)\beta_2 n^2 \omega_m^2 L - \dots$. Therefore, at the fiber output we have the wave

$$E = E_0 e^{i(\omega_0 t - \beta_0 L + \varphi_0)} \sum_{n=-\infty}^{+\infty} C_n e^{in^2 \theta} e^{in \left[\omega_m (t-L/u) + \frac{\varphi_{m1} + \varphi_{m2}}{2} \right]}, \quad (32)$$

where

$$\theta = \pi c (\omega_m / \omega_0)^2 DL \quad (33)$$

is the signal transportation parameter.

The intensity of light at the output from the optical fiber (and, consequently, the photocurrent of detector) will be proportional to the square modulus of the electric field strength E (32). We write down it in the form

$$P_s = \sum_{n=-\infty}^{+\infty} P_n e^{in \left[\omega_m (t-L/u) + \frac{\varphi_{m1} + \varphi_{m2}}{2} \right]}, \quad (34)$$

where

$$\begin{aligned} P_n &= P_0 \sum_{k=-\infty}^{+\infty} C_{n+k} e^{i(n+k)^2 \theta} C_k^* e^{-ik^2 \theta} = \\ &= P_0 \sum_{k=-\infty}^{+\infty} C_{n+k} e^{i(n+k)n\theta} C_k^* e^{ikn\theta} \end{aligned} \quad (35)$$

is the complex amplitude of the harmonic with frequency $n\omega_m$. In calculating (35), we use the Graf's theorem on summation of the Bessel functions (Graf's addition theorem) [44], which, for the purpose of our analysis, can be written in the form [45]

$$J_n(z_3) e^{in\gamma} = \sum_{k=-\infty}^{+\infty} J_{n+k}(z_1) e^{i(n+k)a} J_k(z_2) e^{ik\beta}, \quad (36)$$

where the complex number $z_3 e^{i\gamma}$ is the sum of two other complex numbers $z_1 e^{ia}$ and $-z_2 e^{-i\beta}$. As a result, we obtain the expression

$$\begin{aligned} P_n &= (-1)^n \frac{P_0}{2} \left\{ J_n(\pi u_0 \sin n\theta) \cos \frac{n(\varphi_{m1} - \varphi_{m2})}{2} + \right. \\ &+ \frac{1}{2} e^{i\pi u_b} J_n \left[\pi u_0 \sin \left(n\theta + \frac{(\varphi_{m1} - \varphi_{m2})}{2} \right) \right] + \\ &+ \left. \frac{1}{2} e^{-i\pi u_b} J_n \left[\pi u_0 \sin \left(n\theta - \frac{(\varphi_{m1} - \varphi_{m2})}{2} \right) \right] \right\}. \end{aligned} \quad (37)$$

Simplified version of (37) which is suitable to the balanced Mach-Zehnder modulator was obtained earlier in [46].

4.1. TRANSPORTATION OF THE DOUBLE-SIDEBAND-WITH-CARRIER (DSB+C) MODULATION SIGNAL

After transportation over a dispersive fiber of length L , the signal (21) is transformed to the form

$$P_s = (P_0 / 2) [1 \mp \pi u_0 \cos \theta \cos(\omega_m (t - L/u) + \varphi_m)]. \quad (38)$$

When $\cos \theta$ goes to zero, the signal at the fiber output disappears [47, 48]. This happens at the modulation frequencies

$$\omega_m = \omega_0 \sqrt{\frac{k+1/2}{cDL}}, k = 0, 1, 2, \dots \quad (39)$$

A typical value of the fiber dispersion coefficient $D = 17$ ps/(nm·km), the laser light wavelength 1550 nm corresponds to the frequency $f_0 = \omega_0 / 2\pi = 193.414$ THz.

Thus, the use of this modulation format leads to significant performance degradation of the fiber-optic link. At modulation frequencies (39), transmission of the optical signals is completely suppressed.

4.2. TRANSPORTATION OF THE SINGLE-SIDEBAND-WITH-CARRIER (SSB+C) MODULATION SIGNAL

At the output from fiber of length L , the signals (25), (26) and (27), (28) are transformed, respectively, to the forms

$$P_s = \frac{P_0}{2} \left\{ 1 \mp \frac{\pi u_0}{\sqrt{2}} \cos \left[\omega_m (t - L/u) + \varphi_m - \frac{\pi}{4} \pm \theta \right] \right\}, \quad (40)$$

$$P_s = \frac{P_0}{2} \left\{ 1 \mp \frac{\pi u_0}{\sqrt{2}} \cos \left[\omega_m (t - L/u) + \varphi_m + \frac{\pi}{4} \mp \theta \right] \right\}, \quad (41)$$

and

$$P_s = \frac{3P_0}{4} \left\{ 1 \mp \frac{\pi u_0}{2} \cos \left[\omega_m (t - L/u) + \varphi_m - \frac{\pi}{6} \pm \theta \right] \right\}, \quad (42)$$

$$P_s = \frac{3P_0}{4} \left\{ 1 \mp \frac{\pi u_0}{2} \cos \left[\omega_m (t - L/u) + \varphi_m + \frac{\pi}{6} \mp \theta \right] \right\}. \quad (43)$$

A comparison of these expressions shows that the SSB+C modulation signal transmission does not suffer from the amplitude distortions. The corresponding signals at the input and at the output of a fiber differ only in phase.

4.3. TRANSPORTATION OF THE DOUBLE-SIDEBAND-WITH-SUPPRESSED-CARRIER (DSB+SC) MODULATION SIGNAL

At the receiving end of a fiber-optic link the signal (30) takes the form

$$P_s = \frac{P_0}{2} \left(\frac{\pi u_0}{2} \right) \sin^2 \left(\frac{\varphi_{m1} - \varphi_{m2}}{2} \right) \times \left\{ 1 - \cos 2 \left[\omega_m (t - L/u) + \frac{(\varphi_{m1} - \varphi_{m2})}{2} \right] \right\}, \tag{44}$$

and its particular version (31), corresponding to a mode of balanced modulator, is transformed to

$$P_s = \frac{P_0}{2} \left(\frac{\pi u_0}{2} \right)^2 \{ 1 + \cos 2[\omega_m (t - L/u) + \varphi_m] \}. \tag{45}$$

A comparison of signals at the input and at the output of a fiber indicates that the signals under consideration are transmitted without amplitude distortions. Moreover, the output signal (44) is completely independent of the parameter of transportation θ (33).

5. CONCLUSION

When a light intensity modulation signal travels through a fiber, its power is periodically degraded (this phenomenon is also referred to as signal power fading or signal power penalty). The spatial period of such degradation depends on frequency of the signal. As a result, signals of certain frequencies cannot be transmitted over a fiber of a given length. The reason for such a behavior lies in the chromatic dispersion of the group velocity of electromagnetic waves in the fiber.

In this paper, the special signals of light intensity modulation resistant to dispersion-induced power degradation are considered. Among them, the single-sideband-with-carrier and the double-sideband-with-suppressed-carrier modulation signals. For both kind of signals, only a single electromagnetic wave of beats is formed for which there is no pair wave for destructive interference. The easiest way to generate such signals is to use a dual-drive Mach-Zehnder modulator. The most general analytical expressions for the optical signals at the output

from the modulator and at the receiving end of a fiber-optic link were obtained. These expressions allow us to determine the contribution of any higher order harmonics and can be used to analyze various signal distortions. Based on the performed calculations, a family of new single-sideband modulation formats of the dual-drive Mach-Zehnder modulator was determined

In the framework of linear approximation, the explicit expressions were obtained for the single-sideband-with-carrier and the double-sideband-with-suppressed-carrier modulation signals. Transmission of such signals without dispersion-induced power degradation was clearly demonstrated. In other words, it was shown that the SSB+C and DSB+SC modulation signals are resistant to amplitude distortions. The spectral amplitudes of these signals at the input and at the output of a fiber remain equal in magnitude (without taking into account the attenuation in the fiber). As for phase distortions, these signals behave differently.

The signals of SSB+C modulation at the input (25) - (28) and at the output (40) - (43) of a fiber differ in phase by an amount, which contains the parameter θ . Since the signal transportation parameter θ (33) is a quadratic function of the modulation frequency, the phase-frequency characteristic of the fiber-optic link is non-linear. This leads to violation of the phase relationships between spectral components of the transmitted signal and, thus, to the signal distortion.

The output DSB+SC modulation signal (44) is not dependent on the signal transportation parameter θ . Therefore, such a signal is resistant not only to the amplitude, but also to the phase distortions. It is necessary, however, to bear in mind that under employment of such modulation format, the conversion of an electrical signal into an optical one occurs with frequency doubling.

ACKNOWLEDGEMENTS

This work was partly supported by the Ministry of Science and Education of the Russian Federation, Project No. 8.4853.2017/BCb.

REFERENCES

1. Park J, Sorin WV, Lau KY. Elimination of the fibre chromatic dispersion penalty on 1550 nm millimetre-wave optical transmission. *Electron. Lett.*, 1997, 33:512–513.
2. Yonenaga K, Takachio N. A fiber chromatic dispersion compensation technique with an optical SSB transmission in optical homodyne detection systems. *IEEE Photon. Technol. Lett.*, 1993, 5:949-951.
3. Vourch E, Le Berre D, Herve D. Lightwave single sideband wavelength self-tunable filter using InP:Fe crystal for fiber-wireless systems. *IEEE Photon. Technol. Lett.*, 2002, 14:194-196.
4. Smith GH, Novak D, Ahmed Z. Technique for optical SSB generation to overcome dispersion penalties in fibre-radio systems. *Electron. Lett.*, 1997, 33(1):74-75.
5. Smith G, Novak D, Ahmed Z. Overcoming chromatic-dispersion effects in fiber-wireless systems incorporating external modulators. *IEEE Transactions on microwave theory and techniques*, 1997, 45(8):1410-1415.
6. Vergnol E, Devaud F, Tanguy D, Penard E. Integrated Lightwave Millimetric Single Sideband Source: Design and Issues. *IEEE Journal of Lightwave Technology*, 1998, 16(7):1276-1284.
7. Polo V, Marti J, Ramos F, Moodie D. Mitigation of chromatic dispersion effects employing electroabsorption modulator-based transmitters. *IEEE Photon. Technol. Lett.*, 1999, 7:883-885.
8. Fells JAJ, Gibbon MA, White IH, Thompson GHB, Penty RV, Armistead CJ, Kimber EM, Moule DJ, Thrush EJ. Transmission beyond the dispersion limit using a negative chirp electroabsorption modulator. *Electron. Lett.*, 1994, 30:1168-1169.
9. Hyuk-Kee Sung, Erwin KLau, Ming CWu. Optical single sideband modulation using strong optical injection-locked semiconductor lasers. *IEEE Photonics Technology Letters*, 2007, 19(13):1005-1007.
10. Arahira S, Matsui Y, Kunii T, Oshiba S, Ogawa Y. Transform-limited optical short-pulse generation at high repetition rate over 40 GHz from a monolithic passive mode-locked DBR laser diode. *IEEE Photon. Technol. Lett.*, 1993, 5:1362-1365.
11. Nirmalathas A, Liu HF, Ahmed Z, Novak D, Ogawa Y. Subharmonic synchronous and hybrid mode-locking of a monolithic DBR laser operating at millimeter-wave frequencies. *IEEE Photon. Technol. Lett.*, 1997, 9(4):434-436.
12. Kim DY, Pelusi M, Ahmed Z, Novak D, Liu HF, Ogawa Y. Ultrastable millimetre-wave signal generation using hybrid modelocking of a monolithic DBR laser. *Electron. Lett.*, 1995, 31(9):733-734.
13. O'Reilly JJ, Lane PM, Heidemann R, Hofstetter R. Optical generation of very narrow linewidth millimetre wave signals. *Electron. Lett.*, 1992, 28(25):2309-2311.
14. Montgomery R, De Salvo R. A novel technique for double sideband suppressed carrier modulation of optical fields. *IEEE Photonics Technology Letters*, 1995, 7(4):434-436.
15. Griffin RA, Lane PM, O'Reilly JJ. Dispersion-tolerant subcarrier data modulation of optical millimetre-wave signals. *Electron. Lett.*, 1996, 32:2258-2260.
16. Fuster JM, Marti J, Corral JL. Chromatic dispersion effects in electro-optical upconverted millimetre-wave fibre optic links. *Electron. Lett.*, 1997, 33:1969-1970.
17. Jia Z, Yu J, Chang G-K. A full-duplex radio-over-fiber system based on optical carrier suppression and reuse. *IEEE Photon. Technol. Lett.*, 2006, 18:1726-1728.
18. O'Reilly JJ, Lane PM. Fibre-supported optical generation and delivery of 60 GHz signals. *Electron. Lett.*, 1994, 30(16):1329-1330.
19. Yu J, Jia Z, Yi L, Wang T, Chang GK. Centralized lightwave radio-over-fiber system with photonic frequency quadrupling for high frequency millimeter-wave generation. *IEEE Photon. Technol. Lett.*, 2007, 19(19):1499-1501.

20. Lin CT, Shih PT, Chen J, Xue WQ, Peng PC, Chi S. Optical millimeter-wave signal generation using frequency quadrupling technique and no optical filtering. *IEEE Photon. Technol. Lett.*, 2008, 20(12):1027-1029.
21. Mohamed M, Zhang X, Hraimel B, Wu K. Analysis of frequency quadrupling using a single Mach–Zehnder modulator for millimeter-wave generation and distribution over fiber systems. *Optics Express*, 2008, 16(14):10786-10802.
22. Qin Y, Sun J. Frequency sextupling technique using two cascaded dual-electrode Mach–Zehnder modulators interleaved with Gaussian optical band-pass filter. *Optics Communications*, 2012, 285(12):2911-2916.
23. Zhang H, Cai L, Xie S, Zhang K, Wu X, Dong Z. A novel radio-over-fiber system based on carrier suppressed frequency eightfold millimeter wave generation. *IEEE Photonics Journal*, 2017, 9(5):1-6.
24. Shih PT, Chen J, Lin CT, Jiang WJ, Huang HS, Peng PC, Chi S. Optical millimeter-wave signal generation via frequency 12-Tupling. *IEEE Journal of Lightwave Technology*, 2010, 28(1):71-78.
25. Zhu Z, Zhao S, Li Y, Chu X, Wang X, Zhao G. A radio-over-fiber system with frequency 12-tupling optical millimeter-wave generation to overcome chromatic dispersion. *IEEE Journal of Quantum Electronics*, 2013, 49(11):919-922.
26. Dongfei Wang, Xianfeng Tang, Yichen Fan, Xiaoguang Zhang, Lixia Xi, Wenbo Zhang. A new approach to generate the optical millimeter-wave signals using frequency 12-tupling without an optical filter. *Proc. SPIE Tenth International Conference on Information Optics and Photonics*, 2018, 109641C.
27. Dongfei Wang, Xianfeng Tang, Yichen Fan, Xiaoguang Zhang, Lixia Xi, Wenbo Zhang. A novel filterless scheme for 16-tupled frequency millimeter-wave generation based on only two MZMs. *Proc. SPIE 17th International Conference on Optical Communications and Networks (ICO CN2018)*, 2019, 110482U.
28. Shimotsu S, Oikawa S, Saitou T, Mitsugi N, Kubodera K, Kawanishi T, Izutsu M. Single Side-Band Modulation Performance of a LiNbO₃ Integrated Modulator Consisting of Four-Phase Modulator Waveguides. *IEEE Photonics Technology Letters*, 2001, 13(4):364-366.
29. Chow CW, Wang CH, Yeh CH, Chi S. Analysis of the carrier-suppressed single-sideband modulators used to mitigate Rayleigh backscattering in carrier-distributed PON. *Optics Express*, 2011, 19(11):10973-10978.
30. Loayssa A, Benito D, Garde MJ. Single-sideband suppressed-carrier modulation using a single-electrode electrooptic modulator. *IEEE Photonics Technology Letters*, 2001, 13(8):869-871.
31. Frankel MY, Esman RD. Optical single-sideband suppressed-carrier modulator for wide-band signal processing. *IEEE Journal of Lightwave Technology*, 1998, 16(5):859-863.
32. Cartaxo AVT. Small-signal analysis for nonlinear and dispersive optical fibers and its application to design of dispersion supported transmission systems with optical dispersion compensation. *Proc. Inst. Elect. Eng., Optoelectronics*, 1999, 146(5):213-222.
33. Corral JL, Marti J. General expressions for IM/DD dispersive analog optical links with external modulation or optical up-conversion in a Mach–Zehnder electrooptical modulator. *IEEE Transactions on Microwave Theory and Techniques*, 2001, 49(10):1968-1976.
34. Cheng L, Aditya S, Nirmalathas A. An exact analytical model for dispersive transmission in microwave fiber-optic links using Mach–Zehnder external modulator. *IEEE Photonics Technology Letters*, 2005, 17(7):1525-1527.
35. Ferreira AA, Júnior, Coutinho OL, Martins CS, Fegadolli WS, Ribeiro JAJ, Almeida VR, Oliveira JEB. Effect of fiber optic chromatic dispersion on the performance of analog optical link with external modulation aiming

- at aerospace applications. *Journal of Aerospace Technology and Management*, 2013, 5(2):205-216.
36. Saleh BEA, Teich MC. *Fundamentals of photonics*. New York, John Wiley & Sons Inc., 1991, 947 p.
 37. James ET. *Lithium Niobate Photonics*. Boston, Artech House, 2015, 288 p.
 38. Kong Eric SW (ed.). *Nanomaterials, polymers, and devices: materials functionalization and device fabrication*. New Jersey, John Wiley & Sons Inc., 2015, 567 p.
 39. Okayama H. Lithium Niobate Electro-Optic Switching. In: *Optical Switching*. Edited by El-Bawab TS, Boston MA, Springer, 2006:39-81.
 40. Wooten EL, Kissa KM, Yi-Yan A, Murphy EJ, Lafaw DA, Hallemeier PF, Maack D, Attanasio DV, Fritz DJ, McBrien GJ, Bossi DE. A review of lithium niobate modulators for fiber-optic communications systems. *IEEE J. Select. Topics Quantum Electron.*, 2000, 6:69-82.
 41. Belkin ME, Golovin VV, Tyschuk YuN, Kudzh SA, Sigov AS. Modeling optical intensity modulators based on Mach-Zehnder interferometer by software tool of microwave circuits calculation NI AWR Design Environment. *Russian Technological Journal*, 2016, 4(5):3-16.
 42. Min Xue, Shilong Pan, Yongjiu Zhao. Optical single-sideband modulation based on a dual-drive MZM and a 120° hybrid coupler. *Journal of Lightwave Technology*, 2014, 32(19):3317-3323.
 43. Agrawal GP. *Nonlinear Fiber Optics*. New York, Academic Press, 2013, 648 p.
 44. Abramowitz M, Stegun IA. *Handbook of Mathematical Functions With Formulas, Graphs, and Mathematical Tables*, 10th ed: Wiley, 1972.
 45. Andrews GE, Askey R, Roy R. *Special Functions*. Cambridge, U.K.: Cambridge Univ. Press, 2001.
 46. Shcherbakov VV, Solodkov AF, Zadernovsky AA. Transmission of light intensity modulation signals in analog fiber-optic links. *Radioelectronics. Nanosystems. Information Technologies (RENSIT)*, 2016, 8(1):9-24; doi: 10.17725/rensit.2016.08.009.
 47. Meslener GJ. Chromatic dispersion induced distortion of modulated monochromatic light employing direct detection. *IEEE J. Quantum Electron.*, 1984, 20(10):1208-1216.
 48. Schmuck H. Comparison of optical mm-wave system concepts with regard to chromatic dispersion. *Electron. Lett.*, 1995, 31:1848-1849.

PHOTON LOCALIZATION IN OPTICAL METAMATERIALS WITH A RANDOM CLOSE TO ZERO REFRACTIVE INDEX

Oleg N. Gadomsky, Irina V. Gadomskaya

Ulyanovsk State University, <https://www.ulsu.ru/>
42, ul. L.Tolstoy, Ulyanovsk 432017, Russian Federation

Nikolay M. Ushakov

Kotelnikov Institute of Radioengineering and Electronics of RAS, Saratov branch, <http://www.cplire.ru/rus/sfire>
38, ul. Zelenaya, Saratov 410019, Russian Federation
gadomsky@mail.ru, nmu@bk.ru, gadomskaya@mail.ru

Abstract. The results of a theoretical and experimental study of the effect of photon localization in the composite layer of a nanomaterial (PMMA & Ag) with spherical silver nanoparticles are presented. Composite nanomaterial was a metamaterial with a random refractive index close to zero. The photon localization effect considered in this article is fundamentally different from the transverse localization of electromagnetic waves in 2D periodic structures, since it is considered in homogeneous transparent media far from the resonance of their structural elements. It is theoretically shown that at a vacuum-optical medium interface with a random refractive index close to zero the refraction of the wave occurs not according to Snell's law, but with the localization of photons, when the external plane wave is extinguished at a point. In accordance with the uncertainty relation photons propagate in the medium in all directions determined by a random angle of refraction. A condition under which the values of the angles of refraction of waves in a layer become complex quantities is derived. As a result, a parallel beam of light inside the layer is localized in a small region. A 1 mW helium-neon laser with longitudinal polarization of light and a wavelength of 632 nm has been used in experiment. The diameter of the laser beam was 1 mm. The radiation passing through the sample with a thickness of 10 μm in the longitudinal and transverse directions was recorded using a CD camera. When the sample is irradiated a photon localization region is formed in the composite layer, whose linear dimensions (8 μm) are comparable with the layer thickness.

Keywords: optical metamaterial with randomly close to zero refractive index, polymer composite nanomaterial, silver nanoparticles, polymethyl methacrylate, photon localization in the composite layer

UDC 546.722+546.271

Bibliography - 24 references

Received 14.03.2019, accepted 02.04.2019

RENSIT, 2019, 11(2):177-188

DOI: 10.17725/rensit.2019.11.177

CONTENTS

1. INTRODUCTION (177)
2. THEORY OF PHOTON LOCALIZATION IN THE MEDIUM WITH RANDOMLY A NEAR-ZERO REFRACTIVE INDEX (179)
 - 2.1. LOCALIZATION OF PHOTONS AT THE INTERFACE OF THE VACUUM-OPTICAL MEDIUM (179)
 - 2.2. LOCALIZATION OF PHOTONS INSIDE THE COMPOSITE (181)
3. EXPERIMENTAL DETECTION OF EFFECT OF PHOTON LOCALIZATION IN A COMPOSITE LAYER PMMA&AG (183)

4. RESULTS AND DISCUSSION (184)

5. CONCLUSION (186)

REFERENCES (187)

1. INTRODUCTION

Among unusual transport properties for disordered materials, the phenomenon of Anderson localization predicted by Phillip Anderson in 1957 should be noted [1]. Anderson localization is a disordered phase transition in the behavior of electron transport, in which, unlike the classical diffusion regime with the well-known Ohm's law, in a localized state, the material behaves as an

insulator. The effect is based on the interference of electrons that have passed multiple scattering by defects in a solid. However, the localization of electrons in a disordered solid has not been confirmed experimentally. The main condition for the localization of Anderson is the constancy in time of the potential of disorder in the medium, which cannot be fulfilled for electrons due to the inconstancy in time of phonons, loss of electron coherence during their inelastic interaction with the crystal lattice, the resulting nonlinearity due to multiparticle interactions leading to disorder potential. Unlike electrons, photons do not interact with each other. In this case, the phenomenon of photon localization takes place for multiple scattering of electromagnetic waves in a disordered medium. This makes the transfer of photons in disordered materials an ideal model system for studying the localization of Anderson. The first theoretical works on the localization of photons appeared in the mid-eighties of the twentieth century [2, 3]. The first successful experimental works confirming the phenomenon of transverse localization of photons in disordered media were made only 20 years later [4–6]. After that, the model of transverse localization of light in disordered materials became the main one. However, it is important to point out that the transverse photon localization model is associated with transport effects in one or two dimensions. At the same time, the 3D localization effect of Anderson with the help of short laser pulses propagating in a volume where the disorder of which is constant in time was studied in [7]. In [8] a review of works describing the interaction between disorder and nonlinearity, localization and enhanced transport of photons in photonic crystals, hypertransport stochastic acceleration of photons due to developing disorder and localization with quantum-correlated photons are given.

The condition of the transverse localization of photons observed in 2D disordered optical media can be represented as follows. Let a plane wave propagate along the z axis. The medium in which the wave propagates is a 2D periodic structure or photon lattice with

modulation of the refractive index Δn . Even with a weak modulation of the refractive index of the order of 10^{-4} , it is possible to observe the localization of photons in such a medium. The transverse wave vector (along the y axis, x) is inversely proportional to the aperture of the wave packet $k_{\perp} \propto \frac{1}{A}$ and much less wave vector in homogeneous space $k_{\perp} \ll k = \omega n_0 / c$ refractive index $n_0 > 1$. The length of the photon localization is $\xi_{2d} = l \times \exp\left(\frac{\pi}{2} k_{\perp} l\right)$, where l - photon free path. This condition can be fulfilled not only in 2D periodic structures (photonic crystals), but also in metamaterials with a refractive index $n_{\perp} \ll 1$. In this case, the condition is $k_{\perp} = \omega n_{\perp} / c \ll k = \omega n_0 / c$.

Nanotechnologies are known in which silver or gold nanoparticles are embedded in a dielectric matrix, for example, in polymethyl methacrylate [9, 10]. However, in these works the optical properties of the materials were not investigated. Based on the nanotechnologies developed by us [11, 12] samples were obtained, and in which layers of synthesized metamaterials (PMMA and Ag) with silver nanoparticles were deposited on different surfaces and the reflection and transmission spectra of these layers were studied. The study of these samples allowed us to detect unique optical phenomena such as interference of light in thick layers [13], violation of the principle of reversibility of light fluxes [14], amplification and focusing of light in nanostructures with a near-zero refractive index [15]. The basis of these optical properties is the effect of ideal optical transmission, when the reflection of the layer disappears, and the transmittance of the layer is equal to unity regardless of the wavelength, layer thickness, angle of incidence of external radiation and the refractive index of the framing media [16]. Based on a theoretical analysis of the experimental reflection and transmission spectra of composite layers (PMMA & Ag) of various thickness, it was concluded that the metamaterials synthesized by us have a random refractive index close to zero. Thus, in the reflection and transmission spectra of

thick (considerably longer than the wavelength) composite layers (PMMA and Ag), interference minima and maxima were detected on the glass substrate. At the same time, in the layers of the polymethylmethacrylate matrix for the same thickness, there were no interference peaks. The arrangement of the minima and maxima in these spectra can be used to calculate the region of permissible values of the refractive index of the layer. In this case, the possible values of the refractive index of the layer are in the range $(0, \Delta n_2)$, where $\Delta n_2 < 1$.

Known work on mathematical modeling of the types of structural elements for nanostructures [17, 18], in which structural elements in the form of spirals, rods, nanowires and other types, could be embedded in dielectric matrices in order to obtain metamaterials with zero dielectric permeability and magnetic permeability. However, such metamaterials with zero values and will strongly depend on the wavelength, have strong absorption and anisotropy, since the achievement of zero occurs in areas of anomalous dispersion near the natural frequencies of their structural elements. Optical peculiarity of metamaterials synthesized according to the technologies [11, 12] is that the structural elements in these metamaterials are spherical silver nanoparticles of small size (nanoparticle radius of about 2.5 nm). Isolated resonance of such nanoparticles is in the UV region, therefore, in the wavelength range of at least 450 to 1200 nm, these metamaterials are transparent metamaterials, in which the refractive index is significantly (hundreds of times) larger than the absorption index. Silver nanoparticles are uniformly distributed both over the depth of the layer and its surface, and only in a small neighborhood of nanoparticles, whose dimensions are much smaller than the wavelength, fluctuations in the displacements of nanoparticles relative to each other are taken into account. With a mass content of silver in the composite equal to 3%, the average distance between the centers of neighboring nanoparticles is equal to 30 ± 2 nm. At the same time, in the vicinity of nanoparticles in the region, the linear dimensions of which are

significantly smaller than the wavelength, there are about 30 discretely distributed nanoparticles with fluctuating displacements from the equilibrium position. These fluctuations can be determined using the structure factor in the calculation of the lattice sums. A formula for the complex refractive index of the optical sphere with inclusions with allowance for the structural factor was derived in [19]. On the basis of this formula, in the particular case of M. Garnett transferring to the well-known formula [20], it was shown that the refractive index of the medium can reach zero and close to zero refractive indices in a wide range of wavelengths.

This article is devoted to a theoretical and experimental study of the effect of photon localization in the composite layer (PMMA and Ag) with spherical silver nanoparticles. The effect of localization of photons, considered in this article, is fundamentally different from the known transverse localization of electromagnetic waves in two-dimensional periodic structures, since it is considered in homogeneous transparent media far from the resonance of their structural elements.

2. THEORY OF PHOTON LOCALIZATION IN THE MEDIUM WITH RANDOMLY A NEAR-ZERO REFRACTIVE INDEX

2.1. LOCALIZATION OF PHOTONS AT THE INTERFACE OF THE VACUUM-OPTICAL MEDIUM

The physical meaning of the effect of photon localization in media with a near-zero refractive index will be considered on the example of a single interface between optical media. It is known that for the boundary of two media with deterministic refractive indices n_1 and n_2 have a place rule of choice $n_1 \sin \theta_1 = n_2 \sin \theta_2$, where is the angle of incidence of the wave θ_1 and deterministic angle of refraction θ_2 can be determined with any accuracy [21]. The situation is different if one of the media, for example, medium 2 has a random refractive index n_2 , accepting values in the range of acceptable values $(0, \Delta n_2)$, where $\Delta n_2 < 1$. We assume that different values n_2 , in the interval $n_2, n_2 + dn_2$, with the same probability is implemented

$dW(n_2) = f(n_2)dn_2$, where $f(n_2)$ – distribution function normalized by the normalization condition $\int_0^1 f(n_2)dn_2 = 1$ on the interval (0,1). In this case, the interval (0, Δn_2) is “cut out” from the general interval (0,1), depending on the layer thickness. With the help of experimental reflection spectra you can determine Δn_2 according to the formula $\Delta n_2 = \lambda_1 \lambda_2 / 2d_2(\lambda_2 - \lambda_1)$, where d_2 – layer thickness, λ_1, λ_2 – wavelengths of neighboring minima in the reflection spectrum. In optical media with a random refractive index, in general, $n_1 \sin \theta_1 \neq n_2 \sin \theta_2$ [22]. We assume that n_2 and θ_2 are random values for fixed n_1 and θ_1 . Moreover, we will assume that the quantities n_2 and θ_2 are statically independent quantities. The interface between two media becomes non-uniform. In this case, the inhomogeneity of the boundary is not associated with any geometric inhomogeneities, but is due to the random refractive index.

It is known [21] that when a plane electromagnetic wave interacts with a sharp interface between two media, the wave is extinguished at this boundary and, instead of it, an electromagnetic wave with a different speed propagates in the medium. This phenomenon is described using the Fresnel optics by the extinction theorem, in which the refractive index of the medium is a deterministic quantity, the interface is homogeneous, which allows us to accurately determine the direction of propagation of the refracted wave. In this case, the entire interface surface participates in the wave cancellation. The situation is different if the medium has a random refractive index in the region of quasi-zero values ($\Delta n_2 < 1$) when falling on the boundary of the light beam $z = 0$ with a certain cross-sectional area S_1 . Then, in accordance with the extinction theorem, as shown below, the extinction of the external wave will occur at a point x located at the intersection of the plane of incidence and the surface $z = 0$, satisfying the condition $\Delta n_2 x k_0 \rightarrow 0$, where Δn_2 determines the interval (0, Δn_2) of permissible values of the random refractive index of the medium $k_0 = \omega/c$, where c - the speed of light in vacuum, ω - the frequency of the external wave. This means that the external beam of light is focused in close proximity x , and in accordance

with the uncertainty relation for the coordinate and momentum of the photons, the light flux with some other cross-sectional area will propagate in the medium.

Taking into account the above averaging procedure, we represent the wave in a medium with a random refractive index as a wave packet for the electric fields of a refracted electromagnetic wave, determined using the refractive indices with a random n_2 and θ_2 . Then on the border $z = 0$ we obtain the following relationship between the amplitude of an external plane wave E_{10}^+ and T_0 the amplitude of the refracted wave:

$$E_{10}^+ \exp(-ik_0 x \sin \theta_1) \propto -\frac{\sin(\varphi_2 + \theta_2)}{2 \cos \varphi_2 \sin \theta_2} T_0 F(x, \Delta n_2), \tag{1}$$

where the angle φ_2 is defined by equality $n_2 \sin \theta_2 = \sin \varphi_2$, and the vector \vec{s} has components:

$$s_x = -\sin \varphi_2, s_y = 0, s_z = -\cos \varphi_2, \tag{2}$$

and the function is:

$$F(x, \Delta n_2) = \frac{\cos(-k_0 x \Delta n_2 \sin \theta_2) - 1}{-k_0 x \sin \theta_2} + i \frac{\sin(-k_0 x \Delta n_2 \sin \theta_2)}{-k_0 x \sin \theta_2}. \tag{3}$$

At point $k_0 x \Delta n_2 \sin \theta_2 = 0$ function (3) reaches a maximum equal to Δn_2 , and at points $k_0 x \Delta n_2 \sin \theta_2 = \pi m$, where $m = \pm 1, \pm 2, \dots$ makes vanish. At the same time, it $\Delta x = 2\pi / k_0 \Delta n_2 \sin \theta_2$ represents the spatial extent of the wave packet. The smaller $k_0 \Delta n_2 \sin \theta_2$, then the greater the spatial extent of this wave packet. Given that $k_0 \Delta n_2 \sin \theta_2 = (\Delta p_x) / 2\pi \hbar$ we obtain the uncertainty relation for the pulse and the photon coordinates

$$\Delta x \Delta p_x = 2\pi \hbar. \tag{4}$$

Thus, at the boundary of the vacuum-optical medium with a random refractive index close to zero, the wave refraction does not follow the Snell law, but with the localization of photons, when the external plane wave is extinguished at a point at $k_0 x \Delta n_2 \sin \theta_2 \rightarrow 0$, and then according to the uncertainty relation (4) wave is distributed in the medium in all directions determined by a random angle of refraction θ_2 .

2.2. LOCALIZATION OF PHOTONS INSIDE THE COMPOSITE

We describe the optical properties with a random refractive index close to zero using the integro-differential equation for the propagation of electromagnetic waves [21, 23], and using the procedure of converting the volume integral in this equation into surface integrals for the boundaries 1-2 and 2-3 of the plane-parallel layer 2. We assume that the medium 1, from which the external radiation falls, is a vacuum, and the medium 3 is a semi-infinite optical medium with a refractive index n_3 . The field in the composite layer is represented as a superposition of the electric fields \mathbf{E}_2^+ and \mathbf{E}_2^- , where \mathbf{E}_2^+ is the electric field strength of wave, refracted at the boundary of 1-2 layers, and \mathbf{E}_2^- is the electric field strength of wave reflected from the border 2-3 of this field. We write the electric field strength in the layer as follows:

$$\mathbf{E}_2^{s,p} = f_+^{s,p} \mathbf{E}_1^+ a^+(x, z) + f_-^{s,p} \mathbf{E}_1^+ a^-(x, z),$$

where the indices correspond to s and p to polarized waves, \mathbf{E}_1^+ is the electric field strength of the external wave,

$$a^\pm(x, z) = \frac{1}{ik_0(\mathbf{r}\mathbf{s}_T^\pm)} (\exp[k_0 \Delta n_2(\mathbf{r}\mathbf{s}_T^\pm)] - 1), \quad (5)$$

$k_0 = 2\pi/\lambda$, λ – external radiation wavelength, r – radius-vector of observation points inside the layer, x_2 - the plane of incidence. At the same time $(\mathbf{r}\mathbf{s}_T^\pm) = -x \sin \theta_2 \mp z \cos \theta_2$, \mathbf{s}_T^\pm – unit vectors along the directions of propagation of the refracted and reflected waves inside the layer, θ_2 is the angle of refraction.

The refractive indexes $f_+^{s,p}$ and reflections $f_-^{s,p}$ inside the layer after the necessary calculations are defined as

$$\begin{aligned} f_+^{s,p} &= t_{23}^{s,p} t_{12}^{s,p} \Delta n_2 + \\ &+ \frac{it_{12}^{s,p} t_{23}^{s,p}}{2k_0 d_2 \cos \theta_2} \ln \left(\frac{1 + r_{12}^{s,p} r_{23}^{s,p} \exp[2ik_0 d_2 \Delta n_2 \cos \theta_2]}{1 + r_{12}^{s,p} r_{23}^{s,p}} \right), \\ f_-^{s,p} &= \frac{t_{23}^{s,p} t_{12}^{s,p}}{r_{12}^{s,p}} \Delta n_2 - \\ &- \frac{it_{12}^{s,p} t_{23}^{s,p}}{2k_0 d_2 r_{12}^{s,p} \cos \theta_2} \ln \left(\frac{r_{12}^{s,p} r_{23}^{s,p} + \exp[2ik_0 d_2 \Delta n_2 \cos \theta_2]}{1 + r_{12}^{s,p} r_{23}^{s,p}} \right), \end{aligned} \quad (6)$$

where the non-Fresnel reflection and refraction coefficients at the boundaries of the layer in the case of s-polarization of the waves has the form [24]:

$$\begin{aligned} r_{12}^s &= \frac{n_1 \cos \varphi_2 - n_2 \cos \theta_2}{n_1 \cos \varphi_2 + n_2 \cos \theta_2}, \quad r_{23}^s = \frac{n_2 \cos \theta_2 - n_3 \cos \theta_3}{n_2 \cos \theta_2 + n_3 \cos \theta_3}, \\ r_{13}^s &= \frac{n_1 \cos \theta_1 - n_3 \cos \theta_3}{n_1 \cos \theta_1 + n_3 \cos \theta_3}, \quad t_{12}^s = \frac{2n_1 \cos \varphi_2}{n_1 \cos \varphi_2 + n_2 \cos \theta_2}, \\ t_{23}^s &= \frac{2n_2 \cos \theta_2}{n_2 \cos \theta_2 + n_3 \cos \theta_3}, \quad t_{13}^s = \frac{2n_1 \cos \theta_1}{n_1 \cos \theta_1 + n_3 \cos \theta_3}, \end{aligned} \quad (7)$$

where n_1, n_3 are the refractive indexes of optical media 1 and 3 above and below the layer, respectively, θ_1 is the angle of incidence of external radiation, θ_3 is the angle of refraction in the underlying medium 3.

Similarly, we have the following formulas for the reflection and refraction coefficients at the boundaries of 1-2 and 2-3 layers for p -polarization of waves:

$$\begin{aligned} r_{12}^p &= \frac{n_1 \cos \theta_2 - n_2 \cos \varphi_2}{n_1 \cos \theta_2 + n_2 \cos \varphi_2}, \quad r_{23}^p = \frac{n_2 \cos \theta_3 - n_3 \cos \theta_2}{n_1 \cos \theta_3 + n_3 \cos \theta_2}, \\ r_{13}^p &= \frac{n_1 \cos \theta_3 - n_3 \cos \theta_1}{n_1 \cos \theta_1 + n_3 \cos \theta_3}, \quad t_{12}^p = \frac{2n_1 \cos \varphi_2}{n_1 \cos \theta_2 + n_2 \cos \varphi_2}, \\ t_{23}^p &= \frac{2n_2 \cos \theta_2}{n_2 \cos \theta_3 + n_3 \cos \theta_2}, \quad t_{13}^p = \frac{2n_1 \cos \theta_1}{n_1 \cos \theta_3 + n_3 \cos \theta_1}. \end{aligned} \quad (8)$$

Formulas (7), (8) are obtained in [24] using the extinction theorem separately for boundaries 1-2 and 2-3 for heterogeneous interfaces on which the Snell law is violated due to the random refractive index of medium 2. In this case the angle of incidence is determined from the ratio $n_1 \sin \theta_1 = n_3 \sin \theta_3$, and the angle φ_2 is determined from the relation $n_2 \sin \theta_2 = \sin \varphi_2$. The last relation to the calculation of surface integrals in the cancellation theorem by the stationary phase method is related [21]. In the transition to deterministic values n_2 and θ_2 formulas (7), (8) coincide with the corresponding Fresnel formulas, in which $\varphi_2 = \theta_1$ and $n_1 \sin \theta_1 = n_2 \sin \theta_2$. In the non-Frenelle formulas, considering the reflected radiation with the help of the corresponding surface integral and placing the observation points above the layer, the angle φ_2 is related to the random reflection angle θ_R as $\varphi_2 = \pi - \theta_R$.

The reflectivity of a layer with a random refractive index close to zero in the interval $(0, \Delta n_2)$ is $\Delta n_2 < 1$ calculated as

$$R_{123} = R_{123}^p \cos^2 \alpha_i + R_{123}^s \sin^2 \alpha_i, \quad (9)$$

where α_i is the angle between the electric vector of the electromagnetic wave and the plane of incidence,

$$R_{123}^{s,p} = |r_{123}^{s,p}|^2 \text{ and}$$

$$r_{123}^{s,p} = r_{12}^{s,p} \Delta n_2 - i \frac{1 - (r_{12}^{s,p})^2}{r_{12}^{s,p} \frac{4\pi}{\lambda} d_2 \cos \theta_2} \ln \left(\frac{1 + r_{12}^{s,p} r_{23}^{s,p} \exp \left[\frac{4\pi}{\lambda} i d_2 \Delta n_2 \cos \theta_2 \right]}{1 + r_{12}^{s,p} r_{23}^{s,p}} \right). \quad (10)$$

For natural light $\sin^2 \alpha_i = \cos^2 \alpha_i = 1/2$ [21].

The transmittance of the composite layer is determined using the following formulas:

$$T_{123} = T_{123}^s \sin^2 \alpha_i + T_{123}^p \cos^2 \alpha_i,$$

where

$$T_{123}^{s,p} = \frac{n_3 \cos \theta_3}{n_1 \cos \theta_1} |t_{123}^{s,p}|^2, \quad (11)$$

with optical transmittance layer

$$t_{123}^{s,p} = -i \sqrt{\frac{n_1 \cos \theta_1}{n_3 \cos \theta_3}} + \frac{t_{12}^{s,p} t_{23}^{s,p}}{\frac{4\pi}{\lambda} i d_2 \cos \theta_2 \sqrt{-r_{12}^{s,p} r_{23}^{s,p}}} \times \left\{ \ln \frac{1 + \exp \left[\frac{2\pi}{\lambda} i d_2 \cos \theta_2 \Delta n_2 \right] \sqrt{-r_{12}^{s,p} r_{23}^{s,p}}}{1 + \sqrt{-r_{12}^{s,p} r_{23}^{s,p}}} - \ln \frac{1 - \exp \left[\frac{2\pi}{\lambda} i d_2 \cos \theta_2 \Delta n_2 \right] \sqrt{-r_{12}^{s,p} r_{23}^{s,p}}}{1 - \sqrt{-r_{12}^{s,p} r_{23}^{s,p}}} \right\}, \quad (12)$$

taking into account the fact that $\Delta n_2 < 1$ we have $r_{12}^{s,p} r_{23}^{s,p} < 0$.

When calculating the reflectivity and transmittance of the layer in the non-Frennel coefficients $r_{ik}^{s,p}$ and $t_{ik}^{s,p}$ ($i, k = 1, 2, 3$), the values n_2 will be considered equal Δn_2 , since the main dependence on the random refractive index of the layer is determined by exponential factors in the reflection and transmission coefficients of the layer. The presence of the first term on the right-hand side of formula (12) is due to the effect of ideal optical transmission when the refractive

index tends to zero from the range of permissible values $(0, \Delta n_2)$.

Formulas (9), (11) satisfactorily describe the experimental reflection and transmission spectra of Fig. 5, 6. Indeed, as can be seen from Figs 5, 6, for some values of the layer thickness, the interference of light in the reflection and transmission spectrum disappears. This is because the angle of refraction θ_2 becomes complex. For complex angles of refraction, we have the following relations:

$$\theta_2 = \theta_2' - i\theta_2'', \quad \cos \theta_2 = ish\theta_2'' = i\sqrt{x_2^2 - 1}, \quad (13)$$

$$x_2 = ch\theta_2'', \quad \theta_2' = \pi/2, \quad \sin \theta_2 = x_2,$$

$$\cos \varphi_2 = \sqrt{1 - (n_2)^2 x_2^2}, \quad \sin \varphi_2 = n_2 x_2,$$

where θ_2' is the actual angle of refraction, which determines the direction of wave propagation along the layer, θ_2'' is the angle in the direction of which the wave attenuation occurs. The sign in front of the root in these relations is chosen so that the wave is damped, regardless of its direction of propagation.

Let us calculate the reflective and transmission capacity of the layer using formulas (9), (11), taking into account the above selective properties of these formulas, when the maxima $R_{123}^{s,p}$ and $T_{123}^{s,p}$ are reached at $x_2 \rightarrow 1$. In this case, after eliminating the type uncertainty $(0/0)$, we obtain from (10), (12) the following formulas:

$$r_{123}^s = \Delta n_2 - i \frac{\Delta n_2}{\cos \varphi_2} \frac{1}{k_0 d_2} \beta_{123}^s, \quad (14)$$

$$r_{123}^p = \Delta n_2 + i \frac{1}{\Delta n_2 \cos \varphi_2} \frac{1}{k_0 d_2} \beta_{123}^p,$$

where

$$\beta_{123}^s = \ln \left(1 - i \frac{(2\pi/\lambda)d_2}{(1/\cos \varphi_2) + (1/n_3 \cos_2)} \right),$$

$$\beta_{123}^p = \ln \left(1 - i \frac{(2\pi/\lambda)d_2(\Delta n_2)^2}{(n_3/\cos \theta_3) + (1/\cos \varphi_2)} \right).$$

The transmittance of the layer when $x_2 \rightarrow 1$ after eliminating type uncertainty $(0/0)$ are:

$$t_{123}^s = i \sqrt{\frac{n_1 \cos \theta_1}{n_3 \cos \theta_3}} - i \frac{\Delta n_2}{n_3 \cos \theta_3 (\pi/\lambda) d_2} (\alpha_{123}^s - \gamma_{123}^s), \quad (15)$$

$$t_{123}^p = i \sqrt{\frac{n_1 \cos \theta_1}{n_3 \cos \theta_3}} - i \frac{1}{\Delta n_2 \cos \theta_3 (\pi/\lambda) d_2} (\alpha_{123}^p - \gamma_{123}^p),$$

where $\alpha_{123}^{s,p}$ and $\gamma_{123}^{s,p}$ correspond to the first and second terms in braces in the formula (12). When $x_2 \rightarrow 1$ we get that $\alpha_{123}^{s,p}$ vanishes, and

$$\gamma_{123}^s = \ln \left(1 + i \frac{(2\pi / \lambda)d_2}{(1 / \cos \varphi_2) + (1 / n_3 \cos \theta_3)} \right), \quad (16)$$

$$\gamma_{123}^p = \ln \left(1 + i \frac{(2\pi / \lambda)d_2 (\Delta n_2)^2}{(1 / \cos \varphi_2) + (n_3 / \cos \theta_3)} \right).$$

The presence of the first term on the right-hand side of formulas (15) is due to the fact that with accurate refractive index vanishing from the integration region $(0, \Delta n_2)$, it is necessary to eliminate the type uncertainty $(0/0)$ in the corresponding layer transmittance. As shown in [16], when the refractive index of the layer is exactly zero, the reflection coefficient of the layer is zero, and the transmittance of the layer is 1, which corresponds to the effect of an ideal optical enlightenment.

Consider the optical properties of the composite layer at complex angles of refraction determined by relations (13). This case corresponds to the minimum transmission of the layer, since in the case of complex angles of refraction a wave propagates along the layer at $\theta_2' = \pi / 2$. In this case, part of the external light wave is converted into side waves. In the case of complex angles of refraction, functions (5), which determine the spatial distribution of the field inside the layer, are equal to each other, i.e. $a^+ = a^- = a(x, z)$.

Then

$$|a|^2 = \frac{1}{x^2 x_2^2 + |z|^2 (x_2^2 - 1)} \left(\exp \left[-2k_0 \Delta n_2 |z| \sqrt{x_2^2 - 1} \right] + 1 - 2 \cos(k_0 \Delta n_2 x^2 x_2^2) \exp \left[-k_0 \Delta n_2 |z| \sqrt{x_2^2 + 1} \right] \right).$$

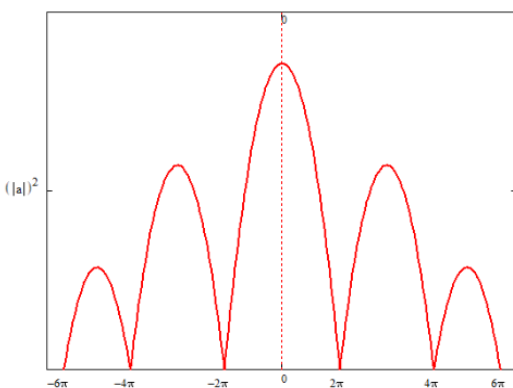


Fig. 1. Spatial distribution of photons inside the composite layer (on the x-axis - wave phase).

When $x_2 \rightarrow 1$, this function takes the following form:

$$|a|^2 = \frac{2 - 2 \cos(k_0 \Delta n_2 x)}{x^2}. \quad (17)$$

Fig. 1 shows the dependence of this function on a dimensionless variable or phase of the wave $k_0 \Delta n_2 x$. When $k_0 \Delta n_2 x = 2\pi m$, where $m = \pm 1, \pm 2, \dots$, is the function $|a|^2 = 0$, when $k_0 \Delta n_2 x = \pm 3\pi, \pm 5\pi, \dots$ this function is equal $|a|^2 = 4(k_0 \Delta n_2)^2 / (3\pi)^2, 4(k_0 \Delta n_2)^2 / (5\pi)^2$ etc. The linear dimensions of the localization volume are determined with the help of the main maximum of the function (17) as $\Delta x = 2\lambda / (\Delta n_2)$.

3. EXPERIMENTAL DETECTION OF EFFECT OF PHOTON LOCALIZATION IN A COMPOSITE LAYER PMMA&AG

The optical scheme for the localization of photons with a normal incidence of a laser beam on the surface of a composite layer 10 microns thick on a glass substrate is shown in Fig. 2. A helium-neon laser with a power of 1 mW with longitudinal polarization of light and a wavelength of 632 nm was used as a coherent radiation. The diameter of the laser beam was 1 mm. Radiation transmitted through the sample in the longitudinal and transverse directions was recorded using a CD camera.

Experimental reflection and transmission spectra of layers (PMMA & Ag) of various thickness on a glass substrate were measured on an Ocean Optics QE65000 spectrophotometer in

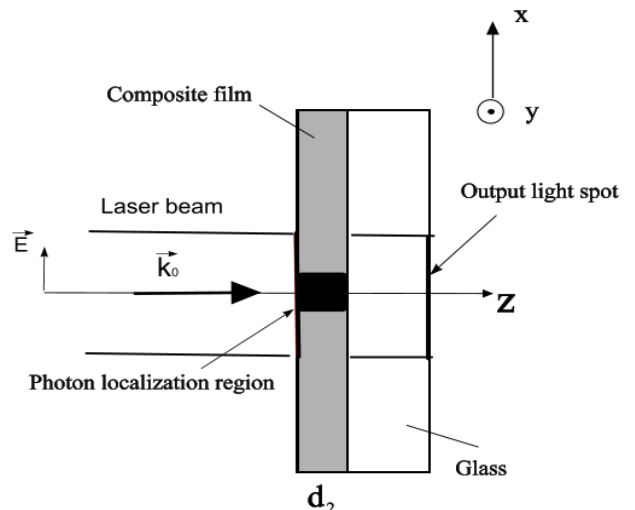


Fig. 2. Optical scheme of laser irradiation of the PMMA&Ag layer.

a wide wavelength range from 300 to 1000 nm. For comparison, the reflection and transmission spectra of the layers of the material of the PMMA matrix of the same thickness were measured separately on glass with a normal incidence of light.

When the sample is irradiated in the composite layer, a photon localization region is formed, the linear dimensions of which are comparable with the layer thickness $d_2 = 10 \mu\text{m}$ (see Fig. 7).

4. RESULTS AND DISCUSSION

Fig. 3 presents the theoretical spectra composite layer reflections calculated according to the formulas (9) and (10), depending on the length wave and parameter selection x_2 . As can be seen

from the figure as x_2 is closer to one the reflectivity of the layer decreases. When $x_2 = 1$ the reflectivity of the layer with numerical values of physical quantities indicated in **Fig. 4** at a wavelength of $\lambda = 632 \text{ nm}$ equal to $R_{123} = 1.926\%$.

Fig. 4 presents theoretical transmittance spectra of the composite layer, calculated using formulas (15) and (16). Using formulas (15), (16), we define the transmittance value of this layer at $x_2 = 1.01$, equal to $T_{123} = 95.37\%$ (Fig. 4a). As can be seen from Fig. 4b with $x_2 = 1.0001$ throughput layer increases significantly, reaches units and practically does not depend on the wavelength in wide wavelength range from 400 to 1200 nm.

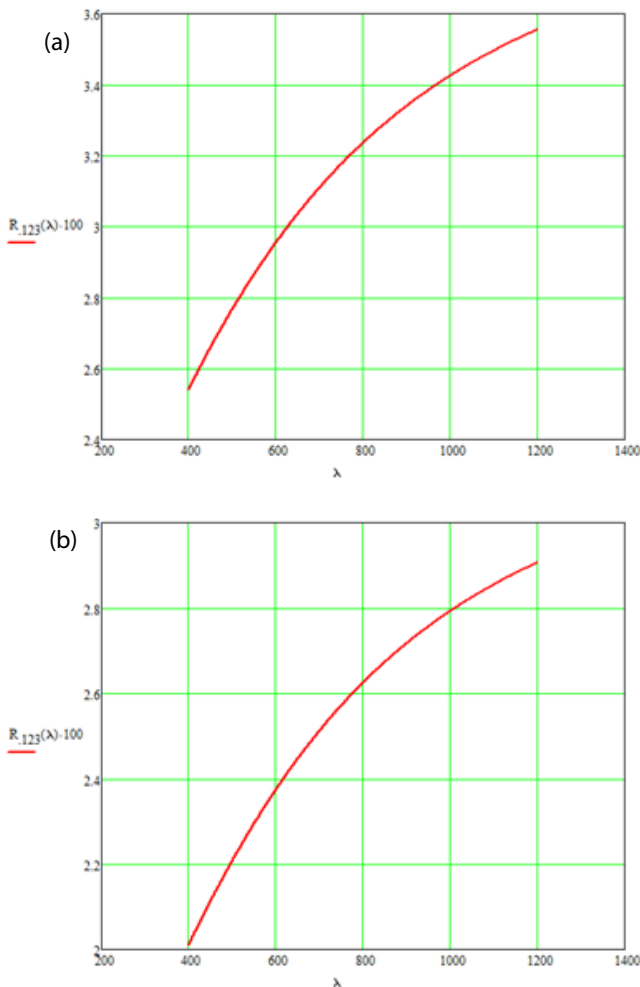


Fig. 3. The theoretical reflectivity of a composite layer with a random refractive index close to zero, depending on the wavelength for a) $x_2 = 1.01$ and b) $x_2 = 1.0001$. The layer thickness is $d_2 = 10 \mu\text{m}$, the refractive index of the glass substrate is $n_2 = 1.5$, $\Delta n_2 = 0.1625$, the wavelengths are indicated in nanometers.

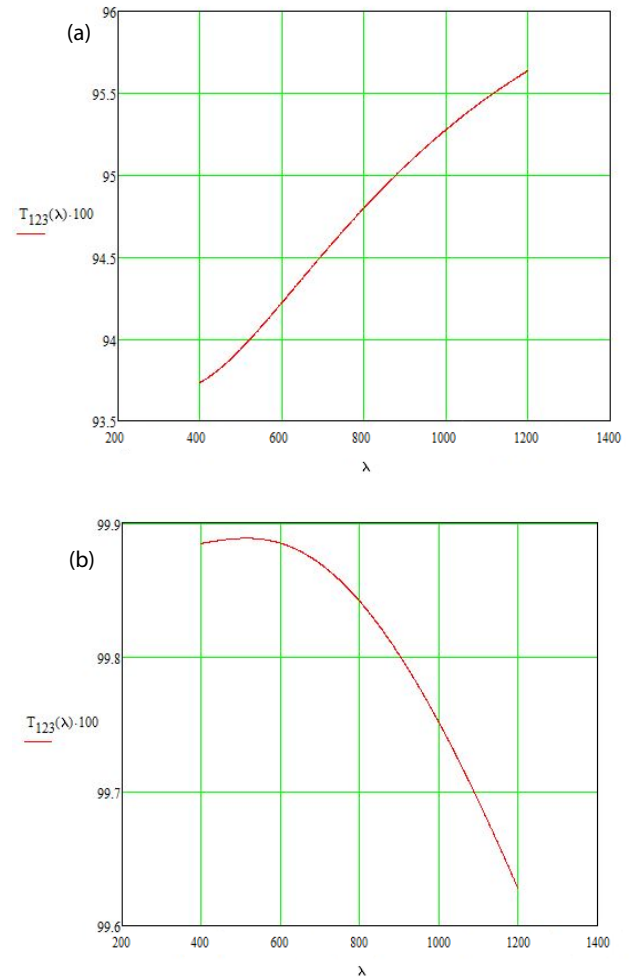


Fig. 4. The theoretical transmittance of the composite layer with a random refractive index close to zero, depending on the wavelength for a) $x_2 = 1.01$ u b) $x_2 = 1.0001$. The layer thickness is $d_2 = 10 \mu\text{m}$, the refractive index of the glass substrate is $n_2 = 1.5$, $\Delta n_2 = 0.1625$, the wavelengths are indicated in nanometers

The ratio between the reflectivity and the transmittance of a composite layer with a random close to zero refractive index is written as follows:

$$R_{123} + T_{123} + W_{123} = 1, \quad (18)$$

where W_{123} is the part of external radiation propagating along the layer. Using the limit values $R_{123} = 0.019$ and $T_{123} = 0.95$ for a sample with a layer thickness of $d_2 = 10 \mu\text{m}$ for a normal incidence of a laser beam with a wave length $\lambda = 632 \text{ nm}$, we get $W_{123} = 0.031$.

Wave flow effect for the flat surface of the composite layer (PMMA & Ag) was discovered by us experimentally [16].

Fig. 5 shows the experimental reflection and transmission spectra of samples with composite Ag&PMMA layers on glass substrates with respect to the spectral values of reflection and transmission

of a glass substrate. When the layer thickness of the $d_2 = 5.20 \text{ mkm}$, as can be seen from Fig. 5a, the interference of light is detected and the refractive index of the composite can be calculated from the location of the minima. The formation of these interference minima is due to the fact that the range of permissible values $(0, \Delta n_2)$ of the random refractive index of the medium is such that $\Delta n_2 \ll 1$.

In the experimental reflection and transmission spectra in Fig. 5, where the interference of light is observed in formulas (9), (11), the angles of refraction should be considered valid. We define these angles using the following relations:

$$\begin{aligned} \cos \theta_2 &= \sqrt{1 - y_2^2}, \quad y_2 = \sin \theta_2, \quad y_2 \leq 1, \\ \sin \varphi_2 &= \Delta n_2 y_2, \quad \cos \varphi_2 = \sqrt{1 - (\Delta n_2)^2 y_2^2}. \end{aligned}$$

The value $x_2 = 1$ separates the areas of complex and real angles of refraction in the layer. At $x_2 > 1$ angles of refraction θ_2 are complex, and at $x_2 < 1$ angles of refraction are real. When $x_2 = 1$ the angle θ_2'' that determines the direction of attenuation of the wave is equal to zero, that is the attenuation of the wave propagating along the layer occurs in the direction perpendicular to the surface of the layer.

The angle θ_2'' is a random variable, varying from $-\pi/2$ to $+\pi/2$, including $\theta_2'' = 0$. In this case, the value $x_2 = \text{ch } \theta_2''$ varies from 0 to 2.53. However, as can be seen from formulas (10), (12), the reflection and transmission coefficients of a layer with a random close to zero refractive index have a sharp maximum at $x_2 = 1$, that is, at $\theta_2'' = 0$. This means that when a random variable x_2 changes, a value $x_2 = 1$ is most likely to be realized, which allows us to simplify the calculation of the reflectance and transmittance of the layer, as well as the field inside the layer with reflection and refraction coefficients $f_{\pm}^{s,p}$ (see relation (6)).

As follows from the transmission spectra of Fig. 5b of composite layers (PMMA&Ag) with silver nanoparticles at a thickness of $d_2 = 10, 30, 50 \mu\text{m}$, the relative transmittance of the layers with respect to the optical transmittance of the glass substrate is greater than 1 and practically does not depend on the wavelength. This means that in these layers an amplified optical transmission of

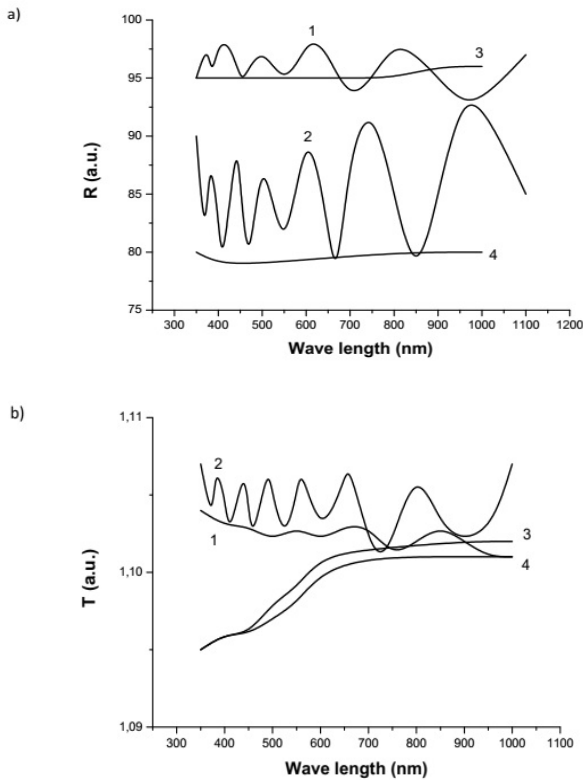


Fig. 5. The experimental reflection spectra (a) and transmittance (b) of the composite layers (PMMA & Ag) with different thickness of silver nanoparticles on a glass substrate. The spectra are presented in relative units with respect to the optical transmission and reflection of a glass substrate 2 mm thick. The relative reflectivity of the glass substrate in Fig. 5a is 100, and its own value is 0.07. Curve 1 - layer thickness $d = 5 \mu\text{m}$; curve 2- $d = 20 \mu\text{m}$; curve 3- $d = 10 \mu\text{m}$; curve 4- $d = 50 \mu\text{m}$

light is detected in a wide range of wavelengths. In the polymer layers of the same thickness, the relative transmittance $T_{\text{PMMA/glass}}/T_{\text{glass}} < 1$, that is, the deposition of polymer layers on the surface of the glass substrate leads to additional absorption of *PMMA/glass* samples. Thus, the addition of silver nanoparticles to the polymer matrix leads to an increase in the transparency of thick composite layers synthesized according to the nanotechnology developed by us.

Fig. 6 shows the experimental reflection and transmission spectra of samples with layers of PMMA polymer on glass substrates with respect to the spectral values of reflection and transmission of the glass substrate itself. In the polymer layers of the same thickness, as can be seen from Fig. 6, the interference of light is not detected, since the refractive index of this polymer is 1.49.

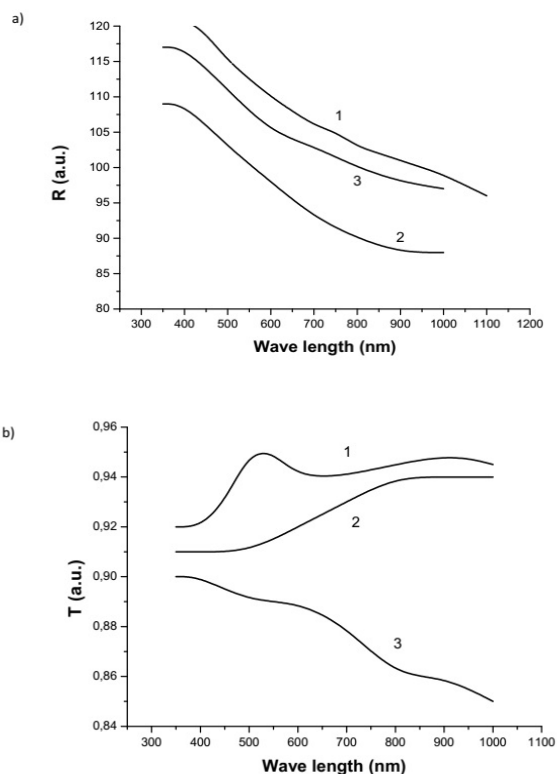


Fig. 6. Experimental reflection (a) and transmittance (b) spectra of polymer layers of different thickness on a glass substrate. The experimental spectra are presented in relative units with respect to the reflectivity and transmittance of the glass substrate. The relative reflectivity of the glass substrate in Fig. 6a is 100, and its own value is 0.07. Curve 1 - layer thickness $d = 5 \mu\text{m}$; curve 2 - $d = 10 \mu\text{m}$; curve 3 - $d = 50 \mu\text{m}$.

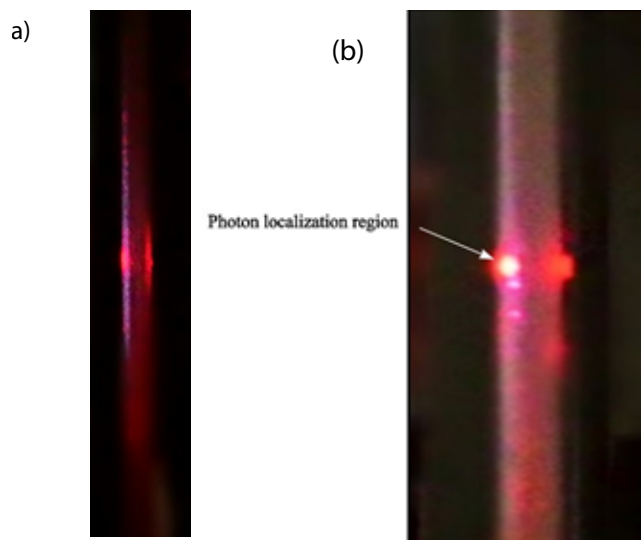


Fig. 7. Localization of photons in the *PMMA&Ag* layer at a normal incidence of a laser beam on the surface of the layer (photo): a) Photo of a *PMMA/glass* sample with a polymer layer; b) Photo sample (*PMMA & Ag*) / glass with a composite layer. The arrow indicates the region of photon localization.

Fig. 7a shows a photograph of a PMMA polymer layer on glass, where the region of photon localization is absent. **Fig. 7b** shows a photograph of the photon localization region in the composite layer. We will consider the effect of photon localization in the composite layer as a spatial transformation of the energy density of external radiation, when the beam of external radiation is localized in a small region inside the layer. At $\lambda = 632 \text{ nm}$ and for $\Delta n_2 = 0.1625$ a composite layer with a thickness of $d_2 = 10 \mu\text{m}$, we obtain a $\Delta x = 7.778 \mu\text{m}$ when linear dimensions of the photon localization region smaller than the layer thickness. Thus, the photon localization region is much smaller than the diameter of the laser beam irradiating the composite layer.

5. CONCLUSION

This article presents theoretical and experimental evidence for the existence of a photon localization effect in a metamaterial layer with a random refractive index close to zero. The detection of this effect indicates that in such optical media the usual beam path characteristic of Fresnel optics is violated. As a result, a parallel beam of light inside the layer is localized in a small region. A violation of the principle of reversibility of light fluxes in the composite layer was experimentally

discovered in [14], and the explanation of this phenomenon was associated with the effect of photon localization. This article provides direct evidence of the existence of a photon localization effect in optical media with a random refractive index close to zero.

As follows from the conservation law (18), the localization of photons inside the composite layer is accompanied by light bending around the flat surface of the layer.

ACKNOWLEDGMENTS

The work was performed as part of the state task.

REFERENCES

1. Anderson PW. Absence of diffusion in certain random lattices. *Phys. Rev.*, 1958, 109:1492-1505.
2. John S. Electromagnetic absorption in a disordered medium near a photon mobility edge. *Phys. Rev. Lett.*, 1984, 53:2169-2172.
3. Anderson PW. The question of classical localization: A theory of white paint. *Phil. Mag.*, 1985, B 52:505-509.
4. Wiersma DS, Bartolini P, Lagendijk A, Righini R. Localization of light in a disordered medium. *Nature*, 1997, 390:671-673.
5. Chabanov AA, Stoytchev M, Genack AZ. Statistical signatures of photon localization. *Nature*, 2000, 404:850-853.
6. Störzer M, Gross P, Aegerter CM, Maret G. Observation of the critical regime near Anderson localization of light. *Phys. Rev. Lett.*, 2006, 96:063904.
7. Sperling T, Buhner W, Aegerter CM, Maret G. Direct determination of the transition to localization in three dimensions. *Nature Photon.*, 2013, 7:48-52.
8. Segev M, Silberberg Y, Christodoulides DN. Anderson localization of light. *Nature Photonics*, 2013, 7:197-204; DOI: 10.1038/NPHOTON.2013.30.
9. Hedayati MK, Faupel F, Elbahzi M. Review of Plasmonic Nanoparticle Metamaterial Absorber. *Materials*, 2014, 7:1221.
10. Goyal A, Sharma A, Saiki I, Chandak N, Sharma P. Tailoring of optical and electrical properties of PMMA by incorporation of Ag nanoparticles. *Bull.Mater.Sci.*, 2017, 40(4):615-621.
11. Gadomsky ON, Ushakov NM et al. Nanokompozitsionnoe prosvetlyayushchee pokrytie v vide tolstoy plenki i sposob ego polucheniya [Nanocomposite antireflection coating in the form of a thick film and method for its production]. *Patent RF, no. 2456710, 2012.*
12. Katnov VE, Gadomsky ON, Stepin SN, Katnova RR. Sposob polucheniya prosvetlyayushchego pokrytiya [A method of obtaining an antireflection coating]. *Patent RF, no. 2554608, 2015.*
13. Gadomsky ON, Stepin SN, Katnov VE, Zubkov EG. Nanostrukturnye kompozitnye sloi s kvazinulevym pokazatelem prelomleniya [Nanostructured composite layers with a quasi-zero refractive index]. *Zhurnal prikladnoy spektroskopii*, 2013, 80(5):738-745 (in Russ.).
14. Gadomsky ON, Ushakov NM, Shchukarev IA. Narushenie printsipa obratimosti svetovykh potokov v opticheskikh sredakh so sluchaynym blizkim k nulyu pokazatelem prelomleniya [Violation of Light Beam Reversibility Principle in Optical Media with a Random Quasi-Zero Refractive Index]. *JETP*, 2017, 125(4):564-571; DOI: 10.1134/S106377611709014X (in Russ.).
15. Gadomsky ON, Stepin SN, Ushakov NM, Gadomskaya IA. Enhancement and focusing of light in nanostructured quasi-zero refractive index films. *Optics Communication*, 2014, 330:99-106.
16. Gadomsky ON, Altunin KK. Ideal'noe opticheskoe prosvetlenie kompozitnykh plenok [Ideal optical antireflection of composite films activated by spherical nanoparticles]. *Pis'ma v JETP*, 2009, 90(4):251-256 (in Russ.).
17. Li Y, Kita S, Munoz P, Reshef O et al. On-chip zero-index metamaterials. *Nature Photonics*, 2015, 198:1-8.
18. Dubinov AE and Mytareva LA. Invisible cloaking of material bodies using the wave flow method. *Physics—Uspekhi*, 2010, 53(5):455-479.
19. Gadomsky ON, Altunin KK, Stepin SN and Katnov VE. Near-field effect in composite

- materials with a quasi-zero refractive index. *Optics Communication*, 2014, 315:286-292.
20. Vinogradov AP et al. On the problem of the effective parameters of metamaterials. *Physics–Uspekhi*, 2008, 51(5):485; DOI: 10.1070/PU2008v051n05ABEH006533.
 21. Born M and Wolf E. *Principles of Optics*. Pergamon Press, 4th Edition, 1968.
 22. Gadomsky ON, Gadomskaya IV. Nezerkalnoe otrazhenie sveta na neodnorodnoy granitse razdela dvukh sred i v nanostrukturnom sloe s blizkim k nulyu pokazatelem prelomleniya [Nonspecular reflection of light at an inhomogeneous interface between two media and in a nanostructured layer with a quasi-zero refractive index]. *JETP*, 2015, 147:195-208; DOI: 10.7868/S0044451015020017 (in Russ.).
 23. Gadomskii ON. Two electron problem and the nonlocal equations of electrodynamics. *Physics–Uspekhi*, 2000, 43:11, 1071–1102; DOI: 10.1070/PU2000v043n11ABEH000795.
 24. Gadomsky ON, Shchukarev IA. Effekt ogibaniya svetom v ploskoparallelnom sloe s kvazinulevym pokazatelem prelomleniya pod deystviem ogranichennykh svetovykh puchkov [The light wave flow effect in a plane-parallel layer with a quasi-zero refractive index under the action of bounded light beams]. *JETP*, 2016, 123(2):184-196; DOI: 10.1134/S1063776116070050 (in Russ.).

FUNCTIONAL ELASTOMERIC MATERIALS BASED ON BUTADIENE-STYRENE RUBBER AND MAGNETITE

Aram A. Khachaturov, Eugene E. Potapov

Lomonosov Moscow State Institute of Fine Chemical Technologies of MIREA-Russian University of Technology, <http://www.chemtech.mirea.ru/>
Moscow 119435, Russian Federation

Alexander S. Fionov, Vladimir V. Kolesov

Kotelnikov Institute of Radioengineering and Electronics of Russian Academy of Sciences, <http://cplire.ru/>
Moscow 125009, Russian Federation

Eugene M. Ilyin

Bauman Moscow State Technical University, <http://www.bmstu.ru/>
Moscow 105005, Russian Federation

xa4aram@mail.ru, fionov@cplire.ru, kvv@cplire.ru, svitar@yandex.ru, evgil45@mail.ru

Abstract. The samples of functional elastomeric composite material based on butadiene-styrene rubber and magnetite with the concentration ranging 0...300 weight parts per 100 weight parts of elastomer were prepared in this work. Stress-strain, electrophysical and microwave properties for these samples were investigated. The concentration dependences of the investigated parameters were obtained. The influence of the magnetic field on the reflectance of samples on the metal in the frequency range 25.86...37.5 GHz were investigated. The developed composites can be used as effective radioabsorbing and shielding materials with controlled properties, including gradient ones.

Keywords: magnetite, functional material, butadiene-styrene rubber, electrophysical properties, stress-strain properties, microwave, reflection coefficient, absorption coefficient

UDC 678.046:678.4:539.4:620.22:620.17:621.315.61:621.37.029.6

Bibliography - 20 references

Received 15.11.2018, accepted 21.01.2019

RENSIT, 2019, 11(2):189-198

DOI: 10.17725/rensit.2019.11.189

CONTENTS

1. INTRODUCTION (189)
 2. MATERIALS, TECHNOLOGIES, RESEARCH METHODS (190)
 3. RESULTS AND DISCUSSION (194)
 4. CONCLUSION (197)
- REFERENCES (197)

1. INTRODUCTION

Composite materials are a heterogeneous system that consist of a matrix (polymers, ceramics or metals) in which are distributed high-strength or high-modulus fibers or particles. Dispersion-strengthened polymeric composite materials are a structure consisting of a matrix in which are uniformly distributed the finely-divided particles. Disperse filler particles are introduced into the matrix by special technological methods. In this case, the particles should not actively interact

with the matrix and should not dissolve in the matrix until the melting point is reached. The matrix perceives the main load in these materials, in which the reinforcing phase of the filler creates a structure that hinders the movement of dislocations. Dispersion-strengthened polymeric composite materials are, as a rule, isotropic.

Strength and hardness of the composite material depends on the properties of the filler, but the matrix influence to the properties of composite materials. For example, the thermal conductivity and electrical conductivity of the composite material strongly depend on the conductivity of the matrix. The matrix serves as an adhesive that connects the filler particles to the material and gives the product the desired shape. The effect of the filler particles in the matrix is consist to change the mechanical and electrophysical properties: an

increase in the tensile modulus, an increase in tensile strength, an increase in resistance to impact load, a decrease in strain relaxation and thermal expansion, an increase in electric conductivity, an increase in permittivity and magnetic permeability. Herewith the total cost of the material is reduced, because the cost of the polymer is more than the cost of the filler.

A significant increase in strength at the micro level is determined by statistical factors. The probability that a sample of material contains a sufficiently large defect, which can cause brittle failure, falls with a decrease in the sample. Also, the defect does not increase and does not affect on other fibers if few fibers were destroyed in matrix. In presence of bonding material the defect of the single fiber is not critical because the stress is distributed between other fibers.

The presence of spherical particles of filler in elastomeric material lead to better tensile modulus. The tensile modulus of filled elastomeric material E_{CM} refers to the tensile modulus of unfilled elastomeric material E as:

$$E_{CM} = E(1 + 2.5f + 14.1f^2), \quad (1)$$

where f – is volume concentration of the dispersion phase [1].

In the area of polymeric materials science the great attention is paid to the issue of search new functional fillers. Based thereon we can obtain polymer composite materials, then have unique characteristics, including controlled properties.

Perspective filler for composite materials is magnetite – is ore mineral, pervasive in nature, ferro-ferrite with chemical formula Fe_3O_4 and spinel structure.

Magnetite has unique electrophysical and magnetic characteristics. In present significant amount of polymer composite materials based on magnetite have been developed. In literature the large amount papers published extensively, in which shows the results of investigation of structure and properties of same materials, also, possible areas of application of this materials were proposed in this papers. Magnetite sheets with thickness

200...300 *nm* were obtained and investigated by authors of this paper [2], it can be used in quality of perspective material in spintronic. Based on results of investigation converse magnetostrictive effect for composite material which consist of synthetic isoprene rubber and magnetite in this paper [3] conclusion about possible of application this materials in quality of dynamic absorber and vibration isolator had been made. In biomedical magnetic polymeric microspheres magnetite has been actively applied [4-6]. Polymeric composites based on polystyrene matrix and magnetite can be used in quality sorption material [7, 8]. In this paper [9] the results of investigation of electrophysical, magnetic and microwave absorption properties of materials, which consist of thermoplastic natural rubber filled nanosized magnetite particles, were described. This materials, according to the author, can be used in areas such as radio technology and electronic engineering.

Thus, polymer composite materials, which consist magnetite as active functional component, can be successfully used in many areas of technique. Herewith elastomeric materials filled of natural magnetite were not uninvestigated completely. Therefore, the main purpose of this work was to obtain elastomeric composite materials based on butadiene-styrene rubber SKS-30 ARK and magnetite and to study the effect of the filler on the technological, elastic-strength, electrophysical and microwave characteristics of the obtained materials.

2. MATERIALS, TECHNOLOGIES, RESEARCH METHODS

In this work, butadiene-styrene rubber SBR-1500 (GOST 15627-79 for a similar SKS-30 ARK) was used as a matrix, and magnetite – Fe_3O_4 , iron-ore concentrate with a mass fraction of iron more than 69.5% (see **Table 1**), technical specifications 0712-030-001186803-99

Table 1.

Chemical composition of iron-ore concentrate [11].

Content, mass fraction, %												
Fe _{eq}	Fe ₂ O ₃	FeO	SiO ₂	Al ₂ O ₃	MgO	CaO	Na ₂ O	K ₂ O	TiO ₂	S	P	Losses
70.1	66.86	29.28	2.79	0.14	0.21	0.09	0.05	0.03	0.03	0.05	0.01	0.27

(Joint-stock company «Lebedinskii ore mining and processing enterprise»), as a filler.

Particle size distribution of iron-ore concentrate powder were determined with a laser diffractometer Analysette 22 MicroTec Plus. Differential and cumulative grading curve of particles distribution of iron-ore concentrate powder is shows on Fig. 1. It can be seen that particles distribution is unimodal particle size range between 0.1 to 100 μm. The maximum distribution corresponds to a particle size of about 20 μm. As can be seen from the integral curve, 90% of the iron-ore concentrate particles are smaller than 40 μm.

Fig. 2 shows the diffraction pattern of iron-ore concentrate powder, which was shoted using diffractometer HZG-4 (Ni-filter) with CuKα = 1.54051 Å on a diffracted beam in a step-by-step mode with a pulse-recruitment time of 10 s and a step size of 0.02° in the 2Θ range 2...80°.

Qualitative analysis of the diffractogram was conducted using the PDF-2 and COD databases. Based on this it can be said that the concentrate of iron ore is magnetite (diffraction reflections at 2Θ ~36°, ~57°, ~63°), in which

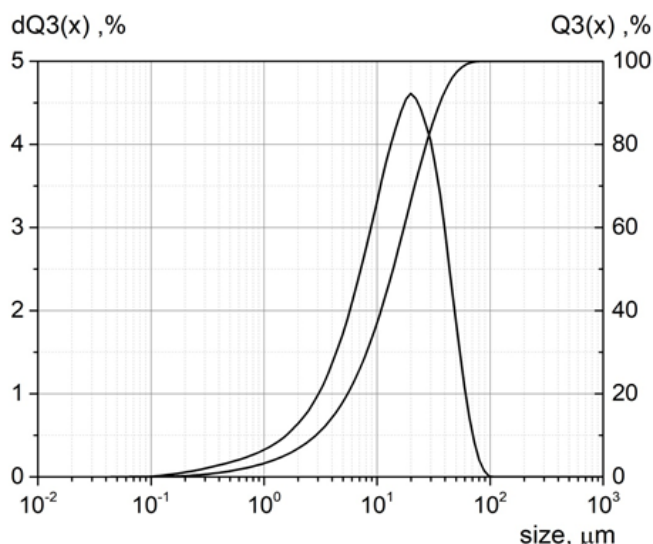


Fig. 1. Differential and cumulative grading curve of particles distribution of iron-ore concentrate powder.

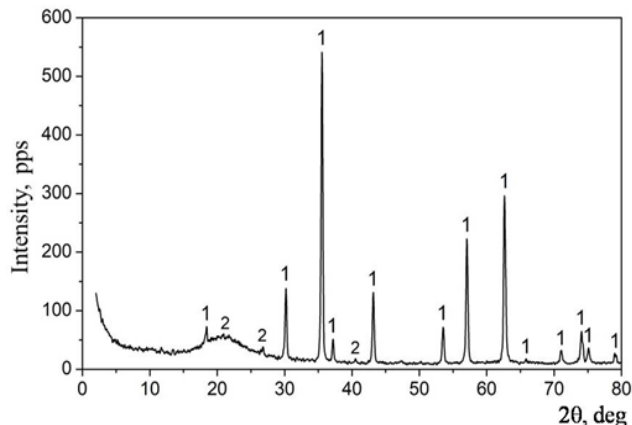


Fig. 2. Diffraction pattern of iron-ore concentrate: 1 – phase Fe₃O₄; 2 – phase SiO₂.

silicon oxide is present as the impurity phase (an amorphous halo is observed in angle range 2Θ ~16°-26° and diffraction reflections at 2Θ ~27°, ~41°, characteristic for quartz [10]) in an amount of about 5-6% (the content of silicon oxide, determined by semi-quantitative analysis of diffraction pattern using the software Match, the content of silicon oxide in the concentrate, according to data provided by «Lebedinskii ore mining and processing enterprise», 2.79% – see Table 1).

The cubic lattice parameter, calculated from the most intense reflections, is a = 8.39113 (0.00289). The average crystallite size, calculated from the Scherrer formula, is D ≈ 230 Å.

Magnetite belongs to the family of ferrites (spinel). The cubic crystal lattice of spinel is formed by oxygen anions O₂, with which Fe³⁺ and Fe²⁺ cations are connected. In this case, iron cations can be surrounded by four anions O²⁻ (tetrahedron) and six anions O²⁻ (octahedron). Accordingly, magnetite has a crystal structure of reversed spinel: (Fe³⁺) [Fe²⁺ Fe³⁺]O₄. In the first part of the structure – (Fe³⁺) there are cations only with valence +3, and in the second part – [Fe²⁺ Fe³⁺] cations are twice as large and they have valence of both 2⁺ and 3⁺.

Unlike ferromagnets, magnetite has a high resistivity value, a lower saturation induction value, and a more complex temperature dependence of induction. Magnetite is a

semiconductor, the specific electrical conductivity of monocrystalline magnetite is maximum at room temperature ($250 \text{ Ohm}^{-1} \cdot \text{cm}^{-1}$), it decreases rapidly with decreasing temperature, reaching a value of about $50 \text{ Ohm}^{-1} \cdot \text{cm}^{-1}$ at the temperature of the Verwey transition (phase transition from cubic to low – temperature monoclinic structure existing below $T_v = 120\text{--}125 \text{ K}$).

Ferromagnetism in metals is formed between contacting atoms. In magnetite, magnetoactive cations are far from each other, because they are separated by oxygen anions that do not have a magnetic moment, and the direct exchange interaction between the cations is very weak or absent (indirect exchange).

Due to the high electrical resistivity, magnetite has low eddy current losses. Saturation induction is approximately 20-25% of iron saturation induction.

Investigated samples were obtained in four stages. Rubber masterbatch, that consist from butadiene-styrene rubber and magnetite in ratio 1:3, were prepared in laboratory mill, tentatively. The remaining components included in the composition (Table 2) were mixed with the masterbatch in a laboratory rubber mixer for 6 minutes at a temperature of $T = 60^\circ\text{C}$. The finished mixtures were processed on laboratory mill.

Purpose of the components of the curing system, which given in Table 2, is as follows:

- Technical stearic acid, $\text{C}_{17}\text{H}_{35}\text{COOH}$ (GOST 6484-96) – vulcanization activator, plasticizer, disperser;

- Zinc oxide, ZnO (GOST 202-84) – vulcanization activator;
- Sulfur, S (GOST 127.4-93) – vulcanizing agent;
- Altax, 2,2'-Dibenzothiazoldisulphide, $\text{C}_{14}\text{H}_8\text{N}_2\text{S}_4$ (GOST 7087-75) – vulcanizing agent and vulcanization accelerator;
- Magnetite, Fe_3O_4 (Technical Specifications 0712-030-001186803-99) – functional filler for increase the electrical conductivity, dielectric permittivity and dielectric loss angle tangent, to give magnetic properties for composites.

Prepared mixtures with magnetite content $C = 0\text{--}300$ weight parts (w.p.) were cured in hydraulic press during that time shown in Table 2 at a temperature of $T = 160^\circ\text{C}$. As a result, smooth elastic plates with a thickness of 1 mm were obtained.

In this work were investigated concentration dependencies of following parameters: tensile strength, breaking elongation, volume resistivity, dielectric permittivity and dielectric loss angle tangent on some frequencies, reflection loss, transmission coefficient and loss coefficient in the frequencies range $25.86\text{--}35.7 \text{ GHz}$.

Stress-strain properties of materials were determined by universal testing system Instron 3365. Tentatively, samples for testing were cut from plates with millimeter thickness by cutting die with work sector width equal 5 mm , and work sector length equal 35 mm . Sample thickness were determined at three points by micrometer, and average value were calculated. Stretching of the samples were conducted at a tensile testing grip speed of 500 mm/min . Tensile strength σ_p , MPa and breaking elongation $\varepsilon_p, \%$ were calculated from the test results [12]:

$$\sigma_p = \frac{P_p}{d \cdot b_0}, \tag{2}$$

$$\varepsilon_p = \frac{l_p - l_0}{l_0} \cdot 100, \tag{3}$$

where P_p – is force, which is a cause of sample breaking, N; d – is mean of sample thickness,

Table 2.

Rubber-stock formula for composites based on SCS-30 ARC with magnetite filler.

Samples Comp.	Component concentration, w.p.						
	RM.1	RM.2	RM.3	RM.4	RM.5	RM.6	RM.7
SCS-30 ARC	100.0	100.0	100.0	100.0	100.0	100.0	100.0
Stearic acid	1.5	1.5	1.5	1.5	1.5	1.5	1.5
ZnO	5.0	5.0	5.0	5.0	5.0	5.0	5.0
S	2.0	2.0	2.0	2.0	2.0	2.0	2.0
Altax	3.0	3.0	3.0	3.0	3.0	3.0	3.0
Magnetite	0.0	10.0	30.0	50.0	100.0	200.0	300.0

before measurement, m ; b_0 – is sample width, before measurement, m ; l_b – is length between marks at breaking moment of sample, mm ; l_0 – is length between marks of sample, before measurement, mm .

Volume resistivity ($\rho_v, \Omega \cdot m$) of samples plates were determined by high resistance meter Agilent 4339B with resistivity cell 16008B. Clamping device of cell provides a tight contact between electrode and sample surface. The value of sample resistivity were measured after storage during that 6 minutes at voltage equal 100 V. Sample thickness were determined at six points by micrometer, and average value were calculated. Calculation of ρ_v were made with formula:

$$\rho_v = \frac{R \cdot S}{L}, \tag{4}$$

where R – is measured sample resistivity, Ω ; S – is surface area of electrodes, m^2 ; L – is sample thickness, m .

Dielectric parameters were determined by precision LCR Meter Agilent E4980A with dielectric test fixture 16451B. The value of gap between electrodes had been determined by built-in micrometer. The determination technique of relative dielectric permittivity ϵ is based on depend dielectric permittivity of material between electrodes upon capacity of parallel-plate capacitor [13]. The amount of ϵ is calculated with formula:

$$\epsilon = \frac{C_\epsilon \cdot d}{\epsilon_0 \cdot S} = \frac{(C_x - C_p) \cdot d}{\epsilon_0 \cdot S}, \tag{5}$$

where C_x – is measured capacity, F ; C_p – is correction, which consist of the amount parasitic and lateral capacitance of measuring capacitor, F ; d – is value of gap between electrodes, sample thickness, m ; ϵ_0 – is dielectrical constant equal $8.854 \cdot 10^{-12} F/m$; S – is area of electrodes of parallel-plate capacitor, m^2 .

The dielectric loss angle tangent $tg\delta_\epsilon$ of investigation composites were calculated with formula:

$$tg\delta_\epsilon = tg\delta_x \cdot \frac{C_x}{(C_x - C_p)}, \tag{6}$$

where $tg\delta_x$ – is measured value of dielectric loss angle tangent of measuring capacitor.

A series of studies of microwave absorption properties of investigation materials has been conducted. Investigation of reflection loss R (dB) and transmission coefficient T (dB) in the frequencies range of 25.86 to 37.5 GHz were determined by vector network analyzer Anritsu MS4644A with guided-wave measurement cell. Calculation of reflection, transmission and losses coefficient has been produced with formula (Fig. 3):

$$T = \frac{P_{trans}}{P_{init}}, R = \frac{P_{refl}}{P_{init}}, L = \frac{P_{loss}}{P_{init}} = 1 - T - R, \tag{7}$$

where P_{init} – is initial wattage of EMI, W ; P_{trans} – is transmission wattage of EMI, W ; P_{refl} – is reflection EMI wattage, W ; P_{loss} – is losses of EMI wattage in material, W .

Magnetic properties of obtained composites were investigation by magnetometer. Magnetization curves of samples upon magnetic field strength 5 kOe were plotted by automatic vibromagnetometer EG&G PAR-155. Discs with a diameter of about five millimeters and thickness of about one millimeter have been cut from composite plates. Discs was glued to holder by glue BF-2.

Interesting from the point of view of practical applications is the possibility to control the reflection coefficient from magnetoelastomeric composite using a magnetic field. Such

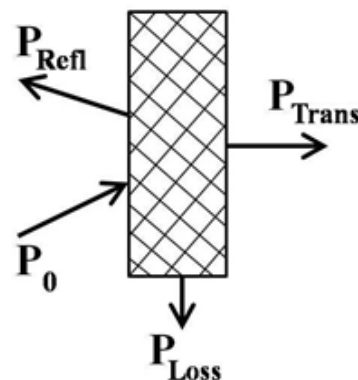


Fig. 3. Scheme of interaction of samples with EMI.

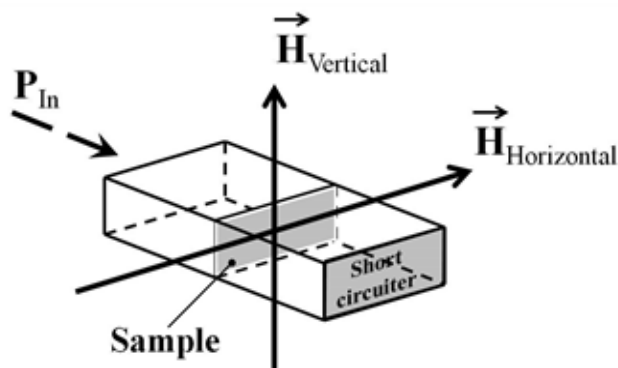


Fig. 4. The scheme of inclusion of the sample in the measuring microwave path with an external magnetic field.

measurements were performed according to the scheme shown in Fig. 4.

The sample was placed in a short-circuited section of the waveguide path with a cross section of $7.2 \times 3.4 \text{ mm}$ (operating frequency band 25.86...37.5 GHz, the main wave type TM_{01}). The magnetic field of 0.4 T has been created by two permanent magnets of high-coercive NdFeB alloy. The amplitude and phase of the scattering matrix coefficient S_{11} (back reflection to the generator) at different directions of the magnetic field vector were measured using a vector analyzer Anritsu MS-4644A.

3. RESULTS AND DISCUSSION

Most important parameter to achieve strengthen effect of materials is interfacial area between rubber matrix and filler particles. Interfacial area of rubber/filler depends on particle size and filler concentration. Key parameter for definition of gain rate rubber is amount of physical-chemical bonds between rubber matrix and filler particles.

The stress-strain measurements results for materials based on butadiene-styrene rubber and magnetite have been illustrated in Fig. 5.

Measurements on extension at tension showed that increase of filler concentration result to increase elasticity modulus at extension and decrease of extension elongation. This improvement of stress-strain properties is due to mobility limiting of polymeric chain in rubber (resulted from distribution of filler particles and interaction with them).

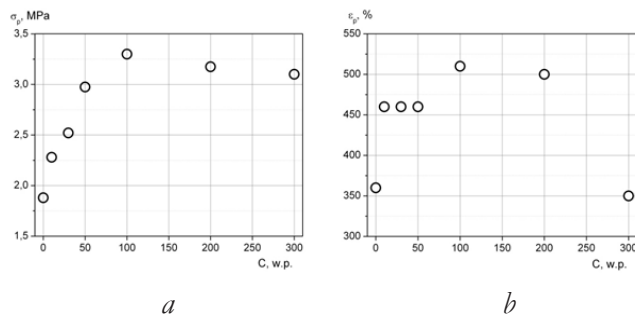


Fig. 5. Dependence of stress-strain properties of elastomeric composites on the filler content: a) tensile strength; b) breaking elongation.

Tensile strength is characterized by persistence to expansion of cracks in rubber. Addition of filler particles significantly increase tensile strength of elastomeric composites. Tensile strength for such materials is due to structure of elastomeric composites, strong interface interactions between filler particles and rubber matrix, also to ability to skid of aggregates during extension. In this case physical barriers is forming in the way of expansion of cracks and crack growing energy is decrease.

Composites have not only greater strength, but also greater hardness in comparison with unfilled materials. Increase of hardness is due to equal distribution of filler particles, which increase degree of interface interactions between filler particles and rubber matrix.

Strength is increasing to certain maximum, which depended of composition components nature, with growing of specific surface of high-dispersity filler. In case of product with small thickness and difficult configuration preference is given to high-dispersity fillers (powders), because they are easy distributed in matrix, thereat saving internal distribution during forming. Application of high-dispersity fillers decrease possibility of destruction, delamination of product during the next mechanical processing.

Solid impurities in extended sample are decreasing stress in the contact area between matrix and filler. For example, in spherical particles stress exceeds in one and a half stress in matrix bulk, in other words filler perceives the main part of stress. The influence of the filler increases, when particles have an ellipsoidal form and have been directed to axis of deformation.

Generally strength of composite material is determined by intermolecular Van der Waals interactions and by bonding force of main chain of macromolecule in polymer matrix. When macromolecules is undirected (low-filled composites), bounds is located at large angles to direction of applied stress. In this case macromolecule have a sufficient flexibility. Destruction of composite material in the direction of stress for the most part is carried out from separation of links and segments of macromolecule at them sliding relative to one another, results from mobility and different length of macromolecule chains. In case when filler increases strength of polymer composite, the amount of cross-links in the polymer network and the amount of bonds between nearest filler particles are increased. Breaking of this three-dimensional hard structure is carried out predominantly from breaking of bonds in main polymer chain. Polymer composites like other construction materials are destructed is due to progressing of initial defects. It should be noted that fact of filling leads to difficult technological defects in composite, which include cracks and pores, which is formed during production. These defects are formed as a result of collateral action by adding the filler in polymer matrix, this action causes the concentrating of stress on aggregates of particles and is a potential reason of starting of distruction. Distribution of initial cracks in the bulk of polymer composite and them geometry of growing are depending of strengths relation and relation of thermal-expansion coefficients of matrix and filler. In this case, hemispherical cracks around filler particles, which later transition in matrix or cracks passing through matrix and particles (the most dangerous for product) are appearing. However filler particles plays a role not only initiator of cracks in composite. Individual particles able to brake and stop growing of cracks at small growing velocity of them. Such cracks, when they meets with particle, break adhesion bonds on the surface of contact between particle and matrix. Thus, the front of crack extends over and local stresses are redeployed in the area of matrix near interface.

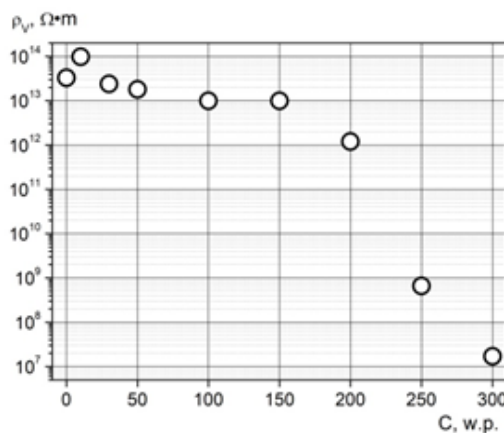


Fig. 6. Dependence of the volume resistivity ρ_V of elastomeric composites on magnetite concentration.

As a result, the strain energy at the front of crack decreases and growing of the crack is stopped [14].

Thus, with increasing of filler concentration the strength characteristics σ_b and ϵ_b increases to a maximum at concentration $C = 200$ w.p. Tensile strength slightly decreases at further increasing of magnetite concentration. The value of breaking elongation ϵ_b at concentration $C = 300$ w.p. is comparable to the value of this parameter for unfilled vulcanizates. That means, that in investigated range of magnetite concentration composite saves satisfactory stress-strain properties.

The value of electrophysical parameters of elastomeric composites also changes at increasing of magnetite concentration C : volume resistivity decreases (Fig. 6), dielectric permittivity ϵ and dielectric loss angle tangent $\text{tg}\delta$ increases (Fig. 7).

The figure shows that the dependence of the permittivity and the dielectric loss tangent at values $C = 200...300$ w.p. at frequencies of 1 kHz and 1 MHz are different. This effect may

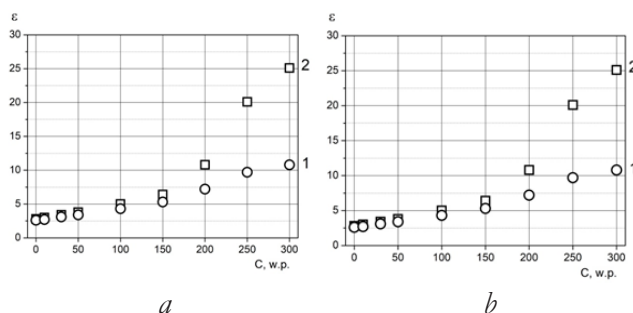


Fig. 7. Dependence of the ϵ (a) and $\text{tg}\delta$ (b) increases of elastomeric composites on magnetite concentration at different working frequencies: 1) 1 KHz; 2) 1 MHz.

be related to wide distribution of filler particles on sizes which is related to aggregation of filler particles in clusters, as well as with a change in the nature of polarization and the mechanism of conductivity of the composite with increasing frequency. The conductivity of magnetite at a temperature above the temperature of the Verwey transition is explained by the presence of a variable valence and has a frequency dependence. In turn, the value of the electrical conductivity of polycrystalline magnetite, depending on the presence of cracks and their orientation may differ hundreds of times.

The results of measurement of reflection R , transmission T and loss L coefficients in dependence of magnetite concentration C is shown on **Fig. 8**. Loss coefficient L increases at growing of magnetite concentration C that is due to increasing loss by electrical conductivity. The best shielding characteristics (minimum of transmission coefficient and maximum of reflection coefficient) are observed in concentration range $C = 100 \dots 200$ w.p.

On the amplitude-frequency characteristic of the reflection coefficient of the sample measured in the configuration Fig. 4, there is an interference peak, the position f and the intensity A of which at different direction of the external magnetic field, as well as in its absence, are presented in the **Table 3**.

The application of an external magnetic field changes the magnetic susceptibility of a magnetically soft composites in the direction

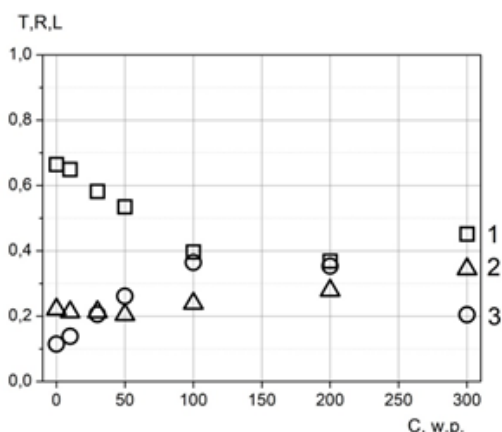


Fig. 8. Dependence of the transmission T (squares), the loss L (triangles) and the reflection R (circles) coefficients on the magnetite concentration C .

Table 3.

Influence of external magnetic field on reflection coefficient.

	f , GHz	A , dB
Without external field	36.4	-13.5 ± 0.5
Horizontal field	36.4	-9.7 ± 0.5
Vertical field	36.4	-14.8 ± 0.5

of the magnetic field, which should affect the nature of the interaction with polarized electromagnetic radiation. The obtained results show the anisotropy of the reflection coefficient of magnetoelastics from the direction of the external magnetic field. Reduction of the magnetic susceptibility of the medium with the application of an external field should lead to a decrease in the reflectance of the sample and to an increase in the transmittance. The reflection from the sample increases with a horizontally applied magnetic field, since the vector of the magnetic field of the wave in the waveguide is also directed horizontally. This effect can also be used in multilayer structures [16].

Magnetization curves for composites are shown on **Fig. 9**. The absence of hysteresis on magnetization curves for composites makes it possible to classify the investigated materials to class low-coercivity materials. The saturation magnetization σ_s in this materials is achieved in magnetic fields 4 kOe and increases at growing of magnetite concentration. The similar results were obtained in a paper [15] for polyethylene/nikel ferrite nanocomposites.

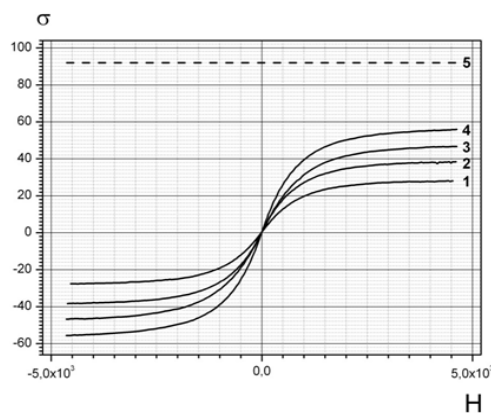


Fig. 9. Magnetization curves for composites at different magnetite concentration C : 1 - 50 weight parts, 2 - 100 weight parts, 3 - 200 weight parts, 4 - 300 weight parts. 5 - level of specific saturation magnetization for pure magnetite [17].

4. CONCLUSION

Thus, elastomeric composite materials based on butadiene-styrene matrix and magnetite are obtained. For them is shown, that:

- At increasing of magnetite concentration in butadiene-styrene rubber strength of vulcanizates increases reaching maximum at concentration 200 weight parts. Breaking elongation is changing similarly;
- The value of magnetite concentration at which is seen significant change of electrophysical parameters and also change of reflection and absorption coefficients is 100 weight parts;
- With increase of magnetite concentration the value of ϵ and $\text{tg}\delta$ grows (at frequense 1 MHz from 2.5 to 12 and from 0.02 to 0.13 consequently) and volume resistivity decrease (from 10^{13} to $10^7 \Omega \cdot \text{m}$);
- With increase of magnetite concentration saturation magnetization grows (for composites $\sigma_s = 27...55$, that comparable with $\sigma_s = 92$ for pure magnetite);
- There is an anisotropy of the reflection coefficient of magnetically elastomeric composite materials from the direction of the external magnetic field.

Elastomeric composites based on butadiene-styrene matrix and magnetite have the next advantages: flexibility, adaptability to manufacture, cost-efficiency, well stress-strain properties. This materials can be used as a screens reflecting EMR, microwave absorption materials, antistatic materials, magnetorheological materials, including materials with controlled parameters. For improving of characteristics are recomended: choose a optimal dispersability of magnetite, master a technique of producing magnetostructural materials, correct a rubber-stock formula.

A promising direction in materials science is the synthesis of elastomeric nanocomposites based on nanophase fillers with different physical properties that can be effectively used not only as electrodynamic media, but also in acoustoelectronic devices [18, 19, 20]

REFERENCES

1. Kabanov V. *Land rent. Polymer Encyclopedia.* 2:325-332. Moscow, Sovetskaya entsiklopedia Publ., 1974.
2. Kon'kov VA, Polyakova KP, Polyakov VV. Magnitnye svoystva mul'tiferroika Fe_3O_4 [Magnetic properties of multiferroic Fe_3O_4]. *Aktual'nye problemy aviatsii i kosmonavтики*, 2011, 1(7):142-143 (in Russ.).
3. Russkikh GS. Raschetno-eksperimental'nye issledovaniya magnitoupругogo effekta v metallonapolnennykh elastomerakh [Calculation-experimental investigation of converse magnetostrictive effect in metal-filled elastomers]. *Proc. 6 Mezhdunarodnoj nauchno-tekhnicheskoy konferentsii "Tekhnika i tekhnologiya neftekhimicheskogo i neftegazovogo proizvodstva"*. Omsk, OSTU Publ., 2016, pp. 156-157 (in Russ.).
4. Gerval'd AYu, Gritskova IA, Prokopov NI. Sintez magnitsoderzhashchikh polimernykh mikrosfer [Synthesis of magnet-containing polymeric microspheres]. *Uspekhi khimii*, 2010, 79(3):249-260 (in Russ.).
5. Caruso F, Susha AS. Magnetic core-shell particles: preparation of magnetite multilayers on polymer latex microspheres. *Advanced materials*, 1999, 11(11):950-952.
6. Gomez-Lopera SA, Plaza RC. Synthesis and characterization of spherical magnetite/biodegradable polymer composite particles. *Journal of colloid and interface science*, 2001, 240(1):40-47.
7. Pastukhov AV, Davankov VA, Volkov VV. Magnitnye nanokompozity na osnove sverkhsshitykh polistirolov [Magnetic nanocomposites based on hypercrosslinked polystyrene]. *Izvestiya rossijskoy akademii nauk. Seriya fizicheskaya*, 2009, 73(4):496-498 (in Russ.).
8. Lubentsova KI, Pastukhov AV, Davankov VA. Sorbtsiya toksichnykh organicheskikh i neorganicheskikh soedinenij kompozitami s nanodispersnymi oksidami zheleza v matritsakh polistirolnykh sorbentov [Sorption of toxic organic and inorganic compounds by

- composites which contain nanosized ferrum oxides in the matrix of polystyrene sorbent]. *Sorbtsionnye i khromatograficheskie protsessy*, 2015, 15(3):333-334 (in Russ.).
9. Ing Kong, Sahrim Hj Ahmad. Magnetic and microwave absorbing properties of magnetite–thermoplastic natural rubber nanocomposites. *Journal of Magnetism and Magnetic Materials*, 2010, 322(21):3401-3409.
 10. Borisov LA, Grishin YuM, Kozlov NP at all. Patent 2516512 *Rossiyskaya Federatsiya*, MPK7 C 30 B 30/02, C 30 B 29/06. Sposob pryamogo polucheniya polikristallicheskogo kremniya iz prirodnogo kvartsa i iz ego osobo chistykh kontsentratorov [The technique of directly obtaining of polycrystalline silicon from natural silica and its high purity concentrate]. N 2012128656/05; zayavl. 09.07.12; opubl. 20.05.14, Byull. N 14, 2014.
 11. Severov VV. Razrabotka protsessa obratnoj flotatsii zhelezistykh kvartsitov s ispol'zovaniem kationnykh i neionogennykh sobiratelej [The develop of reverse flotation process of ferruginous quartzite with using cation and non-ionogenic collector]. *Dis. ... kand. tekhn. nauk, 25.00.13. Natsional'nyj issledovatel'skij tekhnologicheskij universitet «MISiS»*. Mocsow, 2011, 215 p.
 12. Rezina. Obshchie trebovaniya k provedeniyu fiziko-mekhanicheskikh ispytaniy. [Rubber. Common requirements to holding of stress-strain testing]. *GOST 269-66*, Moscow, 2001, 11 p.
 13. Lushchejkin GA. *Metody issledovaniya elektricheskikh svoystv polimerov* [Techniques of investigation the electrophysical properties of polymers]. Moscow, Khimiya Publ., 1988.
 14. Kiseleva OA (compiler). *Polistrukturnaya teoriya prochnosti kompozitsionnykh materialov* [The polystructural theory for strength of composite materials] (metod. ukaz.). Tambov, TGTU Publ., 2013, 22 p.
 15. Fionov AS, Kolesov VV, Yurkov GYu. Kompozitsionnye materialy na osnove nanochastits NiFe_2O_4 i polietilenovoj matritsy [Composite materials based on nanoparticles NiFe_2O_4 and polyethylene matrix]. *Materialy 20 Mezhdunarodnoj Krymskoj konferentsii «SVCH-tehnika i telekommunikatsionnye tekhnologii»* (KryMiKo 2010). 13-17 Sept., 2010, Sevastopol', Krym, Ukraina, pp.769-770.
 16. Gorshenev VN, Kolesov VV, Fionov AS, Erichman NS. Mnogosloynnye pokrytiya s izmenyaemyimi elektrodinamicheskimi kharakteristikami na osnove napolnennykh polimernykh matrits [Multilayer coatings with variable electrodynamic characteristics based on filled polymer matrix]. *Zhurnal radioelektroniki*, ISSN 1684-1719, 2016, 11:1-18 (in Russ.).
 17. Babichev AP at all (eds.). *Fizicheskie velichiny: Spravochnik* [Physical magnitudes: handbook]. Moscow, Energoatomizdat Publ., 1991.
 18. Kuznetsova IE, Zaitsev BD, Shikhabudinov AM. Elastic and viscous properties of nanocomposite films based on low-density polyethylene. *IEEE Transactions on Ultrasonics, Ferroelectric and Frequency Control*, 2010, 57(9):2099-2102, DOI: 10.1109/TUFFC.2010.1658.
 19. Kuznetsova IE, Zaitsev BD, Shikhabudinov AM. Effect of the nanoparticle material density on acoustic parameters of polymer-based nanocomposites. *Technical Physics Letters*, 2010, 36(8):759-761, DOI: 10.1134/S1063785010080249.
 20. Kuznetsova IE, Zaitsev BD, Borodina IA, Shikhabudinov AM, Teplykh AA, Manga E, Feuillard G. The Effect of Nanocomposite Polymeric Layer on the Radiation of Antisymmetric Zero-Order Lamb Wave in a Piezoelectric Plate Contacting with Liquid. *Journal of Applied Physics*, 2013, 113:224507, DOI: 10.1063/1.4810905.

MAGNETOCALORIC EFFECT IN CARBON-CONTAINING COMPOUNDS

Victor V. Koroley, Tatyana N. Lomova, Anna G. Ramazanova

G.A. Krestov Institute of Solutions Chemistry of RAS, <http://www.isc-ras.ru>

Ivanovo 153045, Russian Federation

vvk@isc-ras, tnl@isc-ras.ru, agr@isc-ras.ru

Abstract. The review is devoted to carbon-containing compounds with magnetic properties. It considers recent developments in the problem of synthesis and studying physico-chemical properties of single-molecule magnets (SMMs). It is shown that single-molecule magnets, such as graphene and its donor-acceptor complexes, metal complexes with Schiff's bases, paramagnetic high-spin complexes of porphyrins/phthalocyanines, as well as 3D nanoparticles of metal oxides and hybrid composites of magnetic nanoparticles with graphene have a large and even giant magnetocaloric effect at temperatures close to room conditions, i.e. beyond the temperature range of magnetic transitions. For the first time, the behaviour of such molecular materials has been determined by a direct method on an original microcalorimetric apparatus and the first data on the interconnection between the chemical structure of their molecules and magnetothermal properties have been obtained.

Keywords: single-molecule magnet, magnetocaloric effect, porphyrin, fullerene, graphene, Schiff's base

UDC 544.032.53

Bibliography - 84 references

RENSIT, 2019, 11(2):199-216

Received 10.06.2019, accepted 21.06.2019

DOI: 10.17725/rensit.2019.11.199

CONTENTS

1. INTRODUCTION (199)
 2. STATE-OF-THE ART OF THE PROBLEM OF MAGNETISM IN CARBON-CONTAINING COMPOUNDS (200)
 3. MAGNETOCALORIC EFFECT (MCE) IN PARAMAGNETIC COMPLEXES OF PORPHYRINS AND PHTHALOCYANINES (202)
 4. MAGNETOTHERMAL PROPERTIES IN COMPOUNDS WITH SCHIFF'S BASES (206)
 5. MCE IN GRAPHENE AND OTHER CARBON NANOFORMS (208)
 6. CONCLUSION (211)
- REFERENCES (212)

1. INTRODUCTION

The last two decades have seen active studies of magnetocaloric effect (MCE) in various magnetically ordered materials [1, 2]. Magnetocaloric effect is an adiabatic change in the sample temperature at variations of external magnetic field. MCE is caused by redistribution of internal energy between the system of magnetic atoms and the material crystal lattice. The possibility to use MCE

for creating a magnetic refrigerator that works at room temperature and in medical applications has urged quite a lot of research into this effect [3-5]. The list of works in this field contains several thousand papers and reviews. However, despite the large volume of the experimental data, the physical nature of MCE is not fully understood.

It is extremely important to study magnetocaloric effect in carbon-containing compounds that often display magnetic properties at the level of a simple molecule for solving fundamental problems of magnetism and solid state physics. This is connected with the problem of obtaining information about magnetic phase transitions and magnetic state of a substance [6]. Single-molecule magnets, such as graphene and its donor-acceptor complexes, metal complexes with Schiff's bases, paramagnetic high-spin complexes of porphyrins/phthalocyanines, as well as 3D nanoparticles of metal oxides and hybrid composites of magnetic nanoparticles with graphene have a large and even giant MCE at temperatures close to room conditions, i.e. beyond the temperature range of magnetic transitions.

This review presents data on magnetocaloric behaviour of the above-mentioned molecular materials, the first data about the interconnection between the chemical structure of their molecules and magnetothermal properties.

2. STATE-OF-THE-ART OR RECENT DEVELOPMENTS OF THE PROBLEM OF MAGNETISM IN CARBON-CONTAINING COMPOUNDS

Carbon-containing compounds with magnetic properties have long been of interest to scientists. Materials of this new type with specific spintronics and quantum behavior at the level of a simple molecule were named single-molecule magnets (SMMs). Cooperation of chemists and physicists has allowed them to obtain a large volume of data about the interconnection of molecular structure and magnetic properties of objects and led to the formation of a new field in magnetochemistry. There are a number of research schools dealing with the problems of synthesis of SMMs (high-spin molecules) and studying their electronic structure and magnetic properties [6-11]. One of the indicators of magnetic properties is the magnetocaloric effect (MCE) in a magnetic material. This effect has an extremely wide application range in magnetic cooling and therapy of cancer (in hyperthermia method applications). MCE is a change in the magnetic state of a material caused by changes in the external magnetic field. MCE is defined as a change in magnetic entropy in the isothermal process, ΔS_m and/or as a temperature change in the adiabatic process following changes in the magnetic field, ΔT_{ad} . MCE parameters can be obtained by directly measuring ΔT_{ad} , or indirectly, by calculating ΔS_m and/or ΔT_{ad} from experimental values of heat capacity and/or magnetization at different magnetic field values and temperatures. In most of the works, magnetocaloric effect of single-molecule magnets is determined in the low-temperature region (from 0 to 10 K) from experimentally obtained data on the magnetization temperature dependence. All the attempts made so far to obtain maximum MCE values in the magnetic transition region for single-molecule magnets by the direct calorimetric



Fig. 1. Scheme of the Mn_{12} cluster structure [7].

method have been unsuccessful. However, it is at room temperatures that devices and apparatuses that use magnetocaloric effect work, not taking into account devices for specific purposes.

Among the first research groups who studied the crystal structure and magnetic properties of high-spin manganese clusters was R. Sessoli's group [7]. It was one of the first attempts of targeted design of a single-molecule magnet (**Fig. 1**). Later, studies of this type became much more numerous.

The magnetocaloric effect of $Mn_{12}Cl$ -benzoate was calculated by the authors of [12] based on the temperature dependence of magnetization (from 2 to 20 K), and at the magnetic flux density of 3 T it equals 15 J/mol K.

Work [13] deals with synthesis, description and analysis of single-molecule magnets containing gadolinium and dysprosium. The authors of [13] study the magnetocaloric effect in gadolinium compounds using the characteristics obtained on a SQUID magnetometer. An example of the structure of the compounds that they obtained is shown in **Fig. 2**.

J. Schnack's group [14] studied the magnetothermal properties of antiferromagnetic single-molecule

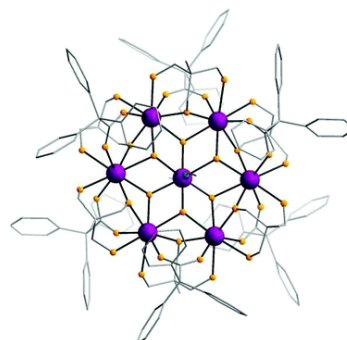


Fig. 2. Structure of $[Gd_7(OH)_6(thmeH_2)_3(thmeH)(tpa)_6(MeCN)_2]^{2+}$ [13].

magnets. They have found that deformations in the geometric structure of an antiferromagnetic increase the magnetocaloric effect.

When studying the magnetothermal properties of the dimer $[(\text{Gd}(\text{OAc})_3(\text{H}_2\text{O})_2)_2] \cdot 4\text{H}_2\text{O}$, the authors of [11] calculated the MCE from experimental data using the temperature dependence of specific heat capacity. At a temperature of 1.8 K, ΔS_m was equal to 40 J/kg K ($B = 7 \text{ T}$). The calculated MCE value of the dimer exceeded ΔT_{ad} of metallic gadolinium.

A large group of Chinese scientists [15] is studying the magnetothermal properties of clusters of rare-earth metals and their complexes with transition 3d metals based on complex organic acids and other macromolecules. For example, they found a giant magnetocaloric effect in the $\text{Gd}(\text{OH})\text{CO}_3$ monocrystal of rhombic structure.

The authors of [16] have synthesized single-molecule magnets based on Mn(II)-Gd(III) and discovered that the magnetism type depends on the compound structure. The entropy change value calculated by the authors using magnetization data at a temperature of 3-8 K and induction of 5 T exceeds the experimental data that were reported in literature earlier.

A tubular, 48-metallic (3d-4f) cluster of $\text{Gd}_{36}\text{Ni}_{12}$ was synthesized in [17] via self-assembly of the metal ions. The authors of the mentioned work calculated the entropy change ΔS_m at different values of magnetic field and temperature and arrived at the value of 36.3 J/kg K at 3 K for $B = 7 \text{ T}$. This value is 45% higher than the highest value reported in literature (25 J/kg K) calculated by the same method for Mn_{14} , [18] but is lower than the value calculated by Evangelisti based on heat capacity [11].

The latest achievements in the field of studying magnetic and magnetocaloric properties in ternary intermetallic compounds of rare earth elements $\text{RE}_2\text{T}_2\text{X}$ (RE - Gd-Tm; T = Cu, Ni, Co; and X = Cd, In, Ga, Sn, Al) are considered in review [19]. Some of these compounds have a high MCE making them attractive in low-temperature magnetic cooling applications. The focus of the work is to understand the connections between magnetocaloric characteristics of the compounds,

their crystal structure, magnetism and magnetic phase transition. The review discusses the physics of MCE appearance and potential applications of the $\text{RE}_2\text{T}_2\text{X}$ compounds.

Naoto Ishikawa [20] has published a number of works on studying the behaviour of phthalocyanine complexes of lanthanides as SMMs. The work confirms the contributions to the magnetic behaviour of the complexes made by the interaction of magnetic moments of the spin density carrier – lanthanide – with magnetic moments of the π -systems of the macrocyclic ligands in the complexes.

The authors of several recent publications report on the magnetocaloric effect for unique single-molecule magnets $\{[\text{Mn}(\text{pyrazole})_4]_2[\text{Nb}(\text{CN})_8] \cdot 4\text{H}_2\text{O}\}_n$ and $[\text{Fe}(\text{pyrazole})_4]_2[\text{Nb}(\text{CN})_8] \cdot 4\text{H}_2\text{O}$. In works [5, 21], the authors calculated changes in the isothermal entropy and the adiabatic temperature change by using the results of heat capacity measurements. They have found that these values are comparable with the data obtained for other representatives of single-molecule magnets. This conclusion also agrees with the results of the first study [22] of this compound that used an indirect approach for determining MCE.

The nature of molecular magnetism was studied by the authors of [23] on heterometallic 3d-4f SMMs. It was shown that the SMM properties depend on a combination of single-ion anisotropies of all the centers of the paramagnetic metal involved and presence of 3d-4f exchange interactions. That is why it is necessary to take into account the internal properties of the d-metal ions involved and the role played by the contributions of both d and f electrons of the participating trivalent lanthanide ions.

The transition from a low spin to a high one caused by the intramolecular transfer of the electron was described in detail when the static magnetic properties and spin dynamics in zero-sized valence cobalt tautomers were studied [24]. It was shown that a spin-crossover can be controlled by temperature, external pressure or light radiation.

The magnetic properties of finite graphene fragments of arbitrary shape were studied using benzenoid graph theory and first-principles electronic structure calculations. It has been demonstrated that the principle of topological frustration of the π -bonds can be used for introducing a large spin and for interesting spin distributions in graphene.

Weak supermagnetism and hysteresis at room temperature were determined for graphite oxide and reduced graphene oxide [27] (MCE, however, was not found). The magnetic behaviour was explained by individual domains, each representing a cluster of defective magnetic moments bound by a ferromagnetic interaction.

The authors of this review in their works discussed below considered the causes of MCE appearance in single-molecule magnets – graphene and its donor-acceptor complexes, metal complexes with Schiff's bases, paramagnetic high-spin complexes of porphyrins/phthalocyanines and their donor-acceptor dyads with substituted fullerenes – at the quantitative level. The magnetocaloric behaviour of the compounds at temperatures close to room conditions was studied. It was shown that, like 3D nanoparticles of metal oxides and hybrid composites of magnetic nanoparticles with graphene, single-molecule magnets have a large and even giant MCE. For the first time, the magnetocaloric behaviour of such molecular materials was determined by a direct method on an original [28] microcalorimetric apparatus and the first data about the interconnection between the chemical structure of their molecules and magnetothermal properties were obtained.

3. MCE IN PARAMAGNETIC COMPLEXES OF PORPHYRINS AND PHTHALOCYANINES

Presence of a paramagnetic metal ion in the axially coordinated metallocporphyrins leads to paramagnetism of their molecules and substances, which is reflected in the NMR spectra and non-indifference to magnetic fields. Mn(III), Fe(III), Co(II) and Ln(III) complexes possess a magnetic moment. Since there is a polarizable electron-excess

aromatic π -system in the complexes, the spin density of the central atom is delocalized, which allows “controlling” their paramagnetic properties. It is especially true in cases when, along with a paramagnetic centre – a metal cation – the molecule has an additional centre with a non-zero spin. Since all paramagnetic materials display this effect, the goal is to find compounds with a large and giant MCE.

The results of the studies of molecular magnetism obtained since the time when this new field of magnetochemistry began to develop are presented in comprehensive review [29]. The work was devoted to the studies of the structure, synthesis, composition, magnetic properties and applicability of magnetic 3d, 3d-4f and 4f-coolants in different spheres of activity. Homometallic gadolinium compounds were studied in different clusters where the values of the magnetic component of the entropy change $-\Delta S_m$, which is a measure of MCE, reached about 27 J/kg at 5 K and changes of magnetic field from 0 to 1 T. Thus, studying zero-sized lanthanides(III) “built” into the coordination sphere of the tetrapyrrole macrocycle is a new field of research with only a small number of studies which include, in addition to the works on SMMs that were partially quoted in the previous section, our research into magnetocaloric properties of paramagnetic metallocporphyrins/metal phthalocyanines [30-40].

The measurements of MCE and heat capacity of the complexes of metallocporphyrins/metal phthalocyanines were made on an automated microcalorimetric unit with an isothermal shell [28]. The microcalorimetric measurement cell with a solid magnetic sample filled to the full volume with water together with the isothermal shell were placed into the pole gap (60 mm) of an electromagnet, which allowed determining the values of MCE and specific heat capacity in magnetic fields of 0 – 1.0 T at temperatures of 278-343 K. Adiabatic magnetization was achieved by quickly varying the magnetic field. The variations of temperature in the thermostatically controlled calorimetric cell during the calorimetric experiment were ± 0.0002 . The error in the measurements of MCE and heat capacity was 1

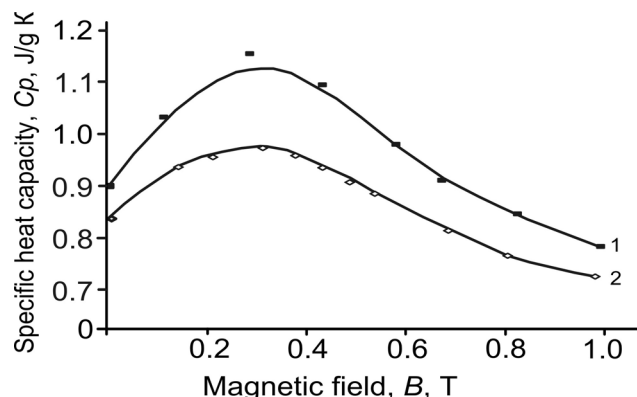


Fig. 3. Field dependence of specific heat capacity of (AcO)Mn(p-^tBuPh)₈TAP (1) and (Cl)MnOEP (2) at 298 K.

and 2%, respectively. Besides, the experimental measurement of the specific heat capacity of the solid samples was made by the DSC method with a DSC 204 F1 Phoenix (NETZSCH).

We have studied the magnetocaloric effect and heat capacity of 20 functionalized metalloporphyrins/metal phthalocyanines (Fig. 3 and 4) (with the composition (X)MeY, where X = Cl, Br, AcO, Acac; Me = Mn, Eu, Tm, Gd, Fe, Yb, Tb; Y = OEP, TPP, Pc, (p-^tBuPh)₈TAP). An example of their formula is given below (Fig. 4.1) at the temperature of 270-350 K and magnetic induction 0 – 1 T [30-40, 41].

The MCE values in manganese(III) complexes at temperatures close to room conditions and magnetic induction of 1.0 T are equal to 0.047–0.85 K, which makes them promising environmentally-friendly materials capable of magnetic cooling and hyperthermia (with possible applications in early cancer detection, magnetic resonance imaging and magnetic cell separation).

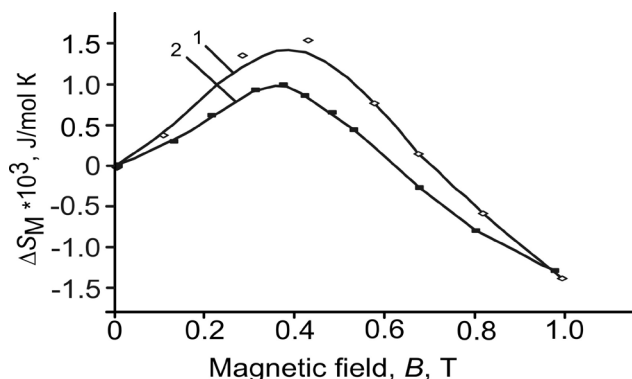


Fig. 4. Field dependence of changes in the entropy magnetic component of (AcO)Mn(p-^tBuPh)₈TAP (1) and (Cl)MnOEP (2) at 298 K.

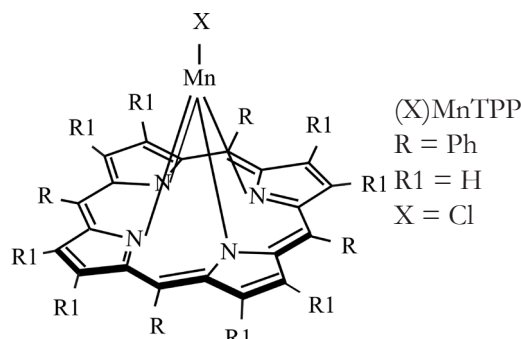


Fig. 4.1. Structure of the manganese(III)porphyrin complex.

The MCE of the complexes is positive over the whole range of magnetic field values and increases nonlinearly as the magnetic field grows. Such MCE behaviour is explained by the paramagnetic properties in manganese complexes. The largest MCE is found in (Cl)MnOEP. The lowest MCE values are observed in the complex with an acetate axial ligand. It means that the magnetocaloric effect is influenced by the nature of the substituent in the macrocycle, while the acetate ligand nature has a less significant effect. The MCE reaction to the nature of the complex is explained by the differences in the mutual position of the energy of the d-orbitals in the field of the ligands [37].

The MCE of the porphyrin tetraderivative (AcO)Mn(p-^tBuPh)₈TAP [36] is lower than that of the unsubstituted (in the mesoposition) analogs.

MCE, like magnetic susceptibility of porphyrin complexes, is connected with the oxidation state and spin configuration of the metal ion. That is why the effect of modifications of the macrocycle structure in the complex on the magnetocaloric properties was explained by the results of the experiments on describing the electron structure of the complexes [40].

For the complexes of europium, thulium and gadolinium with H₂TPP and an acetate- or chloride-ion as the axial ligand [39, 40], we have found that the MCE (ΔT_{MCE}) is equal to 0.127 – 1.45 K at temperatures close to 298 K in magnetic field varying from 0 to 1.0 T. In case of (Cl)GdTPP, the MCE is practically independent of temperature.

For the Gd porphyrin acetate complex, the MCE is much higher than for the chloride one. At temperatures of 275-300 K, the MCE values decrease in the following order: Eu > Gd > Tm

in the chloride complexes of $(Cl)LnTPP$. Since the strength of binding X^- acidoligands in $(X)LnTPP$ is unknown, the differences in the MCE of the two complexes are explained by the macrocycle binding strength in the complexes depending on the nature of the axial ligand. The transition from the chloride complex $(Cl)GdTPP$ to the acetate analog with bidentate coordination of the AcO^- anion is evidently accompanied by a shift in the central ion from the macrocycle plane and spin strengthening.

Unlike $Gd(III)$ complexes, in lanthanide complexes with an asymmetrically filled f-shell, the electronic factor (π -backdonation) begins to prevail over the geometric one. As it has been mentioned, at temperatures of 275 – 300 K, the MCE decreases in the series $Eu > Gd > Tm$, despite a more planar position of the lanthanide ion in the porphyrin plane in the same series due to the effect of “lanthanide contraction”. The $(Cl)EuTPP$ complex is an example of how the presence of π -backdonations between the central atom and the macrocycle does not lead to “compensation” of the spin, but makes it stronger. Thus, the electron configuration of the lanthanide ion in $(X)LnTPP$ determines both the spin state of the spin-carrier itself and the degree of its delocalization due to the π -backdonations in the complex.

Judging by the quantitative data, axial ligand variations are still a more significant factor in regulating magnetothermal properties of $(X)LnTPP$ than changing the lanthanide nature. That is why further research was into the magnetocaloric properties of acetylacetonate

complex gadolinium(III)tetraphenylporphyrin (**Fig. 4.2**) [31, 34].

The effect of the axial acetylacetonate in magnetothermal properties of (porphyrinato) gadolinium(III) manifested itself in a specific temperature dependence of specific heat capacity measured directly and a low maximum on the MCE temperature dependence curves at 305 – 310 K. The specific heat capacity increases as the temperature rises, while the magnetic field effect is not reflected on the temperature dependence.

The MCE of $(Acac)GdTPP$ is by 2 - 4 times lower in magnitude than in the acetate complex of gadolinium(III)tetraphenylporphyrin and one and a half times lower than in the chloride complex. The magnetocaloric properties become weaker due to the formation of a six-member aromatic cycle in case of bidentate coordination of the axial ligand, which leads to the formation of $O \rightarrow N$ π -backdonation and reduces the MCE.

Rare earth element complexes with porphyrins and phthalocyanines as paramagnetic materials have a large magnetocaloric effect (up to 1.45 K when the magnetic induction changes from 0 to 1.0 T) at the temperatures close to room conditions, which can be used for cooling in domestic and industrial refrigerators and other devices. As environmentally friendly paramagnetics, complexes of this class can replace the toxic compounds used in the steam compression cycle. (Porphyrinato)- and (phthalocyaninato)gadolinium(III) complexes contain only a small percentage of expensive gadolinium in comparison with polycrystalline gadolinium. They are soluble in organic media, which makes it possible to form nanostructures of a higher order from these molecules. Since porphyrins, phthalocyanines and their complexes can selectively get accumulated in a tumour of a living body, the considered complexes have good prospects in widening hyperthermia applications in cancer detection and therapy. And, finally, an important thing, in terms of their advantages over paramagnetics, is that we can control their magnetocaloric properties by modifying their molecule structure.

A known strategy of strengthening spin properties is combining in one molecule a

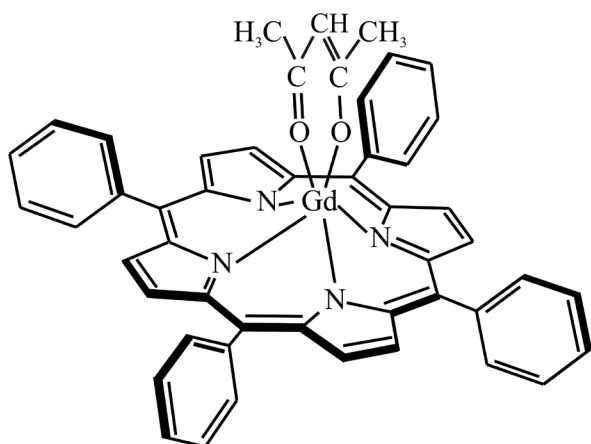


Fig. 4.2. $(Acac)GdTPP$ complex structure.

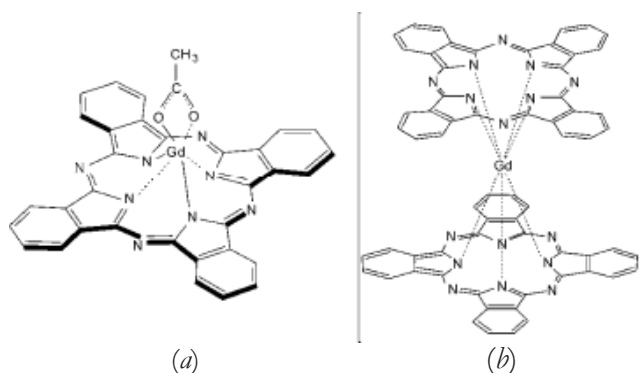


Fig. 4.3. Structure of the complexes: a) (AcO)GdPc; b) GdPc₂^{*}.

spin-carrier and a fragment for spin coupling (overlapping). A similar strategy was used for a paramagnetic – a double-decker one-electron oxidized gadolinium complex whose magnetocaloric properties are described in works [31, 32] in comparison with the corresponding 1:1 complex (formulae (AcO)GdPc and GdPc₂^{*}; (Fig. 4.3) respectively).

The main spin-carrier in the double-decker complex is the central gadolinium atom. In addition to the paramagnetic Gd ion, a GdPc₂^{*} molecule contains one unpaired electron delocalized on one of the macrocycles, which gives hope that the magnetocaloric properties of the complex are better than in the (AcO)GdPc analog.

The temperature dependence of the double-decker complex heat capacity, in contrast to the monophthalocyanine analog, has one pronounced maximum. The character of MCE changes following temperature variations is determined by the temperature dependence of specific heat capacity (Fig. 5 and 6). Contrary to expectations, the MCE values in GdPc₂^{*} are much lower than in (AcO)GdPc. The MCE temperature dependence

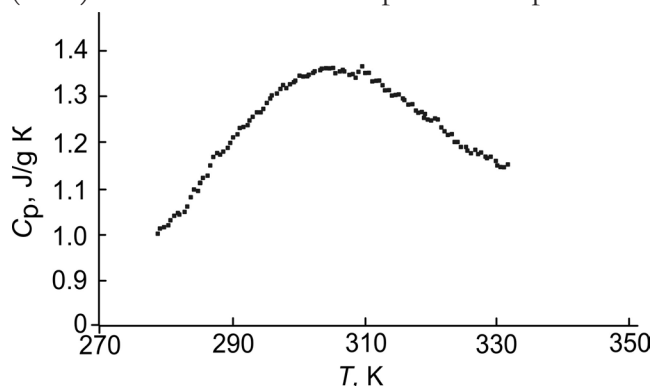


Fig. 5. Temperature dependence of specific heat capacity (C_p) of GdPc₂^{*} in zero magnetic field.

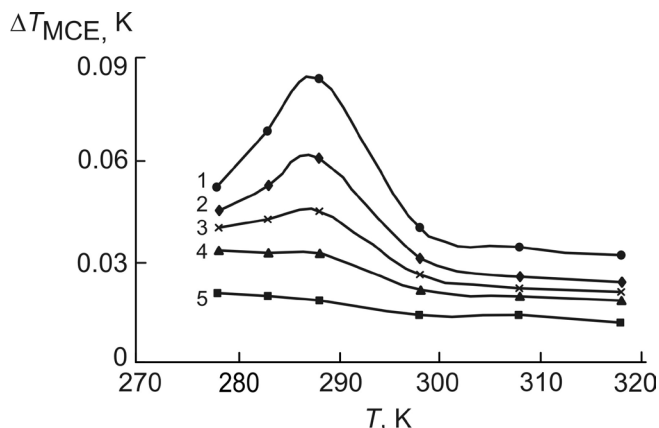


Fig. 6. Temperature dependence of MCE (ΔT_{MCE}) in GdPc₂^{*} at magnetic induction (1) 1.0, (2) 0.8, (3) 0.6, (4) 0.4, (5) 0.2 T.

in GdPc₂^{*} has a maximum at 288 K increasing with the growth in magnetic induction.

Lower MCE values in the series (AcO)GdTPP, (AcO)GdPc, GdPc₂^{*} have allowed us to evaluate the ratio of contributions of the ferromagnetic and antiferromagnetic components to the magnetic behaviour of the GdPc₂^{*} complex. It has been concluded that their MCE is associated with changes in the electron subsystem. Thus, in the double-decker complex, instead of the expected strengthening of spin properties, these properties become weaker, which is only possible when the intermolecular antiferromagnetic coupling prevails over the intramolecular one.

Depending on the electronic configuration, metal-ligand π-backdonation becomes the dominant factor of delocalization of spin density in case of lanthanide complexes with asymmetrically filled f-shells (N → Eu (f⁶) in case of (Cl)EuTPP, N ← Tm (f¹²) in case of (Cl)TmPc).

4. MAGNETOTHERMAL PROPERTIES IN COMPOUNDS WITH SCHIFF'S BASES

An important place among single-molecule magnets is taken by iron(III) complexes with Schiff's bases (d⁵ electronic configuration) as the most stable spin-variable systems [43]. By modifying the ligand chemical structure it is possible to control the magnetic behaviour of the whole complex. In practice, combining liquid crystal and spin-variable behaviour in one material seems quite relevant and promising. The authors of work [44] managed to synthesize a complex that possesses magnetic anisotropy and

depends on the magnetic field in the mesophase. Such materials can be applied as active media for storage and optical devices. Scientists have so far synthesized a number of metal mesogens with the following properties: electric (linear conductors) [45], electro-optical (ferroelectric liquid crystals) [46], optical (strong birefringence, dichroism, nonlinear optical behaviour) [47] and magnetic (paramagnetic liquid crystals, molecule orientation control in magnetic field) [48].

Among the works published around the world there is not a single one devoted to experimental studies of magnetothermal properties of iron(III) azomethine complexes in the region of room temperatures. There are only several works in which the authors conducted a theoretical study of magnetic phase transitions in spin-variable systems [49] or made experimental studies in the region of low (up to 100 K) temperatures [50].

Thanks to their biological activity, iron(III) complexes with Schiff's bases play an important role in medicine [51], as models of iron-containing enzymes in coordination chemistry [52]. Researchers pay special attention to mixed-ligand complexes (that contain N, O and/or S donor atoms) because of their anti-tumour, antifungal and antibacterial activity [53]. Quite interesting are the works aiming to determine the types of ligands that tend to form metal complexes with magnetic properties. Some works represent studies of bis-chelate hexacoordinate iron(III) complexes with Schiff's bases but their liquid crystal analogs have been obtained comparatively recently.

An experimental study of magnetothermal properties of iron(III) complexes with Schiff's bases was for the first time conducted by the calorimetric method in magnetic fields from 0 to 1.0 T in the temperature range of 278-320 K in [54]. As a result, the authors determined the specific heat capacity and magnetocaloric effect of several bis-chelate iron(III) complexes based on azomethine 4,4'-dodecyloxybenzoyloxybenzoyl-4-salicylidene-2-aminopyridine (complexes: (1) - $C_{76}H_{82}N_4O_{12}Fe \cdot NO_3$, (2) - $C_{76}H_{82}N_4O_{12}Fe \cdot PF_6$, (3) - $C_{76}H_{82}N_4O_{12}Fe \cdot BF_4$).

Among the works published around the world there are only some in which the authors conducted

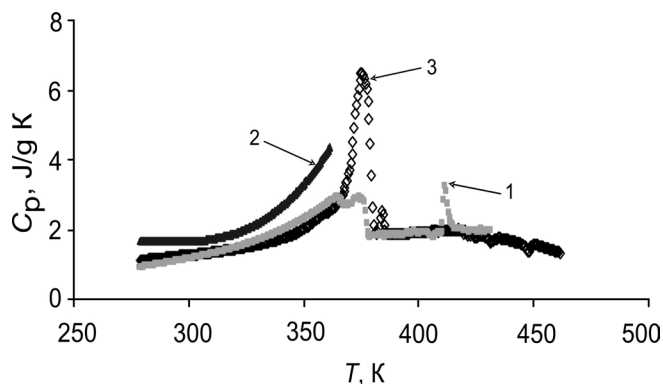


Fig. 7. Temperature dependence of specific heat capacity of complexes: (1) - $C_{76}H_{82}N_4O_{12}Fe \cdot NO_3$, (2) - $C_{76}H_{82}N_4O_{12}Fe \cdot PF_6$, (3) - $C_{76}H_{82}N_4O_{12}Fe \cdot BF_4$.

a theoretical study of magnetic phase transitions in spin-variable systems in the temperature range up to 100 K. Work [54] established a correlation between thermotropic mesomorphism and magnetic phase transition in the complexes.

According to the DSC (Fig. 7) and ESR [55] data, there are no phase transitions in the range of 270 - 360 K in the complexes. However, $f(C_p)$ has maxima at higher temperatures (complex 1 - at 365, 375 and 410 K, complex 3 - at 375 and 383 K). It is probably the specific procedure of the DSC and ESR methods (scanning at certain intervals) and magnetothermal method (keeping a sample at a certain temperature for 4-10 hours) that leads to a shift of the specific heat capacity and absence of maxima in the room temperature region on the ESR curves. The specific heat capacity of the samples at zero magnetic fields (Fig. 7) increases as the temperature becomes higher and is equal to 4.3 J/g K for sample 2, 2.7 J/g K for sample 1 and 25 J/g K for sample 3 at 360 K. No effect of the magnetic field on the temperature dependence is observed. Therefore, we do not show the temperature dependence of specific heat capacity in magnetic field here.

The specific features of the structure of the obtained complexes consisted in the positive values of magnetocaloric effect under the action of magnetic field. In the temperature range of 280 - 320 K, the MCE dependences were extremal, which allowed the authors to suppose a first-order magnetic phase transition (Fig. 9) [54]. The experimentally obtained MCE values of the complexes were positive when magnetic field was

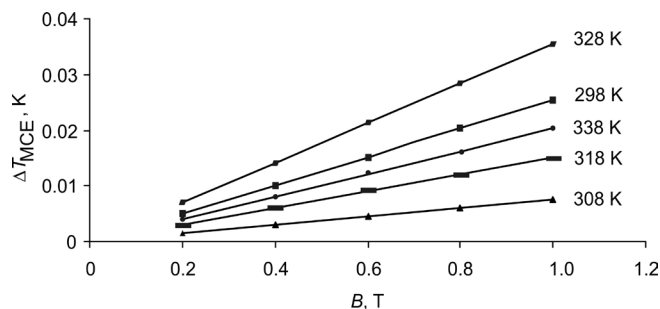


Fig. 8. Field dependence of magnetocaloric effect of complex 3 at different temperatures [54].

switched on and grew linearly as the magnetic induction increased (Fig. 8, for complexes 1 and 2, the dependences are analogous and are not given here).

The maximum MCE value was reached at the temperatures of magnetic phase transition, for example, in the region of Curie and Neel temperatures. Fig. 9 shows temperature dependences of MCE of the BF_4^- complex (3) characterized by an extremal dependence of MCE in the temperature range of 300-350 K, probably due to the magnetic phase transition.

Phase transformations of complexes had been earlier studied by the method of polarization thermal microscopy [55]; it was established that all the substances under study displayed mesomorphic properties and were thermotropic liquid crystals. Analysis of the polarization thermal microscopy and microcalorimetry results shows that there is a correlation between magnetic phase transition and thermotropic mesomorphism. For example, according to the thermal microscopy data, the complex with a BF_4^- counter-ion forms a nongeometrical texture at a temperature of 370 K and later turns into a nematic at about 411 K

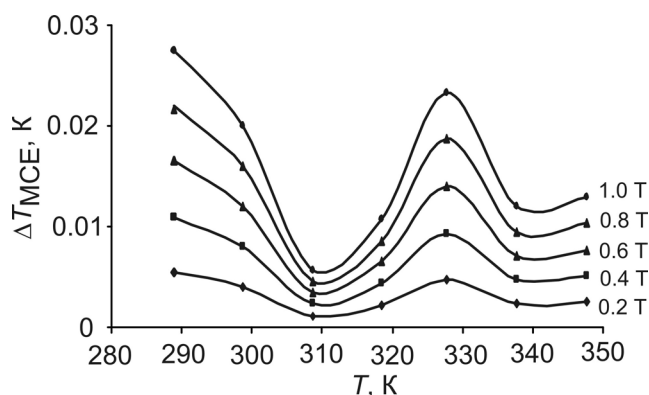


Fig. 9. Temperature dependence of magnetocaloric effect of complex 3 at different magnetic fields.

[54]. Complete destruction of the sample begins at about 425 K. The expected magnetic phase transition is observed at the temperature below the phase transition crystal – mesotropic phase (at 308 K). The complex character of the MCE temperature dependence, probably, indicates a stepwise magnetic phase transition in the sublattice of the complexes.

In order to further study the magnetothermal properties of iron(III) coordination compounds which have mesomorphic and spin-variable properties at the same time, we have tried to modify the paramagnetic ion local environment. It was supposed that this approach would allow combining the liquid crystal state and the properties of the spin-crossover in one temperature range. A new iron(III)-containing complex based on 3,4,5-tri(tetradecyloxy)benzoyloxy-4-salicylidene-N'-ethyl-N-ethylenediamine ($\text{C}_{120}\text{H}_{206}\text{N}_4\text{O}_{12}\text{FePF}_6$ (II.1)) has been synthesized [56]. An experimental study of magnetothermal properties of the obtained complex was carried out in magnetic field from 0 to 1.0 T at a temperature of 293 K. Based on the analysis of the results obtained above, it was supposed that all azomethine iron(III) complexes were capable to display MCE. This hypothesis is based on the Mössbauer spectroscopy data which showed that the iron(III) ion was in a high-spin state at the temperature $T \geq 80$ K; polarization thermal microscopy data which indicated that the complexes had phase transitions; and differential scanning calorimetry data confirming the hypothesis [55, 56]. To confirm these hypotheses, we carried out an experimental study of the magnetocaloric effect of the new synthesized complex when the magnetic field changed from 0 to 1.0 T at a temperature of 293 K. However, contrary to expectations, we found that when the magnetic field was switched on, the complex did not display any magnetocaloric effect. Probably, the formation of an azomethine chelate due to the interaction of the N-ethylenediamine fragment with aldehydes excludes π - π -stacking between the molecules of the complexes, which leads to the repulsion of the molecules' octahedrals, coordination spheres of iron ions. The obtained

complex, due to its structure, probably displays MCE in another temperature range.

5. MCE IN GRAPHENE AND OTHER CARBON NANOFORMS

The computational and experimental works of the last decade have shown that the specific features of the electronic structure of carbon-containing samples can lead to the development of magnetic (including ferromagnetic) or superconductive electronic correlations that do not disappear till room temperature is reached [57]. For example, there are reports about ferromagnetic ordering in samples based on fullerenes [58].

A special place among carbon nanostructures is taken by graphene – a layer of sp^2 -carbon atoms in the form of a hexagonal 2D lattice. Graphene attracts the attention of both theorists and experimentalists with its combination of unique properties caused by the behaviour of its π -electron system determining its high electrophysical characteristics and mechanical strength [59].

Although magnetic ordering in graphene samples of different origins has been observed a number of times, the mechanism of ferromagnetism in such carbon nanostructures is still unclear; however, there is an evident connection between magnetism and defects of different nature in the studied graphene samples [60]. Defects in graphene can be divided into several types [61]: structural defects caused by the presence of “pentagons” or “hexagons”; substitution of C atoms with other atoms in the hexagonal crystal lattice (for example, N and P); defects that are not caused by sp^2 -bonds of carbon atoms (vacancies, breakage of edge bonds, adsorbed atoms, interstitial atoms, deformation of graphene sheets, etc.).

It is noted that along the perimeter of some of the graphene flakes, carbon atoms are in specific edge states with dangling bonds: “armchair”, “zigzag” and “beard” [60]. Unsaturated valence bonds at the edge of graphene flakes are filled with stabilizing elements. It is usually believed that “zigzag” is stabilized by one hydrogen atom. A “bearded” edge is bonded to two hydrogen atoms. There is a great difference between the electron states depending on the edge shape. These

differences are directly connected with magnetic ordering. For example, Fujita [62] applying the Hubbard model, supposed that π -electrons on a “zigzag” edge can produce a ferromagnetic spin system. However, graphene structures of the “armchair” type have no localized states. The structure of the perimeter of arbitrary-shaped graphene flakes is normally described as a combination of zigzag- and armchair edges. Edge states with a poorly developed zigzag structure consisting of three or four teeth significantly change the electron structure.

If both edges of a graphene tape are zigzag-shaped or bearded, the total spin momentum of the graphene tape is equal to zero as the π -electron system produces a two-sublattice structure with the same number of positions in the sublattices, i.e. the local magnetic moments at the edges interact antiferromagnetically.

Such edge effects are strongly dependent on the medium into which the sample under study is placed. For example, hydrogen trapping by dangling bonds along the graphene perimeter can induce finite magnetization or suppress it. A theoretical study of a graphene tape in which every carbon is linked with 2 hydrogen atoms on one edge (bearded edge) and with a single hydrogen atom on the other edge (zigzag edge) has shown that the structure has a finite total magnetic moment: a double lattice is formed with a different number of positions in each sublattice [63].

The unusual magnetism of graphene has been predicted theoretically [64] and observed experimentally [65, 66] in carbon material nanocrystals representing a stack of graphene layers. There is a significant difference in the magnetic behavior of nanographite systems depending on the order of graphene plane positions. A layer displacement by half of a cell value leads to finite magnetization of the sample.

Thus, above we have considered some of the variants of appearance of magnetic ordering in the samples of graphene of different origins and shown that all of them are associated with defects of its structure.

So far, we have found only several theoretical works about MCE in graphene at low temperatures.

For example, works [67, 68] describe oscillatory magnetocaloric and electrocaloric effects and the influence of longitudinal electric field on graphene magnetocaloric properties, respectively. Entropy changes have two contributions, and the temperature at which the entropy changes most of all goes down because of the electric field applied.

MCE can be usually identified by changes in the magnetic state of a magnetic material caused by external magnetic field variations. As it has been mentioned before, depending on conditions of magnetic field application, for quantitative characterization of MCE is usually used either the adiabatic change in the temperature ΔT_{MCE} , or the isothermal decrease in the entropy ΔS_m and heat release Q_{MCE} associated with it. Heat capacity of a material as a function of field and temperature is the third most important parameter showing the material ability to accumulate thermal energy.

Work [69] reports the results of recent studies which found an earlier unknown magnetocaloric effect of flaked multi-layer graphene in the range of room temperatures. Changes in graphene temperature under the action of magnetic field are associated with specific features of its electronic structure and chemical composition.

In this work, magnetic ordering was confirmed by observing MCE of the graphene samples experimentally (reduced graphene oxide RGO) under study.

When the magnetic field induction changed from 0 to 0.1 T, the magnetocaloric effect was positive. The MCE dependence on field was linear (Fig. 10). At 298 K, the MCE values were equal to 0.025 K. The graphene samples obtained by different methods had different degrees of surface imperfection. As a result, it was established that as

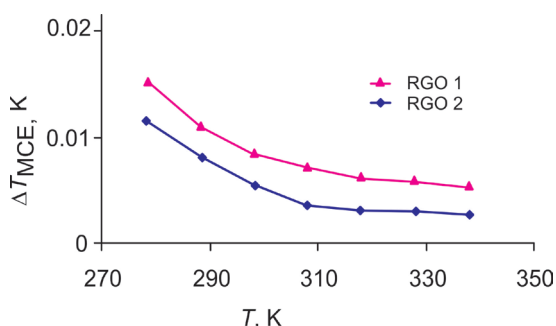


Fig. 10. Temperature dependence of MCE in graphene (RGO 1 and RGO 2) in magnetic field of 1.0 T.

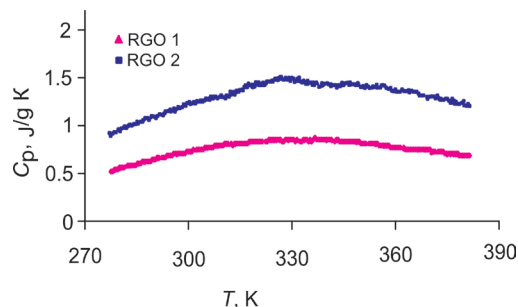


Fig. 11. Temperature dependence of specific heat capacity of graphene (RGO 1/RGO 2) in the zero magnetic field. the graphene surface imperfection became greater, the MCE increased.

As is known, specific heat capacity is a parameter sensitive to the structure of an object and, thus, the DSC analysis of the samples has shown that C_p has different values for the graphene samples with different imperfection degrees. In the range of room temperatures, the values of specific heat capacity of both graphene samples are about 1 J/g K. As the graphene samples' surface imperfection degree becomes greater (Fig. 11), the heat capacity decreases.

A certain place among the carbon-containing materials capable of magnetocaloric effect is taken by compounds based on porphyrins and phthalocyanines (Section 3). Magnetothermal properties of chain and macrocyclic single-molecule magnets of the porphyrin and phthalocyanine types found on the graphene surface have not been studied earlier; there is no literature data about direct measurements of MCE and heat capacity in magnetic fields.

There are a number of works describing the processes of obtaining graphene composites with porphyrins and phthalocyanines. Work [70] reports a method of obtaining a complex of TMPyP and CCG graphene as a result of supramolecular assembly in an aqueous environment (Fig. 12).

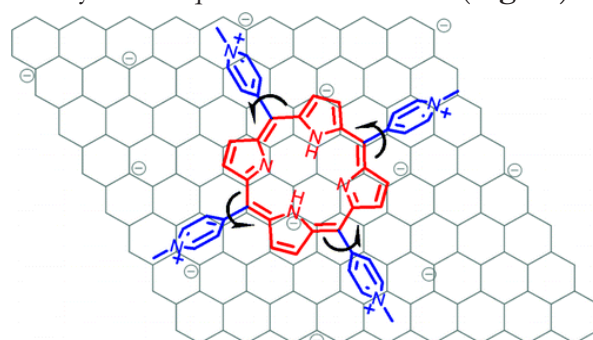


Fig. 12. Structure of the TMPyP/graphene CCG complex [70].

The electrostatic interaction led to a strong compression of the porphyrin on the graphene surface confirmed by a red (bathochromic) shift of the porphyrin Soret band. The authors believe that the TMPyP/graphene CCG complex can be used as a new optical sensor with high sensitivity and selectivity for cadmium ions. In work [71], a composite of reduced graphene oxide (RGO) and copper phthalocyanine tetrasulfonate $\text{CuPc}(\text{HSO}_3)_4$ was obtained. The composite films have lower conductivity but much higher photoconductivity and photosensitivity.

In 2014, Haiou Zhu [72] published a work which described flexible graphene superlattices synthesized by them and consisting of backbones of alternating layers of intercalated vanadium oxide VO_2 and graphene. As a result of electro-donor and deformation effects, the lattice nanostructures display MCE. The maximum value of ΔS_m in the point of phase transition at a temperature of 240 K when the magnetic field changes to 1.5 T is equal to 0.4 J/kg K, which is much higher than the MCE at the phase transition temperature of pure VO_2 .

Soft molecular low-temperature ferromagnetism was observed and studied for n-doped fullerenes obtained when the fullerene was affected by strong organic reducing agents, such as tetrakis(dimethylamino)ethylene [73].

Creating magnetic clusters and hybrids [74, 75] is one of the ways to increase spin density in SMMs [76] and, in general, to improve magnetic properties. In some cases, when there are additional centres with an uncompensated spin in the molecular structure [77, 78], the MCE increases. Molecular forms of carbon, namely fullerene and its functional derivatives, attract the attention of a lot of scientists and engineers because they have high electron transfer characteristics, long-lived charge-separated states, high mobility of carriers and chemical stability [79, 80]. For example, metalloporphyrin-fullerene dyades collected through axial donor-acceptor coordination have been studied in the process of photo-induced electron transfer with acceptable parameters of photocurrent and IPCE [81-83]. Recent studies [84] described below have shown

the first experimental data about the existence of MCE in C_{60} in the room temperature range associated with fullerene antiaromaticity. The aim of study [84] represented in this work was to confirm the magnetocaloric effect and obtain magnetocaloric parameters in the porphyrin-fullerene conjugate built via axial donor-acceptor coordination of the pyridyl substituent in fullerene[60]pyrrolidine with the central cobalt atom in the porphyrin complex. To achieve this, the authors directly determined the thermodynamic parameters of MCE and specific heat capacity of [60] fullerene (C_{60}), 1'-N-methyl-2'-(pyridine-4-yl) pyrrolidino[3',4':1,2][60]fullerene (PyC_{60}), 5,10,15,20-(tetra-4-tret-butylphenyl)21H, 23H-porphyrinato)cobalt(II) ($\text{Co}^{\text{II}}\text{TBPP}$) and the triad (PyC_{60}) $_2\text{Co}^{\text{II}}\text{TBPP}$. The MCE and specific heat capacity were obtained by the original microcalorimetric method [28] and by the method of differential scanning calorimetry (DSC), respectively. As a result, it was shown that the precursors under study and the triad demonstrated a positive magnetocaloric effect at room temperature when the magnetic induction changed from zero to 1.0 T.

By determining the thermodynamic parameters of MCE and specific heat capacity for the donor-acceptor triad in comparison with the fullerene C_{60} and precursors directly by the microcalorimetric method developed by us [28] and by the DSC, respectively, we have shown that carbon nanoforms C_{60} , PyC_{60} , porphyrin complex and the triad have positive MCE values of 0.004, 0.016, 0.028 and 0.007 K, respectively, at 278 K and magnetic field induction of 1.0 T (**Fig. 13**).

The magnetocaloric effect decreases at the formation of the donor-acceptor triad in comparison with PyC_{60} and $\text{Co}^{\text{II}}\text{TBPP}$ but also leads to the appearance of new interesting properties, namely photo-induced electron transfer. Based on the temperature dependences of the thermodynamic parameters – specific heat (Q_{MCE}), enthalpy change (ΔH), entropy change (ΔS) and specific heat capacity, the increase in the MCE following fullerene substitution ($\text{C}_{60} \rightarrow \text{PyC}_{60}$ transition) can be explained by the regions of aromaticity and

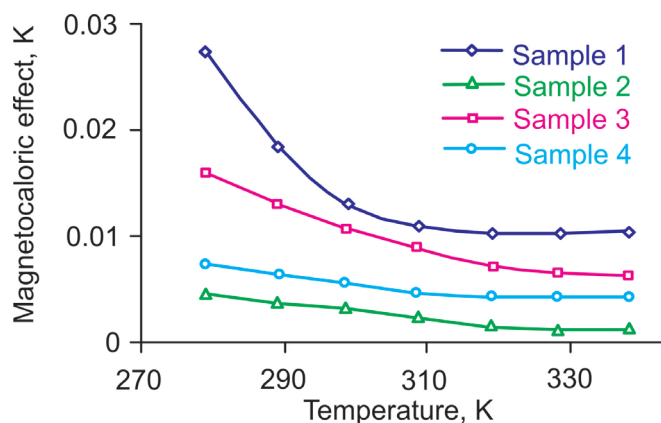


Fig. 13. Temperature dependences of MCE of the samples in magnetic field of 1.0 T: sample 1 - $\text{Co}^{\text{II}}\text{TBPP}$; sample 2 - C_{60} ; sample 3 - PyC_{60} ; sample 4 - $(\text{PyC}_{60})_2\text{Co}^{\text{II}}\text{TBPP}$. The experimental error in the MCE measurements was 2% [84].

antiaromaticity in the fullerene. The decrease in the MCE of the triad, $(\text{PyC}_{60})_2\text{Co}^{\text{II}}\text{TBPP}$, in comparison with the precursors PyC_{60} and $\text{Co}^{\text{II}}\text{TBPP}$ is caused by higher specific heat capacity of the triad (Fig. 14). This fact shows good prospects for the transition from tetracoordinated complexes $\text{Co}^{\text{II}}\text{TBPP}$ to pentacoordinated porphyrin complexes of metals with a non-zero spin, in which there is only one axial coordination position for binding the substituted fullerene.

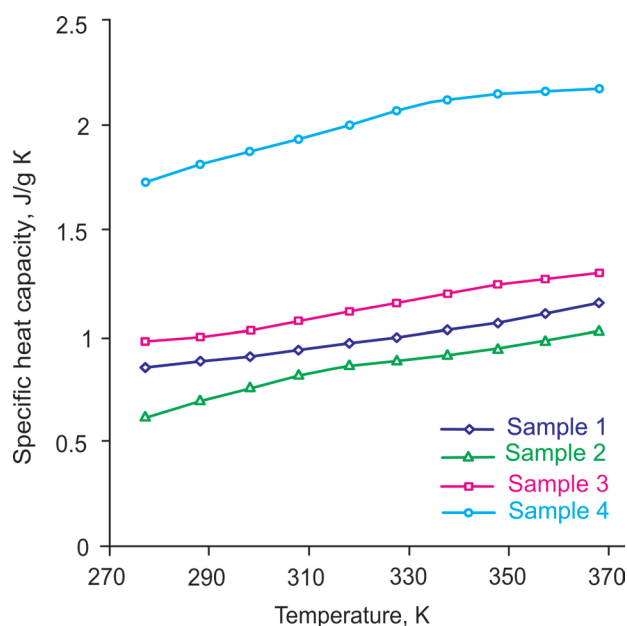


Fig. 14. Temperature dependences of specific heat capacity of the samples in zero magnetic field: sample 1 - $\text{Co}^{\text{II}}\text{TBPP}$; sample 2 - C_{60} ; sample 3 - PyC_{60} ; sample 4 - $(\text{PyC}_{60})_2\text{Co}^{\text{II}}\text{TBPP}$ (DSC data, experimental error 1.5%) [84].

6. CONCLUSION

Thus, the data presented above, allow us to make the following conclusions. Since the data on magnetic and magnetocaloric properties of graphene, fullerene, porphyrins, phthalocyanines are fragmentary, they require systematic studies in order to create, based on them, a series of new materials with non-standard magnetic and electro-optical characteristics.

The mechanism of ferromagnetism in carbon nanostructures, and in graphene in particular, is not clear yet. However, it is now evident that there is a connection between magnetism in graphene and defects in its structure.

The analysed quantitative data allow determining the positive contributions (separation in the ligand field; delocalization of spin density) to the magnetic behaviour of rare earth elements with porphyrins/phthalocyanines along with the negative ones (mass and specific heat capacity increase; interaction of spin-carriers with nuclear spins, higher strength of the bonds with the macrocycle); depending on the electronic configuration of the central atom - metal-to-ligand π -back donation.

In conclusion, it should be said that the method of microcalorimetry allows determining the presence or absence of magnetic phase transition in single-molecule magnets and even now characterizing the behavior of materials at temperatures close to room conditions.

ACKNOWLEDGMENTS

The review was prepared at the Institute of Solution Chemistry of the RAS as a part of a Government assignment, project "Scientific and technical bases of obtaining functional materials and nanocomposites" (a theme of plans No. 0092-2014-0002 and 0092-2017-0003) on the Centre for Joint Use of Scientific Equipment "The Upper Volga Region Centre of Physicochemical Research" and was partially financed by a grant of the Russian Foundation for basic Research (project 18-43-370022-p-a).

REFERENCES

1. Murtaza Bohra, Sahoo SC. Large magnetocaloric effect at Verwey point in nanocrystalline Fe_3O_4 thin films. *J. Alloys. Compd.*, 2017, 699:1118-1121.

2. Jing Zhong, Wenzhong Liu, Ling Jiang, Ming Yang, Paulo Cesar Morais. Real-time magnetic nanothermometry: The use of magnetization of magnetic nanoparticles assessed under low frequency triangle-wave magnetic fields. *Rev. Sci. Instrum.*, 2014, 85:094905. DOI:10.1063/1.4896121.
3. Despoina Sakellari, Mathioudaki Stella, Zoi Kalpaxidou, Konstantinos Simeonidis, Makis Angelakeris. Exploring multifunctional potential of commercial ferrouids bymagnetic particle hyperthermia. *JMMM*, 2015, 380:360.
4. Nemala H, Thakur JS, Naik VM, Vaishnav PP, Lawes G, Naik R. Investigation of magnetic properties of Fe₃O₄ nanoparticles using temperature dependent magnetic hyperthermia in ferrofluids. *J. Appl. Phys.*, 2014, 116:034309. DOI: 10.1063/1.4890456.
5. Pelka R, Gajewski M, Miyazaki Y. Magnetocaloric effect in Mn₂-pyrazole-[Nb(CN)₈] molecular magnet by relaxation calorimetry. *JMMM*, 2016, 419:435. DOI: org/10.1016/j.jmmm.2016.06.074.
6. Buchachenko AL. Organicheskie i molekulyarnye ferromagnetiki: dostizheniya i problemy [Organic and Molecular Ferromagnetics: Achievements and Challenges]. *Uspekhi khimii*, 1990, 59(4):529-550 (in Russ.).
7. Sessoli R, Gatteschi D, Caneschi A, Novak MA. Magnetic bistability in a metal-ion cluster. *Nature*, 1993, 365:141-144.
8. Ovcharenko VI, Sagdeev RZ. Molekulyarnye ferromagnetiki [Molecular Ferromagnetics]. *Uspekhi khimii*, 1999, 68(5):381-400 (in Russ.).
9. Tretyakov EV, Ovcharenko VI. Khimiya nitrosilnyx radikalov v molekulyarnom dizaine magnetikov [Chemistry of nitroxyl radicals in molecular design of magnets]. *Uspekhi khimii*, 2009, 78(11):1051-1093 (in Russ.).
10. Lukov VV, Kogan VA, Cherbakov IN, Popov LD, Levchenko SI. Molekulyarnye magnetiki: eksperimentalno-teoreticheskie osnovy dizaina magnitnikh materialov buduyushchego [Molecular Magnets: Experimental and Theoretical Foundations of the Design of Magnetic Materials of the Future]. *Vestnik Yuzhnogo NC RAN*, 2011, 7(1):24-41 (in Russ.).
11. Evangelisti M, Roubeau O, Palacios E, Camon A, Hooper TN, Brechin EK, Alonso JJ, Cryogenic Magnetocaloric Effect in a Ferromagnetic Molecular Dimer. *Angew. Chem. Int. Ed.*, 2011, 50:6606-6609.
12. Torres F, Bohigas X, Hernandez JM, Tejada J. Magnetocaloric effect in Mn₁₂-2-Cl benzoate. *J. Phys.: Condens. Matter.*, 2003, 15:L119-L123. DOI: stacks.iop.org/JPhysCM/15/L119.
13. Sharples JW, Zheng Y-Zh, Tuna F, McInnesand EJJ, Collison D. Lanthanide discs chill well and relax slowly. *Chem. Comm.*, 2011, 47:7650-7652.
14. Schnack J, Schmidt R, Richter J. Enhanced magnetocaloric effect in frustrated magnetic molecules with icosahedral symmetry. *Phys. Rev. B*, 2007, 76:054413.
15. Zheng Y, Molybdate templated assembly of Ln₁₂Mo₄-type clusters (Ln=Sm, Eu, Gd) containing a truncated tetrahedron core. *Chem. Comm.*, 2013, 49:36-38.
16. Zheng Y-Zh. MnII–GdIII Phosphonate Cages with a Large Magnetocaloric Effect. *Chem. Eur. J.*, 2012, 18:4161-4165.
17. Peng J-B. A 48-Metal Cluster Exhibiting a Large Magnetocaloric Effect. *Chem. Int. Ed.*, 2011, 50:10649-10653.
18. Manoli M, Collins A, Parsons S, Candini A, Evangelisti M, Brechin EK. Mixed-valent Mn supertetrahedra and planar discs as enhanced magnetic coolers. *J Am Chem Soc*, 2008, 130:11129-11139.
19. Zhang Y. Review of the structural, magnetic and magnetocaloric properties in ternary rare earth RE₂T₂X type intermetallic compounds. *Journal of Alloys and Compounds*, 2019, 787:1173-1186. <https://doi.org/10.1016/j.jallcom.2019.02.175>.
20. Ishikawa N, Sugita M, Wernsdorfer W. Quantum tunneling of magnetization in lanthanide single-molecule magnets: bis(phthalocyaninato) terbium and bis(phthalocyaninato) dysprosium anions. *Angew Chem Int Ed*, 2005, 44: 2931–2935.
21. Pelka R, Konieczny P, Zieliński PM, Wasiutyński T, Miyazaki Y, Inaba A, Pinkowicz

- D, Sieklucka B. Magnetocaloric effect in $[\text{Fe}(\text{pyrazole})_4]_2[\text{Nb}(\text{CN})_8] \cdot 4\text{H}_2\text{O}$ molecular magnet. *JMMM*, 2014, 354:359-362.
22. Fitta M, Balanda M, Mihalik M, Pelka R, Pinkowicz D, Sieklucka B, Zentková M. Magnetocaloric effect in M-pyrazole- $[\text{Nb}(\text{CN})_8]$ (M = Ni, Mn) molecular compounds. *J. Phys.: Condens. Matter*, 2012, 24(50):506002.
23. Monteiro B, Coutinho JT, Pereira LCJ. Heterometallic 3d-4f SMMs (in Lanthanide-Based Multifunctional Materials From OLEDs to SIMs). *Advanced Nanomaterials*, 2018, 42:233-261.
24. Caracciolo F, Mannini M, Poneti G, Pregelj M, Janša N, Arčon D, Carretta P. Spin fluctuations in the light-induced high-spin state of cobalt valence tautomers. *Phys. Rev. B*, 2018, 98:054416.
25. Kharisov BI, Kharissova OV (Ed.) *Carbon Allotropes: Metal-Complex Chemistry, Properties and Applications*. Springer, 2019, 350 p., <https://doi.org/10.1007/978-3-030-03505-1>.
26. Wang WL, Sheng Meng, Efthimios Kaxiras. Graphene NanoFlakes with Large Spin. *Nano Letters*, 2008, 8(1):241-245.
27. Sarkar SK, Raul KK, Pradhan SS, Basu S, Nayak A. Magnetic properties of graphite oxide and reduced graphene oxide. *Physica E*, 2014, 64:78-82, <https://doi.org/10.1016/j.physe.2014.07.014>.
28. Korolev VV, Korolev DV, Ramazanova AG. The calorimetric method of evaluating the performance of magnetocaloric materials. *Journal of Thermal Analysis and Calorimetry*, 2019, 136(2):937-941; doi: 10.1007/s10973-018-7704-y.
29. Sharples JW, Collison D. Reprint of "Coordination compounds and the magnetocaloric effect". *Polyhedron*, 2013, 66:15.
30. Korolev VV, Lomova TN, Maslennikova AN, Korolev DV, Shpakovsky DB, Zhang J, Milaeva ER. Magnetocaloric properties of manganese(III) porphyrins bearing 2,6-di-tert-butylphenol groups. *JMMM*, 2016, 401:86.
31. Korolev VV, Lomova TN, Korolev DV, Ramazanova AG, Mozhzhuhkina EG, Ovchenkova EN. New nanoscaled paramagnetic complexes (NPCs) based on Porphyrins/Phthalocyanines for environmental chemistry [In: *RSC Detection Science Advanced Environmental Analysis Applications of Nanomaterials*] Ed. Hussain CM, Kharisov B, Cambridge, Royal Society of Chemistry, 2016, v. 2, 526 p.
32. Korolev VV, Lomova TN, Ramazanova AG, Korolev DV, Mozhzhuhkina EG. Phthalocyanine-based molecular paramagnets. Effect of double-decker structure on magnetothermal properties of gadolinium complexes. *Organometallic Chemistry*, 2016, 819:209.
33. Korolev VV, Lomova TN, Ramazanova AG, Mozhzhuhkina EG. Phthalocyaninato lanthanide (III) acetates as a new class of molecular paramagnets with large magnetocaloric effect. *Mendeleev Commun.*, 2016, 26:301.
34. Korolev VV, Lomova TN, Ramazanova AG, Mozhzhuhkina EG. Molecular paramagnets. The effect of structural modification on (porphyrinato) gadolinium(III) magnetothermal properties. *Synthetic Metals*, 2016, 220:502.
35. Korolev VV, Lomova TN, Klyueva ME, Arefyev IM, Zakharov AG, Korolev DV. Magnetokaloricheskiy effect i teploemkost visokospinovykh kompleksov margantsa v visokodispersnom sostoyanii [Magnetocaloric effect and heat capacity of high-spin manganese complexes in a dispersed state]. *Zhurnal fizicheskoy khimii*, 2010, 84(9):1785 (in Russ.).
36. Korolev VV, Lomova TN, Arefyev IM, Ovchenkova EN, Klyueva ME, Zakharov AG, Korolev DV. Magnitoteplovye svoystva zameshchenogo (tetraazoporfinito) margantsa(III) vodnoy suspenszii [Magnetothermal properties of substituted (tetraazoporfinito) manganese (III) aqueous suspension]. *Zhurnal fizicheskoy khimii*, 2012, 86(7):1285 (in Russ.).
37. Korolev VV, Klyueva ME, Arefyev IM, Ramazanova AG, Lomova TN, Zakharov AG. Regularities of magnetocaloric effect and determining some thermodynamic parameters

- for (2,3,7,8,12,13,17,18-octaethylporphyrinato) chloromanganese(III). *Macrobicycles*, 2008, 1(1):68.
38. Korolev VV, Arefyev IM, Klyueva ME, Lomova TN. Use of magnetocaloric effect for direct experimental determining some thermodynamic parameters of manganese(III) porphyrin. *J Porphyrins Phthalocyanines*, 2008, 12(3-6):584.
39. Lomova TN, Korolev VV, Zakharov AG. Central atom/substituent effects on magnetothermal properties of metal porphyrins in aqueous suspension. *Materials Science & Engineering B*, 2014, 186:54-63.
40. Lomova TN, Korolev VV, Ramazanova AG, Ovchenkova EN. Magnetothermal properties of (octakis-trifluoromethylphenyltetraazaporphinato) manganese(III) acetate in aqueous suspension. *J Porphyrins Phthalocyanines*, 2015, 19:1262.
41. Korolev VV, Korolev DV, Lomova TN, Mozhzhukhina EG, Zakharov AG. Magnitokaloricheskiy effect i teploemkost vodnikh suspenziy porfirinovykh kompleksov redkozemelnykh elementov iz mikrokalorimetriceskikh dannykh [Magnetocaloric effect and heat capacity of aqueous suspensions of porphyrin complexes of rare-earth elements from microcalorimetric data]. *Zhurnal fizicheskoy khimii*, 2012, 86(3):578-582 (in Russ.).
42. Lomova TN, Andrianova LG, Berezin BD. Mekhanizm dissotsiatsii i kineticheskaya ustoychivost tetrafenilporfirinovykh kompleksov lantanoidov ot samariya do lutetsiya [The mechanism of dissociation and kinetic stability of lanthanide tetraphenylporphyrin complexes from samarium to lutetium]. *Zhurnal fizicheskoy khimii*, 1987, 61(11):2921 (in Russ.).
43. Binnemans K, Galyametdinov YG, Van Deun R, Bruce DW, Collinson SR. Rare-earth-containing magnetic liquid crystals. *J Am. Chem. Soc.*, 2000, 122:4335-4344.
44. Galyametdinov Yu, Ksenofontov V, Prosvirin A, Ovchinnikov I, Ivanova G, Gütllich P, Haase W. First Example of Coexistence of Thermal Spin Transition and Liquid-Crystal Properties. *Angew. Chem. Int. Ed.*, 2001, 40(22):4269-4271.
45. Belarbi Z, Sirlin C, Simon J, André JJ. Electrical and magnetic properties of liquid crystalline molecular materials: Lithium and lutetium phthalocyanine derivatives. *J Phys. Chem.*, 1989, 93:8105-8110.
46. Khoo I-C. *Liquid crystals*. Wiley Inc., 2007, 368 p.
47. Bruce DW, Dunmur DA, Hunt SE, Maitlis P.M., Orr R. Linear Dichroism of Mesomorphic TransitionMetal Complexes of Alkoxydithiobenzoates. *J. Mater. Chem.*, 1991, 1:857-861. DOI: 10.1039/JM9910100857.
48. Barberá J, Levelut A-M, Marcos M, Romero P, Serrano JL. X-ray diffraction study of some mesogenic copper, nickel and vanadyl complexes *Liquid crystals*, 1991, 10:119-126; doi: 10.1080/02678299108028235.
49. Bousseksou A, Nasser J, Linares J, Boukheddaden K, Varret F. Ising-like model for the two-step spin-crossover. *Journal de Physique I*, 1992, 2(7):1381-1403.
50. Spiering H, Kohlhaas T, Romstedt H, Hauser A, Bruns-Yilmaz C, Kusz J, Gütllich P. Correlations of the distribution of spin states in spin crossover compounds *Coordination Chemistry Reviews*, 1999, 190-192:629-647.
51. Torayama H, Nishide T, Asada H, Fujiwara M, Matsushita T. Preparation and characterization of novel cyclic tetranuclear manganese(III) complexes: $MnIII_4(X-salmphen)_6$ (X-salmphen $H_2 = N,N'$ -disubstituted-salicylidene-1,3-diaminobenzene (X=H, 5-Br)). *Polyhedron*, 1998, 16(21):3787-3794.
52. Kalwania GS, Mathur R, Shyam R, Mathur P, Mathur SP. Spectrophotometric determination of iron (III) with Schiff's base derived from pyridine -2-carboxaldehyde and 2-aminopyrimidine by adsorption on Polyurethane. *Journal of Natura Conscientia*, 2010, 1(3):240-242.
53. Saxena A, Koacher JK, Tandon JP. Electron-impact Induced Fragmentation Studies on Some Diorganonitrogen Complexes of S-Containing Schiff Bases. *Inorg. Nucl. Chem. Lett.*, 1981, 17(778):229-233.
54. Gruzdev MS, Korolev VV, Ramazanova AG, Chervonova UV, Balmasova OV. Magnetocaloric Properties of Dendrimer

- Complexes of Fe(III) with Substituted Schiff Base. *Liquid Crystals*, 2018, 45(6):907-911.
55. Gruzdev M, Chervonova U, Zharnikova N, Kolker A. Mesomorphic azomethine complexes of Iron(III) based on 4,4'-dodecyloxybenzoyloxybenzoyl-4-salicylidene-2-aminopyridine. *Liquid Crystals*, 2013, 40(11):1541-1549.
56. Chervonova UV, Gruzdev MS, Kolker AM, Akopova OB. Structure and phase transitions of azomethine biligand complexes of iron(III) based on 3,4,5-tri(tetradecyloxy)benzoyloxy-4-salicylidene-N'-ethyl-N-ethylenediamine. *J Structural. Chem.*, 2016, 57(3):478-490. DOI: 10.1134/S0022476616030094.
57. Gonzalez J, Guinea F, Vozmediano M. Electron-electron interactions in graphene sheets. *Phys. Rev. B*, 2001, 63(13):421.
58. Wood RA, Lewis MH, Lees MR, Bennington SM, Cain MG, Kitamura N. Ferromagnetic fullerene. *J Phys.: Condens. Matter*, 2002, 14(22):L385.
59. Avouris P. Graphene: Electronic and Photonic Properties and Devices. *Nano Lett.*, 2010, 10(11):4285-4294.
60. Makarova TL. Magnitnye svoystva uglerodnykh struktur [Magnetic properties of carbon structures]. *Fizika i tekhnika poluprovodnikov*, 2004, 38(6):641-664 (in Russ.).
61. Gubin SP, Tkachev SV. *Grafen i rodstvennye nanoformy ugleroda* [Graphene and related carbon nanoforms]. M., LENAND Publ., 2015, 112 p.
62. Fujita M, Wakabayashi K, Nakada K, Kusakabe K. Peculiar localized state at zigzag graphite edge. *J Phys. Soc. Japan.*, 1996, 65(7):1920-1923.
63. Kusakabe K, Maruyama M. Magnetic nanographite. *Phys. Rev. B*, 2003, 67:092406.
64. Harigaya K. Mechanism of magnetism in stacked nanographite. *J Phys.: Condens. Matter.*, 2001, 13:1295-1302.
65. Shibayama Y, Sato H, Enoki T, Endo M. Disordered magnetism at the metal-insulator threshold in nano-graphite-based carbon materials. *Phys. Rev. Lett.*, 2000, 84(8):1744.
66. Enoki T, Kawatsu N, Shibayama Y, Sato H, Kobori R, Maruyama S, Kaneko K. Magnetism of nano-graphite and its assembly. *Polyhedron*, 2001, 20(11-14):1311-1315.
67. Alisultanov ZZ, Reis MS. Oscillating magneto- and electrocaloric effects on bilayer graphenes. *Solid State Communications*, 2015, 206:17-21. DOI: 10.1016/j.ssc.2015.01.005.
68. Reis MS. Influence of longitudinal electric field on the oscillating magnetocaloric effect of graphenes. *Solid State Communications*, 2013, 161:19-22. DOI: 10.1016/J.ssc.2013.03.002.
69. Korolev VV, Ramazanova AG, Balmasova OV, Soloveva AYu, Buslaeva EYu, Gubin SP, Gruzdev MS. Magnetocaloric effect in reduced graphene oxide. *JMMM*, 2019, 476:604-607.
70. Yuxi Xu, Lu Zhao, Hua Bai, Wenjing Hong, Chun Li, Gaoquan Shi. Chemically Converted Graphene Induced Molecular Flattening of 5,10,15,20-Tetrakis(1-methyl-4-pyridinio) porphyrin and Its Application for Optical Detection of Cadmium(II) Ions. *J Am. Chem. Soc.*, 2009, 131(37):13491.
71. Anindarupa Chunder, Tanusri Pal, Saiful I Khondaker, Lei Zhai. Reduced Graphene Oxide/Copper Phthalocyanine Composite and Its Optoelectrical Properties. *J Phys. Chem. C*, 2010, 114:15129-15135.
72. Haiou Zhu, Chong Xiao, Hao Cheng, Fabian Grote, Xiaodong Zhang, Tao Yao, Zhou Li, Chengming Wang, Shiqiang Wei, Yong Lei, Yi Xie. Magnetocaloric effects in a freestanding and flexible graphene-based superlattice synthesized with a spatially confined reaction. *Nature Communications*, 2014, 3(5):3960. DOI: 10.1038/ncomms4960.
73. Allemand P-M, Khemani KC, Koch A, Wudl F, Holczer K, Donovan S, Grüner G, Thompson DJ. Organic molecular soft ferromagnetism in a Fullerene C₆₀. *Science*, 1991, 253(5017):301-303.
74. Idowu MA, Xego S, Arslanoglu Y, Mark J, Antunes E, Nyokong T. Photophysicochemical behaviour and antimicrobial properties of monocarboxy Mg(II) and Al(III) phthalocyanine-magnetite conjugates. *Spectrochimica Acta, Part A*, 2018, 193:407-414. DOI: 10.1016/j.saa.2017.12.052.
75. Modisha P, Antunes E, Mack J, Nyokong T. Improvement of the Photophysical Parameters of Zinc Octacarboxy Phthalocyanine upon Conjugation to Magnetic Nanoparticles.

- International Journal of Nanoscience*, 2013, 12:1350010-1350010-10. DOI: 10.1142/S0219581X13500105.
76. Giménez-Agully N, de Pipaón CS, Adriaenssens L, Filibian M, Martínez-Belmonte M, Escudero-Adán EC, Carretta P, Ballester P, Galán-Mascarós JR. Single-Molecule-Magnet Behavior in the Family of $[Ln(OETAP)_2]$ Double-Decker Complexes (Ln=Lanthanide, OETAP=Octa(ethyl)tetraazaporphyrin). *Chem. Eur. J.*, 2014, 20:12817-12825. DOI: 10.1002/chem.2014.02.869.
77. Fu X, Xu L, Li J, Sun X, Peng H. Flexible solar cells based on carbon nanomaterials. *Carbon*, 2018, 139:1063-1073. DOI: 10.1016/j.carbon.2018.08.017.
78. Lomova TN, Motorina EV, Klyuev MV. Donor-acceptor fullerene complexes based on metal porphyrins [Kharisov BI, editor *CRC Concise Encyclopedia of Nanotechnology*] London, CRC Press, 2015, p. 215-229.
79. Anikin MS, Tarasov EN, Kudrevatykh NV, Osadchenko VH, Zinin AV. About the role of Fe-ions in the formation of magnetocaloric effect in $H_o(Co_{1-x}Fe_x)_2$ compounds. *Acta Physica Polonica A*, 2015, 127:635-637. DOI: 10.12693/APhysPolA.127635.
80. Bichan NG, Ovchenkova EN, Kudryakova NO, Ksenofontov AA, Gruzdev MS, Lomova TN. Self-assembled cobalt(II)porphyrin–fulleropyrrolidine triads via axial coordination with photoinduced electron transfer. *New J Chem.*, 2018, 42:12449-12456. DOI: 10.1039/C8NJ00887F.
81. Piskorsky VP, Korolev DV, Valeev RA, Morgunov RB, Kunitsyna EI. *Physics and Engineering of permanent magnet*. Ed. Kablov EN, Moscow, VIAM Publ., 2018, 359 p.
82. Prato M, Maggini M, Giacometti C, Scorrano G, Sandona G, Farnia G. Synthesis and electrochemical properties of substituted fulleropyrrolidines. *Tetrahedron*, 1996, 52:5221-5234. DOI: 10.1016/0040-4020(96)00126-3.
83. Bichan NG, Ovchenkova EN, Gruzdev MS, Lomova TN. Formation Reaction and Chemical Structure of a Novel Supramolecular Triad Based on Cobalt(II) 5,10,15,20-(Tetra-4-Tert-Butylphenyl)-21H,23H-Porphyrin and 1-Methyl-2-(Pyridin-4'-Yl)-3,4-Fullero[60]Pyrrolidine. *Rus. J Struct. Chem.*, 2018, 59:711-719. DOI: 10.1134/S0022476618030320.
84. Lomova TN, Korolev VV, Bichan NG, Ovchenkova EN, Ramazanova AG, Balmasova OV, Gruzdev MS. New paramagnets based on nanocarbon and cobalt(II)porphyrin: Magnetocaloric effect and specific heat capacity. *Synthetic Metals*, 2019, 253:116-121, doi: 10.1016/j.synthmet.2019.05.004.

VISUALIZATION OF GRAPHIC INFORMATION IN THE GENERAL-PURPOSE OPERATING SYSTEMS

Konstantin V. Pugin, Kirill A. Mamrosenko, Alexander M. Giatsintov

Scientific Research Institute of System Analysis of the RAS, Center of Visualization and Satellite Information Technologies, <https://niisi.ru>

Moscow 117218, Russian Federation

rilian@niisi.ras.ru, mamrosenko_k@niisi.ras.ru, algts@niisi.ras.ru

Abstract. Article describes solutions for developing programs for interaction between Linux operating system and display controller. Operating system architecture encourages creating a driver — component, which task is to perform interaction of hardware controller and OS kernel with the use of many protocols. The development of drivers for the open source OS is difficult due to continuous changes in the structure of the kernel, which breaks backward compatibility frequently. Several approaches to display controller driver development are provided in the article. Basic concepts of these drivers include Kernel Mode Setting (or KMS), meant to provide driver in the kernel and User Mode Setting, meant to provide driver in graphical server. Specific way is used for develop Linux kernel drivers - it is half-procedural, and half-object oriented. Sometimes it is called as “OOP in C”, because it is based on GNU C Language extensions usage to simulate object-oriented techniques. GNU C usage almost prevents using non-GNU compilers to build a driver. Newest concept of writing display controller driver for Linux kernel is based upon atomic mode setting concept, in modern Linux it is achieved via state concept - intermediate states of an object are stored and modified without side effects to other objects. In order to make this concept work, driver should conform to the principle “disable function undoes all effects of enable and nothing more”. Several approaches for display driver development are provided in this article, and most modern method – atomic KMS mode setting, - is described in detail.

Keywords: drivers, embedded, KMS, kernel module, development

UDC 004.454

Bibliography - 11 references

Received 23.01.2019, accepted 05.02.2019

RENSIT, 2019, 11(2):217-224

DOI: 10.17725/rensit.2019.11.217

CONTENTS

1. INTRODUCTION (217)
 2. COMPONENTS OF THE GRAPHIC SYSTEM (218)
 3. LINUX GRAPHIC SYSTEMS AND DRIVERS (2182)
 4. KERNEL MODE SETTING AND USER MODE SETTING. HISTORICAL BACKGROUND (219)
 5. OBJECT MODEL OF THE LINUX KERNEL (220)
 6. KMS ATOMIC DROVERS. BASIC ENTITIES AND INTERFACES NECESSARY FOR IMPLEMENTATION (221)
 7. DEBUGGING DRIVER (222)
 8. CONCLUSION (223)
- REFERENCES (223)

1. INTRODUCTION

Currently, due to the increase in the share of various wearable and embedded systems, it is a relevant objective to develop drivers for them. Many embedded systems use the Linux OS, which has the support of a large number of processor architectures, as well as the support of loadable modules, which allows the process of adding a driver to be greatly simplified.

On many Linux-based embedded systems, displaying information has its own specifics. Often, a certain embedded system requires the development of specialized drivers for the applicable display controller.

When developing a display controller driver based on the Linux operating system, it is necessary to take into account a number of aspects related to the kernel development style, development patterns, and rapid changes in the kernel interaction interface (API). There are also few documents on the development of open-source display controller drivers, and are mainly limited to extracts from comments in the source code files of the Linux kernel, or schemes based on them. This article will look at a modern approach to writing a display controller driver for the Linux OS.

2. COMPONENTS OF THE GRAPHIC SYSTEM

Due to the need for 3D rendering, high-intensity calculation of shaders, high-resolution video processing and other requirements of a modern user of computer systems, the PC graphic subsystem has become significantly more complicated in comparison with it in the early years, and most often a modern graphic system includes [1]:

1. A Graphic accelerator (Graphics Processing Unit, GPU). It is its performance that is mainly measured by tests and various prototype software (for example, by startup of 3D applications at maximum settings or specially created scenes), it runs the shaders using a specialized multi-threaded architecture.
2. The display controller. This part of the graphics subsystem is used to determine the modes of graphics displaying, as well as to interact with monitors (obtaining available monitor resolutions, sending a finished frame, etc.).
3. You can also find specialized chips in the graphic system for video output, for

interacting with video capture devices, and specialized random access memory (Graphics Double Data Rate, GDDR) for use by the graphic accelerator.

This list of components is not mandatory, since there are graphic subsystems in which one or more components are missing or not involved. For example, in some NVIDIA Optimus solutions installed in laptops, the on-screen display controller is not involved, the entire configuration of monitor modes occurs through the controller of another graphics card - Intel. Only a graphics accelerator is used from NVIDIA. You can also find systems with a different combination of selected components of the graphics system.

3. LINUX GRAPHIC SYSTEMS AND DRIVERS

The graphic system in Linux is represented by a graphic stack and various libraries used in it (Fig. 1) [2].

If we consider the components of the Linux graphical stack from top to bottom, we can say that the vast majority of them are designed to interact with the GPU, in particular: most of the Wayland and libdrm, fully EGL and almost completely X. Only a small part of DDX. (Device Dependent X) (Fig. 1.) and Wayland, as well as libgbm interacts with the on-screen display controller.

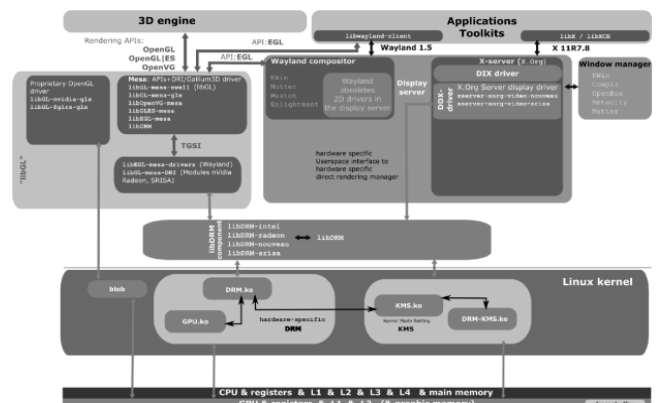


Fig. 1. Graphic stack Linux.

4.KERNEL MODE SETTING AND USER MODE SETTING. HISTORICAL BACKGROUND

Initially, there was only user mode setting, which was produced in the DDX drivers and enabled to set the mode for displaying graphical information. [3] The determination was often executed through mode tables, and was not extensible, or it was done using algorithms within a code that were unique to each chip. There was also a solution such as VBE (Vesa BIOS Extensions), an extension for IBM PC BIOS, which allowed for some limited operations of installing modes with its use (without writing a direct algorithm for interacting with the graphics subsystem). Gradually, most drivers for IBM PCs switched to VBE. But VBE had some serious downsides:

- Lack of support for multiple CRT controllers (in most cases it is necessary to support output from multiple graphic accelerators to several displays or output to TV).
- Problems if there were several different outputs (and they could be different on the same chip series).
- Problems of use of several different timers.

To solve these problems in 2008, an extension was accepted to the kernel [4], which provided support for setting modes inside the kernel (kernel mode setting, or KMS). Along with the problems that this extension brought (such as some decrease in the stability of the kernel due to the fact that the drivers are written not very properly, as well as the expansion of the kernel because it includes many graphic drivers), there were also some advantages, such as simplified debugging (because there is the entire mode tuning code inside the kernel), simplified

power management, and deleting the old code of the frame buffer drivers (in the era of tables and VBE (and for some drivers even now), the kernel also contained a frame buffer management subsystem, which allowed graphic output to be used without loading the graphic server for displaying console messages, or for drawing console programs).

The first version of the KMS protocol [5] was built on the XRandR 1.2 model, which was good enough at that time to install modes on ordinary workstations. But with the advent of mobile devices, the capabilities of the first KMS specification began to be insufficient - in order to reduce energy consumption, the concept of unified planes was developed, which was used to display video on a certain screen, to activate the hardware cursor (in the first versions of KMS, the hardware cursor interacted with the screen mode controller according to a separate protocol), and for other such cases.

Then support for other KMS objects was added, which allowed the gamma of the displayed output to be changed, the displayed image to be rotated directly in the driver, and so on [6].

There is one problem with all of this - for the interaction of these subsystems with the kernel, a large number of ioctl was required. And when trying to interact, each device had to check every ioctl, which was very inconvenient.

Due to these KMS problems on mobile devices, Google has developed its own interface to set modes, the Android Atomic Display Framework (ADF), for the Linux kernel as part of the Android OS [7].

Despite many advantages (atomic update of layers, ease of new drivers' development), ADF had the following disadvantages:

- There is only one update queue, and, therefore, the support of multi-screen modes is very poor. If there were 2 displays with different update rates, the update rate was led to the same (most often less) one, which resulted in either jerking at a faster display or slowing down at a slower one.
- ADF assumed that in user space there is a specific driver for the graphic chip, which necessarily provides 2D or 3D acceleration, which did not satisfy the developers of the main kernel, since it cut off all the "common" drivers (designed for devices not yet supported and providing minimal functionality) of the `xf86-video-modesetting` type.
- The ADF also had difficulties with updating the chain of outputs. Since drivers with support for multiple outputs have a lot of shared resources that require a one-time update regardless of the number of outputs, whereas the ADF had a requirement for an atomic update of the entire chain of one output. For multiple outputs, this could be implemented in a cycle, but this implementation did not work in the case of multiple outputs and shared resources.
- ADF used the midlayer pattern that is not recommended in kernel development. This pattern is not used, because despite the seeming usability and ease of developing drivers for the midlayer, there can always be a vendor that will be not satisfied with the midlayer - this is unacceptable for the kernel.
- ADF was new and there was no backward compatibility with old interfaces and APIs.

Therefore, it was decided not to save ADF, but to introduce its best features in KMS [5].

This is how KMS introduced the concept of atomic updates. The modern driver of the display controller must be written in the kernel space using this concept.

5. OBJECT MODEL OF THE LINUX KERNEL

To write a driver in kernel space, it is necessary to use its object model. [8] Despite the fact that the Linux kernel is written in C, there is an object model inside it that allows some object-oriented approaches to be applied when writing kernel drivers. To build this object model the following methods are most often used:

- Establishment of a mutually one-to-one correspondence between structures of a special type and objects (within the meaning of the OOP). The structure of a special type contains:
 - pointers to functions or a pointer to a vtable structure (where virtual methods are connected);
 - a pointer of the `void*` type, where the closed part of the structure data is connected (analogue of the closed type of inheritance);
 - contains the entire object of the base type (not in the form of a pointer) to ensure the connectivity between the parent and the heir through special compiler commands.
- Use of a special name and function signature (`object_type_name_operation_name (object_type* object, ...)`), which allows the type of object for which this function is intended to be precisely defined. It is possible to establish a one-to-one correspondence between methods in understanding the OOP and such functions.

- Vtable structures. C (unlike C++) does not have such an entity as virtual functions, tables of the virtual function, and similar things. Therefore, to store virtual methods, the developers of the kernel use structures consisting only of pointers to functions or storing in addition to such pointers also variables that are similar to the variables of the protected type of inheritance in OOP. These structures can be compared to a vtable from C++.
- To build private fields in some structures there are void* variables in which a closed structure can be assigned (in particular, when initializing the KMS driver, it is necessary to create a closed structure in the drm_device structure) - container_of together with storing the structure of the "base class" in the "heir". To simplify the implementation of inheritance in kernel structures, a method such as storing a complete basic structure within a derivative one is often used, and if it is necessary to obtain a derived structure from the basic one, the container_of macros is used, which internally uses the offsetof compiler command enabling to find the basic structure within the derivative one.

All of these things in general make writing code for the Linux kernel much easier and are used in most of the existing drivers.

6. KMS ATOMIC DROVERS. BASIC ENTITIES AND INTERFACES NECESSARY FOR IMPLEMENTATION

This section will consider the issue of creating a Linux kernel module that works through DRM and KMS with a display controller and does not use other components of the

graphic subsystem. Such a driver is most often written for embedded systems, since components from different manufacturers (for example, a 3D chip from Mali, and on-screen display controller from Kirin) can be used in them, which must be considered when developing a driver for each component.

The main components of the KMS driver (Fig. 2) [9]:

1. Driver object (drm_driver). General parameters (such as its version, creator, and supported interfaces) are written in the driver structure body, and the general issues of driver operation (work with GEM, interrupts, and device files) are defined. As opposed to the general practice of writing objects in the kernel, the driver object contains most of the pointers to virtual methods (only file operations are added to the vtable structure). Initially, also work with vblank was determined there, but was transferred to CRTC (since in the case of multiple CRTC they may have different work with vblank events).
2. Controller of CRT (CRTC). The state of the mode displayed, objects of the main plane and cursor, the atomic state of the CRTC, and the activation bit are stored in CRTC. Functions assigned by CRTC

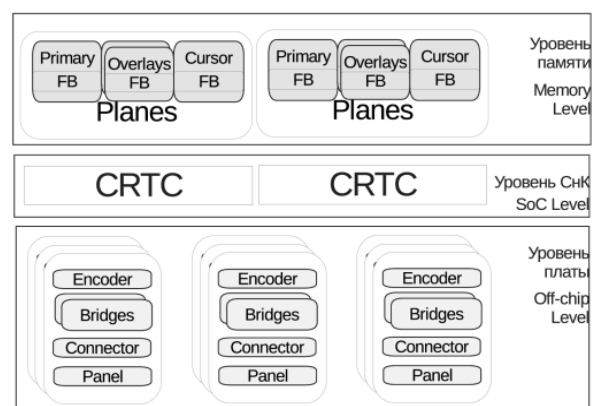


Fig. 2. An example of the main components of the KMS driver.

- working with vblank, with planes (main plane, cursor and overlay planes) and with pages.

3. One or several planes. For each CRTC there should be exactly one primary plane, no more than one cursor plane, and as many overlay planes as you want. Planes are attached to the CRTC that created them.
4. One or more encoders. The encoders must convert the signal from the internal DRM format to the output format and vice versa if a non-trivial conversion is required. It adjusts the mode, and also has functions for managing the power consumption of the information output device. The encoder is not rigidly linked to the CRTC, but instead it sets the bits possible to use by CRTC. The encoder may also check the set mode for admission, but usually it is used only in non-trivial cases.
5. Connector. The connector defines the output and connects the device directly and, through it, with one or more CRTC and encoders. Also, the connector has a status and it is there that the driver determines the mode check for whether it is possible to set it in this output. Most often the number of connectors corresponds to the number of video outputs. In many cases, the connector itself converts data into the necessary format, in this case it is linked to an empty encoder.
6. Bridge (`drm_bridge`). The bridge connects several encoders if the signal needs to be converted several times. In terms of functionality, it is similar to the connector and encoder.
7. Panel (`drm_panel`). The panel is a software representation of LCD panel

control functions and is linked to the connector. It sets the functions for obtaining permissible modes and timings of the parent connector.

7. DEBUGGING DRIVER

To debug the kernel space driver [10], it is possible to use:

1. The kernel assembled in the Debug mode (and the interfaces of such a kernel, output via debugfs). Inside the kernel assembled supported by dynamic debugging, there is a debugfs virtual file system, in pseudo-files of which various debugging information is output on user request. The disadvantages of this system consist in the fact that it works only on the loaded kernel and it is necessary to read the files through the debugged PC, and this system also works only with the areas of the kernel code considered fit by the developers themselves. For arbitrary debugging it is necessary to make own debugging changes on the kernel.
2. The KGDB debugger. The KGDB debugger is GDB started up on a remote PC connected via a serial port interface to a debugged board. To do this, inside the kernel, there is an opportunity to assemble with support of waiting for a connection from the GDB interface, with a support of displaying error messages and stack tracing to the serial port. On the part of the remote user's PC, it is necessary to install the GDB debugger, as well as a kernel sample assembled in debug mode with debug information, only in this case KGDB will provide information about what is happening inside the kernel. To separate the regular output and the debugging output, special mixer programs working as an interlayer

between the debugger and the kernel are used.

3. Specialized FPGA (Field-Programmable Gate Array), such as Palladium, which allow graphics subsystem to trace the receipt of signals [11]. FPGA data has access to signals and values in the registers of devices that they emulate, which allows the value of kernel to be compared with the recorded values when debugging the drivers.

8. CONCLUSION

When developing an on-screen display controller driver for embedded systems, it is necessary to take into account a number of aspects, such as debugging difficulties, a special object model of the Linux kernel, the specifics of interaction with the hardware component. Since on-screen display controllers are available in almost each embedded system (except for those that do not use on-screen display at all), the problem of developing controller drivers for them, approaches to their design, debugging and testing in accordance with the Linux kernel object model is an relevant objective. Currently, the development of these drivers is carried out mainly in a closed way in large companies that make only the final result available to the public, which has not very positive impact on the development of a single approach to the development of on-screen display controller drivers and approaches to the methods of screen display modes setting in general.

This article considers the approaches to writing driver output controller modes used at different times in Linux OS, as well as reviews the latest approach to the development of data drivers for embedded systems in details. The practical implementation of the driver

of such type can be used both with GPU drivers and with new developments in the field of software rasterization (in particular, llvmpipe).

ACKNOWLEDGMENT

Publication is made as part of national assignment for fundamental scientific researches (GP 14) on the topic (project) No.0065-2019-0001.

REFERENCES

1. Madieu J. *Linux Device Drivers Development*. Birmingham, Packt Publishing, 2017, 586 p.
2. Efremov IA, Mamrosenko KA, Reshetnikov VN. *Metody razrabotki drajverov graficheskoy podsystemy* [Methods of development graphics subsystem drivers]. *Programmnyye produkty i sistemy*, 2018, 31(3):425-429 (in Russ.).
3. Verhaegen L. *X and Modesetting: Atrophy illustrated*. 2006, p. 7.
4. Airlie Dave, Barnes Jesse, Bornecrantz Jakob. DRM: add mode setting support [Electronic resource]. URL: <https://git.kernel.org/pub/scm/linux/kernel/git/torvalds/linux.git/commit/?id=f453ba0460742ad027ae0c4c7d61e62817b3e7ef> (last access date: 04.09.2018).
5. Vetter Daniel. Atomic mode setting design overview, part 1 [Electronic resource]. URL: <https://lwn.net/Articles/653071/> (last access date: 04.09.2018).
6. Pinchart L. Why and How to use KMS as Your Userspace Display API of Choice. *LinuxCon Japan Tokyo*, 2013, 52 p.
7. Syrjäla V, Clark R, Hackmann G. [RFC 0/4] Atomic Display Framework [Electronic resource]. URL: <https://lists.freedesktop.org/archives/dri-devel/2013-August/044522.html> (last access date: 20.11.2018).
8. Brown Neil. Object-oriented design patterns in the kernel, part 1 [Electronic

- resource]. URL: <https://lwn.net/Articles/444910/> (last access date: 04.09.2018).
9. The Linux Kernel Documentation [Electronic resource]. URL: <https://www.kernel.org/doc/html/v4.11/gpu/drm-kms.html> (last access date: 20.04.2018).
10. Bazhenov PS, Mamrosenko KA, Reshetnikov VN. Issledovanie i otladka komponentov dlya obrabotki trexmernoy grafiki operatsionnykh sistem [Research and debugging components for processing three dimensional graphics in operating systems]. *Programmnye produkty, sistemy i algoritmy*, 2018, 4:5 (in Russ.).
11. Bogdanov AYu. Opyt primeneniya platformy prototipirovaniya na PLIS "Protium" dlya verifikatsii mikroprotssessorov [Experience in applying the Protium SOC prototyping platform for verification of microprocessors]. *Trudy NIISI RAN*, 2017, 7(2):46-49 (in Russ.).

INVESTIGATION OF THE 0.5-4 HZ LOW-FREQUENCY RANGE IN THE WAVE TRAIN ELECTRICAL ACTIVITY OF MUSCLES IN PATIENTS WITH PARKINSON'S DISEASE AND ESSENTIAL TREMOR

Olga S. Sushkova, Alexei A. Morozov

Kotelnikov Institute of Radioengineering and Electronics of RAS, <http://www.cplire.ru/>
Moscow 125009, Russian Federation

Alexandra V. Gabova

Institute of Higher Nervous Activity and Neurophysiology of RAS, <http://ihna.ru/>
Moscow 117485, Russian Federation

Alexei V. Karabanov, Larisa A. Chigaleychik

FSBI Research Center of Neurology, <https://www.neurology.ru/>
Moscow 125367, Russian Federation

o.sushkova@mail.ru, morozov@cplire.ru, agabova@yandex.ru, doctor.karabanov@mail.ru, chigalei4ick.lar@yandex.ru

Abstract. An investigation of the 0.5-4 Hz little-studied frequency range electromyograms (EMG) was performed in patients with Parkinson's disease (PD) and essential tremor (ET). In this frequency range, new neurophysiological regularities were revealed that were not previously described in the literature. There are statistically significant differences between groups of patients with PD/ET and a control group of subjects. A new method for analyzing wave train electrical activity of the muscles based on the wavelet analysis and ROC analysis was used. This method enables to study the time-frequency features of EMG signals in patients with PD and ET. The idea of the method is to find local maxima (that correspond to the wave trains) in the wavelet spectrogram and to calculate various characteristics describing these maxima: the leading frequency, the duration in periods, the bandwidth, the number of wave trains per second. The degree of difference of the group of patients from the control group of subjects is analyzed in the space of these parameters. ROC analysis is used for this purpose. The functional dependence of AUC (the area under the ROC curve) on the values of the bounds of the ranges of the parameters under consideration is investigated. This method is aimed at studying changes in the time-frequency characteristics (the shape) of signals including changes that are not related to the power spectral density of the signal. The application of the method allowed revealing new statistical regularities in EMG signals, which previously were not detected using standard spectral methods based on the analysis of the power spectral density of signals.

Keywords: Parkinson's disease, essential tremor, trembling hyperkinesia, electromyogram, EMG, tremor, wave trains, wavelet spectrogram

UDC 519.67, 612.8, 53.088

Bibliography - 39 references

Received 28.06.2019, *accepted* 30.06.2019

RENSIT, 2019, 11(2):225-236

DOI: 10.17725/rensit.2019.11.225

CONTENTS

1. INTRODUCTION (225)
 2. EXPERIMENTAL SETTING (228)
 3. SIGNAL ANALYSIS METHOD (228)
 4. CONCLUSION (233)
- REFERENCES (234)

1. INTRODUCTION

Preclinical diagnosis is very important for the treatment of Parkinson's disease (PD) and essential tremor (ET). Although PD and ET have been intensively studied in recent decades, the preclinical indicators of these movement disorders remain to be established

[1].

EMG signal investigations are objective methods for assessing neuromuscular function in PD and ET. Surface EMG signals are often analyzed using amplitude and spectral methods. These methods are used to measure the degree of muscle activation and fatigue. The neuromuscular function can also be measured indirectly by analyzing the tremor of the extremities that it controls. This can be done using motion sensors, such as accelerometers [2].

Usually, the frequency range below 4 Hz is not investigated in EMG, since it is considered that it is impossible to find statistically significant differences between groups of patients and healthy subjects in this range. In the EEG, the frequency ranges of theta (4-7 Hz), alpha (8-12 Hz), beta (13-24 Hz), and gamma (25-48 Hz) [3,4] are mainly studied. It is rare to find papers where the delta (1-4 Hz) range is studied in EEG [5]. In EMG, mostly studied frequency varies from 5 to 18 Hz [6]. In the works devoted to the study of tremor coherence on EMG with tremor components on EEG, ranges above 4 Hz are also studied [7]. The resting tremor itself in patients with PD is commonly studied on EMG in the classical frequency range 4-7 Hz, and essential tremor is studied in patients with ET in the frequency range from 4 to 12 Hz [8]. However, there are works in which the frequency range below 4 Hz on the EMG is still being studied. In particular, the authors of [9] are engaged in the search for the characteristics of the basal ganglia of the brain associated with tremor in movement in patients with PD.

Mathematical approaches used for the analysis of EMG in PD include spectral methods (average frequency, power fraction in certain frequency bands) [10,11], analysis

of the characteristics of bursts of EMG (quantity, amplitude, duration, and frequency) [12-15], analysis of the morphology of the EMG signal [16], and methods of nonlinear analysis of EMG [10].

Studies that analyze EMG signals are focused on analyzing the regularity of hand tremor and their low-frequency coherence in PD. In particular, it was shown in [2] that tremor in patients with PD is more regular (that is, with lower entropy) than physiological tremor measured in neurologically healthy subjects (frequencies from 1 to 1000 Hz were investigated, but significant differences were discovered only in the frequency ranges from 8 to 12 Hz and from 20 to 25 Hz). In addition, in work [2], it was shown that the tremor regularity of patients with PD is reduced due to medicament treatment and deep brain stimulation [17] (the frequency range from 1 to 8 Hz was studied). EMG coherence studies have shown that the coherence between EMG of the extensor muscles and EMG of the flexor muscles is higher for patients with PD than for healthy subjects [18].

Measurements of EMG and tremor of the limbs can be used for an objective and quantitative assessment of neuromuscular function and movement disorders in PD. In the future, they can help in the diagnosis and subsequent treatment of PD. In addition, such measurements can improve the understanding of the neurological mechanisms of the disease [19]. According to the authors of the paper [19], these measurements are still rarely used in the evaluation of PD. Since EMG is a spike (a wave of a pulsed form), according to the authors of [19], nonlinear and morphological methods can be more effective in analyzing EMG than traditionally used methods (amplitudes and average,

median frequencies, etc.). The method used in our work is non-linear, since the calculation of extremes of the wavelet spectrogram is a non-linear operation, and indirectly involves analyzing changes in the waveform. However, the method does not involve the extraction and analysis of any signal samples, as it is implemented in the classical morphological analysis of the signals. Of course, if one does not consider the wavelets as such samples.

An approach to the study of neurological diseases based on a comparison of electromyographic signals of the extensor muscles and flexor muscles was proposed in [20]. It was shown that the power spectral density of the EMG signal in the 1-30 Hz frequency range in the ulnar flexion of the hand is significantly higher in the PD group compared with the ET group [20]. However, these results were obtained by standard methods (Fourier spectra, wavelets, etc.). Note that in the paper [11], where frequency ranges above 5 Hz are studied, there was a significant positive correlation between the power ratio in the frequency range from 5 to 15 Hz of the EMG agonist signal and the UPDRS-Motor indicator (the Unified Parkinson's Disease Rating Scale), as well as a significant negative correlation between the fraction of power in the frequency range from 15 to 30 Hz and the UPDRS-Motor indicator.

In work [21], the electromyographic method of registration and a quantitative assessment of the disorders of muscular activity of the person arising in connection with motor pathology have been offered. The basis of the method is the selection of the frequency range of the EMG spectrum corresponding to the motor act and spectral analysis of signals in the selected range. The developed method was used in studies of

extrapyramidal disorders in parkinsonism and ET. The main disadvantage of this method of EMG analysis is a long measurement time necessary for the subsequent averaging (up to 20 one-minute records).

Earlier, we developed a method for analyzing the wave train electrical activity of the cerebral cortex, based on wavelet analysis and ROC analysis [22,23]. The idea of this method of analysis is in that an electroencephalogram (EEG) is considered as a set of wave trains [24]. In contrast to works on the detection of the electrical activity of one or two specific types, such as alpha spindles [25] and sleep spindles [26-31], we analyze any type of the wave train electrical activity in the cerebral cortex over a wide frequency range. In addition, we consider the wave train as a typical component of EEG, but not as a special kind of EEG signals. Previously, such an approach was proposed in [32,33].

To analyze the EMG signals, the developed signal analysis algorithm [22,23] was modified [34]. The method of analysis considered in this paper is based on the statistical analysis of wavelet spectrograms, a new method of visualizing the results of statistical analysis, and a new wave train detection algorithm in the EMG signals. In particular, an additional step of smoothing the wavelet spectrograms of signals was added to the signal analysis algorithm. Smoothing is required because the standard fast algorithms for calculating wavelets have the following problem: wavelet spectrograms (when processing signals of complex shape) are inevitably contaminated by digital artifacts (outliers and high-frequency vibrations). These artifacts can be mistakenly recognized as "wave trains" in EMG.

The use of the method of analysis of

wave train electrical activity allowed us to reveal new neurophysiological regularities in patients with PD and ET in the poorly studied frequency range 0.5-4 Hz in EMG signals.

2. EXPERIMENTAL SETTING

Data from untreated (that is, previously not taking specific medicine) patients with PD and ET in the early stages were compared with data from healthy volunteers. Note that the group of patients with PD included patients at the first stage of PD on the Hoehn and Yahr scale with left-hand tremor (9 people) and patients at the first stage of PD with right-hand tremor (11 people), 20 people in total. The number of patients with ET was 13 people. The number of healthy volunteers was 8 people. All patients and healthy volunteers were right-handed. No statistically significant differences between the ages of patients and healthy volunteers were found. EMG electrodes were located both on the outer sides of the arms, on the extensor muscles, and on the inner sides of the arms, on the flexor muscles. The surface EMG signals were recorded in a special pose of the subject. The subject was sitting in a chair, his arms were straight in front of him, and his legs were quietly on the floor. Eyes were closed during all recordings. To record the EMG, the Neuron-Spectrum-5 multifunctional 41-channel complex for the neurophysiological studies (Neurosoft Company) was used. The sampling rate of EMG was 500 Hz. For EMG, a high-pass filter with the 0.5 Hz cut-off frequency and the 50 Hz notch filter were used. In addition, the Butterworth filter with the 60-240 Hz bandwidth was applied to EMG. After filtering, the Hilbert transform was

applied to the EMG signals to compute the envelope of the signals. The duration of each record was about two minutes. Records were analyzed as is, without selecting individual areas in the signal.

3. SIGNAL ANALYSIS METHOD

For the study, the method of analysis of the wave train electrical activity of the muscles was used, based on wavelet analysis and ROC analysis [22,23]. The idea of the method is to search for local maxima ("wave trains") on the wavelet spectrogram and calculate various characteristics describing these maxima: the leading frequency of the wave trains, the duration of the wave trains in periods, the width of the wave train frequency band, the number of wave trains per second. The degree of difference in the group of patients with PD and ET from the control group of subjects in the space of these parameters is analyzed. For this, ROC analysis is used. The functional dependence of AUC (the area under the ROC curve) on the values of the bounds of the ranges of the parameters under consideration is investigated. This method is aimed at studying changes in the time-frequency characteristics (the shape) of signals, including those not related to changes in the power spectral density of the signal.

The tremor in patients in the first stage of PD, studied in this work, appears only on one side of the body. In contrast to PD, in patients with ET, tremor appears on both sides of the body at once. Further, we will conditionally call the PD patient's hand, on which the tremor manifests, as "tremor" hand and we will conventionally call the second hand as "healthy" hand.

Let us consider an example of a wave train detected by our method on the wavelet

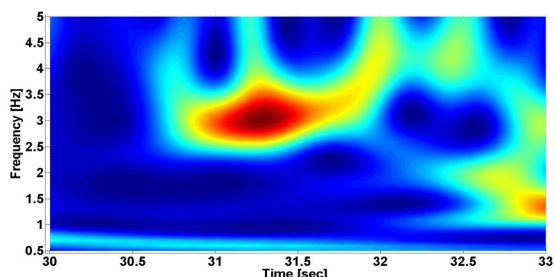


Fig. 1. A wave train in the wavelet spectrogram of the EMG signal envelope.

spectrogram of an EMG signal on the patient’s “healthy” (left) hand with the tremor of the right side of the body on the extensor muscle (**Fig. 1**). The central frequency of the wave train is 3 Hz, the signal clearly localized in time and in frequency.

The envelope of the EMG signal, which was used to calculate the spectrogram in Fig. 1, is represented in **Fig. 2**. On the signal envelope, one can see 4 periods of the wave train envelope. Note that the signal envelope is used to analyze tremor in accordance with the classical method [21], however, to calculate the signal envelope, we apply the Hilbert transform, but not signal detection. For Fig. 2, after calculating the envelope, additional filtering of the signal was applied with the 0.5-7 Hz band-pass filter to improve the signal image.

In **Fig. 3**, one can see the original EMG signal. Note that it is almost impossible to observe the investigated wave train in the original signal; therefore classical methods

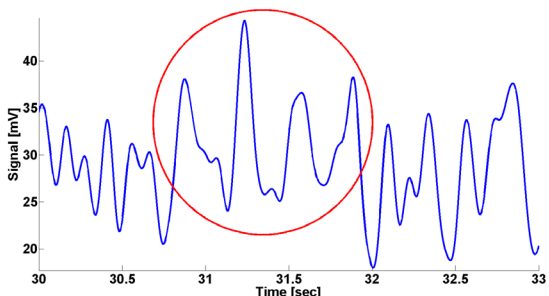


Fig. 2. The EMG signal envelope. The wave train is indicated by the red circle.

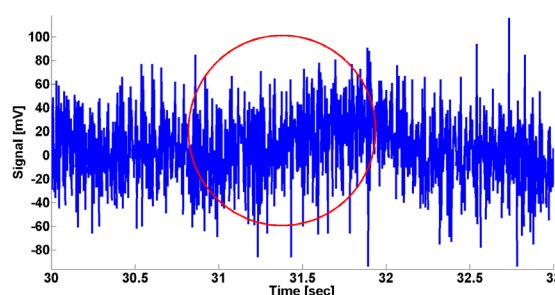


Fig. 3. The original EMG signal. The wave train is indicated by the red circle.

of morphological analysis of signals are not applicable to the analysis of these signals.

In this paper, we study the number of wave trains (per second) in the 0.5-4 Hz frequency range in EMG of patients with PD and ET. The number of wave trains is compared with the healthy subject data using special AUC-diagrams and Mann-Whitney non-parametric statistical test. A detailed description of the AUC diagrams is given in [23,24,34-39].

4. RESULTS

Statistically significant differences between the patient groups and the control group of subjects were found both on the “tremor” hands and on the “healthy” hands of patients with PD (with a tremor on the left hand and with a tremor on the right hand) and in patients with ET on both hands.

We calculated wave trains in the frequency range from 0.5 to 4 Hz for EMG signals (both for extensor muscles and flexor muscles) in each patient with PD (patients with left-hand tremor and patients with right-hand tremor were investigated separately), every patient with ET, and every healthy volunteer. From these data, AUC values were calculated for different frequency ranges in the interval from 0.5 to 4 Hz.

The frequency AUC diagram for the extensor muscles of the “tremor” left hands

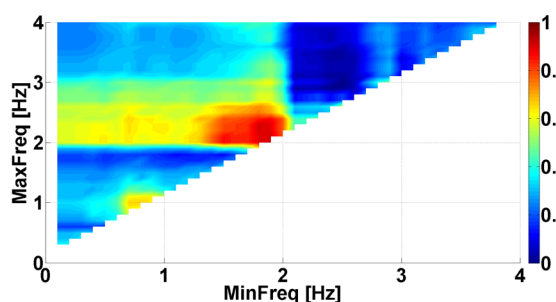


Fig. 4. An AUC diagram for extensor muscles. EMG of the left (“tremor”) hand of patients with PD. The abscissa is the lower bound of the frequency ranges. The ordinate is the upper bound of the frequency ranges. The frequencies from 0.5 to 4 Hz with the 0.1 Hz step are considered.

of patients with PD is presented in **Fig. 4**.

The blue color in the AUC diagram means that the number of wave trains in patients is less than in healthy subjects. Red color indicates that the number of wave trains in patients is greater than in healthy subjects. In the diagram in Fig. 4, pronounced regularities (red and blue areas) are visible in the frequency ranges 0.1-1.8 Hz (a blue spot), 1.8-2.3 Hz (a red spot), and 2.1-3.9 Hz (a blue spot). Let's perform a statistical analysis of the number of wave trains per second using the Mann-Whitney test.

The p-values (the level of statistical significance) for extensor muscles for patients with PD (for “tremor” hands and “healthy” hands) and for patients with ET are listed in **Table 1**. Statistically significant differences were found for extensor muscles in the frequency ranges 0.1-1.8 Hz (the blue spot), 1.8-2.3 Hz (the red spot), and 2.1-3.9 Hz (the

Table 1

The p-values for the extensor muscles.

Frequency ranges, Hz	PD, left "tremor" hand	PD, right "healthy" hand	PD, left "healthy" hand	PD, right "tremor" hand	ET, left hand	ET, right hand
0.1-1.8	0.02	not significant	not significant	0.01	not significant	not significant
1.8-2.3	0.003	not significant	not significant	not significant	not significant	not significant
2.1-3.9	0.001	not significant	not significant	0.01	not significant	not significant

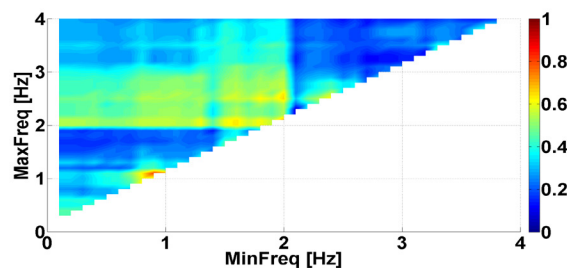


Fig. 5. An AUC diagram for extensor muscles. EMG of the right (“tremor”) hand of patients with PD. Along the axes, frequencies are similar to Fig. 4.

blue spot) only on the “tremor” hands of the patients with PD.

The frequency AUC diagram for the extensor muscles of the “tremor” right hands of the patients with PD is presented in **Fig. 5**. The results of the statistical analysis and AUC diagrams demonstrate that on the left and right “tremor” hands of the patients with PD, similar regularities are observed, however, on the right “tremor” hands these regularities are less pronounced. Statistically significant differences in the considered frequency ranges were not found in patients with ET. This indicates that the observed regularities are specific for PD.

A comparison of the parameters of the tremor in the extensor muscles and flexor muscles of patients with PD and ET is of great interest. Frequency AUC diagrams for the flexor muscles of the “tremor” arms of the patients with PD are shown in **Fig. 6** and **7**.

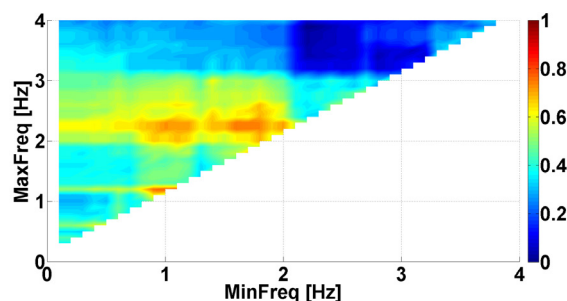


Fig. 6. An AUC diagram for flexor muscles. EMG of the left (“tremor”) hand of patients with PD. Along the axes, frequencies are similar to Fig. 4.

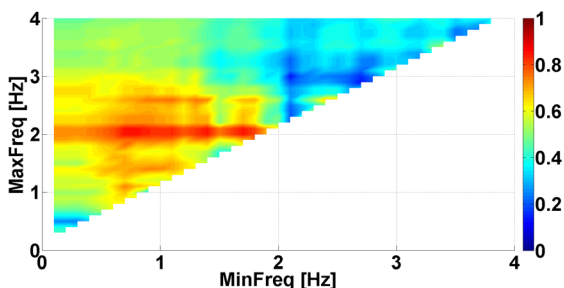


Fig. 7. An AUC diagram for flexor muscles. EMG of the right (“tremor”) hand of patients with PD. Along the axes, frequencies are similar to Fig. 4.

Frequency AUC diagrams for the flexor muscles of the “healthy” hands of the patients with PD are shown in **Fig. 8** and **9**.

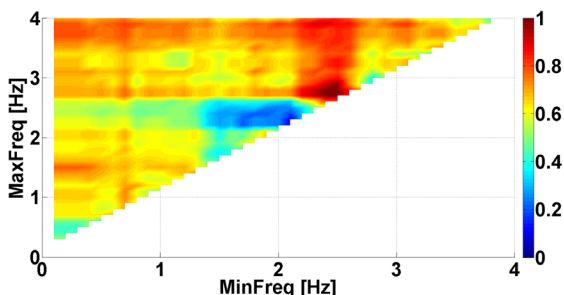


Fig. 8. An AUC diagram for flexor muscles. EMG of the right (“healthy”) hand of patients with PD. Along the axes, frequencies are similar to Fig. 4.

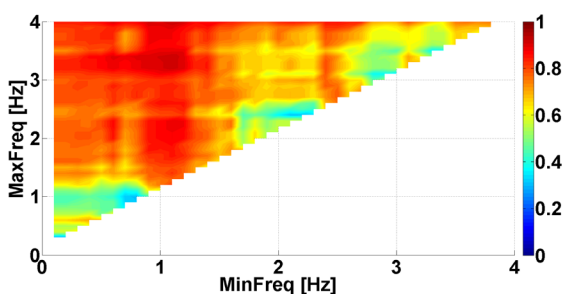


Fig. 9. An AUC diagram for flexor muscles. EMG of the left (“healthy”) hand of patients with PD. Along the axes, frequencies are similar to Fig. 4.

Unlike the extensor muscles, there are differences in the flexor muscles not only in the “tremor” hands but also in the “healthy” hands of the patients with PD. The following frequency ranges were analyzed: 1.1-3.1 Hz (a red spot on the AUC diagram on the left “healthy” hand of the patients with PD), 2.1-3 Hz (a blue spot on the AUC diagram

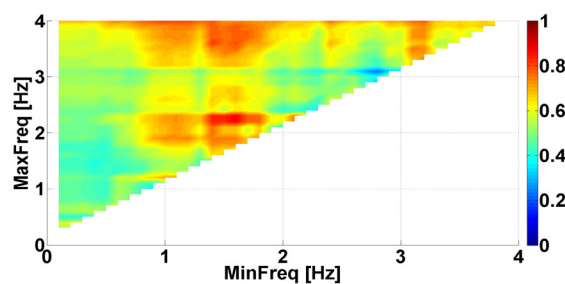


Fig. 10. An AUC diagram for flexor muscles. EMG of the left hand of patients with ET. Along the axes, frequencies are similar to Fig. 4.

on the right “tremor” hand of the patients with PD), and 2.2-3.9 Hz (a blue spot on the AUC diagram on the left “tremor” hand of the patients with PD). In addition, the frequency range 1.6-2.3 Hz was analyzed, because it corresponds to a red spot on the AUC diagram on the left hand of the patients with ET (see **Fig. 10**). The AUC diagram on the right hand of the patients with ET (see **Fig. 11**) also contains regularities, but in this paper, they are not considered because it was discovered that they are not specific for ET.

The p-values for the flexor muscles for the patients with PD and ET are shown in **Table 2**. For the flexor muscles, statistically significant differences were found in the frequency ranges 1.1-3.1 Hz (the red spot), 2.1-3 Hz (the blue spot), and 2.2-3.9 Hz (the blue spot). Statistically significant differences in ET were found in the 1.6-2.3 Hz frequency range (the red spot), but only in the left hand. Thus, specific regularities were found for PD and ET. However, these regularities are

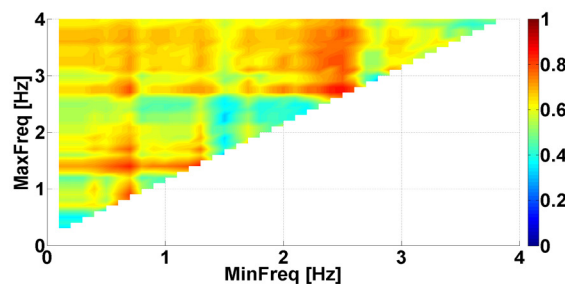


Fig. 11. An AUC diagram for flexor muscles. EMG of the right hand of patients with ET. Along the axes, frequencies are similar to Fig. 4.

Table 2

The p-values for the flexor muscles.

Frequency ranges, Hz	PD, left "tremor" hand	PD, right "healthy" hand	PD, left "healthy" hand	PD, right "tremor" hand	ET, left hand	ET, right hand
1.1-3.1	not significant	not significant	0.006	not significant	not significant	not significant
1.6-2.3	not significant	not significant	not significant	not significant	0.005	not significant
2.1-3.0	not significant	not significant	not significant	0.006	not significant	not significant
2.2-3.9	0.00008	0.01	not significant	not significant	not significant	not significant

observed in different frequency ranges in different hands of the patients; this makes it difficult to use them for the differential diagnosis of PD and ET.

AUC diagrams were computed to compare the extensor muscles and the flexor muscles of the subjects (see Fig. 12 and 13). These diagrams are interesting because regularities in the “healthy” hands of patients with PD are observed. Two distinct frequency ranges were found in which the number of wave trains in the extensor muscles and flexor muscles differs: 1.8-3.9 Hz (a blue spot) and 2.1-2.5 Hz (a red spot). The p-values are given in Table 3. Statistically significant differences were found between the extensor muscles and the flexor muscles in both frequency ranges. There were no statistically significant differences in ET.

The found regularities on the “healthy” hands of the patients with PD are of

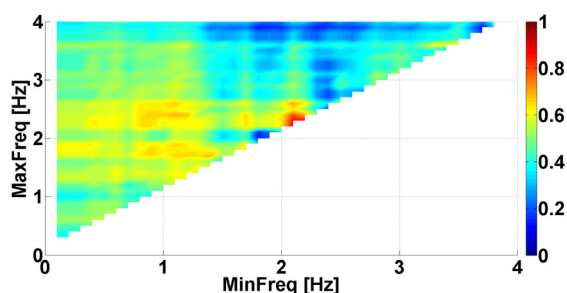


Fig. 12. An AUC diagram based on a comparison of extensor muscles with flexor muscles of the “healthy” right hands of patients with PD. Along the axes, frequencies are similar to Fig. 4.

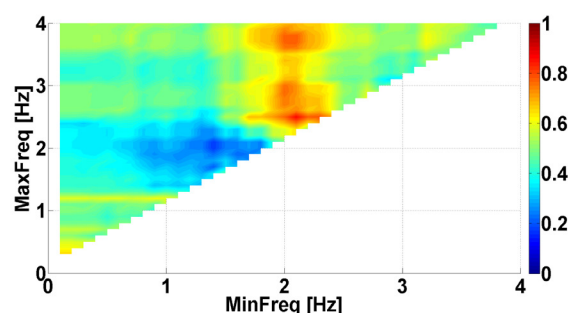


Fig. 13. An AUC diagram based on a comparison of extensor muscles with flexor muscles of the “healthy” left hands of patients with PD. Along the axes, frequencies are similar to Fig. 4.

considerable interest for early diagnosis of PD because the “healthy” hands of patients with PD can be used as a model of the processes occurring at the preclinical stages of PD.

5. CONCLUSION

A new method of exploratory data analysis was developed. This method involves calculating AUC values and non-parametric testing of statistical hypotheses to detect significant differences in the characteristics of electrical “wave train” activity of muscles. A detailed analysis of the data of patients with Parkinson's disease and essential tremor in the poorly studied frequency range 0.5-4 Hz was carried out. Statistically significant differences from the control group of subjects were found both in the “tremor” hands and in the “healthy” hands of the patients. It was demonstrated that the analysis of patients with Parkinson's disease using surface EMG

Table 3

The p-values for the comparison of the extensor muscles and the flexor muscles.

Frequency ranges, Hz	PD, left "tremor" hand	PD, right "healthy" hand	PD, left "healthy" hand	PD, right "tremor" hand	ET, left hand	ET, right hand
1.8-3.9	not significant	0.008	not significant	not significant	not significant	not significant
2.1-2.5	not significant	not significant	0.003	not significant	not significant	not significant

on the extensor muscles and flexor muscles gives different results; differences between the extensor muscles and flexor muscles in patients with ET were not detected. Found regularities in EMG can be useful for early diagnosis of Parkinson's disease.

It can be assumed that wave trains in the 0.5-4 Hz frequency range reflect the increased electrical activity of the muscle fiber groups that make up the muscles. The obtained results indicate an individual picture of frequency characteristics in the 0.5-4 Hz frequency range for specific diseases, which can be useful for the differential diagnosis of PD and ET.

Parkinson's disease is a systemic disease, and manifestations of this disease include impaired muscle tone, both in the shaking hands and non-shaking hands. The reason for this is in that, due to the disease, the reciprocal (cross) connections and the downward effect of the extrapyramidal system on the segmental level of tone control (alpha motoneurons, etc.) of the muscles are disrupted. The harmonious work of the agonists/antagonist muscle groups is violated. Identification of these changes allows determining the degree of decompensation from the "healthy", intact side, and also allows predicting the clinical manifestation of focal neurological symptoms. Monitoring of these changes can be used as a promising prognostic parameter of decompensation and an assessment of the effectiveness of a specific treatment.

The application of the developed signal analysis method allowed us to identify new regularities in the EMG signals that previously could not be detected using standard spectral methods based on the analysis of the power spectral density of the signals.

ACKNOWLEDGMENTS

The authors are grateful to the corresponding member of RAS S.N. Illarioshkin for helping with the work. The work was carried out within the framework of the state task. The study was supported by the scholarship of the President of the Russian Federation to young scientists and graduate students No. SP-5247.2018.4 and partially was supported by the Russian Foundation for Basic Research in the framework of the research project No. 18-37-20021.

REFERENCES

1. Meigal AY, Rissanen SM, Tarvainen MP, Airaksinen O, Kankaanpää M, Karjalainen PA. Non-linear EMG parameters for differential and early diagnostics of Parkinson's disease. *Frontiers in neurology*, 2013, 4:135.
2. Rissanen SM, Kankaanpää M, Meigal A, Tarvainen MP, Nuutinen J, Tarkka IM, Airaksinen O, Karjalainen PA. Surface EMG and acceleration signals in Parkinson's disease: feature extraction and cluster analysis. *Medical & biological engineering & computing*, 2008, 46(9):849-858.
3. Herz DM, Florin E, Christensen MS, Reck C, Barbe MT, Tscheuschler MK, Tittgemeyer M, Siebner HR, Timmermann L. Dopamine replacement modulates oscillatory coupling between premotor and motor cortical areas in Parkinson's disease. *Cerebral cortex*, 2013, 24(11):2873-2883.
4. Timmermann L, Florin E, Reck C. Pathological cerebral oscillatory activity in Parkinson's disease: a critical review on methods, data and hypotheses. *Expert review of medical devices*, 2007, 4:651-661.
5. Chung JW, Burciu RG, Ofori E, Coombes SA, Christou EA, Okun MS, Hess CW, Vaillancourt DE. Beta-band oscillations in the supplementary motor cortex are

- modulated by levodopa and associated with functional activity in the basal ganglia. *NeuroImage: clinical*, 2018, 19:559-571.
6. Caviness JN, Shill HA, Sabbagh MN, Evidente VG, Hernandez JL, Adler CH. Corticomuscular coherence is increased in the small postural tremor of Parkinson's disease. *Movement disorders: official journal of the Movement Disorder Society*, 2006, 21(4):492-499.
 7. Holobar A, Gallego JÁ, Kranjec J, Rocon E, Romero JP, Benito León J, Pons J, Glaser V. Motor unit-driven identification of pathological tremor in electroencephalograms. *Frontiers in neurology*, 2018, 9:879.
 8. Joundi RA, Brittain JS, Jenkinson N, Green AL, Aziz T. Rapid tremor frequency assessment with the iPhone accelerometer. *Parkinsonism & related disorders*, 2011, 17(4):288-290.
 9. Burgess JG, Warwick K, Ruiz V, Gasson MN, Aziz TZ, Brittain JS, Stein J. Identifying tremor-related characteristics of basal ganglia nuclei during movement in the Parkinsonian patient. *Parkinsonism & related disorders*, 2010, 16(10):671-675.
 10. Fattorini L, Felici F, Filligoi G, Trabbalesi M, Farina D. Influence of high motor unit synchronization levels on non-linear and spectral variables of the surface EMG. *Journal of neuroscience methods*, 2005, 143(2):133-139.
 11. Robichaud JA, Pfann KD, Vaillancourt DE, Comella CL, Corcos DM. Force control and disease severity in Parkinson's disease. *Movement disorders*, 2005, 20(4):441-450.
 12. Flament D, Vaillancourt D, Kempf T, Shannon K, Corcos D. EMG remains fractionated in Parkinson's disease, despite practice-related improvements in performance. *Clinical neurophysiology*, 2003, 114(12):2385-2396.
 13. Pfann KD, Buchman AS, Comella CL, Corcos DM. Control of movement distance in Parkinson's disease. *Movement disorders*, 2001, 16(6):1048-1065.
 14. Robichaud JA, Pfann KD, Comella CL, Brandabur M, Corcos DM. Greater impairment of extension movements as compared to flexion movements in Parkinson's disease. *Experimental brain research*, 2004, 156(2):240-254.
 15. Robichaud JA, Pfann KD, Comella CL, Corcos DM. Effect of medication on EMG patterns in individuals with Parkinson's disease. *Movement disorders*, 2002, 17(5):950-960.
 16. Rissanen S, Kankaanpää M, Tarvainen MP, Nuutinen J, Tarkka IM, Airaksinen O, Karjalainen PA. Analysis of surface EMG signal morphology in Parkinson's disease. *Physiological measurement*, 2007, 28(12):1507.
 17. Sturman MM, Vaillancourt DE, Metman LV, Bakay RA, Corcos DM. Effects of subthalamic nucleus stimulation and medication on resting and postural tremor in Parkinson's disease. *Brain*, 2004, 127(9):2131-2143.
 18. Vaillancourt DE, Newell KM. The dynamics of resting and postural tremor in Parkinson's disease. *Clinical neurophysiology*, 2000, 111(11):2046-2056.
 19. Valls-Solé J, Valldeoriola F. Neurophysiological correlate of clinical signs in Parkinson's disease. *Clinical neurophysiology*, 2002, 113(6):792-805.
 20. Ivanova EO, Fedin PA, Brutyan AG, Ivanova-Smolenskaya IA, Illarioshkin SN. Analysis of tremor activity of antagonist muscles in essential tremor and Parkinson's

- diseases. *Neurological journal*, 2014, 4:11-18.
21. Andreyeva EA, Khutorskaya OE. Spektral'nyy metod analiza elektromiograficheskoy aktivnosti myshts [Spectral method for the analysis of muscle electromyographic activity]. Moscow, Nauka Publ., 1987, p. 192.
 22. Sushkova OS, Morozov AA, Gabova AV. A method of analysis of EEG wave trains in early stages of Parkinson's disease. *Proceedings of International Conference on Bioinformatics and Systems Biology (BSB-2016)*, IEEE, 2016, pp. 1-4.
 23. Sushkova OS, Morozov AA, Gabova AV. Data Mining in EEG Wave Trains in Early Stages of Parkinson's Disease. *Advances in Soft Computing. MICAI 2016. Lecture Notes in Computer Science*, 2017, 10062:403-412.
 24. Sushkova OS, Morozov AA, Gabova AV, Karabanov AV. Data mining in EEG wave trains in early stages of Parkinson's disease. *Proceedings of the 12th Russian-German Conference on Biomedical Engineering*, 2016, pp. 80-84.
 25. Lawhern V, Kerick S, Robbins KA. Detecting alpha spindle events in EEG time series using adaptive autoregressive models. *BMC neuroscience*, 2013, 14:101, <http://www.biomedcentral.com/1471-2202/14/101>.
 26. Parekh A, Selesnick I, Rapoport D, Ayappa I. Sleep spindle detection using time-frequency sparsity. *IEEE Signal Processing in Medicine and Biology Symposium*, IEEE, Philadelphia, PA, 2014, pp. 1-6.
 27. O'Reilly C, Nielsen T. Automatic sleep spindle detection: benchmarking with fine temporal resolution using open science tools. *Frontiers in human neuroscience*, 2015, 9:353, <http://doi.org/10.3389/fnhum.2015.00353>.
 28. Huupponen E, Clercq WD, Gómez-Herrero G, Saastamoinen A, Egiazarian K, Värri A, Vanrumste B, Vergult A, Huffel SV, Paesschen WV, Hasan J, Himanen SL. Determination of dominant simulated spindle frequency with different methods. *Journal of neuroscience methods*, 2006, 156:275-283.
 29. Nonclercq A, Urbain C, Verheulpen D, Decaestecker C, Bogaert PV, Peigneu P. Sleep spindle detection through amplitude-frequency normal modelling. *Journal of neuroscience methods*, 2013, 214:192-203.
 30. Jaleel A, Ahmed B, Tafreshi R, Boivin DB, Streletz L, Haddad N. Improved spindle detection through intuitive pre-processing of electroencephalogram. *Journal of neuroscience methods*, 2014, 233:1-12.
 31. Camilleri TA, Camilleri KP, Fabri SG. Automatic detection of spindles and K-complexes in sleep EEG using switching multiple models. *Biomedical signal processing and control*, 2014, 10:117-127.
 32. Zhirmunskaya EA. *Klinicheskaya elektroentsefalografiya (tsifry, gistogrammy, illyustratsii)* [Clinical electroencephalography (numbers, histograms, illustrations)]. Moscow, Mezhotraslevoy nauchno-issledovatel'skiy inzhenerno-tekhnologicheskiiy tsestr "Skan" Publ., 1993.
 33. Obukhov YV, Korolev MS, Gabova AV, Kuznetsova GD, Ugrumov MV. Method of early encephalographic diagnostics of Parkinson disease. *Patent no. 2484766 Russian Federation*, 20.06.2013.
 34. Sushkova OS, Morozov AA, Gabova AV, Karabanov AV. Investigation of Surface EMG and Acceleration Signals of Limbs' Tremor in Parkinson's Disease Patients

- Using the Method of Electrical Activity Analysis Based on Wave Trains. *Advances in Artificial Intelligence. Proceedings of 16th Ibero-American Conference on AI*, Eds Simari GR, Ferme E, Segura FG and Melquiades JAR. Springer International Publishing, 2018, pp. 253-264.
35. Sushkova OS, Morozov AA, Gabova AV, Karabanov AV. Primenenie metoda analiza vspleskoobraznoy elektricheskoy aktivnosti mozga dlya vyyavleniya osobennostey EEG patsientov na ranney stadii bolezni Parkinsona [Application of brain electrical activity burst analysis method for detection of EEG characteristics in the early stage of Parkinson's disease]. *S.S. Korsakov journal of neurology and psychiatry*, 2018, 118(7):45-48, (in Russ.).
36. Sushkova OS, Morozov AA, Gabova AV, Karabanov AV. An investigation of the specificity of features of early stages of Parkinson's disease obtained using the method of cortex electrical activity analysis based on wave trains. *Journal of physics: conference series*, 2018, 1096:012078.
37. Sushkova OS, Morozov AA, Gabova AV. *Proc. 13th International Conference on Signal-Image Technology & Internet-Based Systems (SITIS)*, IEEE, 2017, pp. 168-172.
38. Sushkova OS, Morozov AA, Gabova AV. Development of a method of analysis of EEG wave packets in early stages of Parkinson's disease. *Proceedings of the International Conference "Information Technology and Nanotechnology" (ITNT-2016)*, CEUR Workshop Proceedings, 2016, 1638:681-690. DOI: 10.18287/1613-0073-2016-1638-681-690.
39. Sushkova OS, Morozov AA, Gabova AV, Karabanov AV. Issledovanie problemy mnozhestvennogo sravneniya pri analize vspleskoobraznoy elektricheskoy aktivnosti myshts u patsientov s bolezniyu Parkinsona [Investigation of the multiple comparisons problem in the analysis of the wave train electrical activity of muscles in Parkinson's disease patients]. *Proceedings of ITNT-2019: V International Conference and Youth School "Information Technologies and Nanotechnologies"*, May 21-24, 2019. Ed. V.A. Fursov. Samara, New Technique, 2019, Vol. 4: Data Science, pp. 329-337 (in Russ.).

NEW APPROACH TO THE DETECTION OF EPILEPTIFORM ACTIVITY IN EEG SIGNALS AND METHODS TO DIFFERENTIATE EPILEPTIC SEIZURES FROM CHEWING ARTIFACTS

Ivan A. Kershner, Yuri V. Obukhov

Kotelnikov Institute of Radioengineering and Electronics of RAS, <http://www.cplire.ru/>
11/7, Mokhovaya str., Moscow 125009, Russian Federation

Mikhail V. Sinkin

Sklifosovsky Scientific Research Institute for Emergency Medicine of Moscow Department of Health,
<https://sklif.mos.ru/>

3, Sukharevskaya sq., Moscow 129090, Russian Federation

ivan_kershner@mail.ru, mvsinkin@gmail.com, yuvobukhov@mail.ru

Abstract. The new approach based on Morlet wavelet spectrograms ridges analysis and allowing automatic detecting different activity in long term EEG signals is developed. To distinguish epileptiform activity from chewing artifacts two approaches are proposed. The quantitative characteristics of events wavelet spectrogram ridges were studied, as well as the frequency of broadband peaks at time points corresponding to peak-wave epileptiform activity on the one hand, and the peaks of myographic activity during chewing on the other hand. Signs by which one can qualitatively divide the group containing epileptic discharges from chewing artifacts were found.

Keywords: EEG; wavelet spectrogram; ridges; epileptic seizure; chewing artifacts; seizure detection

UDC 004.67, 004.93"11

Bibliography - 8 references

RENSIT, 2019, 11(2):237-242

Received 28.06.2019, accepted 2.07.2019

DOI: 10.17725/rensit.2019.11.237

CONTENTS

1. INTRODUCTION (237)
 2. APPROACH (238)
 3. SIGNAL PROCESSING (238)
 4. CONCLUSION (241)
- REFERENCES (241)

1. INTRODUCTION

During data analysis of long-term electroencephalographic (EEG) of patients with traumatic brain injury neurophysiologists manually mark up the EEG records by comparing individual fragments of EEG with epileptic seizures, chewing artifacts, etc. That is time-consuming process when marking daily and longer EEG signals. Automatic marking of epileptic and epileptiform seizures in EEG signals of patients with posttraumatic epilepsy, as well as differentiation seizures fragments from chewing artifacts will help to neurophysiologists accelerate the process of detecting epileptiform seizures.

The problem of detecting epileptic seizures

of various types [1], as well as various artifacts [2] is widely known and remains relevant. For example, in [3] attention is paid to the finding of muscle artifacts, including chewing artifacts through the study of amplitude and frequency components. In paper proposes to divide the signal into epochs and calculate the minimum, maximum amplitude values and the first derivative, the absolute and relative powers of the Fourier spectrum, the boundary frequency of the spectrum, up to which the sum of the spectral power is at the level of 95% of the total spectral power of the entire spectrum. Then the parameters were compared with the parameters of the control record, which does not contain artifacts. Control record is selected manually for each EEG record. It should be noted that the method is aimed at finding artifacts with a frequency of more than 25 Hz.

The article [4] presents the use of support vector machine (SVM) to distinguish different types of artifacts. The features for SVM are obtained from EEG and gyroscopic channels.

Records are collected from 7 people who do not have any neurological and psychiatric disorders. The subject had to make five kinds of movements similar to motion artifacts. Each action records within 30 seconds, then 20 seconds of a break as a control record without motion artifacts. Automatic detection of artifacts by the method is not provided.

The paper [5] describes application of Bayes statistics to real-time recognition of epileptic seizures in with the removal of artifacts associated with wire breakage and muscle activity outside the range of 12-25 Hz. Alpha activity (8-13 Hz), characteristic of both artifacts and epileptic seizures (3-25 Hz), is marked as seizure, i.e. differentiation between epileptic seizure and artifacts in this frequency range was not carried out.

The article [6] presents the method of recognition of epileptic seizures based on Fourier analysis. The method works fast enough that it can be used in the system of informing doctors about the onset of the seizure, but at the same time, the authors provide information that the analysis of EEG signals by their method did not recognize epileptic seizures in EEG of 3 patients. Neurophysiology experts at the same time mark 3, 5 and 6 epileptic seizures for them.

We propose a new approach based on Morlet wavelet spectrograms ridges analysis for the automatic detection of all suspicious fragments of electroencephalographic signals of patients with posttraumatic epilepsy on long term EEG records (a day or more) with the possibility of their further classification.

2. APPROACH

Since EEG signals contain both artifacts and epileptic discharges, there is a need for their automatic detection. It is proposed to find the beginning and the end of signal fragments in which suspicious activity with increased values of the power spectral density is observed by segmenting the Morlet wavelet spectrogram ridges. For that purpose, we calculate the

histogram of the ridges of the wavelet spectrograms. For fragmented ridges, frequency and time parameters are calculated, according to which it is possible to classify the fragments of the ridge into the corresponding event in the future. In addition, sections of wavelet spectrograms in frequency are considered to identify additional features of the difference between epileptic seizures and chewing artifacts.

3. SIGNAL PROCESSING

Consider the approach to detect specific events step by step on the example of a signal containing an epileptic seizure, obtained in the Department of neurosurgery research of Sklifosovsky Scientific Research Institute for Emergency Medicine (Fig. 1).

Initially, the signal is filtered by 2nd order Butterworth bandpass filter with a bandwidth of 0.5 to 22 Hz, as well as notch filters multiples of 25 Hz to remove noise and network interference. Then the wavelet spectrogram S is calculated as follows [7]:

$$S(\tau, f) = |W(\tau, f)|^2, \tag{1}$$

$$W(\tau, f) = \sqrt{f} \int x(t) \psi^*((t - \tau)f) dt, \tag{2}$$

$$\psi(\eta) = \frac{1}{\sqrt{\pi F_b}} \exp(2\pi i F_c \eta) \exp\left(-\frac{\eta^2}{F_b}\right), \tag{3}$$

where ψ^* is the complex conjugation of the Morlet mother function ψ , $F_c = F_b = 1$, x is the original signal, and W is the wavelet transform.

At each t_i time moment in the frequency-power spectral density (PSD) plane, the maximum values of the PSD are calculated. Then the phase characteristic P of the signal x is calculated:

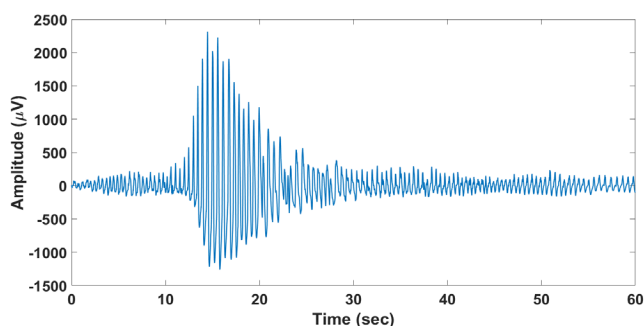


Fig. 1. The signal of EEG containing an epileptic seizure.

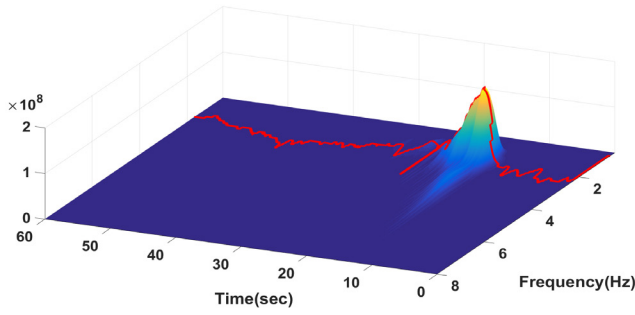


Fig. 2. Wavelet spectrogram of an EEG signal containing an epileptic seizure, projected on the frequency-time-PSD axis with maximum PSD values (red line).

$$P(k) = \tau_k f_r(\tau_k), \quad (4)$$

where $f_r(\tau_k)$ is the instantaneous frequency of the signal at the time τ_k . Moreover, $f_r(\tau_k)$ coincides with the frequency value at the point of the wavelet spectrogram ridge at the time τ_k , if the following condition is satisfied [8]:

$$\frac{\tau^2 F_b}{2} \frac{d^2 P}{d\tau^2} \ll 1. \quad (5)$$

Further, the ridge points that do not satisfy the inequality (5) wavelet spectrograms should be removed from the consideration. The line connecting points with the maximum values of PSD on the wavelet spectrogram, which have the property of phase stationarity (5), is called the ridge of the wavelet spectrogram. **Fig. 2** shows a wavelet spectrogram in the frequency-time-power spectral density projection with a calculated ridge. It shows a peak in the time period from 10 to 30 seconds, which neurophysiologists refer to an epileptic seizure.

Further, the histogram of the number of fragments depending on the selected PSD

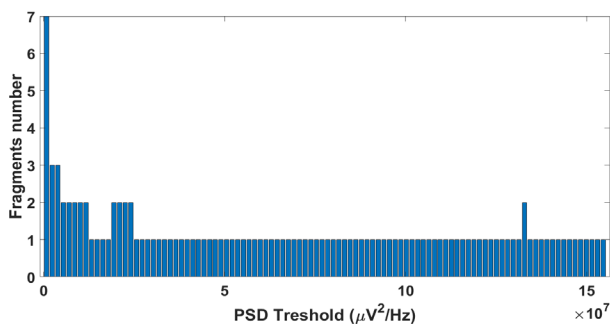


Fig. 3. Histogram of fragments of the ridge of the wavelet spectrogram for the threshold values of spectral power density.

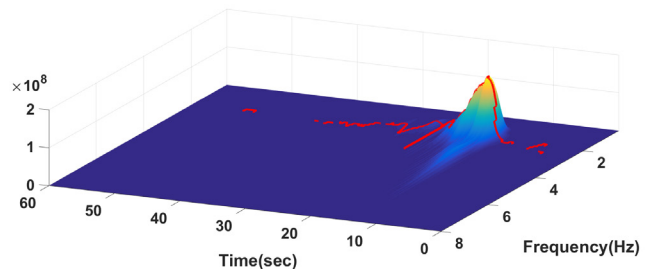


Fig. 4. A fragmented ridge of the wavelet spectrogram of an EEG signal containing an epileptic seizure, with remote points in accordance with the formula (5).

threshold value is analyzed to separate the background and activity (**Fig. 3**). The threshold at which the maximum number of ridge fragments is selected. At **Fig. 3** $PSD_{\text{threshold}} = 1.2 \cdot 10^7 \mu V^2 / \text{Hz}$. Fragments of the ridge, in this case, are such points of the ridge, which PSD values are above the threshold and are next to each other in sequence number. An example of a fragmented ridge is shown in **Fig. 4**.

The following are calculated for each fragment: duration; maximum and minimum values of frequency and spectral power density; time at which the maximum value of the spectral power density was recorded; arithmetic mean and standard deviation of frequency.

Table 1 shows the values of the calculated parameters for EEG records containing epileptic seizures and chewing artifacts.

From the data given in the table, the maximum and minimum frequency values and the mean frequency in chewing artifacts are lower than in

Table 1

Parameters calculated for epileptic seizures (ES) and chewing artifacts (CA).

Activity	$T_b - T_e$	F_{\min}	F_{\max}	F_{std}	F_{mean}	$\frac{F_{\text{std}}}{F_{\text{mean}}}$	PSD_{\max}	PSD_{\min}	$T_{P_{\max}}$
CA	100.5-103.8	0.50	0.50	0.00	0.50	0.00	5.08E+06	1.03E+06	102.42
CA	198-201	0.70	1.00	0.07	0.87	0.08	1.38E+06	2.37E+05	199.21
CA	270.2-273.9	0.50	0.50	0.00	0.50	0.00	9.95E+06	2.10E+06	272.09
CA	3-9.39	0.50	0.70	0.06	0.62	0.10	2.65E+05	6.05E+04	7.83
CA	16.49-22.49	0.50	0.50	0.00	0.50	0.00	3.98E+05	7.83E+04	19.30
CA	26.29-30.09	0.50	0.70	0.08	0.64	0.12	3.53E+05	6.01E+04	28.38
ES	133.68-139.9	1.60	1.90	0.08	1.79	0.04	1.43E+08	3.28E+07	135.44
ES	85.5-92.1	2.80	6.20	0.56	4.09	0.14	7.27E+06	4.85E+05	90.65
ES	92.41-98	2.10	3.60	0.32	3.08	0.10	4.31E+06	3.23E+05	93.22

T_b and T_e are the start and end time of activity; F_{\min} and F_{\max} – minimum and maximum frequency value; F_{mean} and F_{std} is the mean and the standard deviation; PSD_{\max} and PSD_{\min} – minimum and maximum values of PSD; $T_{P_{\max}}$ – time, when there was higher PSD value.

Table 2
Parameters calculated for epileptic seizures.

$T_b - T_e$	F_{min}	F_{max}	F_{std}	F_{mean}	$\frac{F_{std}}{F_{mean}}$	PSD_{max}	PSD_{min}	T_{Pmax}
1.99 - 7.99	0.60	0.80	0.07	0.67	0.10	3.02E+04	9.63E+03	6.78
122.49 - 124.49	0.90	1.60	0.21	1.21	0.17	3.67E+04	1.13E+04	123.55
128.2 - 129.39	1.70	2.00	0.09	1.78	0.05	3.25E+04	1.11E+04	128.77
356.49 - 358.79	0.70	1.10	0.13	0.96	0.14	2.40E+04	7.90E+03	357.77
83.7 - 85.29	1.20	2.40	0.42	1.82	0.23	1.78E+05	3.06E+04	84.73
98.7 - 98.39	3.90	4.40	0.14	4.08	0.03	2.32E+05	9.22E+04	99.03
100 - 100.39	3.20	3.80	0.20	3.45	0.06	1.79E+05	9.04E+04	100.27
100.79 - 101.19	3.50	4.30	0.19	3.92	0.05	1.36E+05	6.59E+04	101.03
102 - 102.69	2.90	3.30	0.09	3.08	0.03	2.93E+05	9.11E+04	102.35
103.79 - 104.29	3.30	4.90	0.53	3.77	0.14	2.82E+05	9.90E+04	104.09
104.79 - 105.29	2.20	2.80	0.14	2.55	0.05	1.61E+05	1.01E+05	105.02
106.09 - 106.49	2.90	5.30	0.99	3.99	0.25	1.29E+05	8.47E+04	106.20
113.59 - 118.09	1.70	2.40	0.12	2.15	0.06	2.41E+05	3.83E+04	115.75

T_b and T_e are the start and end time of activity; F_{min} and F_{max} – minimum and maximum frequency value; F_{mean} and F_{std} are the mean and the standard deviation; PSD_{max} and PSD_{min} – minimum and maximum values of PSD ; T_{Pmax} – time, when there were maximal PSD value.

epileptic discharges.

If we take $F_{min} = 0.7$, $F_{max} = 1$, $F_{mean} = 0.87$ as the threshold values, then the two groups are well separated. Consider the parameters of epileptic discharges only (Table 2).

At selected thresholds $F_{min} = 0.7$, $F_{max} = 1$, $F_{mean} = 0.87$, only one epileptic seizure from table 2 has characteristics similar with chewing artifacts parameters. In the remaining 12 cases, epileptic seizures satisfy the specified conditions.

Another approach to differentiate epileptic activity from chewing artifacts is to analyze the broadband peaks of wavelet. The peaks of the EEG signal during the seizure and chewing are sharp, so the wavelet spectrograms at the time of these peaks are broadband. Therefore, in addition to calculating the parameters of the

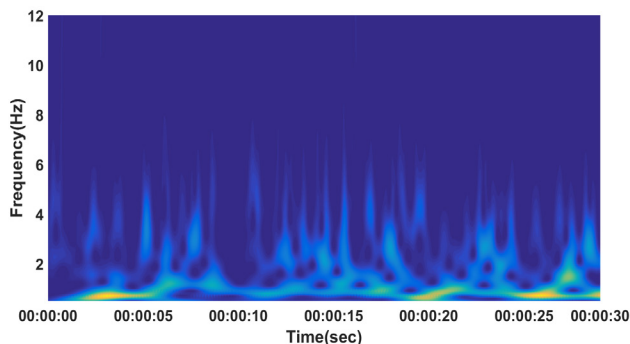


Fig. 5. Wavelet spectrogram of an EEG signal containing a chewing artifact.

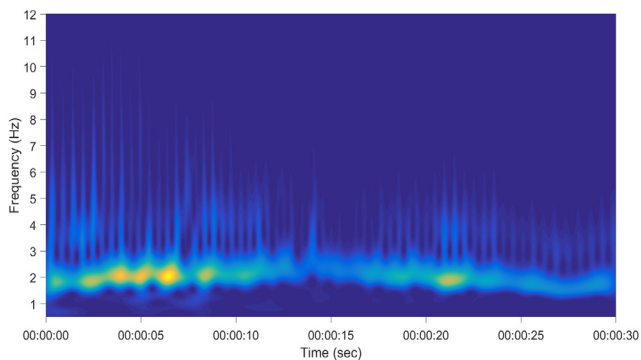


Fig. 6. Wavelet spectrogram of an EEG signal containing an epileptic seizure.

ridges, the frequency of broadband peaks of EEG wavelet spectrograms was studied.

We describe the new approach by the example of fragments of EEG wavelet spectrograms with a chewing artifact and epileptic seizure presented in Fig. 5 and 6. From the matrix S (1) were selected the values in the wavelet rows corresponding to the frequency F_{cur} from 3.5 Hz to 6 Hz with step 0.5 Hz over the entire time interval:

$$V_{cur}(\tau_k) = S(\tau_k, F_{cur}), \tau_k = 0 : T. \tag{6}$$

Vector V_{cur} represents a row of the wavelet spectrogram at the frequency F_{cur} . For the resulting vectors V_{cur} calculated Fourier spectra. Fig. 7 shows examples of Fourier spectra of V_{cur} for epileptic seizure and chewing artifact at $F_{cur} = 4$ Hz on wavelet spectrogram. For each Fourier spectrum, the frequency at which the main peak and half-width of the main peak are located at half-height for each frequency level of the wavelet spectrogram was calculated.

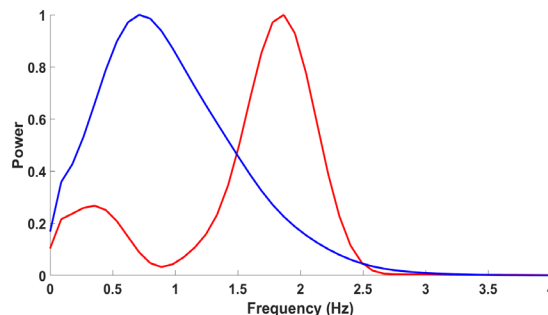


Fig. 7. Fourier spectra at the frequency of the wavelet spectrogram EEG $F_{cur} = 4$ Hz. The red line is the Fourier Spectrum for an epileptic seizure, the blue line for a chewing artifact.

Table 3

The parameters of the Fourier spectra of the wavelet spectrograms rows of the EEG with chewing and epileptic seizure.

Wavelet spectrogram frequency, Hz	Peak frequency (chewing)	Peak frequency (epileptic seizure)	Half-width of peak (chewing)	Half-width of peak (epileptic seizure)
3.5	0.71	1.86	1.06	0.62
4	0.71	1.86	1.2	0.64
4.5	0.71	1.86	1.25	0.69
5	0.71	1.86	1.33	0.65
5.5	0.71	1.95	1.51	0.67
6	0.71	1.95	1.91	0.63

Table 3 shows the frequency at which the main peak and the half-width of the main peak are located at half-height, depending on the wavelet spectrogram frequency.

Fig. 7 $F_{cur} = 4$ Hz shows differences between epileptic seizures and chewing artifacts in the frequency of the Fourier spectrum peak, for example, for the chewing artifact it is at 0.71 Hz, and for the epileptic seizure at 1.86 Hz. This can be interpreted as the presence of peak-wave activity in an epileptic seizure. The half-width of the Fourier spectrum peaks in the chewing artifact is almost 2 times greater than that of an epileptic seizure. This may mean greater stability of the peak-wave activity period during the seizure compared to chewing. With an increase in the frequency of wavelet spectrograms of EEG signals, the frequency ratio of the Fourier peaks of the epileptic seizure to chewing remains approximately the same. While the half-width of the Fourier spectrum peaks increases for chewing artifacts.

4. CONCLUSION

A new approach for detection epileptic seizures and chewing artifacts in electroencephalographic signals based on the analysis of their wavelet spectrograms and finding the parameters of wavelet spectrogram ridges is presented. It was found that the maximum value of the frequency and the standard deviation of the frequency of the wavelet spectrogram ridge can be attributed

to the epileptic discharge or chewing artifact. We studied the wavelet spectrogram rows at frequencies larger than ridge frequency. It is shown that on Fourier spectra of wavelet spectrogram rows at frequencies from 3.5 to 6 Hz at epileptic discharge, the frequency of the peak of the wavelet spectrogram rows is more than 2.5 times higher than the frequency of the Fourier peak of the wavelet spectrogram for chewing. The half-width of the Fourier picks of rows of the wavelet spectrograms of the EEG on the frequencies above 3.5 Hz at chewing artifacts in 1.5-3 times more compared to the half-width of the Fourier spectra in epileptic seizure. This meaning greater stability of the peak-wave activity period during the seizure compared to chewing. By combining those two approaches it is possible to reliably differentiate an epileptic seizure from a chewing artifact.

ACKNOWLEDGMENTS

The work was carried out within the framework of the state task and partially was supported by the Russian Foundation for Basic Research, the project No 18-29-02035.

REFERENCES

1. Fergus P, Hignett D, Hussain A, Al-Jumeily D, Abdel-Aziz K. Automatic epileptic seizure detection using scalp EEG and advanced artificial intelligence techniques. *BioMed research international*, 2015, vol. 2015, article ID 986736, 17 pages; doi: 10.1155/2015/986736.
2. Islam MK, Rastegarnia A, Yang Z. Methods for artifact detection and removal from scalp EEG: A review. *Neurophysiologie Clinique/ Clinical Neurophysiology*, 2016, 46(4-5):287-305.
3. Van de Velde M, van Erp G, Cluitmans PJ. Detection of muscle artefact in the normal human awake EEG. *Electroencephalography and clinical Neurophysiology*, 1998, 107(2):149-158.
4. O'Regan S, Faul S, Marnane W. Automatic detection of EEG artefacts arising from head movements using EEG and gyroscope signals. *Medical engineering & physics*, 2013,

- 35(7):867-874.
5. Saab ME, Gotman J. A system to detect the onset of epileptic seizures in scalp EEG. *Clinical Neurophysiology*, 2005, 116(2):427-442.
 6. Hopfengärtner R, Kasper B, Graf W, Gollwitzer S, Kreiselmeyer G, Stefan H, Hamer H. Automatic seizure detection in long-term scalp EEG using an adaptive thresholding technique: a validation study for clinical routine. *Clinical Neurophysiology*, 2014, 125(7):1346-1352.
 7. Mallat SG. *A Wavelet Tour of Signal Processing, The Sparse Way*. Burlington, Academic Press, 2009, 562 p.
 8. Tolmacheva RA, Obukhov YuV, Polupanov AF, Zhavoronkova LA. New Approach to Estimation of Interchannel Phase Coupling of Electroencephalograms. *Journal of Communications Technology and Electronics*, 2018, 63(9):1070-1075.

ESTIMATION OF INTER-CHANNEL PHASE SYNCHRONIZATION OF EEG SIGNALS IN THE RIDGES OF THEIR WAVELET SPECTROGRAMS IN PATIENTS WITH TRAUMATIC BRAIN INJURY

Renata A. Tolmacheva, Yuri V. Obukhov

Kotelnikov Institute of Radioengineering and Electronics of RAS, <http://www.cplire.ru/>
11/7, Mokhovaya str., Moscow 125009, Russian Federation

Lyudmila A. Zhavoronkova

Institute of Higher Nervous Activity and Neurophysiology of RAS, <http://www.ihna.ru/>
5a, Butlerova str., Moscow 117485, Russian Federation

tolmacheva@ya.ru, yuvobukhov@mail.ru, lzhavoronkova@hotmail.com

Abstract. Identical inter-channel phase coherency of electroencephalogram (EEG) signals is determined for healthy subjects during cognitive and motor tests. EEG signal phase is evaluated at the points of its wavelet-spectrogram ridge. Areas of interest of the cortex at cognitive and motor tests for group of healthy subjects are determined. Inter-channel EEG phase coherency for patients after a traumatic brain injury are represented.

Keywords: electroencephalogram, wavelet-spectrogram, ridge, phase synchronization

UDC 53.088

Bibliography - 11 references

RENSIT, 2019, 11(2):243-248

Received 18.06.2019, accepted 27.06.2019

DOI: 10.17725/rensit.2019.11.243

CONTENTS

1. INTRODUCTION (243)
 2. METHODS (244)
 3. RESULTS (245)
 4. CONCLUSION (247)
- REFERENCES (247)

1. INTRODUCTION

Usually coherency or phase connectivity of EEG signals use to the estimation of inter-channel EEG connectivity [1-3]. The coherency $Cob_{xy}(f)$ is determined by the normalized complex cross correlation of signals x and y :

$$C_{xy}(f) = \frac{S_{xy}(f)}{(S_{xx}(f)S_{yy}(f))^{1/2}}, \quad (1)$$

$$Cob_{xy}(f) = |C_{xy}(f)|. \quad (2)$$

In coherent analysis, due to the modulus of normalized complex cross correlation $C_{xy}(f) = 1$, the coherency $Cob_{xy}(f)$ is averaged in different of time intervals and in a certain frequency interval that is determined using neurophysiological data. Normally, such intervals correspond to the delta (2–4 Hz), theta (4–8 Hz), and alpha (8–12 Hz) EEG rhythms. Such an averages and the presence of the threshold level of coherence that is used to select the phase-coupled

pairs of signals are disadvantages of the coherent analysis that lead to instability in the determination of the inter-channel phase synchronization of EEG signals. These disadvantages are considered in detail in [4]. The validity of the coherent analysis of essentially non-stationary EEG signals is questioned [2, 4].

Analytical signal also can be used for the estimation of phase connectivity $x^*(t) = x(t) + iH(x(t))$, where $H(x(t))$ is the Hilbert transform. The phase synchronization of two signals takes place when [5]:

$$|\Phi_{x,y}(t)| \leq const, \quad (3)$$

where $\Phi_{x,y}(t) = n\Phi_x(t) - m\Phi_y(t)$, Φ is the phase of the signal, n, m are integers.

We proposed an approach to the estimation of the inter-channel phase connectivity of the EEG [6] based on the phases calculation and comparison of the signals at the points of the ridges of their wavelet spectrograms having the property of stationarity of the phase, which does not exist in both of the above approaches. Under this the approach, phase-coupled pairs of EEG signals are considered for the group of healthy subjects and for the group of patients with traumatic brain injury during two cognitive and motor tests.

2. METHODS

The ridges of the wavelet spectrograms are defined as the points of the stationary phase [7] that is in them the derivative of the phase with respect to time is equal to the frequency. In [8], devoted to computer modeling of smooth music, it was shown that at the points of time- and frequency-asymptotic ridges of wavelet spectrograms the phase is stationary in the sense that at these points $d\Phi/dt \approx \omega$.

The EEG signal responds the asymptotic properties under the conditions:

$$\left| \frac{d\Phi(t)}{dt} \right| \gg \left| \frac{1}{A(t)} \frac{dA(t)}{dt} \right|, \left| \frac{1}{A(t)} \frac{dA(t)}{dt} \right| \ll \left| \frac{1}{\psi(t)} \frac{d|\psi(t)|}{dt} \right|. \quad (4)$$

The approach to estimating the inter-channel phase connectivity of the EEG at the points of the ridges of their wavelet-spectrograms with the stationary phase is considered as an inverse task to the problem of modeling ridges. In [6] it is shown that for the amplitude and phase of the amplitude-modulated signal $x(t) = A(t)e^{i\Phi(t)}$ is true:

$$A(t) \approx |W(t, f_r)| \text{ and } \Phi(t) \approx \arctan \left(\frac{\text{Im}W(t, f_r)}{\text{Re}W(t, f_r)} \right). \quad (5)$$

Based on this, first we find the ridge with the maximum value $|W(t, f_r)|$ at each reference point τ_i of the Morlet wavelet:

$$W(\tau, f) = \sqrt{f} \int x(t)\psi((t - \tau)f)dt, \quad (6)$$

$$\psi(\eta) = \frac{1}{\sqrt{\pi F_b}} e^{2\pi i F_c \eta} e^{-\frac{\eta^2}{F_b}}, \quad (7)$$

where $F_b = F_c = 1$.

Then, we calculate the phase difference of two signals $x(t)$ and $y(t)$ at the points of the ridges t_k of their wavelet spectra and select *const* to estimate their phase synchronization.

In this case, the points of wavelet spectrograms with nonstationary phase are not included in the estimation of the phase of signals. However, such points are used in the estimation of coherence and phase with the aid of the Hilbert transform and coherency approach [1-3]. When the ridge points do not satisfy the condition for asymptotic ridges (4), we obtain errors in the calculations of the phase difference. However, we assume that such an error is significantly less than the errors related to the averaging of the phase difference in a certain interval of the ridge frequencies. After elimination

the frequency range of the processed ridge, we employ the above algorithm to select the next ridge with a lower power spectral density in a different frequency range.

The international system of the location of scalp electrodes «10–20%» is used to the EEG record (Fig. 1). The records of 19-channel EEG were analyzed, therefore the number of pairs of channels is 171 for the group of the healthy subjects (8 people) and for the group of the patients with traumatic brain injury (5 people).

The sampling frequency of the EEG was 250 Hz in the processing of EEG signals. The original signals were recorded with a high-pass filter with cut-off frequency of 0.5 Hz, a low pass filter with a cut-off frequency of 70 Hz. Then, a 50 Hz notch filter and a Butterworth filter were used. The signals were filtered by a fourth-order Butterworth bandpass filter with a bandwidth of 2 to 10 Hz. The duration of every EEG record was 60 seconds. Also, the removing of outliers in the EEG signals was with the Huber’s X84 method [9].

Fig. 2 shows an example of the power spectral density of Morlet wavelet spectrograms in a pair of EEG channels with selected points of the maximum spectral power density (ridge). Fig. 3 shows the phases time dependencies of two EEG signals $x(t)$ and $y(t)$ at the points of the ridges of their wavelet spectrograms.

Then, we plot the histograms of values of the phase difference of two signals $x(t)$ and $y(t)$ as in [5].

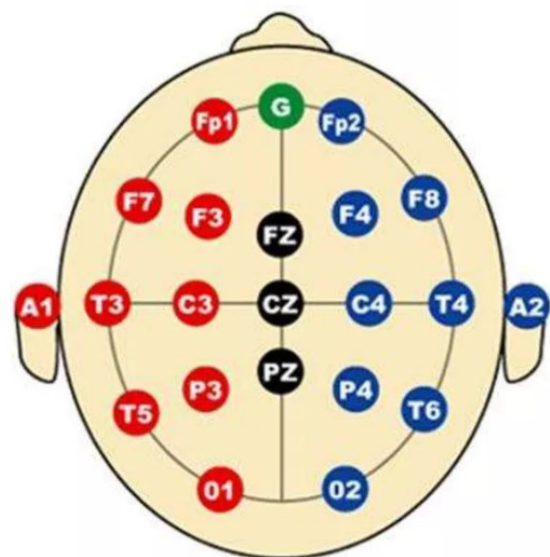


Fig. 1. The international system of the location of scalp electrodes «10–20%».

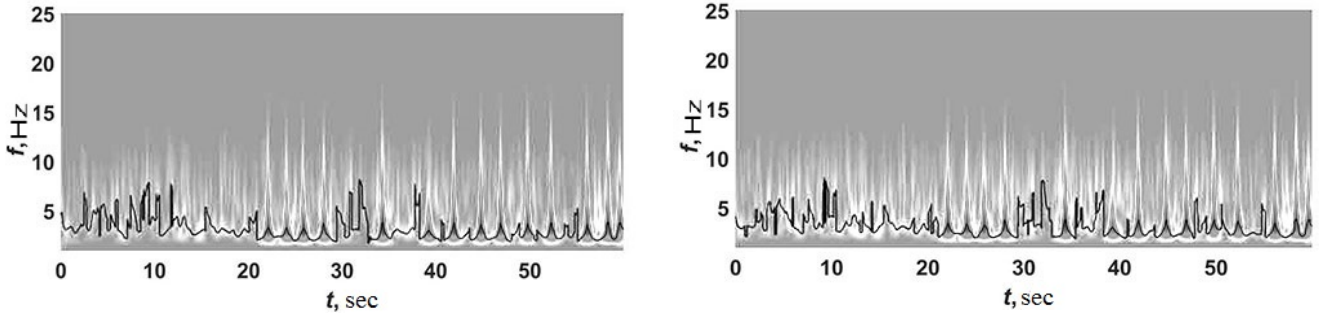


Fig. 2. Morlet wavelet spectrograms of the signal for a pair of the EEG channels with the selected ridge: a) first channel; b) second channel.

Fig. 4 represents the normalized histograms $\rho_{x,y} = n_{x,y}/N$, where $n_{x,y}$ is number of reference points of ridges with the discretization of the histogram $|\Delta\Phi_{x,y}(t_k)| < 0.05\pi$, N is a total number of EEG signal reference points during the test. The first pair of channels Fp1-Fp2 (Fig. 4a) can be referred to a phase-coupled pair. Another pair Fp1-O2 (Fig. 4b) can be referred to a phase-unconnected pair. Fig. 4a shows that $\rho_{x,y} < 0.1$ can be considered as a background. We consider the threshold $\rho_{x,y}^{thr} = 0.1$ and we will assume that the values of the portions of the ridge points above it will correspond to the phase-coupled pairs of channels. Note that the phase difference of two EEG channels (e.g., Fp1-Fp2) can be used to characterize the phase-locking dynamics. Fig. 5 presents the plot of the phase difference for two channels of the EEG signal (Fp1-Fp2) vs. time.

Distributions graphs of the maximum values of portions $\max \rho_{x,y}$ over pairs of EEG channels, based on the histograms obtained (Fig. 4), were arranged in the ascending order $\max \rho_{x,y}$ without tests, with the cognitive calculation-logical test, with the cognitive spatial-pattern test and with the motor test are represented in Fig. 6.

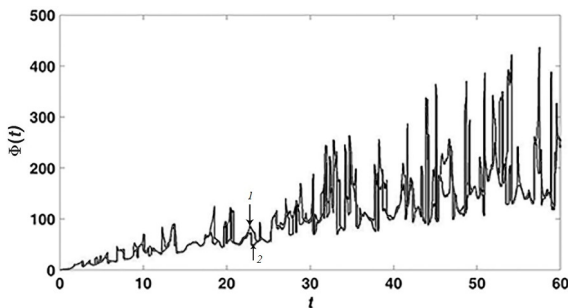


Fig. 3. Dependences of phases on time of two EEG channels. Line 1 is the phase of EEG signal of FP1 channel. 2 – the phase of EEG signal of FP2 channel.

3. RESULTS

By the new approach of estimation [10], the inter-channel EEG the phase synchronization during two cognitive (calculation-logical and spatial-pattern) and motor tests for the group healthy subjects (8 people) and for the group patients with traumatic brain injury are considered. During the cognitive calculation-logical test, doctor randomly called some items that belong to the category "clothes" or "food" to the subject. During the test, the subject counts in the mind the quantity of items belonging to one of these categories. At the end of the test, he declares the result of quantity of items. When performing the cognitive spatial-pattern test, the doctor randomly called the time. The subject must imagine in the mind the dial of the clock and the position of the clock hands on it in accordance with the time mentioned. If both clock hands are in the same half of the dial, he says "yes," and if they are in different halves, he keeps silent. When performing the motor test, the subject stands on a stabilographic platform. The position of his center of gravity is displayed on the screen. He must hold center of gravity inside a circle of a certain diameter. The duration of every test was 60 seconds. The EEG record was performed both during the tests and without them.

From the dependences of Fig. 6 it can be distinguished phase-coupled pairs of the EEG

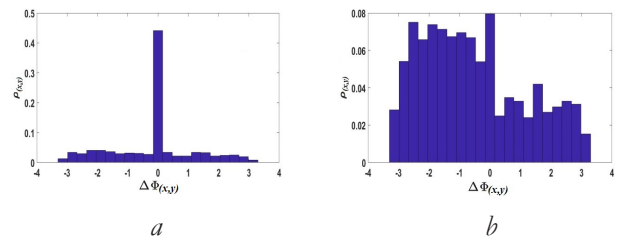


Fig. 4. Histograms of portions $\rho_{x,y}$ for the phase difference at ridge points of the wavelet spectrograms for two EEG channels: a) phase-coupled pair of EEG channels; b) uncoupled pair of EEG channels.

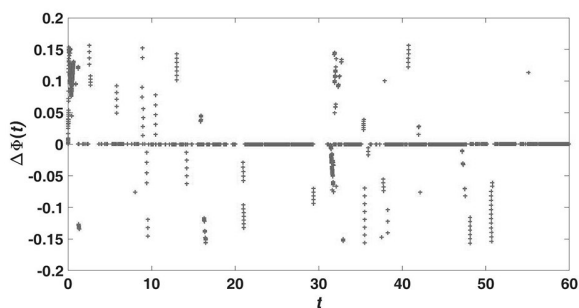


Fig. 5. The phase difference of two EEG signals (Fp1–Fp2) vs. a time.

channels that appear only during the test, by comparing the phase-coupled pairs of the EEG record without the test and at the time of the EEG records during one of the tests. Phase-coupled pairs that are absent in EEG records without tests and that appear only during tests are shown in Fig. 7 for the group of the healthy subjects and in Fig. 8 for the group of patients with traumatic brain injury.

Based on the obtained pairs of EEG channels (Fig. 6), it is possible to find phase-coupled pairs of the EEG channels that appear in a group of 8 healthy subjects during the cognitive calculation-logical test, the cognitive spatial-pattern test and motor test (Fig. 7).

Fig. 7 shows that the greater number of the phase-coupled pairs of the EEG channels that appear in the group of the healthy subjects during the cognitive calculation-logical test is in the left hemisphere. And, the greater number of the phase-coupled pairs of the EEG channels that appear in the group of the healthy subjects during the cognitive spatial-pattern test is in the right hemisphere. In accordance with published works, the prefrontal regions of the left

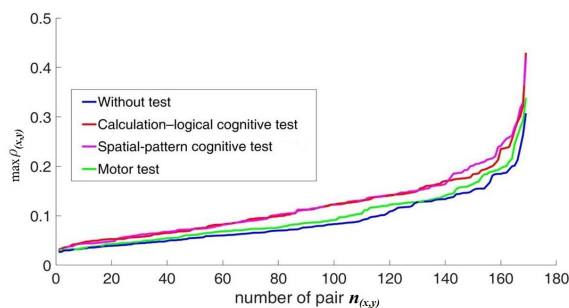


Fig. 6. Distributions graphs of the maximum values of portions $\max \rho_{x,y}$ over pairs of EEG channels arranged in the ascending order $\max \rho_{x,y}$. Numbers of pairs EEG channels are plotted on the abscissa. Purple line is the EEG record without test; red line is the EEG record with the calculation-logical cognitive test; blue line is the EEG record with the spatial-pattern cognitive test; green line is the EEG record with the motor test.

and right hemispheres are predominantly activated in the calculation-logical and spatial-pattern tests, respectively for healthy subjects [11]. Our method confirms this.

Also, a larger number of phase-coupled pairs reflects the different efforts required to perform each of the tests, which, according to the complexity of performing from easy to difficult, can be arranged in the following sequence: motor test – calculation-logical cognitive test – spatial-pattern cognitive test.

Fig. 8 shows phase-coupled pairs of channels for the group of patients with traumatic brain injury (5 people). Phase-coupled pairs of EEG channels for each patient are represented by special color.

Fig. 8 represents that phase-coupled pairs that appear in the group of patients with traumatic brain injury practically are absent. Coincident phase-coupled pairs are represented in only two patients during the cognitive calculation-logical test: Fp1 – Fp2

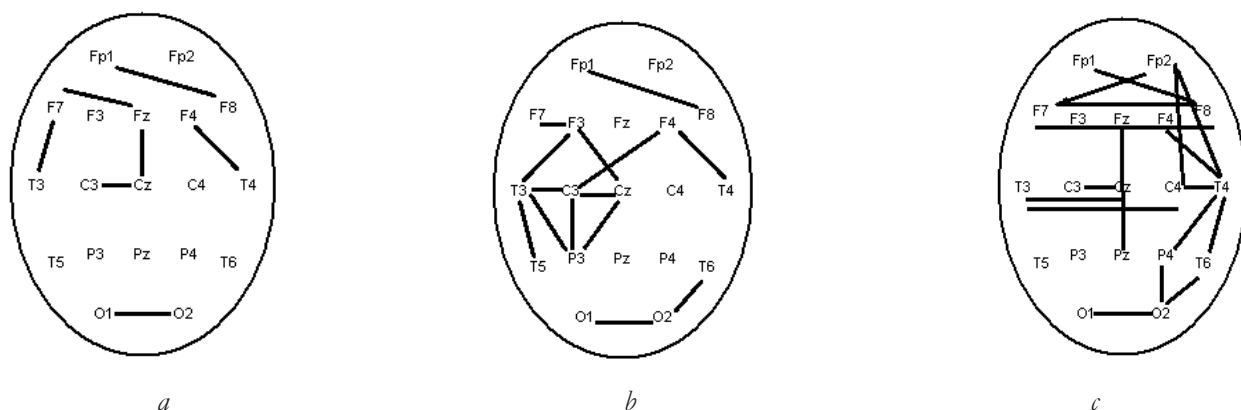


Fig. 7. Phase-coupled pairs that appear in the group of 8 healthy subjects during calculation-logical cognitive test, spatial-pattern cognitive test and motor test. a) motor test; b) calculation-logical cognitive test; c) spatial-pattern cognitive test.

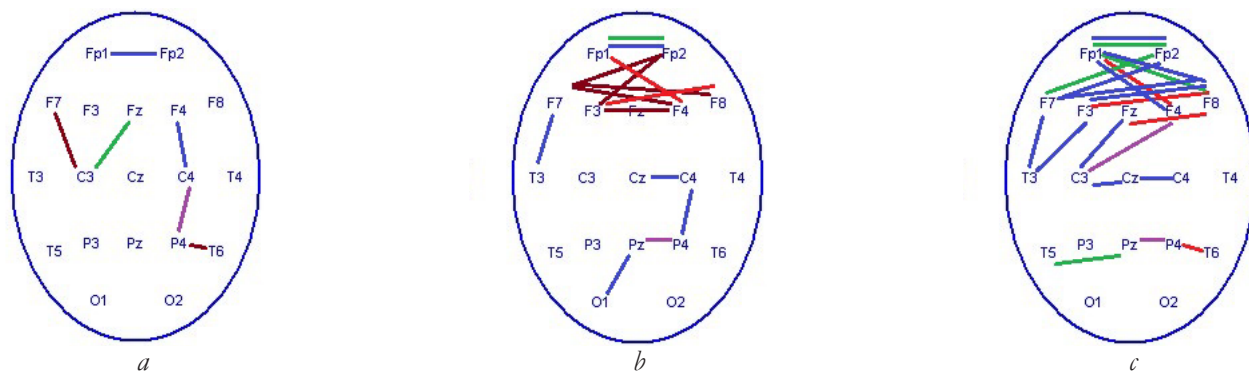


Fig. 8. Phase-coupled pairs that appear in the group 5 patients with traumatic brain injury during calculation–logical cognitive test, spatial-pattern cognitive test and motor test. a) motor test; b) calculation–logical cognitive test; c) spatial-pattern cognitive test. Phase-coupled pairs of EEG channels for each patient are represented by special color.

and coincident phase-coupled pairs are represented in three patients during the cognitive spatial-pattern test: Fp1-Fp2, Fp1-F8, Fp2-F7, F3- F8 и Fp1-F4. These are EEG channels of the frontal region of the brain. The activation of the left hemisphere during the performance of the cognitive calculation-logical test is absent by patients with traumatic brain injury. Also, the activation of the right hemisphere during the performance of the cognitive spatial-pattern test is absent by patients with traumatic brain injury.

4. CONCLUSIONS

By the new approach of the estimation the inter-channel phase synchronization of the EEG signals in different channels, based on the calculation and comparison of the phases of the signals at the points of the wavelet spectrograms ridges, phase-coupled pairs of EEG channels that appear for the group of 8 healthy subjects during two cognitive and motor tests are considered. Areas of interest of the cortex at two cognitive (calculation-logical and spatial-pattern) and motor tests for healthy subjects are determined. The prefrontal regions of the left hemisphere are predominantly activated in the calculation–logical cognitive test for healthy subjects, but these regions aren’t activated for patients with traumatic brain injury. The prefrontal regions of the right hemisphere are predominantly activated in the spatial-pattern cognitive test for healthy subjects, but these regions aren’t activated for patients with traumatic brain injury. The definition of phase-coupled pairs of EEG signals can be useful for the monitoring the treatment of people with traumatic brain injury. The recovery of phase-coupled EEG pairs can be used as indicator of proper treatment.

ACKNOWLEDGMENTS

The work was carried out within the framework of the state task and partially was supported by the Russian Foundation for Basic Research, the project no. 18-07-00609.

REFERENCES

1. Wending F, Ansari-Asl K, Bartolomei F, Senhadji L. From EEG signals to brain connectivity: a model based evaluation of interdependence measures. *Journal of Neuroscience Methods*, 2009, 183(1):9-18.
2. Nolte G, Bai O, Wheaton L, Mari Z, Vorbach S, Hallett M. Identifying true brain interaction from EEG data using the imaginary part of coherency. *Clin. Neurophysiol.*, 2004, 115:2292-2307.
3. Zhan Y, Halliday D, Jiang P, Liu X, Feng J. Detecting time-dependent coherence between non stationary electrophysiological signals. A combined statistical and time-frequency approach. *Journal of Neuroscience Methods*, 2006, 156:322-332.
4. Kulaichev A. Ob informativnosti kogerentnogo analiza [On the informativeness of coherent analysis.]. *Zh. Vysshei Nerv. Deyatel’nosti im. I. P. Pavlova*, 2009, 59(6):766-775 (in Rbss.).
5. Tass P, Rosenblum MG, Weule J, Kurths J, Pikovsky A, Volkmann J, Schnitzler A, Freund H-J. Detection of n:m Phase Locking from Noisy Data: Application to Magnetoencephalography. *Physical Review Letters*, 1998, 81(15):3291-3294.
6. Tolmacheva RA, Obukhov YuV, Polupanov AF, Zhavoronkova LA. New Approach to Estimation of Interchannel Phase Coupling of Electroencephalograms. *Journal of Communications Technology and Electronics*, 2018, 63(9):1070-1075.
7. Mallat SG. *A Wavelet Tour of Signal Processing. The Sparse Way*. Burlington, Academic Press, 2009,

- 562 p.
8. Guillemain P, Kronland-martinet R. Characterization of Acoustic Signals Through Continuous Linear Time-Frequency Representations. *Proc. IEEE*, 1996, 84(4):561-585.
 9. Hampel FR, Ronchetti EM, Rousseeuw PJ, Stahel WA. Robust Statistics: The Approach Based on Influence Functions. Wiley, 1986, 526 p.
 10. Obukhov YuV, Tolmacheva RA, Polupanov AF, Zhavoronkova LA. On an approach to assessing the inter-channel phase synchronization of electroencephalogram signals. *Proc. Intern. Conf. Information Technology and Nanotechnology (ITNT-2018, Samara, Russia, April 24-27, 2018)*. Samara, CEUR, 2018, pp. 84-88; <http://ceur-ws.org/Vol2212/paper11.pdf>.
 11. Zhavoronkova L, Shevtsova T, and Maksakova O. *How Does Human Brain Simultaneously Solve Two Problems?* LAP LAMBERT, Academic Publ., Saarbrücken, 2017.